



# Biomedical applications of polarimetric imaging contrast. Initial studies for scattering media and human tissues

Maria Rosaria Antonelli

## ► To cite this version:

Maria Rosaria Antonelli. Biomedical applications of polarimetric imaging contrast. Initial studies for scattering media and human tissues. Medical Physics [physics.med-ph]. Ecole Polytechnique X, 2011. English. NNT : . pastel-00652201

**HAL Id: pastel-00652201**

**<https://pastel.hal.science/pastel-00652201>**

Submitted on 15 Dec 2011

**HAL** is a multi-disciplinary open access archive for the deposit and dissemination of scientific research documents, whether they are published or not. The documents may come from teaching and research institutions in France or abroad, or from public or private research centers.

L'archive ouverte pluridisciplinaire **HAL**, est destinée au dépôt et à la diffusion de documents scientifiques de niveau recherche, publiés ou non, émanant des établissements d'enseignement et de recherche français ou étrangers, des laboratoires publics ou privés.

---

# BIOMEDICAL APPLICATIONS OF POLARIMETRIC IMAGING CONTRAST. INITIAL STUDIES FOR SCATTERING MEDIA AND HUMAN TISSUES

by

Maria Rosaria Antonelli

A Dissertation Submitted In the Fulfillment of the Requirements

For the Degree of

DOCTOR IN PHYSICS

from the Graduate School

ÉCOLE POLYTECHNIQUE

PARIS 2011

## Commission

BOURG-HECKLY Geneviève	AnBioPhy, Université Pierre et Marie Curie	President
SAINT-JALMES Hervé	LTSI, Université de Rennes 1	Reviewer
TUALLE Jean-Michel	LPL, Université Paris 13	Reviewer
GUYOT Steve	LiSSi-UPEC, Université Paris 12	Examiner
JACQUES Steven L.	D&BME, OHSU of Portland	Examiner
PALANGE Elia	DIEI, Università degli studi dell'Aquila	Examiner
DE MARTINO Antonello	École polytechnique	Supervisor
NOVIKOVA Tatiana	École polytechnique	Co-Supervisor



# Contents

<b>List of publications</b>	<b>5</b>
<b>Acknowledgements</b>	<b>7</b>
<b>General introduction</b>	<b>9</b>
<b>1 Light polarization formalism</b>	<b>13</b>
1.1 Introduction . . . . .	13
1.2 Totally polarized states . . . . .	14
1.2.1 The polarization ellipse . . . . .	16
1.2.2 The Jones formalism . . . . .	17
1.3 The Stokes formalism for partially polarized states . . . . .	21
1.3.1 The degree of polarization . . . . .	24
1.3.2 The Poincaré sphere representation . . . . .	26
1.4 The Mueller matrix . . . . .	28
1.4.1 Definition and general properties . . . . .	28
1.4.2 Elementary polarization components . . . . .	31
1.4.3 Decompositions of Mueller matrices into elementary components . . . . .	34
1.5 Conclusion . . . . .	35
<b>2 Polarized light propagation in scattering media</b>	<b>37</b>
2.1 Introduction . . . . .	37
2.2 Single scattering . . . . .	38
2.2.1 Scattering cross-section for spherical scatterers . . . . .	38
2.2.2 Scattering of polarized waves . . . . .	40
2.2.3 Short-cutting the Mie theory: the scattering regimes . . . . .	43
2.3 Multiple scattering . . . . .	46
2.3.1 The essential assumptions . . . . .	46
2.3.2 The usual scattering parameters . . . . .	47
2.3.3 The Radiative Transfer Equation . . . . .	50
2.4 Methods of solution of the RTE . . . . .	53
2.5 Conclusion . . . . .	56
<b>3 Monte Carlo solution of the VRTE</b>	<b>57</b>
3.1 Introduction . . . . .	57
3.1.1 Overview of the applications of Monte Carlo method . . . . .	57
3.1.2 Application to the radiative transfer problem . . . . .	59
3.2 The algorithm . . . . .	61
3.2.1 Generation of random numbers with given probability distributions . . . . .	62



3.2.2	Individual photon trajectories . . . . .	64
3.2.3	Evaluation of the Mueller matrix . . . . .	73
3.3	Conclusion . . . . .	75
<b>4</b>	<b>Experimental activity</b>	<b>77</b>
4.1	Introduction . . . . .	77
4.2	Mueller imaging with focussed illumination . . . . .	78
4.2.1	The instrument . . . . .	78
4.2.2	Results on suspensions of polystyrene spheres in water . . . . .	82
4.3	Angle resolved Mueller imaging of thin tissues . . . . .	86
4.3.1	The sample preparation . . . . .	87
4.3.2	The polarimetric components and measurement procedure . . . . .	88
4.3.3	The goniometric polarimeter . . . . .	90
4.3.4	The Fourier space imaging polarimeter . . . . .	91
4.3.5	Results . . . . .	95
4.4	Real space Mueller imaging of thick tissues . . . . .	100
4.4.1	Overview of this activity . . . . .	100
4.4.2	The Mueller imaging polarimeter . . . . .	102
4.4.3	Typical results on cone biopsies . . . . .	104
4.4.4	Typical results on colon samples . . . . .	107
4.5	Conclusion . . . . .	109
<b>5</b>	<b>Towards a realistic model of colon tissue</b>	<b>113</b>
5.1	The proposed model of <i>ex vivo</i> colon optical response . . . . .	113
5.2	Results and discussion . . . . .	114
5.2.1	Multilayered structures with monodisperse scatterers within each layer . . . . .	114
5.2.2	Multilayered structures with bimodal populations of scatterers . . . . .	119
5.3	Conclusion . . . . .	122
	<b>Conclusion and perspectives</b>	<b>125</b>
	<b>Appendix</b>	<b>125</b>
	<b>A Jones and Mueller matrices</b>	<b>127</b>
	<b>B Outline of Mie theory</b>	<b>135</b>
	<b>C Wavelength dependence of model parameters</b>	<b>145</b>
	<b>Bibliography</b>	<b>147</b>

# List of publications

## Publications in peer reviewed journals

1. M. R. Antonelli, A. Pierangelo, T. Novikova, P. Validire, A. Benali, B. Gayet, and A. De Martino, "Impact of model parameters on Monte Carlo simulations of backscattering Mueller matrix images of colon tissue," *Biomed. Opt. Express* **2**(7) 1836-1851 June 2011.  
<http://www.opticsinfobase.org/abstract.cfm?URI=boe-2-7-1836>
2. A. Pierangelo, A. Benali, M. R. Antonelli, T. Novikova, P. Validire, B. Gayet, and A. De Martino, "Ex-vivo characterization of human colon cancer by Mueller polarimetric imaging," *Opt. Express* **19**(2), 1582-1593, January 2011.  
<http://www.opticsinfobase.org/abstract.cfm?uri=oe-19-2-1582>
3. M. R. Antonelli, A. Pierangelo, T. Novikova, P. Validire, A. Benali, B. Gayet, and A. De Martino, "Mueller matrix imaging of human colon tissue for cancer diagnostics: how Monte Carlo modeling can help in the interpretation of experimental data," *Opt. Express* **18**(10), 10200-10208, May 2010.  
<http://www.opticsinfobase.org/abstract.cfm?uri=oe-18-10-10200>

## Scientific conference proceedings

1. M. R. Antonelli, A. Pierangelo, T. Novikova, P. Validire, A. Benali, B. Gayet, and A. De Martino, "Monte Carlo simulations of polarimetric response of healthy and cancerous human tissues," accepted for oral presentation to be presented 21-26 January 2012 at the conference *Biomedical Applications of Light Scattering VI* of SPIE **BiOS** in San Francisco, California, United States
2. M. R. Antonelli, A. Pierangelo, T. Novikova, P. Validire, A. Benali, B. Gayet, and A. De Martino, "Towards a realistic numerical modeling of the polarimetric response of healthy and pathological colon tissue," *Proc. SPIE* **8087**, June 2011, ISBN : 9780819486844.  
[http://spie.org/x648.html?product\\_id=896635](http://spie.org/x648.html?product_id=896635)
3. A. Pierangelo, S. Manhas, A. Benali, M. R. Antonelli, T. Novikova, P. Validire, B. Gayet, P. Validire, and A. De Martino, "Use of Mueller imaging for the staging of human colon cancer," *Proc. SPIE* **7895**, 78950E, March 2011, ISBN : 9780819484321.  
<http://dx.doi.org/10.1117/12.878248>
4. A. M. Winkler, M. R. Antonelli, S. Jacques, J. Barton, T. Novikova, and A. De Martino, "Thin tissue polarimetry to examine the combined effect of birefringence and scattering," American Society for Laser Medicine and Surgery 30th Annual

Conference Phoenix, Arizona, 16-18 April 2010. Abstracts. Lasers in Surgery and Medicine, **42**(22) 1-125. doi : 10.1002/lsm.20916.

<http://onlinelibrary.wiley.com/doi/10.1002/lsm.20916/abstract>

5. M. R. Antonelli, T. Novikova, and A. De Martino, "Monte Carlo modeling of backscattering Mueller matrix of healthy and cancerous tissues," 1st NanoCharM Workshop on Polarization-based Optical Techniques Applied to Biology and Medicine, Massy, France, 30-31 March 2009. 1st Workshop Proceedings 39-43.  
<http://www.nanocharm.org/images/stories/Library/\\Proceedings/1st%Workshop/1stWorkshopProceedings.pdf/>

### Communications at scientific conferences

1. M. R. Antonelli, A. Pierangelo, T. Novikova, P. Validire, A. Benali, B. Gayet, and A. De Martino, "Monte Carlo simulations of polarimetric response of healthy and cancerous human tissues" accepted for oral presentation to be presented at Photonics West, **BiOS** 2012, 21-26 January 2012, San Francisco, California, United States
2. M. R. Antonelli, A. Pierangelo, T. Novikova, P. Validire, A. Benali, B. Gayet, and A. De Martino, "Towards a realistic numerical modeling of the polarimetric response of healthy and pathological colon tissue," SPIE/OSA European Conference on Biomedical Optics, International Conference Center Munich, 22-26 May 2011. Poster
3. M. R. Antonelli, A. Pierangelo, T. Novikova, P. Validire, A. Benali, B. Gayet, and A. De Martino, "Illuminating cancer with a new light," Matinale de rencontres: *L'instrumentation dans le domaine de la Santé*, de l'Ecole Polytechnique, Palaiseau, 25 Nvember 2010. Poster
4. M. R. Antonelli, A. Pierangelo, T. Novikova, A. De Martino, B. Huynh, P. Validire, and H. Cohen, "Polarimetric imaging of human tissue for cancer diagnostics : experiment and Monte Carlo modeling," 4th International Graduate summer school Biophotonics, Ven, Suède, 6-13 June 2009. Poster
5. M. R. Antonelli, A. Pierangelo, T. Novikova, A. De Martino, B. Huynh, P. Validire, and H. Cohen, "Imagerie polarimétrique de tissus humains pour le diagnostic du cancer : expériences et modélisation de Monte Carlo," 7th OPTDIAG Workshop on *Diagnostic and optical imaging in medicine* ESPCI, Paris, 13-15 May 2009. Poster
6. M. R. Antonelli, T. Novikova, and A. De Martino, "Monte Carlo modeling of backscattering Mueller matrix of healthy and cancerous tissues," 1st NanoCharM Workshop on Polarization-based Optical Techniques Applied to Biology and Medicine, Massy, France, 30-31 Mars, 2009. Oral presentation

# Acknowledgements

Every PhD carries his own story. Mine starts by a phone call from Prof. Antonello De Martino on April 2007. That call made my dream to graduating in Paris come true! I am infinitely grateful to Antonello for that call and giving a chance to motivated students to grow up! Thank you for your comprehension and encouragement during these years, your kindness and love for life combined to your professional skills that make you "someone special"! However, I would never met Prof. De Martino without the help of his *camarade* Prof. Palange. Thank you for your presence during these years.

Many other persons have contributed to make my PhD experience a memorable one. I thank all members of the jury of PhD defence : Madame Tatiana Novikova, who as been my co-supervisor, I am grateful to you for patience and teaching ; the president Madame Bourg-Heckly, who as been my tutor at the School of Biomedical Sciences that I have attended in parallel to my PhD, I thank you for kindness and collaboration during these years ; Prof. Jacques, whom I have met in the occasion of a conference in Paris and who gave me the unique chance of doing some research in his laboratory at the Oregon Health & Science University in Portland (USA), I am thankful to you for your energy and passion for research ; I thank Messieurs Steve Guyot, Hervé Saint-Jalmes and Jean Michel Tualle, for their availability and understanding in the most stressful period of my PhD. LPICM has been my enlarged family during my staying in Paris. I am sincerely grateful to the director of the laboratory, Monsieur Drévillon, to the other PhD students, the post-doctoral fellows, with a special mention for Angelo who took an essential part in the experimental activities, the researchers, the technical and support teams and the administrative staff. Thank you for your excellence as workers and persons ; thank you for your patience, your kindness, your presence, your effort to make me feel comfortable in any situation ; thank you as well for having shared with me pleasant and difficult events and having welcomed and fostered me during my staying here! All these and even more constitute *le charme* of LPICM and make this laboratory a special place to spend a period of my life!!

I am also thankful to all people in other sections of the Ecole polytechnique and the medical doctor at the Institut Mutualiste Montsouris : your exceptional availability breaks all Italian *clichés* about the French people!!! I thank all other teachers and students that I have met at the School of Biomedical Sciences of the Institut Gustave Roussy and at the ENPC International School of Management in Paris, thank you for your friendship and companionship.

I am highly thankful to my uncles Claire and Marcel that are my adoptive family in Paris, thank you for taking care of me and receiving me at home every day back from work!! Of course I am heartily grateful to my own family, thank you for loving me what-

ever happens and wherever I am. Without you I am a paper with a broken pencil.

I am grateful as well to you who are going through my dissertation and are showing evident interest in my work! Hope you'll enjoy the reading!!

# General introduction

The work described in this manuscript has been carried out at *Laboratoire de Physique des Interfaces et des Couches Minces*, or LPICM (Laboratory of Physics of Interfaces and Thin Films), a CNRS-Polytechnique Joint Research Unit, located at Ecole polytechnique in Palaiseau (France), as a new aspect of the now well established research activity at LPICM on biomedical applications of polarimetry.

Historically, LPICM was created in 1986 to develop solar cells based on thin films deposited by Plasma Enhanced Chemical Vapor Deposition. Ellipsometric instrumentation was developed first as a highly performing tool to monitor thin film growth and to characterize the multiple layer structures at the core of solar cells. Later, though thin film characterization was still a major application of ellipsometry, complete Mueller polarimetry was developed independently, in spectroscopic and imaging configurations. New applications of this technique were investigated, among which semiconductor metrology and biomedical diagnostics.

This last topic is now a major activity at LPICM, with collaborations with medical teams at Institut Mutualiste Montsouris and Kremlin Bicêtre hospitals of Paris. One goal of this activity is to improve the visualization of dysplastic regions of uterine cervix *in vivo*, to allow a better definition of the locations to biopsy as well as the boundaries of surgical removal of anomalous regions, if needed. *Ex vivo* samples are also being studied, to help defining the best acquisition procedures and data treatments for *in vivo* diagnosis. Besides, *ex vivo* studies may be of interest for their own sake, to improve the efficiency of whole pathology examination procedures.

However, instrumental and data treatment optimizations may be very difficult to achieve only on an empirical basis, especially for *in vivo* studies including clinical trials. As a result, besides its intrinsic interest, the development of realistic yet tractable models of the tissue polarimetric responses is mandatory for the envisioned medical applications. The work presented in this manuscript is the first step made at LPICM towards this goal.

Many optical techniques are currently being developed and evaluated for medical diagnostics. One major advantage of optics over X-rays or PET is the use of non-ionizing harmless radiation. Moreover, optics may provide specific contrasts not available by other techniques, such as the very widely used evaluation of the level of oxygen saturation of hemoglobin based on near IR spectroscopy.

However, optical radiation is strongly scattered over typical depths in the millimeter range. As a result, optical characterization of deep organs is usually realized endoscopically. Direct non invasive measurements of scattered light may also be performed, but at definitely lower spatial resolutions.

If X-ray or magnetic resonance imaging are currently the most performing techniques for non-invasive in-depth imaging, optics is much more effective to characterize superficial tissues, and is thus widely used in dermatology, stomatology, gynaecology and ophthal-

mology.

Traditional intensity imaging, possibly with endoscopic or other optical devices such as binocular microscopes, is obviously the most widespread optical technique. The diagnosis is thus based on the visual aspect of the organs, their color and texture. However, optics may provide complementary information, not visible by usual imaging.

Fluorescence and Raman spectroscopy are sensitive to the chemical composition of the tissue, which can change from healthy to pathologic regions due to metabolic modifications occurring in diseased tissues. While fluorescence involves electronic transitions, with typically rather broad spectra without fine structures, Raman spectroscopy is sensitive to vibrational spectra, which are extremely detailed. As a result, fluorescence may be implemented in imaging mode with relatively broad spectral filtering of the excitation and emission wavelengths with little loss of chemical information with respect to full spectral resolution. Conversely, Raman typically requires high spectral resolution with very low signal levels and is thus difficult to implement in full field imaging mode.

Other techniques are sensitive to the tissue *structure*, at both macroscopic and microscopic levels, rather than its chemical composition. Confocal microscopy and Optical Coherence Tomography (OCT) provide microscopic tomographic images from ballistic (non-scattered) photons. These images are thus extremely detailed and in some cases they can be directly exploited by pathologists along the same lines as histological plates. The price to be paid for this advantage is a very small field of view (typically less than 1 mm<sup>2</sup>) and a penetration depth in the millimeter range.

Alternatively, the backscattered light from the sample can be analyzed spectrally and/or angularly, to determine the size of the scatterers, which may be cell nuclei, organelles, or collagen structures in connective tissue. As scattered photons contribute to the signal, for these techniques the relevant penetration depths may be significantly larger than for OCT or confocal imaging. Spatial imaging with focussed illumination can also be used to obtain the scattering coefficients from the analysis of the "halo" observed around the illuminated spot, but this technique can be used only on spatially homogeneous samples, which may be problematic in many practical cases.

Actually the size of the scatterers as well as the macroscopic multilayer structure of the tissue determines not only the angular and spectral distributions of backscattered light, but also its *polarization*. Typically, tissues exhibit substantial depolarization, with, possibly, other polarimetric properties such as *birefringence* and *diattenuation*, corresponding respectively to a dependence of the phase or the intensity of the backscattered light on the incident polarization. As a result, complete polarimetric characterization of the tissue requires *Mueller polarimetry*, which is the most complex polarimetric/ellipsometric technique, but which can be implemented, at reasonable cost, in full field imaging mode. Provided the polarimetric contrasts can be well correlated to specific diseases, polarimetric imaging may constitute a promising alternative/complementary technique for medical diagnostics.

Many studies involving polarimetric imaging have already been carried out in ophthalmology, often in conjunction with OCT (with, however, incomplete polarimetric analysis). Several studies have also been reported in dermatology while, to the best of our knowledge, LPICM has been the first to implement this technique to gynaecology.

This manuscript comprises five main chapters and three appendixes.

The first chapter is devoted to a brief description of the mathematical formalisms describing the light polarization, together with the changes that this polarization may

suffer when the light beam interacts with material systems. These formalisms are well known; we thus introduced this chapter to keep the manuscript reasonably self-contained and readable by non-specialists. After an elementary description of the polarization ellipse, we introduce the Jones formalism, which is well suited for totally polarized states characterized by simple, deterministic time-space evolution of the electric field. We then consider partially polarized states and the relevant Stokes formalism based on the statistical characterization of the electric field by a real, four component vector, the Stokes vector. The interaction of light with a material system then induces a linear transformation of this vector described by a  $4 \times 4$  real matrix, the Mueller matrix. We then present the essential features of the Mueller matrices of elementary polarimetric components, namely the diattenuators, the retarders and the depolarizers. In the last part of this chapter, we outline the various mathematical methods currently available to decompose any Mueller matrix into a product of matrices of elementary components, which allow a physical interpretation of the polarimetric response of the sample under study. The mathematical formulas for Jones and Mueller-Stokes formalisms are listed in Appendix A.

In the second chapter we provide the essential notions relevant to the propagation of polarized light in scattering media. The first part is focussed on single scattering, with a derivation of the scattering cross-section of a spherical particle in the scalar approximation first, and for polarized light afterwards. In this latter case, the result is given in terms of the development coefficients derived from Mie theory, which is summarized in Appendix B. We then consider multiple scattering, in the independent scattering regime, without any interference effects. The essential parameters relevant to this regime, namely the *scattering mean free path* and the *anisotropy* are introduced prior to the derivation of the radiative transfer equation (RTE), both in scalar and vectorial forms, i.e. for unpolarized and polarized light respectively. The last part of this chapter reviews the available methods of solution of the RTE, including the Monte Carlo algorithm that we used throughout this work.

The third chapter describes the Monte Carlo solution of RTE. We first present a broad overview of the problems which can be efficiently solved by using this approach, and then we specialize this presentation to the radiative transfer. The bulk of the chapter is devoted to the detailed description of the algorithm itself, including the generation of random numbers with prescribed probability distributions, the study of individual photon trajectories including free flight, scattering by spherical particles, refraction or reflection at interfaces, and eventually detection or loss in free space. The photon polarization is fully taken into account, as well as the geometry of the scattering system (with multiple layers and possibly different scatterer populations within each layer, and a totally depolarizing lambertian which "lumps" the contributions of the bottom, thick layers). Various possible detection geometries are also described. The Mueller matrix is evaluated by proper statistical averaging of the individual trajectories of photons in large "packages" with identical input parameters. The convergence of the statistics is greatly improved by a "non analog" game, which evaluates the probability for each photon to reach the detector directly after each event, instead of "waiting" for the photon trajectory to actually hit the detector.

The fourth chapter is devoted to the experimental part of this work, which provided the data taken with three different polarimeters and used afterwards to evaluate the simulation procedures described in Chapter 5. The first polarimeter, a manually driven setup



mounted at LPICM, was designed for full Mueller imaging measurements on scattering samples in the backward scattering geometry with focussed illumination. This instrument was used with various known samples, among which two aqueous suspensions of polystyrene spheres, to validate the Monte Carlo code.

The second instrument was set up and used during a three month stay at the Oregon Healthy and Science University of Portland, Oregon, in Pr. Steven Jacques' team. The purpose was to perform polarimetric measurements with angular, rather than spatial, resolution. Similarly to the first instrument, the input and output polarizations were determined by manually adjusting polarizers and retardation plates. The angular resolution was achieved in two ways. In a first implementation, the detection system was set on a goniometric mount. Then the polarimeter was coupled to a Fourier optics imaging system, for snapshot acquisition of two dimensional angular distributions. This instrument was used to study various samples, such as polystyrene sphere suspensions, honey and mice tendon, sufficiently thin to ensure an almost single scattering regime.

The last instrument was a real-space imaging full Mueller polarimeter, installed at the Pathology Department of Institut Mutualiste Montsouris, where it was used for polarimetric imaging of *ex vivo* samples, at five different wavelengths. We studied uterine cervix cone biopsies, as well as colon samples, with healthy and cancerous regions. These samples were also thoroughly studied with improved pathology procedures, to map the lesions and correlate these maps with the observed polarimetric contrasts.

The last chapter supplemented by Appendix C describes the theoretical model we developed to account for the main features of the observed polarimetric responses of colon samples. We first considered tissue structures with one or two layers including monodisperse scatterers above a totally depolarizing lambertian of variable albedo. The variable parameters were the layers' thickness, the scatterers' radius, their volume fraction, the optical index contrast and the lambertian albedo. These simple models did not account for an essential property of all observed tissues, namely a systematic Rayleigh-like response, with larger depolarization for linear vs circular incident polarization. This issue could be solved by considering bimodal scatterer populations.

Finally, the essential results and the perspectives opened by this work are summarized in the Conclusion.

# Chapter 1

## Light polarization formalism

### 1.1 Introduction

Light is said to have a dual behavior: the wave-like behavior and the particle-like behavior, which means that light behaves simultaneously as a wave and a flux of particles. Each description is better suited to some phenomena rather than others. For example, light propagation in free space or homogeneous media, as well as interferences between coherent beams, can be easily described by Maxwell wave equations (*the classical theory*), whereas some aspects of light-matter interaction such as spontaneous light emission involve *quantum effects* which can be understood only in the particle-like description of light [1].

In this chapter we will extensively use the classical wave theory to describe the polarization properties of light. Conversely, in Chapter 4 and 5 the propagation of polarized light in layered scattering media such as biological tissues will be modelled by using a Monte Carlo approach: light then is described as a flux of particles which may be scattered, absorbed, refracted or reflected, according to known probability functions. We point out, however, that these functions are derived from classical wave theories, namely the Mie theory of light scattering by spherical particles (see Appendix B) and the Snell-Fresnel's equations for light interaction with interfaces. As a result, the particles involved in Monte Carlo calculations are only virtual particles whose statistical distribution satisfies the radiative transfer equation rather than the "true" photons considered in quantum theory of light. However, in the following we will call these particles "photons" as seen in virtually all publications on Monte Carlo simulations.

Within the classical theory the essential quantity describing the light properties is its electric field vector  $\mathbf{E}(\mathbf{r}, t)$ , which oscillates in the plane perpendicular to the propagation direction and whose characteristics depend on the time and space coordinates as light propagates.

Polarization, as well as intensity, wavelength and coherence, is a fundamental property of light. In terms of the classical theory polarization refers to the pattern described by the electric field vector  $\mathbf{E}(\mathbf{r}, t)$  as a function of time  $t$  at a fixed location  $\mathbf{r}$ . When the electric field vector oscillates in a single direction, light is said to be linearly polarized. As discussed in more detail in the following paragraphs, if the direction of the electric field rotates, light is said to be elliptically polarized, as in this case the electric field vector traces out an ellipse at a fixed point in the space in function of time. If the ellipse happens to be a circle, light is said to be circularly polarized. Finally, if the motion of the electric field is somewhat disordered, this disorder (which is quantified by means of

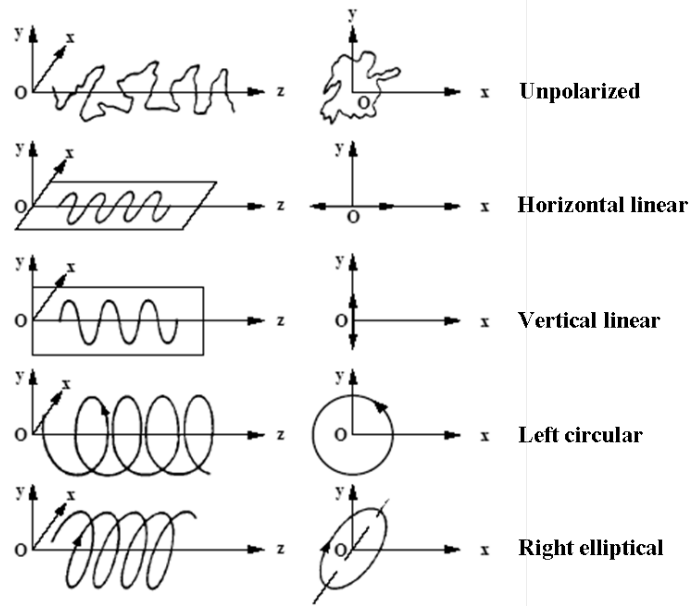


Figure 1.1: Different states of polarization [2].

the correlation functions of the electric field components) induces a depolarization, which may be complete if the field trajectory is "totally" chaotic. Fig. 1.1 illustrates these different states of polarization.

In practice, light is either unpolarized or partially polarized. Completely polarized light is an idealization of natural light, similar to the perfectly monochromatic light without any frequency spread. Sir George Gabriel Stokes (1819-1903) issued an experimental definition of unpolarized light, namely "*unpolarized light is light whose intensity is unaffected when a polarizer is rotated or by the presence of a retarder of any retardance value*" [3]. However, by means of a polarizer and a retarder, we can change the characteristic of polarization of natural light. The process of polarization introduces an order to the oscillation of the electric field and reduces the intensity of the polarized light. On the other hand, polarized light can lose its specific polarization as it propagates through a medium which introduces disorder in the oscillation of the electric field.

In this chapter we recall the essential aspects of the Jones and Stokes-Mueller formalisms used to describe the polarization within the frame of the electromagnetic theory. While the Jones formalism is well adapted to totally polarized states, the Stokes-Mueller formalism is needed when depolarization is to be taken into account.

## 1.2 Totally polarized states

**Electric field of a plane wave.** Time-space light propagation, like all electromagnetic phenomena, can be fully described in terms of Maxwell's equations. In these equations the electric and magnetic fields appear to be coupled. For homogenous non-magnetic linear optical media, without any charge and current densities, Maxwell's equations simplify and can be formulated for electric and magnetic fields separately (see Appendix B). The electric field then obeys the well-known wave equation

$$\nabla^2 \mathbf{E}(\mathbf{r}, t) - \mu\epsilon \frac{\partial^2 \mathbf{E}(\mathbf{r}, t)}{\partial t^2} = 0 \quad (1.1)$$

whose general solution is written as

$$\mathbf{E}(\mathbf{r}, t) = \Re\{\mathbf{E}_0(\mathbf{r}, t)e^{j\delta(\mathbf{r}, t)}\} \quad (1.2)$$

where the  $\mathbf{E}_0(\mathbf{r}, t)$  and  $\delta(\mathbf{r}, t)$  are the amplitude and the phase of the wave respectively.

A monochromatic plane wave is a particular solution of the wave equation, characterized by the phase factor  $\delta(\mathbf{r}, t) = \omega t - n_m \mathbf{k} \cdot \mathbf{r}$ , where  $k = 2\pi/\lambda$  is the propagation constant (or wave number) and  $\lambda$  is the wavelength *in vacuum*. Consider a monochromatic plane wave propagating in the positive  $z$  direction in an isotropic medium of refractive index  $n_m$  (real)

$$\mathbf{E}(\mathbf{r}, t) = \Re\{\mathbf{E}_0 e^{j(-kn_m z + \omega t)}\}. \quad (1.3)$$

The amplitude vector  $\mathbf{E}_0$  of the electric field is in general complex. The direction of the amplitude vector in the  $(x, y)$  plane perpendicular to  $z$  represents the light polarization:

$$\begin{aligned} \mathbf{E}_0 &= \mathbf{E}_{0x} + \mathbf{E}_{0y} = \\ &= E_{0x} e^{j\delta_x} \hat{\mathbf{x}} + E_{0y} e^{j\delta_y} \hat{\mathbf{y}} \end{aligned} \quad (1.4)$$

where  $\hat{\mathbf{x}}$  and  $\hat{\mathbf{y}}$  are unit vectors along the  $x$  and  $y$  directions, respectively, and  $E_{0x}$  and  $E_{0y}$  are positive real numbers. By replacing Eq.(1.4) in Eq.(1.3) and extracting the real part, the monochromatic plane wave propagating in  $z$  direction takes the form

$$\mathbf{E}(x, y, z, t) = E_{0x} \cos(\omega t - kn_m z + \delta_x) \hat{\mathbf{x}} + E_{0y} \cos(\omega t - kn_m z + \delta_y) \hat{\mathbf{y}} \quad (1.5)$$

where

$$E_x(z, t) = E_{0x} \cos(\omega t - kn_m z + \delta_x) = E_{0x} \cos(\tau + \delta_x) \quad (1.6a)$$

$$E_y(z, t) = E_{0y} \cos(\omega t - kn_m z + \delta_y) = E_{0y} \cos(\tau + \delta_y) \quad (1.6b)$$

are the transverse components of the electric field, in  $x$  and  $y$  directions respectively.  $E_{0x}$  and  $E_{0y}$  are the peak amplitudes,  $\delta_x$  and  $\delta_y$  the time independent phases of the two relative components,  $\tau = \omega t - kn_m z$  is the overall time dependent phase of the wave and  $kn_m$  is the propagation constant, or wave number, in the medium with refractive index  $n_m$  ( $k$  is the propagation constant *in vacuum*). For the totally polarized waves considered in this section, the four parameters  $E_{0x}$ ,  $E_{0y}$ ,  $\delta_x$  and  $\delta_y$  are constant in time.

**Intensity.** The intensity of a propagating wave in a given point of the space is the temporal average of the associated Poynting vector, proportional to the square of the field amplitude. If we drop the "extra" constant factors which are irrelevant for our purposes, we can write

$$I = I_x + I_y = \langle E_x(t)^2 + E_y(t)^2 \rangle \quad (1.7)$$

where  $I_x$  and  $I_y$  are the intensities associated with the components  $E_x$  and  $E_y$  of the electric field and the symbol  $\langle \dots \rangle$  represents the average. Due to the constancy of the peak amplitudes  $E_{0x}$ ,  $E_{0y}$  and the sinusoidal temporal variation of the fields, Eq.(1.7) can be rewritten as

$$I = I_x + I_y = \frac{1}{2} (E_{0x}^2 + E_{0y}^2). \quad (1.8)$$

### 1.2.1 The polarization ellipse

The two transverse waves in Eq.(1.6) are said to be "instantaneous", since the electric field takes only about  $10^{-15}$  seconds to complete a single oscillation at the optical frequencies [4], [5]. Hence the electric field vector traces a single curve almost instantaneously with respect to all other time constants which may be experimentally relevant, such as the time resolution of the detectors for example. In order to obtain this curve we need to write  $\cos(\tau + \delta_i)$  as a function of  $\tau$  and  $\delta_i$  ( $i = x, y$ ) separately, then we multiply the two equations by  $\sin \delta_y$  and  $\sin \delta_x$ , respectively, before subtracting them from one another; similarly we multiply the two equations by  $\cos \delta_y$  and  $\cos \delta_x$  and subtract them. Squaring the two final equations and adding them together gives the expression [5]:

$$\frac{E_x^2(t)}{E_{0x}^2} + \frac{E_y^2(t)}{E_{0y}^2} - 2 \frac{E_x(t)E_y(t)}{E_{0x}E_{0y}} \cos \delta = \sin^2 \delta \quad (1.9)$$

where  $\delta = \delta_y - \delta_x$  is the phase retardation of one the transversal component of the electric field with respect to the other.

We easily recognize in Eq.(1.9) the equation of a rotated ellipse (because of the "product" term  $E_x E_y$ ), with an ellipticity angle ( $\chi$ ) and angle of orientation ( $\psi$ ) with respect to the axes of reference. We define the angle  $\alpha$  by

$$\tan \alpha = \frac{E_{0y}}{E_{0x}}. \quad (1.10)$$

As both  $E_{0x}$  and  $E_{0y}$  are positive,  $\alpha$  is limited to the  $[0, \frac{\pi}{2}]$  interval. The ellipticity and orientation angles are then related to  $\alpha$  and  $\delta$  by [6]

$$\cos(2\chi) \cos(2\psi) = \cos(2\alpha) \quad (1.11a)$$

$$\cos(2\chi) \sin(2\psi) = \sin(2\alpha) \cos \delta \quad (1.11b)$$

$$\sin(2\chi) = \sin(2\alpha) \sin \delta. \quad (1.11c)$$

In Eq.(1.11a), when  $\alpha$  varies from 0 to  $\frac{\pi}{2}$ ,  $\cos(2\alpha)$  can take all possible values from -1 to 1. In the following two equations  $\sin(2\alpha)$  is positive, but the right members can also take any values between -1 and 1 due to the  $\cos \delta$  and  $\sin \delta$  factors. As a result, the ellipticity and orientation angles can be taken in the following intervals [5]:

$$-\frac{\pi}{4} \leq \chi \leq \frac{\pi}{4} \quad \text{and} \quad -\frac{\pi}{2} \leq \psi \leq \frac{\pi}{2}. \quad (1.12)$$

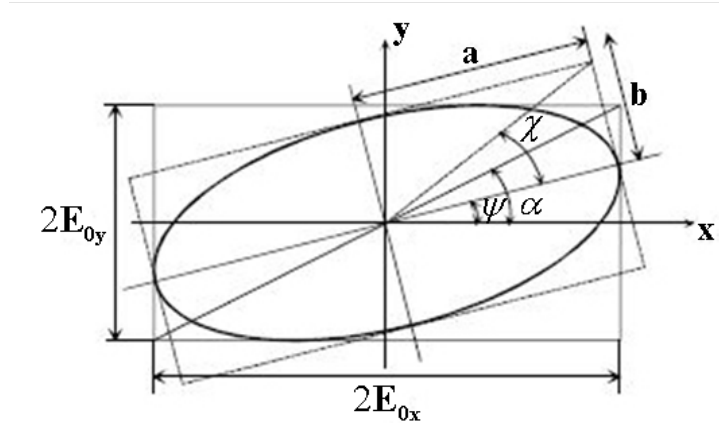


**Figure 1.2:** The polarization ellipse. The light is propagating along  $+z$ , towards the observer (the frame of reference  $(\mathbf{x}, \mathbf{y}, \mathbf{z})$  is right handed).

Moreover, the sign of  $\chi$  determines the *handedness* of the considered elliptical polarization state. We assume that the observer is looking into the  $-z$  direction, as in Fig. 1.2 (the observer is receiving the wave traveling in the  $+z$  direction) [5]:

- if  $\chi$  is negative, then  $\delta$  is also negative and the field rotates counterclockwise, from  $x$  to  $y$ , and the state is a *left-oriented* elliptical state,
- conversely, if  $\chi$  is positive, the polarization state is *right-oriented*.

### 1.2.2 The Jones formalism

**Jones vectors.** The matrix approach to describe the polarization of light comes along with the fact that the components of a light field after a polarizing device are linearly related to its components before the device [6]. Several matrix representations of the polarization states of a plane wave have been defined. In the following we will consider the most widely used, namely the Jones formalism. We rewrite Eqs.(1.6) as

$$\begin{bmatrix} E_x \\ E_y \end{bmatrix} e^{-j\tau} = \begin{bmatrix} E_{0x} e^{j\delta_x} \\ E_{0y} e^{j\delta_y} \end{bmatrix}, \quad (1.13)$$

where the two column (complex) time-independent vector on the right-hand side, which completely specifies the amplitude and phase of a light fields and hence its polarization, is called the *Jones vector* [6].

The above definition of the Jones vector can be simplified if this vector is used merely to label the polarization state of light, with no need of any absolute phase reference. If so, only the phase difference  $\delta = \delta_y - \delta_x$  is needed to determine the polarization state of the wave. Accordingly we can write the Jones vector as

$$\mathbf{J} = \begin{bmatrix} E_x \\ E_y \end{bmatrix} e^{-j\tau} = e^{j\delta_x} \begin{bmatrix} E_{0x} \\ E_{0y} e^{j\delta} \end{bmatrix}. \quad (1.14)$$

The common phase factor  $e^{j\delta_x}$  can be removed without losing any information about the

state of polarization of the light field. We may notice that this simplification cannot be done, for example, if we consider the interference of this wave with another one, in which case the overall relative phases of the two waves are crucial. Moreover, if only the polarization is to be described and not the total intensity of the considered wave, the Jones vector can be *normalized*:

$$\mathbf{J}^* \cdot \mathbf{J} = E_{0x}^* E_{0x} + E_{0y}^* E_{0y} = E_{0x}^2 + E_{0y}^2 = 1 \quad (1.15)$$

where  $\mathbf{J}^*$  is the transpose conjugate of  $\mathbf{J}$  (corresponding to a total intensity  $I=1/2$ ) and takes the form

$$\mathbf{J} = \begin{bmatrix} E_x \\ E_y \end{bmatrix} e^{-j\tau} = \begin{bmatrix} \cos \alpha \\ \sin \alpha e^{j\delta} \end{bmatrix}, \quad (1.16)$$

where the angle  $\alpha$  is the same as in Eq.(1.10). The Jones vectors ( $\mathbf{J}$ ) for horizontally (H), vertically (V),  $\pm 45^\circ$ -oriented linearly (P and M), left and right circularly (L and R), left and right elliptically (LE and RE -with principal axes coinciding with the horizontal and vertical directions; GLE and GRE -with principal axes generally oriented) polarized light are listed in Table 1.1.

**Orthogonal states.** In this paragraph we consider a *coherent* superposition of two waves, characterized by their Jones vectors  $\mathbf{J}_1$  and  $\mathbf{J}_2$ , defined as in Eq.(1.13), to avoid any loss of generality and include overall phase difference between the two waves. The Jones vector of the resulting wave is simply  $\mathbf{J} = \mathbf{J}_1 + \mathbf{J}_2$ . Its intensity  $I$  is then given by

$$2I = \mathbf{J}^* \cdot \mathbf{J} = (\mathbf{J}_1 + \mathbf{J}_2)^* \cdot (\mathbf{J}_1 + \mathbf{J}_2) = I_1 + I_2 + 2\Re(\mathbf{J}_1^* \cdot \mathbf{J}_2) \quad (1.17)$$

where the last term describes the interference between the two waves.

The polarization states defined by the Jones vectors  $\mathbf{J}_1$  and  $\mathbf{J}_2$  are said to be *orthogonal* if this interference term vanishes, independently of the overall relative phase of the two waves. This last point is essential, as the interference term always vanishes for two waves oscillating in quadrature, i.e. with an overall phase difference equal to  $90^\circ$ . Actually, if we change the relative overall phase shift between the two waves by  $\delta_s$ , the intensities  $I_1$  and  $I_2$  remain unchanged, while the scalar product  $\mathbf{J}_1^* \cdot \mathbf{J}_2$  is multiplied by  $e^{j\delta_s}$ . As a result, the polarization states defined by  $\mathbf{J}_1$  and  $\mathbf{J}_2$  are orthogonal if and only if their scalar product  $\mathbf{J}_1^* \cdot \mathbf{J}_2$  is zero.

Once this condition has been clarified, we can consider normalized Jones vectors. Taking for  $\mathbf{J}_1$  the expression in Eq.(1.16), the scalar product with  $\mathbf{J}_2$  vanishes if and only if  $\mathbf{J}_2$  is of the form

$$\mathbf{J}_2 = e^{j\bar{\delta}} \begin{bmatrix} -\sin \alpha e^{-j\delta} \\ \cos \alpha \end{bmatrix} \quad (1.18)$$

where the factor  $e^{j\bar{\delta}}$  represents the overall phase shift between the two waves (including  $e^{j\delta_x}$  and  $e^{j\delta_s}$ ). Eq.(1.18) shows that  $\mathbf{J}_2$  is deduced from  $\mathbf{J}_1$  by merely adding  $\frac{\pi}{2}$  to  $\alpha$ . Then Eqs.(1.11) show that  $\sin(2\chi)$ ,  $\sin(2\psi)$  and  $\cos(2\psi)$  all change sign, implying that  $\chi$  is changed into  $-\chi$  while  $\psi$  becomes  $\psi \pm \frac{\pi}{2}$ , depending on which of these two possible angles is found between  $-\frac{\pi}{2}$  and  $\frac{\pi}{2}$ . As a result:

- the handedness of the considered state is reversed,
- the major and minor axes of the ellipse are exchanged.

The relationship between two orthogonal states is illustrated in Fig. 1.3.

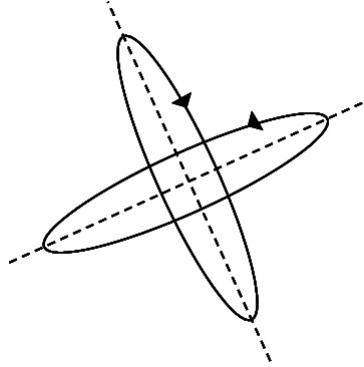


**Figure 1.3:** Two orthogonal elliptical states.

**Jones matrices.** In general the action of a non-depolarizing optical system transforming the state of polarization of a plane wave can be described by the matrix equation:

$$\begin{bmatrix} \cos \alpha' \\ \sin \alpha' \end{bmatrix} = \begin{bmatrix} T_{11} & T_{12} \\ T_{21} & T_{22} \end{bmatrix} \begin{bmatrix} \cos \alpha \\ \sin \alpha e^{j\delta} \end{bmatrix}, \quad (1.19)$$

where the 2 x 2 matrix

$$\mathbf{T} = \begin{bmatrix} T_{11} & T_{12} \\ T_{21} & T_{22} \end{bmatrix} \quad (1.20)$$

is the *Jones matrix* of the optical system. The Jones matrix ( $\mathbf{T}$ ) of some optical devices are listed in Tables A.1, A.2, A.5 (see Appendix A). The same matrix transformation can be used to describe the action of a complex system constituted of  $n$  elementary optical devices characterized by their Jones matrices  $\mathbf{T}_i$ . Then, the transformation matrix that changes the Jones vector of the light at the entrance of the optical system  $\mathbf{J}^i$  in to the Jones vector at the exit  $\mathbf{J}^o$  has the expression:

$$\mathbf{J}^o = \mathbf{T}_n \cdot \mathbf{T}_{n-1} \dots \mathbf{T}_1 \cdot \mathbf{J}^i. \quad (1.21)$$

In the most general case, an elliptical input polarization state is transformed into another elliptical state.

**Polarization eigenstates.** The polarization eigenstates of an optical system are the polarization states which are not modified by the system. Therefore, their Jones vectors are not modified either, except for an overall factor corresponding to the overall amplitude or phase (or both) of the light wave. In other words, these Jones vectors are nothing else but the eigenvectors  $\mathbf{J}_1$  and  $\mathbf{J}_2$  of the Jones matrix  $\mathbf{T}$  of the system:

$$\begin{aligned} \mathbf{T} \cdot \mathbf{J}_1 &= \lambda_1 \cdot \mathbf{J}_1 \\ \mathbf{T} \cdot \mathbf{J}_2 &= \lambda_2 \cdot \mathbf{J}_2, \end{aligned} \quad (1.22)$$



<b>J</b>	$\begin{bmatrix} \cos \alpha \\ \sin \alpha e^{j\delta} \end{bmatrix}$	$\alpha = 0$	$\begin{bmatrix} 1 \\ 0 \end{bmatrix}$	<b>J<sub>H</sub></b>
		$\alpha = \frac{\pi}{2}$	$\begin{bmatrix} 0 \\ 1 \end{bmatrix}$	<b>J<sub>V</sub></b>
		$\alpha = \frac{\pi}{4}$ $\delta = 0$	$\frac{1}{\sqrt{2}} \begin{bmatrix} 1 \\ 1 \end{bmatrix}$	<b>J<sub>P</sub></b>
		$\alpha = \frac{\pi}{4}$ $\delta = \pi$	$\frac{1}{\sqrt{2}} \begin{bmatrix} 1 \\ -1 \end{bmatrix}$	<b>J<sub>M</sub></b>
		$E_{0x} = E_{0y}$ $\delta = \frac{\pi}{2}$	$\frac{1}{\sqrt{2}} \begin{bmatrix} 1 \\ -i \end{bmatrix}$	<b>J<sub>L</sub></b>
		$E_{0x} = E_{0y}$ $\delta = -\frac{\pi}{2}$	$\frac{1}{\sqrt{2}} \begin{bmatrix} 1 \\ i \end{bmatrix}$	<b>J<sub>R</sub></b>
		$E_{0x} = a$ $E_{0y} = b$ $\delta = \mp \frac{\pi}{2}$	$\frac{1}{\sqrt{a^2+b^2}} \begin{bmatrix} a \\ -ib \end{bmatrix}$	<b>J<sub>LE</sub></b>
			$\frac{1}{\sqrt{a^2+b^2}} \begin{bmatrix} a \\ ib \end{bmatrix}$	<b>J<sub>RE</sub></b>
		$E_{0x} = a$ $E_{0y} = \sqrt{b^2 + c^2}$ $\delta = \mp \tan^{-1}(\frac{c}{b})$	$\frac{1}{\sqrt{a^2+b^2+c^2}} \begin{bmatrix} a \\ b - ic \end{bmatrix}$	<b>J<sub>GLE</sub></b>
			$\frac{1}{\sqrt{a^2+b^2+c^2}} \begin{bmatrix} a \\ b + ic \end{bmatrix}$	<b>J<sub>GRE</sub></b>

**Table 1.1:** Jones vectors of totally polarized states.

where  $\lambda_1$  and  $\lambda_2$  are the corresponding eigenvalues.

In the most general case, the eigenvalues associated to the eigenvectors are complex and defined as

$$\begin{aligned} \lambda_1 &= P_1 e^{j\delta_1} \\ \lambda_2 &= P_2 e^{j\delta_2}, \end{aligned} \tag{1.23}$$

ordered so that  $P_2 > P_1$ . Although the eigenvectors form a base, they are not necessarily orthogonal. The eigenvalues and eigenvectors of some optical devices are listed in Tables A.1, A.2, A.5 (see Appendix A).

**Homogeneous systems.** A non depolarizing system is *homogeneous* if its two polarization eigenstates are orthogonal.

Let's consider a homogeneous system with the following orthogonal eigenvectors:

$$\mathbf{J}_1 = \begin{bmatrix} a \\ b \end{bmatrix} \quad \mathbf{J}_2 = \begin{bmatrix} -b^* \\ a^* \end{bmatrix}. \quad (1.24)$$

Since these eigenvectors are normalized their components verify the relation

$$aa^* + bb^* = 1. \quad (1.25)$$

The Jones matrix can be rewritten as

$$\mathbf{T} = \mathbf{M}_J \cdot \mathbf{\Lambda} \cdot [\mathbf{M}_J]^{-1} = \begin{bmatrix} \lambda_1 aa^* + \lambda_2 bb^* & (\lambda_1 - \lambda_2)ab^* \\ (\lambda_1 - \lambda_2)ba^* & \lambda_2 aa^* + \lambda_1 bb^* \end{bmatrix} \quad (1.26)$$

where

$$\mathbf{M}_J = [\mathbf{J}_1 \ \mathbf{J}_2] = \begin{bmatrix} a & -b^* \\ b & a^* \end{bmatrix}, \quad (1.27a)$$

$$[\mathbf{M}_J]^{-1} = [\mathbf{J}_1 \ \mathbf{J}_2]^{-1} = \begin{bmatrix} a^* & b^* \\ -b & a \end{bmatrix}, \quad (1.27b)$$

$$\mathbf{\Lambda} = \begin{bmatrix} \lambda_1 & 0 \\ 0 & \lambda_2 \end{bmatrix}. \quad (1.27c)$$

**Rotation of the reference frame.** If the  $x$  and  $y$  axes are rotated by an angle  $\varphi$ , the Jones vectors are transformed by the usual rotation matrix  $\mathbf{R}_J(\varphi)$ :

$$\mathbf{S}' = \begin{bmatrix} a' \\ b' \end{bmatrix} = \mathbf{R}_J(\varphi) \cdot \mathbf{J} = \begin{bmatrix} \cos \varphi & -\sin \varphi \\ \sin \varphi & \cos \varphi \end{bmatrix} \cdot \begin{bmatrix} a \\ b \end{bmatrix} \quad (1.28)$$

while we get for the Jones matrices

$$\mathbf{T}' = \mathbf{R}_J(\varphi) \cdot \mathbf{T} \cdot [\mathbf{R}_J(\varphi)]^{-1}. \quad (1.29)$$

### 1.3 The Stokes formalism for partially polarized states

So far, we have been considering only totally polarized states, for which the electric field describes a well defined ellipse in the  $xy$  plane. In practice, the motion of the electric field can be somewhat disordered, and can be defined only statistically, by means of *correlation functions*. Even though higher order correlation functions may be measured, in the following we will restrict ourselves to second order ones, which are in turn directly related to *intensities*.

In particular, as it has been already discussed in the first section of this chapter the intensities related to the components of the electric field along the  $x$  and  $y$  axes are

$$I_x = \langle E_x^2(t) \rangle, \quad I_y = \langle E_y^2(t) \rangle \quad (1.30)$$

where the brackets mean "overall" averages. We now discuss in more detail the nature of this averaging process for partially polarized states.

In the following we'll always consider quasi-monochromatic waves, meaning that Eqs.(1.6) are still valid. However, the  $E_{0x}$ ,  $E_{0y}$ ,  $\delta_x$ ,  $\delta_y$  are no longer constant, but they vary much more slowly than the optical angular frequency  $\omega$ . As a result, the intensities  $I_i$  ( $i = x, y$ ) defined above can be rewritten as

$$I_i = \langle E_i^2(t) \rangle = \frac{1}{2} \langle E_{0i}^2 \rangle \quad (1.31)$$

which corresponds to a two-step averaging procedure:

1. We first take the average, at each spatial location, of the  $\cos^2(\tau + \delta_i)$  factor, which oscillates at twice the optical frequency. Such an average can thus be taken over times of the order of the inverse of the optical frequency, which is much shorter than typical variation times of  $E_{0i}$ , which can then be considered as a constant at this point. As a result, this first averaging step merely divides by a factor of 2 the "instantaneous" values of  $E_{0i}^2$ . This step has been already described for totally polarized states, for which the amplitudes  $E_{0i}$  (and the phase difference  $\delta = \delta_y - \delta_x$ ) are constant in time;
2. In a second step, we take the average, over much longer times, of  $E_{0i}^2$ . Moreover, in this second step, we can also include other types of averaging, which may be relevant to various experimental conditions:
  - if the detector size is larger than the spatial coherence domains at the detector location, then the polarization state may vary over the detector cross-section, and a *spatial* averaging may be required,
  - if the polarization varies inside the light spectral range, then a *spectral* averaging may be necessary.

We now generalize the previous notions to the whole second order correlation matrix of the two components of the electric field. This matrix is most easily defined from the complex formulation of the electric field:

$$E_i^c = E_{0i} e^{j(\tau + \delta_i)} \quad \text{where } i = x, y. \quad (1.32)$$

If we remove the terms oscillating at optical frequencies, whose time average is zero, the field correlation matrix reduces to:

$$\mathbf{C} = \begin{bmatrix} \langle E_x^c E_x^{c*} \rangle & \langle E_x^c E_y^{c*} \rangle \\ \langle E_y^c E_x^{c*} \rangle & \langle E_y^c E_y^{c*} \rangle \end{bmatrix} = \begin{bmatrix} \langle E_{0x}^2 \rangle & \langle E_{0x} E_{0y} e^{-j\delta} \rangle \\ \langle E_{0x} E_{0y} e^{j\delta} \rangle & \langle E_{0y}^2 \rangle \end{bmatrix}. \quad (1.33)$$

**The Stokes parameters.** From the correlation matrix  $\mathbf{C}$  we can define four real parameters, the Stokes parameters, which define all possible, totally or partially polarized,

states:

$$S_0 = \frac{1}{2} (C_{xx} + C_{yy}) = \frac{1}{2} \langle E_{0x}^2 + E_{0y}^2 \rangle \quad (1.34a)$$

$$S_1 = \frac{1}{2} (C_{xx} - C_{yy}) = \frac{1}{2} \langle E_{0x}^2 - E_{0y}^2 \rangle \quad (1.34b)$$

$$S_2 = \frac{1}{2} (C_{xy} + C_{yx}) = \frac{1}{2} \langle 2E_{0x}E_{0y} \cos \delta \rangle \quad (1.34c)$$

$$S_3 = \frac{i}{2} (C_{xy} - C_{yx}) = \frac{1}{2} \langle 2E_{0x}E_{0y} \sin \delta \rangle. \quad (1.34d)$$

From Eq.(1.31) the interpretation of the first two Stokes parameters is straightforward: these parameters are nothing else but the sum and the difference of the intensities  $I_x$  and  $I_y$  measured after ideal polarizers respectively aligned along the  $x$  and  $y$  axes.

The interpretation of  $S_2$  and  $S_3$  is a little bit more involved. The intensities  $I_{P/M}$  measured after the same ideal polarizers, set at  $\pm 45^\circ$  are given by the rms values of the projections of the field on these axes:

$$I_{P/M} = \frac{1}{2} \langle (E_x(t) \pm E_y(t))^2 \rangle \quad (1.35a)$$

$$= \frac{1}{2} \langle (E_{0x} \cos(\tau + \delta_x) \pm E_{0y} \cos(\tau + \delta_y))^2 \rangle \quad (1.35b)$$

$$= \frac{1}{2} \left\langle \frac{1}{2} E_{0x}^2 + \frac{1}{2} E_{0y}^2 \pm 2E_{0x}E_{0y} \cos(\tau + \delta_x) \cos(\tau + \delta_y) \right\rangle \quad (1.35c)$$

from which we easily deduce

$$I_P - I_M = \langle 2E_{0x}E_{0y} \cos(\tau + \delta_x) \cos(\tau + \delta_y) \rangle \quad (1.36a)$$

$$= \langle E_{0x}E_{0y} (\cos(2\tau + \delta_x + \delta_y) + \cos(\delta)) \rangle \quad (1.36b)$$

$$= \langle E_{0x}E_{0y} \cos \delta \rangle = S_2 \quad (1.36c)$$

where, again, we used the fact that the time average of the term oscillating at the optical frequency  $2\tau$  is zero.

The physical meaning of the parameter  $S_3$  can easily be deduced from that of  $S_2$  if we manage to replace  $\cos \delta$  by  $\sin \delta$ , which is equivalent to subtracting  $90^\circ$  from the incoming wave phase difference  $\delta = \delta_y - \delta_x$ . This can be achieved by setting an ideal quarter-wave plate before the linear analyzer, with its slow axis along the  $x$  direction.

As it has been described in section 1.2.1 left circularly polarized light is a wave for which the electric field has constant modulus and rotates counterclockwise (from  $x$  to  $y$ ) for an observer looking in the  $-z$  direction. For such a wave, the electric field components are of the form

$$\begin{bmatrix} E_x(t) \\ E_y(t) \end{bmatrix} = \begin{bmatrix} E_{0x} \cos(\omega t + \varphi) \\ E_{0y} \sin(\omega t + \varphi) \end{bmatrix}. \quad (1.37)$$

The quarter wave plate with its slow axis along  $x$  adds a  $90^\circ$  phase to  $E_x(t)$ , which transforms the factor  $\cos(\omega t + \varphi)$  into  $-\sin(\omega t + \varphi)$ . The incoming left circular polarization is

thus transformed into a linear one, oriented at  $-45^\circ$ . Conversely, if the incoming wave is circularly right polarized (rotating clockwise in the same conditions of observation) the quarter wave plate will again transform this polarization into a linear one, along the  $+45^\circ$  direction. As a result, we can consider that the quarter-wave plate followed by a linear analyzer set at  $-45^\circ$  is equivalent to a *left circular analyzer*; if the linear analyzer is set parallel to the  $+45^\circ$  the whole setup is a *right circular analyzer*. Finally, considering again that  $S_3$  can be measured as  $S_2$  with the quarter wave placed before the linear analyzers with its slow axis along  $x$ , we get from Eq.(1.36)

$$S_3 = I_R - I_L \quad (1.38)$$

where  $I_L$  and  $I_R$  are the intensities measured after ideal left and right circular analyzers, respectively.

Finally, the four Stokes parameters can be seen as the four components of the (real) *Stokes vector*  $\mathbf{S}$ :

$$\mathbf{S} = \begin{bmatrix} S_0 \\ S_1 \\ S_2 \\ S_3 \end{bmatrix} = \begin{bmatrix} I \\ Q \\ U \\ V \end{bmatrix} = \begin{bmatrix} I_x + I_y \\ I_x - I_y \\ I_P - I_M \\ I_L - I_R \end{bmatrix}. \quad (1.39)$$

We can recast the meaning of the Stokes parameters as follows. The first parameter  $S_0$  (also often called  $I$ ) is the total light intensity. The parameter  $S_1$  (or  $Q$ ) describes the amount of linear horizontal ( $x$ ) or vertical ( $y$ ) polarization. The parameter  $S_2$  (also called  $U$ ) quantifies the amount of linear polarization along the  $+45^\circ$  or  $-45^\circ$  azimuths, while  $S_3$  (or  $V$ ) is a measure of the amount of circular polarization, together with its handedness.

The vectors of the most usual polarization states are summarized in Table 1.2.

For totally unpolarized light all Stokes parameters but  $S_0$  vanish, as for unpolarized light the intensity measured after any ideal analyzer (be it linear at any azimuth, or circular, or even elliptical) is always one half of the total intensity.

### 1.3.1 The degree of polarization

Jones vectors are "true" vectors, as the electric fields they represent, in the sense that no limitations are imposed on their components. Conversely, this is not true for Stokes vectors, as we'll see now. From the well known Schwarz inequality applied to random variables

$$\langle ab \rangle^2 \leq \langle a^2 \rangle \langle b^2 \rangle \quad (1.40)$$

we deduce that

$$S_2^2 + S_3^2 = \langle E_{0x} E_{0y} \cos \delta \rangle^2 + \langle E_{0x} E_{0y} \sin \delta \rangle^2 \leq \langle E_{0x}^2 E_{0y}^2 \rangle \langle \cos^2 \delta + \sin^2 \delta \rangle = E_{0x}^2 E_{0y}^2 \quad (1.41)$$

and

$$S_1^2 + S_2^2 + S_3^2 \leq \frac{1}{4} \langle (E_{0x}^2 - E_{0y}^2)^2 \rangle + \langle E_{0x}^2 E_{0y}^2 \rangle = S_0^2. \quad (1.42)$$

<b>S</b>	$\frac{1}{2} \begin{bmatrix} \langle E_{0x}^2 + E_{0y}^2 \rangle \\ \langle E_{0x}^2 - E_{0y}^2 \rangle \\ \langle 2E_{0x}E_{0y} \cos \delta \rangle \\ \langle 2E_{0x}E_{0y} \sin \delta \rangle \end{bmatrix}$	$E_{0x} = 0$ $E_{0y} \neq 0$ $I_0 = E_{0y}^2$	$\delta = \forall$	$I_0 \begin{bmatrix} 1 \\ 1 \\ 0 \\ 0 \end{bmatrix}$	<b>S<sub>H</sub></b>
		$E_{0x} \neq 0$ $E_{0y} = 0$ $I_0 = E_{0x}^2$	$\delta = \forall$	$I_0 \begin{bmatrix} 1 \\ -1 \\ 0 \\ 0 \end{bmatrix}$	<b>S<sub>V</sub></b>
		$E_{0x} = E_{0y}$ $I_0 = 2E_0^2$	$\delta = 0$	$I_0 \begin{bmatrix} 1 \\ 0 \\ 1 \\ 0 \end{bmatrix}$	<b>S<sub>P</sub></b>
			$\delta = \pi$	$I_0 \begin{bmatrix} 1 \\ 0 \\ -1 \\ 0 \end{bmatrix}$	<b>S<sub>M</sub></b>
			$\delta = \frac{\pi}{2}$	$I_0 \begin{bmatrix} 1 \\ 0 \\ 0 \\ 1 \end{bmatrix}$	<b>S<sub>R</sub></b>
			$\delta = -\frac{\pi}{2}$	$I_0 \begin{bmatrix} 1 \\ 0 \\ 0 \\ -1 \end{bmatrix}$	<b>S<sub>L</sub></b>

**Table 1.2:** Stokes vectors of usual polarization states.

The inequality 1.42 becomes an equality for *totally polarized states*, for which  $E_{0x}$  and  $E_{0y}$  are no longer random variables, but constants. It is then natural to define the *degree of polarization*  $\rho$  of any polarization state as

$$\rho = \frac{\sqrt{Q^2 + U^2 + V^2}}{I}. \quad (1.43)$$

This degree of polarization varies from 0, for totally unpolarized states (i.e. when  $Q$ ,  $U$  and  $V$  all vanish) to 1, for totally polarized states, as seen above. This limitation of  $\rho$  is the usual criterion of *physicity* of a Stokes vector: a four-dimensional (4D) real vector for which  $\rho > 1$  cannot represent any actual polarization state. In this sense Stokes vectors are not "real" vectors. Moreover, they do not transform through rotations as vectors. The degree of polarization quantifies the amount of polarized light in the total beam intensity. Experimentally, this polarized component can be extinguished by a suitable elliptical analyzer, which may consist of a quarter wave plate followed by a linear analyzer, both elements being adjusted in azimuth to minimize the transmitted intensity, which in turn represents the non-polarized component.

In a way analogous to the (total) degree of polarization  $\rho$ , we can define:

- the *linear* degree of polarization

$$\rho_l = \frac{\sqrt{Q^2 + U^2}}{I}, \quad (1.44)$$

- the *circular* degree of polarization

$$\rho_c = \frac{\sqrt{V^2}}{I}, \quad (1.45)$$

which respectively represent the fraction of the light intensity which can be extinguished by a suitably oriented linear analyzer or a circular analyzer. In practice, these quantities are the most useful when the system to be characterized has already known specificities which make it possible to choose the most relevant among the degrees of polarizations defined above, and to measure it more easily than the full Stokes vector.

So far, the Stokes formalism has been providing a "dictionary" of mathematical words to define any state of polarization; the Poincaré sphere defined in the next section offers a geometrical tool to visualize any state of polarization within a three-dimensional (3D) picture, including its degrees of polarization.

### 1.3.2 The Poincaré sphere representation

We first consider totally polarized states. Eqs.(1.11) can be rewritten by taking into account

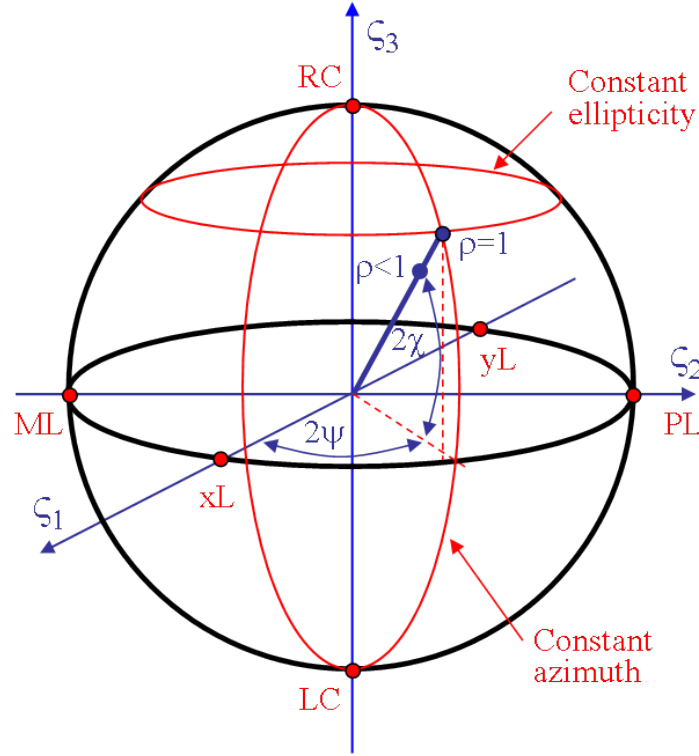


**Figure 1.4:** The Poincaré sphere.

$$\cos(2\alpha) = \cos^2 \alpha - \sin^2 \alpha = \frac{E_{0x}^2 - E_{0y}^2}{E_{0x}^2 + E_{0y}^2} \quad (1.46a)$$

$$\sin(2\alpha) = 2 \sin \alpha \cos \alpha = \frac{2E_{0x}E_{0y}}{E_{0x}^2 + E_{0y}^2} \quad (1.46b)$$

which immediately yields:

$$\cos(2\chi) \cos(2\psi) = \cos(2\alpha) = \frac{S_1}{S_0} = \varsigma_1 \quad (1.47a)$$

$$\cos(2\chi) \sin(2\psi) = \sin(2\alpha) \cos \delta = \frac{S_2}{S_0} = \varsigma_2 \quad (1.47b)$$

$$\sin(2\chi) = \sin(2\alpha) \sin \delta = \frac{S_3}{S_0} = \varsigma_3 \quad (1.47c)$$

As a result, we can represent a totally polarized state by a point on the surface of a sphere with unit radius, the *Poincaré sphere*: the position of this point is determined by the "longitude"  $2\psi$  and the "latitude"  $2\chi$ . The "usual" polarization states listed in Table 1.2 are easily found on the sphere surface:

- the linearly polarized states are on the "equator", where those aligned along the  $x$  and  $y$  axes (identified as xL and yL in Fig. 1.4) are on the " $\varsigma_1$ " axis, while those oriented at  $\pm 45^\circ$  (identified as PL and ML) are on the " $\varsigma_2$ " axis,



- the right and left circularly polarized states (identified as RC and LC) are respectively at the "North" and "South" poles, along the " $\varsigma_3$ " axis.

More generally, all the "right-handed" elliptical states are on the "Northern hemisphere", while the opposite holds for the "left-handed" states, with constant ellipticity on "parallels" and constant azimuth on the "meridians". Orthogonal states are on diametrically opposed positions on the sphere surface.

Finally, for partially polarized states, Eq.(1.43) can be rewritten as

$$\varsigma_1^2 + \varsigma_2^2 + \varsigma_3^2 = \rho^2 \quad (1.48)$$

where  $\rho$  is the degree of polarization. The points representing such states are thus inside the sphere, at a distance  $\rho$  from the center. Totally unpolarized states are at the center of the sphere.

## 1.4 The Mueller matrix

### 1.4.1 Definition and general properties

**Definition.** The action of a generic medium on the incident light can be described by the matrix equation as

$$\begin{bmatrix} S_0^o \\ S_1^o \\ S_2^o \\ S_3^o \end{bmatrix} = \begin{bmatrix} M_{11} & M_{12} & M_{13} & M_{14} \\ M_{21} & M_{22} & M_{23} & M_{24} \\ M_{31} & M_{32} & M_{33} & M_{34} \\ M_{41} & M_{42} & M_{43} & M_{44} \end{bmatrix} \cdot \begin{bmatrix} S_0^i \\ S_1^i \\ S_2^i \\ S_3^i \end{bmatrix} \quad (1.49)$$

where the 4 x 4 transformation matrix  $\mathbf{M}$  is called the *Mueller matrix* (by Hans Mueller, 1940s). The Mueller matrix  $\mathbf{M}$  of a medium transforms the incident Stokes vector  $\mathbf{S}^i$  into the corresponding output Stokes vector  $\mathbf{S}^o$ ,  $\mathbf{S}^o = \mathbf{M} \cdot \mathbf{S}^i$ . Obviously the Stokes vector of the output light depends on the Stokes vector of the incident light, conversely the Mueller matrix carries information on the medium only. The 16  $M_{ij}$  coefficients of the matrix are real and measurable. Hence the Mueller matrix can be used to fully characterize the optical properties of the medium, whether it is non-depolarizing or depolarizing. The Mueller matrix ( $\mathbf{M}$ ) of some optical devices are listed in Tables A.3, A.4, A.6 (see Appendix A).

Similarly to the Jones formalism, the Mueller matrix can be used to characterize a complex optical system defined by  $n$  elementary optical systems in cascade. The expression of the Mueller matrix of the complex system is:

$$\mathbf{S}^o = \mathbf{M}_n \cdot \mathbf{M}_{n-1} \cdot \dots \cdot \mathbf{M}_1 \cdot \mathbf{S}^i. \quad (1.50)$$

**Physical realizability.** In a similar way as for Stokes vectors, any 4 x 4 real matrix is not necessarily the Mueller matrix of any physical system. A first criterion in this respect is the following: a realizable Mueller matrix never "overpolarizes" the incoming light. For

any input Stokes vector  $\mathbf{S}^i$ , the corresponding output vector must never feature a degree of polarization  $\rho$  larger than 1. More detailed information is provided by Refs. [7, 8, 9].

**Rotation of the reference frame.** This transformation is analogous to that previously described for Jones vectors and matrices. If the  $x$  and  $y$  axes are rotated by an angle  $\varphi$ , the Stokes vectors are transformed by the rotation matrix  $\mathbf{R}_M(\varphi)$ :

$$\mathbf{J}' = \begin{bmatrix} S'_0 \\ S'_1 \\ S'_2 \\ S'_3 \end{bmatrix} = \mathbf{R}_M(\varphi) \cdot \mathbf{S} = \begin{bmatrix} 1 & 0 & 0 & 0 \\ 0 & \cos(2\varphi) & -\sin(2\varphi) & 0 \\ 0 & \sin(2\varphi) & \cos(2\varphi) & 0 \\ 0 & 0 & 0 & 1 \end{bmatrix} \cdot \begin{bmatrix} S_0 \\ S_1 \\ S_2 \\ S_3 \end{bmatrix} \quad (1.51)$$

while we get for the Mueller matrices

$$\mathbf{M}' = \mathbf{R}_M(\varphi) \cdot \mathbf{M} \cdot [\mathbf{R}_M(\varphi)]^{-1}. \quad (1.52)$$

**Depolarizing and non-depolarizing Mueller matrices.** As it has been already discussed, a partially depolarized Stokes vector can be seen as an incoherent superposition of various non-depolarizing Stokes vectors. In the same way, a depolarizing Mueller matrix characterizes a system for which the Jones matrix is defined statistically as a superposition of "elementary" Jones matrices distributed according to a (usually unknown) probability function. Such an indeterminacy of the Jones matrix may come from the system itself: for example, interaction of polarized light in biological tissues involves many scattering events with particles at random locations, and possibly also in motion. Depolarization may also occur as a consequence of the observation conditions: for example, a white light source involves a broad spectrum of wavelengths. Even in cases where the system would not depolarize monochromatic light, if its "monochromatic" Jones matrix varies with the wavelength, then its "polychromatic" counterpart is a statistical superposition of the monochromatic contributions, leading to depolarization.

As for the electric field, as long as only intensity measurements are concerned, only the second moments of the distributions of the Jones matrix elements are relevant. More precisely, the elements of the Mueller matrix  $\mathbf{M}$  of a system described by a statistically defined Jones matrix  $\mathbf{T}$  are given by [10]

$$\mathbf{M} = \left\langle \begin{bmatrix} \frac{1}{2}(|T_{xx}|^2 + |T_{yy}|^2 + |T_{xy}|^2 + |T_{yx}|^2) & \frac{1}{2}(|T_{xx}|^2 - |T_{yy}|^2 - |T_{xy}|^2 + |T_{yx}|^2) \\ \frac{1}{2}(|T_{xx}|^2 - |T_{yy}|^2 + |T_{xy}|^2 - |T_{yx}|^2) & \frac{1}{2}(|T_{xx}|^2 + |T_{yy}|^2 - |T_{xy}|^2 - |T_{yx}|^2) \\ \Re(T_{xx}^* T_{yx} + T_{xy}^* T_{yy}) & \Re(T_{xx}^* T_{yx} - T_{xy}^* T_{yy}) \\ \Im(T_{xx}^* T_{yx} + T_{xy}^* T_{yy}) & \Im(T_{xx}^* T_{yx} - T_{xy}^* T_{yy}) \\ \Re(T_{xx}^* T_{xy} + T_{yx}^* T_{yy}) & -\Im(T_{xx}^* T_{xy} + T_{yx}^* T_{yy}) \\ \Re(T_{xx}^* T_{xy} - T_{yx}^* T_{yy}) & -\Im(T_{xx}^* T_{xy} - T_{yx}^* T_{yy}) \\ \Re(T_{xx}^* T_{yy} + T_{xy}^* T_{yx}) & -\Im(T_{xx}^* T_{yy} - T_{xy}^* T_{yx}) \\ \Im(T_{xx}^* T_{yy} + T_{xy}^* T_{yx}) & \Re(T_{xx}^* T_{yy} - T_{xy}^* T_{yx}) \end{bmatrix} \right\rangle \quad (1.53)$$

where the average values become exact values if the system is not depolarizing, and is thus described by a well determined Jones matrix  $\mathbf{T}$  (see Appendix A). Such Mueller matrices are usually called Mueller-Jones matrices. More information about the conditions for a Mueller matrix to be a Jones-Mueller matrix are given in Refs. [11, 12].

**An example of procedure to determine  $\mathbf{M}$ .** The Mueller matrix can be experimentally obtained from measurements of the output light with several settings of the source polarizer and the detection analyzer. In the most general case, a  $4 \times 4$  Mueller matrix has 16 independent elements; therefore at least 16 measurements are required. In this paragraph, we provide an example of such procedure.

We may express the Mueller matrix as  $\mathbf{M} = [\mathbf{M}_1 \ \mathbf{M}_2 \ \mathbf{M}_3 \ \mathbf{M}_4]$  where  $\mathbf{M}_1$ ,  $\mathbf{M}_2$ ,  $\mathbf{M}_3$  and  $\mathbf{M}_4$  are four column vectors of four elements each. We may choose to use as the input Stokes vector the normalized Stokes vectors of horizontal, vertical,  $+45^\circ$ -linear and right circular state of polarization defined in Table (1.2) and hence denote them as  $\mathbf{S}_H^i$ ,  $\mathbf{S}_V^i$ ,  $\mathbf{S}_P^i$ ,  $\mathbf{S}_R^i$ , respectively, where  $i$  stays for *incident*. The four output Stokes vectors corresponding to the four incident states of polarization, H, V, P and R can be defined as  $\mathbf{S}_H^o$ ,  $\mathbf{S}_V^o$ ,  $\mathbf{S}_P^o$ ,  $\mathbf{S}_R^o$ , where  $o$  stays for *output*. Each output Stokes vector associated to any of the input Stokes vector is obtained from four measurements of intensity of the output light as given in Eq.(1.34) and can be expressed by multiplying the input Stokes vector for Eq.(1.4.1) as

$$\begin{cases} \mathbf{S}_H^o = \mathbf{M} \cdot \mathbf{S}_H^i = \mathbf{M}_1 + \mathbf{M}_2 \\ \mathbf{S}_V^o = \mathbf{M} \cdot \mathbf{S}_V^i = \mathbf{M}_1 - \mathbf{M}_2 \\ \mathbf{S}_P^o = \mathbf{M} \cdot \mathbf{S}_P^i = \mathbf{M}_1 + \mathbf{M}_3 \\ \mathbf{S}_R^o = \mathbf{M} \cdot \mathbf{S}_R^i = \mathbf{M}_1 + \mathbf{M}_4. \end{cases} \quad (1.54)$$

Solving for the column vectors of  $\mathbf{M}$  yields

$$\begin{cases} \mathbf{M}_1 = \frac{1}{2}(\mathbf{S}_H^o + \mathbf{S}_V^o) \\ \mathbf{M}_2 = \frac{1}{2}(\mathbf{S}_H^o - \mathbf{S}_V^o) \\ \mathbf{M}_3 = \frac{1}{2}(2\mathbf{S}_P^o - (\mathbf{S}_H^o + \mathbf{S}_V^o)) \\ \mathbf{M}_4 = \frac{1}{2}(2\mathbf{S}_R^o - (\mathbf{S}_H^o - \mathbf{S}_V^o)) \end{cases} \quad (1.55)$$

and

$$\mathbf{M} = \frac{1}{2} [\mathbf{S}_H^o + \mathbf{S}_V^o \quad \mathbf{S}_H^o - \mathbf{S}_V^o \quad 2\mathbf{S}_P^o - (\mathbf{S}_H^o + \mathbf{S}_V^o) \quad 2\mathbf{S}_R^o - (\mathbf{S}_H^o - \mathbf{S}_V^o)]. \quad (1.56)$$

This procedure gives an example of the determination of the full Mueller matrix from 16 raw data obtained with input and output polarizations described each by a set of four linearly independent Stokes vectors. In contrast, the determination of the total, linear and circular degrees of polarization would need less measurements. However, only special samples can be fully characterized by one of three degrees of polarization. In the most general case, the full Mueller matrix is needed for such a characterization.

**Diattenuation and polarizance.** As discussed below, once the Mueller matrix has been obtained, its interpretation is by no means trivial, as some properties are not directly accessible from the  $M_{ij}$  elements. Typically, the matrix to be studied is "decomposed" into products of "elementary" components, such as homogeneous diattenuators and retarders, and various types of depolarizers. The properties of the matrix are then nothing else but the properties of these elementary components. However, as several decomposition schemes are available, these properties are not uniquely defined. As a result, in principle the decomposition procedure should be applied with the scheme which best suits the physical system under study.

However, two properties are directly "visible" on the  $M_{ij}$  elements, and these are:

- the *diattenuation*, or *dichroism*, which describes the variation of the output intensity with the input polarization (for constant overall input intensity),
- the *polarizance*, which describes the capability of the system to polarize a totally unpolarized input beam.

Any Mueller matrix  $\mathbf{M}$  may be rewritten in the following form:

$$\mathbf{M} = T_0 \begin{bmatrix} 1 & \mathbf{D}^T \\ \mathbf{P} & \mathbf{m} \end{bmatrix} \quad (1.57)$$

where  $T_0$  is the transmission for incident unpolarized light,  $\mathbf{D}$  is the 3D *diattenuation vector*,  $\mathbf{P}$  the 3D *polarizance vector* and  $\mathbf{m}$  a 3 x 3 real matrix.

We now assume that the incident light is characterized by the (normalized) Stokes vector  $\mathbf{S}^i = [1, \mathbf{s}^i]^T$ . From the very definition of the Mueller matrix, it immediately follows that the emerging intensity, given by the first component  $S_0^o$  of the output Stokes vector  $\mathbf{S}^o$ , varies in the interval

$$T_{min} = T_0 (1 - D) \leq S_0^o \leq T_{max} = T_0 (1 + D) \quad (1.58)$$

the maximum and minimum transmission values  $T_{max}$  and  $T_{min}$  being reached when  $\mathbf{s}^i = \pm \mathbf{D}/\|\mathbf{D}\|$ . From the diattenuator vector we can also define the scalar diattenuation  $D$  as:

$$D = \frac{T_{max} - T_{min}}{T_{max} + T_{min}}, \quad 0 \leq D \leq 1. \quad (1.59)$$

This parameter quantifies the variation of transmission with incident polarization independently of the input polarization states which reach the values  $T_{max}$  and  $T_{min}$  of the transmission.

On the other hand, if the input Stokes vector is totally depolarized, the output Stokes vector is nothing else but  $\mathbf{S}^o = [1, \mathbf{P}]^T$ , showing that the polarizance actually quantifies the capability of the system to polarize an incident totally depolarized beam.

### 1.4.2 Elementary polarization components

**Homogeneous diattenuators.** A diattenuator (also known as partial polarizer or dichroic polarizer) is a non-depolarizing optical device with nonzero diattenuation but zero retardance (a property which will be defined in the next paragraph). Here we'll consider only *homogeneous* diattenuators, which feature two orthogonal eigenstates and these are elliptical in the most general case. The action of such a component on these states is illustrated in Fig. 1.5.

As a homogeneous diattenuator does not introduce any phase shift between its eigenvectors, the eigenvalues of its Jones matrix can be taken both real, their moduli  $P_i$  being related to the transmissions by

$$T_{max} = P_1^2, \quad T_{min} = P_2^2. \quad (1.60)$$

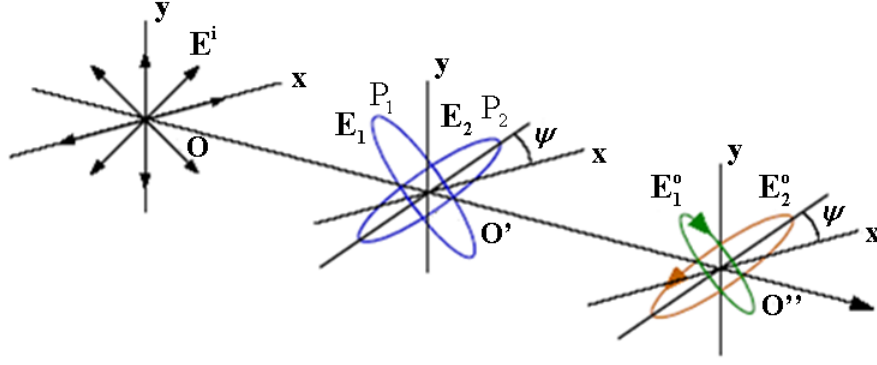


**Figure 1.5:** Action of a homogeneous diattenuator with elliptically polarized eigenstates [2].

The Mueller matrix of such a component is:

$$\mathbf{M}_D = T_0 \begin{bmatrix} 1 & \mathbf{D}^T \\ \mathbf{D} & \mathbf{m}_D \end{bmatrix} \quad (1.61)$$

with

$$\mathbf{m}_D = \sqrt{1 - D^2} \mathbf{I}_3 + (1 - \sqrt{1 - D^2}) \hat{\mathbf{D}} \hat{\mathbf{D}}^T \quad (1.62)$$

where  $\hat{\mathbf{D}}$  is the unit vector parallel to the diattenuation vector  $\mathbf{D}$  and  $\mathbf{I}_3$  is the 3 x 3 identity matrix. This choice ensures that  $\mathbf{m}_D \mathbf{D} = \mathbf{D}$ . Due to its homogenous nature,  $\mathbf{M}_D$  actually describes a rotation on the Poincaré sphere of the incident polarization state towards the highest transmission axis, in the plane containing incident and exiting polarization states and both transmission axes.

Of course, the most widely used homogeneous diattenuators are the linear polarizers, characterized by linear eigenstates and a scalar diattenuation  $D = 1$ .

**Homogeneous phase retarders.** A phase retarder (also called retardation plate, phase shifter or birefringent) transmits its two eigenstates with identical transmissions (no diattenuation) but different phases. The difference between these phases is called the *phase retardation*. In this paragraph we'll consider only *homogeneous* retarders. The action of such components on their eigenstates is illustrated in Fig. 1.6.

The Jones matrix of a homogeneous retarder is *unitary*. Its eigenvalues, and the retardation  $\delta_R$  are of the form:

$$\lambda_1 = e^{j\delta_s}, \quad \lambda_2 = e^{j\delta_f}, \quad \delta_R = \delta_s - \delta_f. \quad (1.63)$$

The Mueller matrix of a phase retarder can be expressed in the synthetic format [13]:

$$\mathbf{M}_R = \begin{bmatrix} 1 & \mathbf{0}^T \\ \mathbf{0} & \mathbf{m}_R \end{bmatrix} \quad (1.64)$$

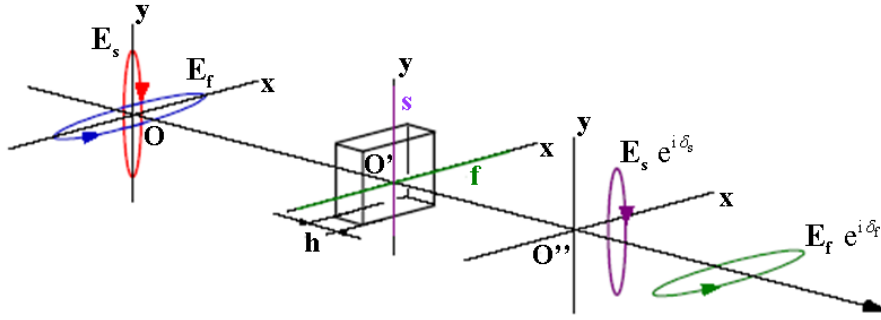


**Figure 1.6:** Action of a homogeneous phase retarder with elliptically polarized eigenstates [2].

where

- $\mathbf{0}^T$  is the zero vector: a pure retarder features zero diattenuation and polarizance,
- $\mathbf{m}_R$  is the reduced 3 x 3 matrix of the retarder. This matrix is a 3D rotation matrix, which actually describes a rotation by an angle  $\delta_R$  on the Poincaré sphere, the axis being defined by the two diametrically opposed points representing the orthogonal eigenstates.

A very common example of homogeneous retarders is a plate of thickness  $h$  cut in a birefringent crystal. Provided the plate is not cut perpendicular to an optical axis of the crystal, the eigenstates are linearly polarized along the axes with refractive indexes  $n_s$  and  $n_f$ , respectively. The retardation is then

$$\delta_R = \delta_s - \delta_f = (k_s - k_f)h = \frac{2\pi}{\lambda}(n_s - n_f)h, \quad (1.65)$$

where  $k_s$  and  $k_f$  are the propagation constants along the axes of the crystal. Another quite common example of homogeneous retarders is provided by optically active media: in this case, the two eigenstates are circularly polarized.

**Depolarizers.** A pure depolarizer does not feature any diattenuation nor birefringence: it merely reduces the degree of polarization of the incoming beam. Of course, in the most general case, this depolarization depends on the incident polarization state. It can be shown that the most general Mueller matrix of a pure depolarizer is of the form [13]:

$$\mathbf{M}_\Delta = \begin{bmatrix} 1 & \mathbf{0}^T \\ \mathbf{0} & \mathbf{m}_\Delta \end{bmatrix} \quad (1.66)$$

where  $\mathbf{m}_\Delta$  is symmetric, semi-positive definite. This matrix can be diagonalized by a unitary transformation into

$$\mathbf{m}_{\Delta d} = \begin{bmatrix} 1 & 0 & 0 & 0 \\ 0 & a & 0 & 0 \\ 0 & 0 & b & 0 \\ 0 & 0 & 0 & c \end{bmatrix} \quad \text{with } a, b, c \geq 0. \quad (1.67)$$

This result shows that a pure depolarizer does not have eigenstates analogous to those of the homogeneous diattenuators and/or retarders: the eigenvectors of interest are not the 4D complete Stokes vectors, but the 3D eigenvectors  $\mathbf{s}_r$  ( $r = 1, 2, 3$ ) of  $\mathbf{m}_\Delta$ . An incoming beam with a Stokes vector of the form  $\mathbf{S}^i = [1, \mathbf{s}_r]^T$  is not "mixed" with other states: its degree of polarization will be reduced by a factor equal to the relevant eigenvalue among  $a, b$  or  $c$ . Its representative point on the Poincaré sphere will migrate from the surface to the center along a radius of the sphere.

A practical case of great importance in this work is that of isotropic scattering media observed in backscattering configuration. Due to the medium isotropy, all linearly polarized states will suffer the same reduction of their degree of polarization. However, this reduction may be different for incident circular polarizations. As a result, for such systems the Mueller matrix in the usual basis is of the form in Eq.(1.67) with  $a = b \neq c$ .

### 1.4.3 Decompositions of Mueller matrices into elementary components

The physical interpretation of the Mueller matrix makes the subject of a debate which has been lasting over the past twenty years and is not closed yet. Ten years ago Lu and Chipman [13] proposed a three-factor decomposition of an arbitrary Mueller matrix  $\mathbf{M}$  comprising a diattenuator ( $\mathbf{M}_D$ ), a retarder ( $\mathbf{M}_R$ ), and a depolarizer ( $\mathbf{M}_\Delta$ ), in this same order. This decomposition is a generalization to depolarizing systems of the polar decomposition developed previously for Jones-Mueller matrices. Thus the initial Mueller matrix  $\mathbf{M}$  is written as

$$\mathbf{M} = \mathbf{M}_\Delta \cdot \mathbf{M}_R \cdot \mathbf{M}_D. \quad (1.68)$$

The properties of the elementary components are then attributed to the initial Mueller matrix. We point out that  $\mathbf{M}_\Delta$  is not the matrix of a "pure" depolarizer: besides the symmetric  $3 \times 3$  matrix, the polarizance is not zero. This choice of a "polarizing depolarizer" is necessary to properly take into account the 16 elements of the initial matrix  $\mathbf{M}$ . On the other hand, this procedure always provides physically realizable matrices for the elementary components.

However, this decomposition really makes sense for systems which can be reasonably seen as serial combinations of a diattenuator, a retarder and a depolarizer in this order. As a result, if the depolarization occurs mainly in the first part of the propagation through the system, before a more "diattenuating" part, then the parameters provided by the Lu and Chipman decomposition may be irrelevant.

A first attempt to generalize the serial decomposition to cases where the depolarizer precedes the diattenuator has been proposed by Morio *et al.* [14], with the same form of "polarizing depolarizer" as the standard Lu and Chipman decomposition, with zero diattenuation and nonzero polarizance. However, in cases of strong depolarization, this method could provide unphysical matrices, and in some cases it could not converge.

These issues have been solved by Ossikovski [15], who introduced a new type of depolarizer, with zero polarizance and nonzero diattenuation. This procedure features the same advantages as the standard Lu and Chipman decomposition in terms of convergence and physical realizability of the elementary matrices, for the components in "reverse" order (with the depolarizer before the diattenuator). Later on Anastasiadou *et al.* [16]

experimentally demonstrated the validity of the Ossikovski reverse decomposition, on *ad-hoc* systems made of elementary components (diattenuator, retarder and diagonal depolarizer) which could be measured individually or stacked up to provide a composite Mueller matrix which could be decomposed, to compare the result of the decomposition with the individual measurements.

Recently, Ossikovski [17] proposed another decomposition, the "symmetrical" one, which recasts (almost) any input Mueller matrix under a product of five factors:

$$\mathbf{M} = \mathbf{M}_{\mathbf{D2}} \cdot \mathbf{M}_{\mathbf{R2}} \cdot \mathbf{M}_{\Delta\mathbf{d}} \cdot \mathbf{M}_{\mathbf{R1}} \cdot \mathbf{M}_{\mathbf{D1}} \quad (1.69)$$

where  $\mathbf{D1}$  and  $\mathbf{D2}$  are two homogeneous diattenuators,  $\mathbf{R1}$  and  $\mathbf{R2}$  two homogeneous retarders and  $\Delta\mathbf{d}$  a *diagonal* depolarizer, with zero polarizance and diattenuation. This decomposition may be better suited than the two previous ones for isotropic tissues, for which diattenuation and/or retardance may occur essentially at the tissue surface, while diagonal decomposition is expected from backscattering in the bulk.

However, in biological tissues we can anticipate that the three basic effects (diattenuation, retardance and depolarization) are not necessarily so well localized, and may occur simultaneously, though to various extents. If so, none of the currently available decomposition methods is expected to provide a realistic description of polarized light propagation in tissues. To address this issue, we can imagine to model the sample as a stack of finite number of thin tissue "slices", with equally distributed polarimetric properties. The effect of each tissue slice on the incident light is represented by means of a Mueller matrix whose decomposition provides the values of the incremental properties of the thin tissue. From the incremental values we may obtain the global polarimetric properties which hopefully will be close to the real ones. The actual implementation of this approach is under study.

## 1.5 Conclusion

This chapter was intended as an introduction to the Jones and Stokes-Mueller formalisms, the latter being the only one adapted to the tissue samples studied in the following. Of course, no original information was presented: the purpose of this chapter was to make the manuscript reasonably self-contained and easily readable by non-specialists.

We first recalled the usual description of polarization states and their transformation by propagation through optical systems in terms of electric fields – the Jones formalism. We then provided what we hope to be a "pedagogical" description of partially polarized states in terms of electric field correlation functions, recast as Stokes parameters and "vectors", together with the practically very important notion of degree of polarization. We then presented the essential features of the geometrical representation of polarization states on (or inside) the Poincaré sphere.

The second (and last) part of the chapter was devoted to Mueller matrices. Again, in this relatively short presentation we tried to emphasize the basic notions behind these matrices, which are most relevant when depolarization is present and the Jones formalism does not apply. In pretty much the same way as for polarization states, in presence of depolarization the system Jones matrix is defined only statistically: then for linear optics only the second order correlation functions of the various matrix elements are meaningful. The Mueller matrix is nothing else but the relevant linear combination of these functions



which describes most easily the transformation of the light Stokes vector by propagation through an optical system.

We discussed several general properties of Mueller matrices, such as their physical realizability, their depolarizing or non-depolarizing character, a possible experimental procedure to measure them and the polarimetric parameters which can be unambiguously extracted from the matrices themselves (diattenuation and polarizance). Then we provide the Mueller matrices of elementary polarization components (homogeneous diattenuators and retarders, depolarizers) for their own sake and because they are used in the decomposition schemes presented in the last part. These procedures recast the initial Mueller matrix into a product of several elementary components, as if they were stacked in a well-defined order.

These decompositions can provide useful information about the properties of Mueller matrices other than the diattenuation and polarizance. However, several decompositions may be applied to a given Mueller matrix, with different final results. It is then important to choose the scheme which best suits the system under study. For the polarimetric imaging based on backscattered light in tissues, as we'll see later, the available decomposition schemes already provide interesting results. However, new decomposition schemes taking into account the fact that the polarimetric changes take place over the full propagation length are being developed to improve the relevance of the data treatments.

# Chapter 2

## Polarized light propagation in scattering media

### 2.1 Introduction

As it is well known, when a light beam propagates in an homogeneous medium its phase velocity is reduced to  $c/n_m$ , where  $n_m$  is the real part of the medium refractive index, while its intensity decreases exponentially, according to the Beer-Lambert law

$$I(z) = I_0 e^{-\mu_a z} \quad (2.1)$$

where  $z$  is the coordinate along the beam propagation direction and  $\mu_a$  the absorption parameter, whose dimension is the reciprocal of a length. We write the medium complex refractive index  $n_m^c$  as

$$n_m^c = n_m + j n'_m \quad (2.2)$$

where  $n_m$  and  $n'_m$  are real. The absorption coefficient is then:

$$\mu_a = 4\pi \frac{n'_m}{\lambda} \quad (2.3)$$

where  $\lambda$  is the light wavelength in vacuum. We can then define the mean absorption length as

$$\ell_a = \frac{1}{\mu_a}. \quad (2.4)$$

In inhomogeneous media, such as biological tissues, in addition to a possible absorption, the essential other process is the *scattering* by material inhomogeneities, which may change both the propagation direction and the polarization of the light beam. Throughout this work, we'll restrict the scope to the case of *non-absorbing spherical scatterers* suspended in homogeneous (possibly absorbing) media.

We first recall the essential theoretical features of *single scattering* processes, which may occur in sufficiently thin samples or at low enough scatterer concentrations, both in the scalar and vector descriptions of the light wave.

We then consider *multiple scattering*, which is the dominant process for the samples studied in the experiments and the numerical simulations described in the following chapters. After introducing the main phenomenological parameters relevant to multiple scattering, we establish the radiative transfer equation (RTE), which describes the evolution of radiance in scattering media. We first consider the scalar form of this equation, which is suitable for unpolarized light. Then we generalize this approach to the vector form (VRTE), which is needed if the light polarization is to be taken into account. Finally, we outline the main methods currently available to solve this equation, including the Monte Carlo approach that we extensively used in the numerical simulation part of this work.

## 2.2 Single scattering

### 2.2.1 Scattering cross-section for spherical scatterers

This part is a reformulation of the calculation presented in Ref. [18]. Our purpose is to evaluate the attenuation of a plane wave by a single non-absorbing scatterer. The scattering cross-section is then defined as the area of an opaque small screen which would lead to the same attenuation of the incoming beam.

As the scatterer is assumed to be non-absorbing the attenuation of the incident plane wave is due to a redistribution of a (typically small) fraction of the incident beam into a scattered spherical wave, centered on the scatterer. As we will see in the following, this redistribution is due to destructive interferences of the incident wave and the part of the scattered wave propagating in the forward direction (i.e. along the propagation direction of the incident wave).

The interaction geometry is illustrated in Fig. 2.1. A plane wave propagating along the  $z$  axis impinges onto the scatterer  $S_c$ , which generates a spherical wave centered on  $S_c$ . The scattered wave carries a much lower intensity than the incident wave. The purpose of the following calculation is to evaluate the energy flux through a circular aperture of radius  $R_0$  in a plane  $\Pi$  perpendicular to the  $z$  axis and at a distance  $z_d$  from  $S_c$ . In order to evaluate the extinction of the incoming wave due to the scattering, we will show that when  $z_d$  increases, the angle  $\theta_0$  which subtends the aperture can be made arbitrarily small, meaning that the final intensity can be interpreted as that of the attenuated incident wave.

Due to the spherical shape of the scatterer and the small angles involved in the calculation, the polarization of the incident wave is not modified by the scattering process. The results are thus independent of this incident polarization, meaning that the incident and scattered waves can be described by the scalar approximation: their electric fields  $E_0$  and  $E_s$  are numbers and not vectors. More precisely, if we drop the temporal evolution of these fields, their amplitudes are:

$$E_0(\mathbf{r}) = u_0 e^{-jkn_m z} \quad (2.5a)$$

$$E_s(\mathbf{r}) = u_s e^{-jkn_m r} \quad (2.5b)$$

where  $r = |\mathbf{r} - \mathbf{r}_{S_c}|$  is the distance between the point  $\mathbf{r}$  and the scatterer  $S_c$ . The phase factors  $kn_m z$  and  $kn_m r$  respectively account for the plane and spherical nature of the two

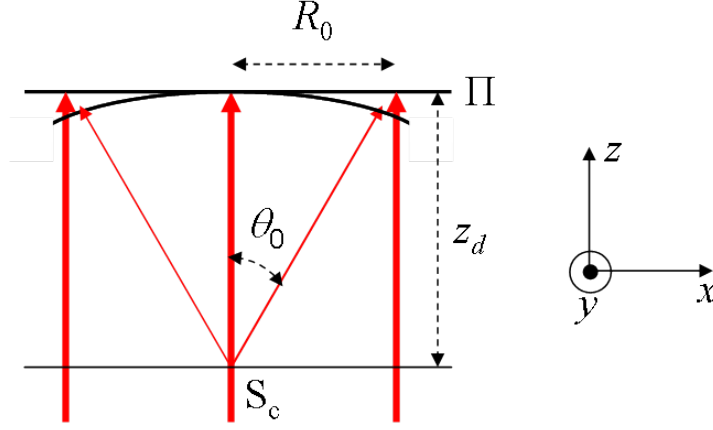


**Figure 2.1:** Geometry of the interaction of a plane wave and the spherical wave centered on the scatterer  $S_c$ .

waves. Moreover, the scattered amplitude  $u_s$  can be written as

$$u_s = u_0 \frac{S(\theta)}{jkn_m r} \quad (2.6)$$

where the amplitude function  $S$ , which determines the angular distribution of the scattered light, depends only on the polar angle  $\theta$ , as expected from the symmetry of the problem, and the factor  $r$  in the denominator comes from the conservation of the total energy when the wave propagates in a medium which is assumed to be non-absorbing. The intensity at the plane  $z = z_d$  is then given by

$$|E_0 + E_s|^2 = |E_0|^2 + 2\Re\{E_0 E_s^*\} + |E_s|^2 \quad (2.7)$$

where the last term may be neglected due to the weakness of the scattered wave with respect to the incident one. The Eq.(2.7) then becomes

$$|E_0 + E_s|^2 = u_0^2 \left\{ 1 + \frac{j}{kn_m z_d} [S^*(\theta) e^{jkn_m(z_d-r)} - S(\theta) e^{jkn_m(r-z_d)}] \right\} \quad (2.8)$$

where we took into account that for the denominator we can replace the distance  $r$  from  $S_c$  by  $z_d$ . Now, due to the smallness of the angle  $\theta_0$ , the distance  $r$  between  $S_c$  and the point with coordinates  $(x, y)$  in the plane ( $\Pi$ ) can be approximated as

$$r \approx z_d + \frac{x^2 + y^2}{2z_d}. \quad (2.9)$$

By taking into account this approximation in Eq.(2.7) we evaluate the energy flux through the aperture of radius  $R_0$  and area  $A = \pi R_0^2$  as

$$F = \iint_A |E_0 + E_s|^2 dx dy = u_0^2 \left[ \pi R_0^2 + \frac{j}{kn_m z_d} K \right] \quad (2.10)$$

where the integral  $K$  is

$$K = \iint_A \left[ S^*(\theta) e^{-jkn_m \left( \frac{x^2+y^2}{2z_d} \right)} - S(\theta) e^{jkn_m \left( \frac{x^2+y^2}{2z_d} \right)} \right] dx dy. \quad (2.11)$$

In Eq.(2.11) when  $(x^2 + y^2)$  increases the exponential terms oscillates faster and faster and contributes less and less to the integral  $K$ . We can consider that the "active" region actually contributing to  $K$  is the circular domain of  $\Pi$  with radius

$$R_a = 2\pi \sqrt{\frac{z_d}{\lambda}} \quad (2.12)$$

for which the phase factors are of the order of  $2\pi$ . As a result, if we keep the angle  $\theta_0$  constant and increase  $z_d$ , the ratio  $R_a/R_0$  tends to zero, implying that in the integral  $K$  or  $F$  we can take the integration limits at infinity. We can thus consider arbitrarily small values of  $\theta_0$ , meaning that what we are considering is actually the superposition of the incident and the forward scattered wave. Then, we can assume that in the integral  $K$ ,  $\theta \approx 0$  independently of  $x$  and  $y$  coordinates. From

$$\int_{-\infty}^{+\infty} e^{j\alpha x^2} dx = \left( \frac{j\pi}{\alpha} \right)^{\frac{1}{2}} \quad (2.13)$$

we easily deduce the expression of  $K$  and rewrite Eq.(2.10) as

$$F = u_0^2 \left[ \pi R_0^2 + \frac{4\pi}{k^2 n_m^2} \Re\{S(\theta = 0)\} \right]. \quad (2.14)$$

In Eq.(2.14) the distance  $z_d$  does not appear any more. This equation shows that the effect of the particle in the forward direction (the same as the incoming wave) is a reduction of the energy flux equivalent to that obtained if an opaque screen of area

$$\sigma_s = \frac{4\pi}{k^2 n_m^2} \Re\{S(\theta = 0)\} \quad (2.15)$$

had been placed at the location of the scatterer  $S_c$ .

## 2.2.2 Scattering of polarized waves

**Scattering by particles of arbitrary shapes.** We now consider a single scattering event for which we explicitly take into account the polarizations of the incident and scattered waves. The scattering in any direction of the space by a particle of arbitrary shape is described by four amplitude functions,  $S_1$ ,  $S_2$ ,  $S_3$  and  $S_4$ , all dimensionless, in general complex, and dependent on the orientation of the particle as well as on the angles  $\theta$  and  $\varphi$ , which describe the direction of propagation in respect to the direction of propagation of the incident light, but not on the distance  $r$  from the particle. The four amplitude functions form a matrix  $\mathbf{S}(\theta, \varphi)$  of four elements that describes the relation between the component of the incident wave and the components of the scattered wave, such that:

$$\begin{bmatrix} E_{s\parallel} \\ E_{s\perp} \end{bmatrix} = \begin{bmatrix} S_2 & S_3 \\ S_4 & S_1 \end{bmatrix} \cdot \frac{e^{jkn_m r - jkn_m z}}{jkn_m r} \cdot \begin{bmatrix} E_{0\parallel} \\ E_{0\perp} \end{bmatrix} \quad (2.16)$$

where  $\parallel$  and  $\perp$  refer respectively to the components of the field parallel and perpendicular to the scattering plane. This matrix is nothing else but the Jones matrix describing the single scattering event, with the  $\parallel$  and  $\perp$  directions as a reference frame for both the incident and the scattered wave.

**Scattering by spherical particles.** If the scattering particle is spherical, then the symmetry of the system forbids any intensity transfer between  $\perp$  to  $\parallel$  components of the fields (see Appendix B). As a result, both  $S_3$  and  $S_4$  vanish, while the diagonal amplitude functions  $S_1$ ,  $S_2$  depend on  $\theta$ , but not on the azimuth  $\varphi$ . Then:

$$E_{s\parallel} = S_2(\theta) \frac{e^{jkn_m r - jkn_m z}}{jkn_m r} E_{0\parallel} \quad (2.17a)$$

$$E_{s\perp} = S_1(\theta) \frac{e^{jkn_m r - jkn_m z}}{jkn_m r} E_{0\perp}. \quad (2.17b)$$

Both parallel and perpendicular components of the scattered wave are spherical waves outgoing from the particle. The corresponding intensities are:

$$I_{s\parallel} = |E_{s\parallel}|^2 = \frac{|S_2(\theta)|^2}{k^2 n_m^2 r^2} I_{0\parallel}, \quad I_{s\perp} = |E_{s\perp}|^2 = \frac{|S_1(\theta)|^2}{k^2 n_m^2 r^2} I_{0\perp}. \quad (2.18)$$

Moreover, for forward scattering ( $\theta = 0$ ) by a spherical particle the two amplitude functions become equal:  $S_1(0) = S_2(0)$ , and will be denoted as  $S(\theta)$ , as in the previous subsection, which justifies the scalar approximation.

For a spherical particle of radius  $r_s$  we define the parameter  $x = kn_m r_s$ , which determines the size of the particle with respect to  $\lambda$ . From the particle cross-section  $\sigma_s$  given by Eq.(2.15) we define the scattering efficiency factor:

$$Q_s = \frac{4}{x^2} \text{Re}\{S(0)\}. \quad (2.19)$$

The formal solution of Maxwell's equations for the problem of plane wave scattering by a spherical particle by the Mie theory provides the expressions of the fields both inside and outside the scatterer. These expressions, in spherical coordinates are explicated in Appendix B.

This theory provides the amplitude function as two infinite series of the form:

$$S_1(\theta) = \sum_{n=1}^{\infty} \frac{2n+1}{n(n+1)} \{a_n \pi_n(\cos \theta) + b_n \tau_n(\cos \theta)\}, \quad (2.20a)$$

$$S_2(\theta) = \sum_{n=1}^{\infty} \frac{2n+1}{n(n+1)} \{b_n \pi_n(\cos \theta) + a_n \tau_n(\cos \theta)\} \quad (2.20b)$$

where again the coefficients  $a_n$  and  $b_n$  and the functions  $\pi_n$  and  $\tau_n$  are explicated Appendix B.

For the forward direction ( $\theta = 0$ ) we get:

$$S(0) = \sum_{n=1}^{\infty} (2n+1)(a_n + b_n), \quad (2.21)$$

where we have used the relations:

$$\pi_n(1) = \tau_n(1) = \frac{1}{2}(n+1). \quad (2.22)$$

Then, the extinction cross-section due to the scattering is given by:

$$\sigma_s = \frac{4\pi}{k^2 n_m^2} \text{Re} \left\{ \sum_{n=1}^{\infty} (2n+1)(a_n + b_n) \right\}. \quad (2.23)$$

The Mueller matrix of a single scattering sphere can be obtained from the Jones matrix (defined in Eq.(2.30)) as:

$$\mathbf{M}(r, \theta) = \frac{1}{k^2 n_m^2 r^2} \mathbf{M}(\theta) = \frac{1}{k^2 n_m^2 r^2} \begin{bmatrix} M_{11} & M_{12} & 0 & 0 \\ M_{12} & M_{11} & 0 & 0 \\ 0 & 0 & M_{33} & M_{34} \\ 0 & 0 & -M_{34} & M_{33} \end{bmatrix}, \quad (2.24)$$

where the nonvanishing elements of the matrix  $\mathbf{M}(\theta)$  are

$$M_{11} = \frac{|S_2(\theta)|^2 + |S_1(\theta)|^2}{2} \quad (2.25a)$$

$$M_{12} = \frac{|S_2(\theta)|^2 - |S_1(\theta)|^2}{2} \quad (2.25b)$$

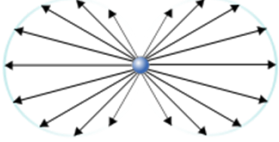
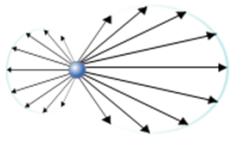
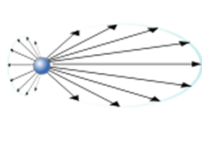
$$M_{33} = \frac{1}{2} [S_1(\theta)S_2^*(\theta) + S_2(\theta)S_1^*(\theta)] \quad (2.25c)$$

$$M_{34} = \frac{j}{2} [S_1(\theta)S_2^*(\theta) - S_2(\theta)S_1^*(\theta)] \quad (2.25d)$$

$\mathbf{m}$  has the block-diagonal form of a Mueller matrix derived from the diagonal Jones matrix describing the scattering by a single sphere by the relation given in subsection 1.4.1 and

- the two 2 x 2 blocks out of the diagonal are zero,
- $M_{22} = M_{11}$ ,  $M_{21} = M_{12}$ ,  $M_{43} = M_{34}$ ,  $M_{44} = M_{33}$ ,
- $M_{11}$ ,  $M_{12}$ ,  $M_{33}$ ,  $M_{34}$  are linearly independent and verify the relation

$$M_{11}^2 = M_{12}^2 + M_{33}^2 + M_{34}^2. \quad (2.26)$$

$m > 1$		
$x \ll 1$	$x \sim 1$	$x \gg 1$
<b>Rayleigh scattering</b>	<b>Mie scattering</b>	<b>Geometrical optics</b>
		

**Figure 2.2:** Illustration of the regime of scattering ( $x = kn_m r_s$ ) [19].

### 2.2.3 Short-cutting the Mie theory: the scattering regimes

The Mie theory detailed in Appendix B provides the formal solution of the Maxwell's equations for the scattering of an electromagnetic wave by a sphere embedded in a medium. However, it may be convenient in practice to identify the essential *scattering regimes* which may occur, depending on the values of the size parameter ( $x = kn_m r_s$ ) and the refractive index contrast ( $m = \frac{n_s}{n_m}$ ). These two parameters provide complementary information about the scattering medium: the size parameter  $x = \frac{2\pi}{\lambda} n_m r_s$  gives information on the "size or length of the wave" in the medium where the wave is travelling, i.e. the *wavelength* denoted as  $\lambda$ , the refractive index of medium  $n_m$  and the size (radius) of the sphere  $r_s$ ; the refractive index contrast  $m$  takes into account the refractive indexes of the medium inside  $n_s$  and outside the sphere  $n_m$ .

We consider the case where  $m > 1$ , that is  $n_s > n_m$ , (see Fig. 2.2). Then depending on the value of the size parameter we distinguish the following regimes of scattering:

- **Rayleigh scattering regime.** This regime carries the name of the physicist who wrote on the first theory of light scattering (1871). In this case, the scattering sphere is much smaller than the wavelength of the incident light in the hosting medium. As a result, the electric field  $\mathbf{E}_0$  associated to the incident wave is uniform on the sphere, which then behaves as a single dipole. This is so provided that

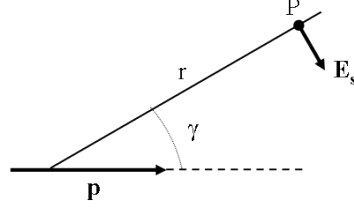
$$kn_m r_s \ll 1. \quad (2.27)$$

The magnitude of this dipole  $\mathbf{p}$  is proportional to the incident field:  $\mathbf{p} = \wp \mathbf{E}_0$  where  $\wp$  is the sphere polarizability. Since  $\mathbf{E}_0$  has the dimension of a charge per area and  $\mathbf{p}$  is a charge times length, then  $\wp$  has the dimension of a volume. In general  $\wp$  is a tensor, which implies that the directions of  $\mathbf{p}$  and  $\mathbf{E}_0$  coincide only if the field is applied along one of the three mutually perpendicular directions by the eigenvectors of  $\wp$ .

In the specific case of a spherical scatterer the polarizability is isotropic, then the directions of  $\mathbf{p}$  and  $\mathbf{E}_0$  always coincide, and  $\wp$  in the previous formula can be taken as a scalar. [20]

The scattered field and its amplitude in a point P in the far field-zone ( $r \gg \lambda$ ) of the spherical scatterer in a direction that makes an angle  $\gamma$  with  $\mathbf{p}$  is



**Figure 2.3:** Electric dipole scattering [20].

$$E_s = \frac{k^2 n_m^2 p \sin(\gamma)}{r} e^{-j k n_m r} \quad (2.28)$$

times the unit vector directed as the component of  $\mathbf{p}$  perpendicular to the radius vector (see Fig. 2.3).

The angle  $\gamma$  is the angle of a direction of scattering with the incident electric field  $\mathbf{E}_0$ . If  $\theta$  is the scattering angle, the perpendicular ( $\perp$ ) component has  $\gamma = 90^\circ$  and the parallel ( $\parallel$ ) component has  $\gamma = 90^\circ - \theta$ . Then, the scattered field is obtained by substituting the following scattering tensor in Eq.(2.16)

$$\begin{bmatrix} S_2 & S_3 \\ S_4 & S_1 \end{bmatrix} = j k^3 n_m^3 \wp \begin{bmatrix} \sin(90^\circ - \gamma) & 0 \\ 0 & \sin 90^\circ \end{bmatrix} = j k^3 n_m^3 \wp \begin{bmatrix} \cos \theta & 0 \\ 0 & 1 \end{bmatrix} \quad (2.29)$$

and we obtain

$$E_{s\parallel} = \frac{k^2 n_m^2 \wp \cos(\theta)}{r} e^{-j k n_m r + j k n_m z} E_{0\parallel} \quad (2.30a)$$

$$E_{s\perp} = \frac{k^2 n_m^2 \wp}{r} e^{-j k n_m r + j k n_m z} E_{0\perp}. \quad (2.30b)$$

The scattered intensity for incident natural light  $I_0$  is

$$I_s = \frac{(\cos^2 \theta + 1) k^4 n_m^4 |\wp|^2}{2r^2} I_0 \quad (2.31)$$

where the term  $\cos^2 \theta$  comes from  $S_2(\theta)$  and corresponds to the  $\parallel$ -component and 1 comes from  $S_1(\theta)$  and corresponds to the  $\perp$ -component.

The scattering diagram in Fig. 2.4 illustrates the equations above. The black line denotes the total intensity of the unpolarized light; the red and green lines the parallel and the perpendicular polarized component, respectively.

We remark that for the scattering by a sphere both  $\parallel$ - and  $\perp$ - components, and then the unpolarized light, are symmetrically scattered in the space. In particular, the scattering of the  $\parallel$ - component reduces as we move from  $\theta = 0^\circ$  to the directions given by the angles  $\theta = 90^\circ$  and  $\theta = 270^\circ$ , while the scattering of the  $\perp$ - component is independent from the direction. In fact, at  $\theta = 90^\circ$  or  $\theta = 270^\circ$  light is completely polarized and consists of  $\perp$ -component, since the  $\parallel$ -component is zero; as we move to  $\theta = 0^\circ$  and  $\theta = 180^\circ$  directions the  $\parallel$ - and  $\perp$ - components sum together into the total scattered light.

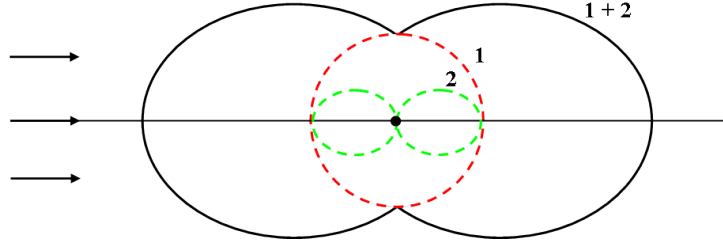


**Figure 2.4:** Rayleigh scattering: polar diagram of scattered intensity if incident radiation is unpolarized, 1 = polarized with electric vector perpendicular to the plane of drawing, 2 = polarized with electric vector parallel to the plane of drawing, 1 + 2 = total. The incident light is travelling from left to right [20].

Although the diagram in Fig. 2.4 is commonly referred as *the diagram for the Rayleigh scattering* it is valid only if the incident light is natural and the scatterer is isotropic ( $\varphi$  is a scalar).

- **Mie scattering regime.** (1908) In this regime of scattering the sphere is comparable to the wavelength of the light travelling in the medium:

$$0.1 < kn_m r_s < 10. \quad (2.32)$$

We can visualize the single sphere ( $r_s$ ) as an aggregate of many smaller spherical scatterers ( $dr_s$ ,  $dr_s \ll r_s$ ) that look small to the eye of the incident light ( $dr_s$ ,  $dr_s \ll \lambda$ ) of similar size and optical properties. The applied electrical field  $\mathbf{E}_0$  is not homogenous on the large sphere, and induces a different dipole on any small sphere included in the large sphere. As a consequence the field irradiated by a single sphere ( $dr_s$ ) is modified and distorted by the field irradiated by any others and the scattering from the large sphere ( $r_s$ ) is not isotropic anymore. In particular the scattering by the large sphere exceeds in the forward direction ( $\theta = 0^\circ$ ) and lacks in the backward direction ( $\theta = 180^\circ$ ) in respect to isotropic scattering. Also the excess of forward scattering increases as the size of the sphere gets bigger.

- **Geometrical optics regime.** This regime of scattering occurs when

$$kn_m r_s \gg 0.1. \quad (2.33)$$

The sphere looks very large to the eye of light traveling in the medium. Indeed the incident light perceives the spherical scatterer as another infinitely extended medium with different optical properties from the embedding medium, rather than a confined body. In this case we do not talk anymore of scattering by a sphere but of *reflection*, *refraction* and *diffraction* at the interfaces between the two homogenous media, which are treated by the laws of geometric optics.

- **Rayleigh-Gans scattering regime.** We now consider the case  $|m - 1| \ll 1$ . This is specific of a sphere embedded in a medium whose refractive indexes ( $n_s$ ,  $n_m$ , respectively) almost match, then the refractive index contrast approximates one ( $m \approx 1$ ). In this case we talk about *soft scattering medium*. We do not make any restriction on the size of the sphere for a moment. In the most general case the

scattering sphere is large at the eyes of the incident light, then the description of the large sphere ( $r_s$ ) as an aggregate of smaller spheres ( $dr_s$ ) is still appropriate and in general the incident field is different from one small sphere to another and as a consequence the scattering from the large sphere is not isotropic anymore. In particular we make the hypothesis of small phase shift for the incident wave, written as

$$2kr_s|m - 1| \ll 1, \quad (2.34)$$

and ensuring a small value of the efficiency factor for the scattering

$$Q_s \ll 1. \quad (2.35)$$

Under this condition the incident field  $\mathbf{E}_0$  to the "large" sphere ( $r_s$ ) is still homogeneous on the sphere, and it is the same for any "small" sphere ( $dr_s$ ) included in the large sphere. Then the incident wave induces identical electric dipole moment on any small sphere and any small sphere irradiates isotropically in the space as any other was there (we talk about independent scattering). Due to their different locations inside the volume of the large sphere the single waves of independent scattering interfere to each other producing Rayleigh-Gans scattering regime.

## 2.3 Multiple scattering

### 2.3.1 The essential assumptions

We now consider a sample consisting of many scatterers embedded in an homogeneous medium. While in the previous section we considered single scattering events, now we take into account the possibility that multiple scattering can take place before the wave emerges from the sample. Throughout this work, we make the two following basic assumptions:

- The interaction takes place in the *independent scattering regime*. This means that the scattering spheres are sufficiently far away from each other so that in each sequence of two successive scattering events one can neglect the light backscattered by the second sphere into the first one. Then, the spherical wave generated by a single scatterer is almost a plane wave when it reaches the next particle in its trajectory. A crude, but conservative criterion in this respect is that the mean distance between the scatterers is much larger than their radius. If so we can consider that the overall scattering process is a sequence of single events which can be described as in the previous section;
- We neglect *any interference effects* among scattered waves which have followed different paths to eventually emerge with sufficiently close geometrical parameters to be detected "together", as it would be the case for waves emerging at the same point of the sample surface for real space imaging, or with the same direction for Fourier space imaging. So in all cases we'll add the *intensities* due to individual emerging waves and not their fields. In other words, we *do not consider the speckles* which are seen in the light scattered by a static sample illuminated with spatially and

temporally coherent light. This assumption is valid for the experiments described in the following chapters. Actually, in the first experimental investigations we used coherent illumination, but on "moving samples", such as suspensions of polystyrene spheres in water: due to the Brownian motion of the spheres, the speckle pattern was blurred in very short times with respect to the detector integration time, thus destroying any coherence effects. To image "real" tissue samples, we used spectrally filtered classical sources (halogen lamps) featuring too small coherence lengths to see any speckle pattern in the polarimetric images.

In the following of this section, we define the main parameters (mean free paths, anisotropy...) useful to describe the multiple scattering process.

### 2.3.2 The usual scattering parameters

**Mean free path.** Let us consider a well collimated light beam with unit section traveling along the  $z$  axis. Calling  $I(z)$  its intensity at a depth  $z$  and  $N_s$  the scatterer number density (i.e. the number of scatterers per unit volume), from the previous definition of the scattering cross-section and a straightforward evaluation of the average number of scatterers found in a slice of thickness  $dz$ , we get

$$I(z + dz) - I(z) = -I N_s \sigma_s dz \quad (2.36)$$

which can be recast into a Beer-Lambert law

$$\frac{dI}{dz} = -\mu_s I \Rightarrow I(z) = I_0 e^{-\mu_s z} \quad (2.37)$$

where  $\mu_s$  is the scattering coefficient. Its reciprocal

$$\ell_s = \frac{1}{\mu_s} \quad (2.38)$$

is the *scattering mean free path*. The parameters  $\mu_s$  or  $\ell_s$  quantify the progressive extinction of the beam due to the successive scattering events, in way analogous to their counterparts  $\mu_a$  or  $\ell_a$  for absorption. Moreover,  $\mu_s$  is nothing else but the average distance between two successive scattering events.

Of course, the above formulas are easily generalized to cases where several populations of scatterers are simultaneously present in the homogeneous medium. Such samples will be called "polydisperse", while samples with a single population of scatterers are called "monodisperse". If we identify these populations by the index  $i$ , the overall scattering parameter is simply the sum of the scattering parameters of all the populations

$$\mu_s = \sum_i \mu_{s,i} = \sum_i N_{s,i} \sigma_{s,i}. \quad (2.39)$$

If both scattering and absorption by the homogeneous medium are present, then the extinction of the incoming beam is still governed by a Beer-Lambert law, with the extinction parameter

$$\mu_e = \mu_a + \mu_s. \quad (2.40)$$

Let's consider a scattering medium whose shape is that of a slab with thickness  $h$  along the direction of light propagation. Then, assuming the homogeneous medium is non-absorbing the average number  $\nu_s$  of scattering events the light beam suffers during its propagation over the length  $h$  is

$$\nu_s = \frac{h}{\ell_s} \quad (2.41)$$

**Scattering anisotropy.** The parameters which have been defined so far essentially describe the behavior of the *incident beam*, and more particularly its attenuation when it propagates. We now introduce the parameters which characterize the *scattered light*, with particular emphasis on the asymmetry parameter (or anisotropy)  $g$ . However, this semiquantitative description will be currently restricted to the scattering of unpolarized light by spherical particles. The effects of polarization will be fully taken into account in the next section, where we establish the vector radiative transfer equation (VRTE).

Under this assumptions, the angular distribution function of the scattered intensity, for an incident unpolarized beam and without any polarization selection on the scattered beam is directly related to the *phase function*  $p(\theta)$  which is the probability of a scattered wave to be found in the solid angle  $d\Omega = 2\pi \sin \theta d\theta$  which subtends all directions with a polar angle in an interval  $d\theta$  around  $\theta$ . As the phase function is a probability distribution, it is normalized according to

$$\int_{4\pi} p(\theta) d\Omega = \int_0^\pi p(\theta) 2\pi \sin \theta d\theta = 1. \quad (2.42)$$

This phase function can be expressed in terms of the  $S_i(\theta)$  amplitude functions defined previously. From Eqs.(2.18) we obtain for the total intensity  $I$  scattered in the  $\theta$  direction

$$I_s(\theta) = \frac{1}{2} (I_{s\parallel} + I_{s\perp}) = \frac{|S_1(\theta)|^2 + |S_2(\theta)|^2}{2k^2 n_m^2 r^2} I_0 \quad (2.43)$$

where  $I_0$  is the total intensity of the unpolarized incident beam.

The energy flux  $F(\theta)d\Omega$  in the solid angle  $d\Omega$  around the polar angle  $\theta$  is the product of the probability per unit time to see a scattering event and the normalized phase function:

$$F(\theta) d\Omega = I_s(\theta) r^2 d\Omega = \sigma_s I_0 p(\theta) d\Omega \quad (2.44)$$

which, combined with the previous equation, yields

$$p(\theta) = \frac{|S_1(\theta)|^2 + |S_2(\theta)|^2}{4\pi k^2 n_m^2 \sigma_s}. \quad (2.45)$$

The anisotropy parameter  $g$  is then defined as

$$g = \langle \cos \theta \rangle = \int_0^\pi p(\theta) \cos \theta \, 2\pi \sin \theta \, d\theta. \quad (2.46)$$

This parameter, always comprised between -1 and 1, may take the following values

- $g = 0$  for isotropic scattering (Rayleigh scattering),
- $g = 1$  for purely forward scattering ( $\theta = 0^\circ$ ),
- $g = -1$  for purely backward scattering ( $\theta = 180^\circ$ ).

More in general, when  $g$  is positive the scattering by the medium is principally in the forward direction, while for negative  $g$  values the scattering is principally in the backward direction. As a good approximation, we can assume that  $g$  ranges from 0.6 to 0.99 [21] for most biological tissues. Hence, the corresponding maximal scattering angles range most frequently from  $8^\circ$  to  $45^\circ$  from the forward direction.

Several analytical approximations for phase functions  $p(\theta)$  have been proposed. The most widely used is the *Henye-Greenstein* function defined as:

$$p(\theta) = \frac{1}{4\pi} \frac{1 - g^2}{(1 + g^2 - 2g \cos \theta)^{\frac{3}{2}}}. \quad (2.47)$$

From the anisotropy factor we define another mean free path:

$$\ell'_s = \frac{\ell_s}{(1 - g)} \quad (2.48)$$

which characterizes the mean distance needed for the scattered light to significantly deviate from the direction of the incoming beam. If  $g \approx 1$ , at each scattering event the light is only very slightly deviated and many scattering events will be needed to reach a significant deviation. In this case  $\ell'_s \gg \ell_s$ . Otherwise, if the scattering is more isotropic (or even backward oriented) then  $g \leq 0$  and the two mean free paths become comparable: the light is strongly deviated at each scattering event.

When the absorption and scattering mean free paths are comparable it is very convenient to define an additional parameter called as *optical albedo* and expressed as the ratio between the scattering coefficient and the total attenuation coefficient:

$$a = \frac{\mu_s}{\mu_a + \mu_s}. \quad (2.49)$$

For  $a = 0$  the incident beam attenuation is exclusively due to absorption, whereas  $a = 1$  only to the scattering. In general, both effects take place with variable weights.

In presence of absorption, the normalization of the phase function as given by Eq.(2.42) must be modified:

$$\int_{4\pi} p(\theta) d\Omega = a. \quad (2.50)$$

### 2.3.3 The Radiative Transfer Equation

Transport equations, such as that formulated by Boltzmann for the motion of gases, are based on local balance for the relevant quantities (particle number, energy, momentum...). Such equations have been used, among many other applications, to calculate fission rates in nuclear reactors [22]. However, photons and neutrons differ in two principal aspects: the polarization and the nature of the interaction with the scatterers. The polarization of photons is essential in the description of photons propagation and scattering, while the spin of neutrons, in general, is neglected [23]. On the other hand, collision of polarized photons with scattering particles looks simpler to describe in comparison with that of neutrons with atoms, as the nature of the collision neutron-atom depends on the energy of the incident neutron. However, all analytical and numerical methods developed to solve the neutron transport equation can be applied to the case of polarized-photon traversing scattering media.

In this part, we will introduce the radiative transfer equation (or RTE), which governs the evolution of light in a scattering medium. We shall first restrict ourselves to the scalar approximation, meaning that we neglect the polarization effects. The corresponding equation is usually called radiative transfer equation. This approach provides reasonable results for the intensity, and becomes more and more accurate when the scattering light gets strongly depolarized. In a second step, we will derive the vector RTE, which fully takes into account the polarization effects.

**Derivation of the scalar RTE.** At each spatial location  $\mathbf{r}$  inside a scattering medium one finds light rays propagating in various directions, as, for, example, at the output of an extended light source. The *intensity*  $dI$  of the light propagating in a solid angle  $d\Omega$  around the direction defined by the unit vector  $\mathbf{\Omega}$  is given by

$$dI(\mathbf{r}, \mathbf{\Omega}, t) = L(\mathbf{r}, \mathbf{\Omega}, t) d\Omega \quad (2.51)$$

where the function  $L$  is the *radiance*, expressed in units homogeneous to  $[\text{W cm}^{-2} \text{ sr}^{-1}]$ .

To establish the radiative transfer equation, we "follow" the propagation, over a time interval  $\Delta t$ , of the light directed into the solid angle  $d\Omega$  around the unit vector  $\mathbf{\Omega}$ . This light propagates with the velocity  $v=c/n$ . During its propagation, the evolution of the radiance is the result of three contributions

- an *attenuation* due to absorption by the medium and the scattering of the considered beam into directions different from  $\mathbf{\Omega}$ . As described above, this attenuation is quantified by the extinction coefficient  $\mu_e$ ,
- an *intensification* due to the scattering into  $d\Omega$  of light beams initially travelling into other directions  $\mathbf{\Omega}'$ ,
- the contribution of *internal sources*, if any. We add this contribution for completeness, but it will be dropped for the modelling of tissues, where such sources are obviously absent, except for modelling fluorescence imaging, which is outside the scope of this work. Internal sources continuously distributed within the system are defined by their radiance  $\Sigma(\mathbf{r}, \mathbf{\Omega}, t)$  per unit volume

$$L_{\Sigma}(\mathbf{r}, \mathbf{\Omega}, t) d\Omega = \Sigma(\mathbf{r}, \mathbf{\Omega}, t) dV d\Omega \quad (2.52)$$

where  $L_\Sigma$  is the radiance of the sources found within  $dV$ .

The overall variation of radiance over a distance  $v\Delta t$  along the direction  $\mathbf{\Omega}$  is thus

$$\begin{aligned} L(\mathbf{r} + v\Delta t\mathbf{\Omega}, \mathbf{\Omega}, t + \Delta t) - L(\mathbf{r}, \mathbf{\Omega}, t) = & -\mu_e L(\mathbf{r}, \mathbf{\Omega}, t) v\Delta t + \\ & + \int_{\mathbf{\Omega}'} \mu_e v\Delta t p(\mathbf{\Omega}' \rightarrow \mathbf{\Omega}) L(\mathbf{r}, \mathbf{\Omega}', t) d\mathbf{\Omega}' + \Sigma(\mathbf{r}, \mathbf{\Omega}, t) v\Delta t. \end{aligned} \quad (2.53)$$

In this equation, the three terms on the right side correspond to the contributions cited above. The first and third terms corresponds respectively to the beam extinction and the contribution of the sources. In the second term, the factor  $\mu_s v\Delta t$  is the probability for a scattering to occur over the distance  $v\Delta t$ .  $p(\mathbf{\Omega}' \rightarrow \mathbf{\Omega})$  is a phase function, normalized as above:

$$\int_{4\pi} p(\mathbf{\Omega}' \rightarrow \mathbf{\Omega}) d\mathbf{\Omega} = a. \quad (2.54)$$

As a result, the second term is the product of the number of scattering events per second and the probability, once the scattering has taken place, that it corresponds to a deviation from  $\mathbf{\Omega}'$  to  $\mathbf{\Omega}$ . The previous relationship is valid only if the scattering and extinction coefficients are time-independent. If we divide all terms of Eq.(2.53) by  $v\Delta t \rightarrow 0$ , the increase of  $I$  in the first term can be expressed in terms of time and space partial derivatives:

$$\begin{aligned} \frac{\partial L(\mathbf{r}, \mathbf{\Omega}, t)}{\partial t} + \mathbf{\Omega} \cdot \nabla L(\mathbf{r}, \mathbf{\Omega}, t) = & -\mu_e L(\mathbf{r}, \mathbf{\Omega}, t) + \\ & + \int_{\mathbf{\Omega}'} \mu_s p(\mathbf{\Omega}' \rightarrow \mathbf{\Omega}) L(\mathbf{r}, \mathbf{\Omega}', t) d\mathbf{\Omega}' + \Sigma(\mathbf{r}, \mathbf{\Omega}, t). \end{aligned} \quad (2.55)$$

**Derivation of the vector RTE.** To take into account the polarization in the radiative transfer equation we define a *vectorial radiance*  $\mathbf{L}$  in an analogous way as the scalar radiance  $L$ , with the components of the Stokes vector replacing the intensity  $I$

$$dS_i(\mathbf{r}, \mathbf{\Omega}, t) = L_i(\mathbf{r}, \mathbf{\Omega}, t) d\mathbf{\Omega} \quad (i = 1..4). \quad (2.56)$$

The vectorial radiance  $\mathbf{L}$  is thus the density probability distribution of the four components of the Stokes vector (which are actually intensities) in the  $\mathbf{\Omega}$  space. Similarly, if internal sources are to be considered, the  $L_\Sigma$  and  $\Sigma$  also become four-dimensional "vectors"  $\mathbf{L}_\Sigma$  and  $\mathbf{\Sigma}$ .

The phase function  $p(\mathbf{\Omega}' \rightarrow \mathbf{\Omega})$  must also be adapted to the vectorial description of radiances. This phase function now provides the probabilities for an input  $\mathbf{L}$  vector of a wave propagating along  $\mathbf{\Omega}'$  to be scattered into a small solid angle  $d\mathbf{\Omega}$  around the direction  $\mathbf{\Omega}$ . Of course, the polarization of the scattered photon is described by a Stokes vector. As a result, the phase function  $\mathbf{P}$  takes the form of an angle-resolved 4 x 4 real matrix, similar to a Mueller matrix. However, the normalization conditions imply that this "matrix" depends on the input vector radiance  $\mathbf{L}$ , and therefore it is not a "true" Mueller matrix.



For completeness here we outline the essential steps of the calculation, which is described in more detail in the next chapter. We define an orthonormal frame of reference  $(\mathbf{e}_x^0, \mathbf{e}_y^0, \mathbf{e}_z^0)$  for the "incident" wave travelling along  $\mathbf{\Omega}'$ , with  $\mathbf{e}_z^0 = \mathbf{\Omega}'$ . In this frame, the direction  $\mathbf{\Omega}$  is given by its two usual polar and azimuthal angles  $(\theta, \varphi)$ . As shown in subsection 3.2.2, if we first assume that the incident wave is well collimated along  $\mathbf{\Omega}'$ , with a polarization  $\mathbf{S}^0$ , the Stokes vector  $\mathbf{S}^s(\theta, \varphi)$  of the wave "scattered" along  $\mathbf{\Omega}$  is given by

$$\mathbf{S}^s(\theta, \varphi) = \mathbf{M}(\theta) \cdot \mathbf{R}_M(\varphi) \mathbf{S}^0 \quad (2.57)$$

where the matrix  $\mathbf{M}(\theta)$  was explicited in Eqs.(2.24) and  $\mathbf{R}_M(\varphi)$  is the rotation matrix for Mueller matrices defined in Eq.(1.51). If we now take into account that both the incident and scattered waves are continuously distributed in the solid angle space, according to their respective radiances, the Eq.(2.57) can be rewritten as

$$d^2\mathbf{S}^s(\mathbf{r}, \mathbf{\Omega}, t) = \mathbf{L}(\mathbf{r}, \mathbf{\Omega}, t) d\Omega' d\Omega = \frac{1}{I_s(\mathbf{L})} \mathbf{M}(\theta) \cdot \mathbf{R}_M(\varphi) \mathbf{L}(\mathbf{r}, \mathbf{\Omega}', t) d\Omega' d\Omega \quad (2.58)$$

where the normalization factor  $I_s$  is the integral, over the full solid angle, of the scattered intensity, which is nothing else but the  $d^2S_0^s$  component of the scattered Stokes vector  $d^2\mathbf{S}^s$  vector defined above:

$$I_s(\mathbf{L}) = d\Omega' \int_{4\pi} [\mathbf{M}(\theta) \cdot \mathbf{R}_M(\varphi) \mathbf{L}(\mathbf{r}, \mathbf{\Omega}, t)]_0 d\Omega. \quad (2.59)$$

Finally, we define the vector phase function as

$$\mathbf{P}(\mathbf{\Omega}' \rightarrow \mathbf{\Omega}, \mathbf{L}) = \frac{1}{I_s(\mathbf{L})} \mathbf{M}(\theta) \cdot \mathbf{R}_M(\varphi). \quad (2.60)$$

On the other hand, as it has been shown in section 2.2.1, the total scattering cross-section does not depend on the polarization of the incoming wave for the spherical scatterers considered throughout this work. In other words,  $\mu_s$  and  $\mu_e$  are polarization independent.

Finally, with the above definitions, the vector radiative transport equation (VRTE) takes the form:

$$\begin{aligned} \frac{\partial \mathbf{L}(\mathbf{r}, \mathbf{\Omega}, t)}{\partial t} + \mathbf{\Omega} \cdot \nabla \mathbf{L}(\mathbf{r}, \mathbf{\Omega}, t) = & -\mu_e \mathbf{L}(\mathbf{r}, \mathbf{\Omega}, t) + \\ & + \int_{\mathbf{\Omega}'} \mu_s \mathbf{P}(\mathbf{\Omega}' \rightarrow \mathbf{\Omega}, \mathbf{L}) \mathbf{L}(\mathbf{r}, \mathbf{\Omega}', t) d\Omega' + \Sigma(\mathbf{r}, \mathbf{\Omega}, t). \end{aligned} \quad (2.61)$$

The above equation is the integro-differential formulation of the VRTE. This equation may be converted into an integral form, which, however, we will not use in this study. The interested reader is referred to Ref. [24].

## 2.4 Methods of solution of the RTE

For realistic media and boundary conditions the (V)RTE tends to be rather complex and often intractable, without exact analytical solutions. Efficient numerical methods are therefore crucial. However, approximate analytical methods are available, such as the transfer matrix method, the singular eigenfunction method, the perturbation method, the small-angle approximation... with various conditions to be fulfilled for their validity. On the other hand, several numerical techniques have been used: the adding-doubling method, the discrete-ordinate (DISORT) method, the invariant embedding method, the matrix operator method, the spherical harmonics method, the multi-component method, the spherical harmonics discrete ordinate method and the Monte Carlo method. A brief description of most of these techniques can be found in Ref. [25].

In the following we will outline only a few of these techniques including the Monte Carlo method extensively described in the next chapter.

**First-order solution.** This straightforward approach is adequate when the scattering medium is illuminated (from outside) by a well collimated (parallel) beam propagating along the direction  $\mathbf{\Omega}_0$ . The radiance inside the medium can be written as

$$\mathbf{L} = \mathbf{L}_0 + \mathbf{L}_s \quad (2.62)$$

where the first term is the radiance of the illuminating beam and the second is the contribution due to the scattering. If the scattering contribution is sufficiently weak (meaning that the medium is also weakly scattering or optically thin) the second term may be neglected, while the radiance of the incoming beam decreases exponentially:

$$\mathbf{L} \approx \mathbf{L}_0(z) = I_0 \delta_D(\mathbf{\Omega} - \mathbf{\Omega}_0) e^{-\mu_e z} \quad (2.63)$$

where  $I_0$  is the incoming intensity, the Dirac  $\delta_D$  function reflects the "perfect" directionality of the beam, and the exponential factor is nothing else but the attenuation factor already introduced in this chapter.

In practice, the Eq.(2.63) may be useful even if the medium is not weakly scattering. Actually, as the contribution of the scattered light around  $\mathbf{\Omega}_0$  is diffuse while that of the incoming beam is much "sharper", with an adequate spatial filtering, e.g. with a sufficiently small pinhole at the image focus of a suitably chosen lens, the diffuse contribution may be reduced enough to make it possible to "follow" the exponential decay of  $\mathbf{L}_0$  over a sufficient dynamical range, determine  $\mu_e$  and thus the mean free path in the medium. This "rejection" of the scattered contribution has indeed been used in the first experiments carried out in this work.

**Discrete ordinates approximation.** A more general solution of the RTE is provided the discrete-ordinates (DISORT) approximation which is behind the so called multi-flux theory. In this method, the integro-differential equation are transformed into a system of ordinary differential equations and then into a matrix differential equations, by considering the radiance along only along discrete directions (angles). Of course, this approximation becomes more and more accurate as the number of angles increases. The number of equations, equal to the number of fluxes, gives the name to the theory: two

(Kubelka-Munk theory [26]), three, four, seven (by Yoon *et al.* [27]), twenty-two (by Mudgett and Richards, 1971 [28]) and multi-flux theory whose comprehensive description can be found in the book by Ishimaru (1978) [29]. The seven-flux method is the simplest three-dimensional representation of scattered radiation and an incident beam in a semi-infinite medium. In general, the multi-flux theory is still restricted to linear geometries and to the assumption that the incident light is already diffuse

$$\mathbf{L}_0 = 0. \quad (2.64)$$

Moreover, this approach requires extensive computer calculations [30].

**Spherical harmonics and diffusion approximation.** The scalar diffuse radiance  $L_s$  may be expanded in spherical harmonics. This expansion leads to a system of  $(N + 1)^2$  connected differential partial derivative equations known as  $P_N$  approximation. This system is reducible to a single differential equation of order  $(N + 1)$  [31]. For  $N = 1$  we obtain the diffusion equation for  $L_s$

$$(\nabla^2 - \mu_d^2)L_s = -\frac{\Sigma}{D_d} \quad (2.65)$$

where

$$\mu_d = [3\mu_a((1 - g)\mu_s + \mu_a)]^{1/2} \quad (2.66)$$

is the diffusion parameter and  $\Sigma$  represents the internal sources. Moreover

$$D_d = \frac{v}{3}((1 - g)\mu_s + \mu_a). \quad (2.67)$$

The diffusion approximation provides a good approximation for small scattering anisotropy factor  $g \leq 0.1$  and large albedo ( $a \rightarrow 1$ ). This approximation can also be used at  $g < 0.9$  when the optical thickness  $\tau = \int_0^s \mu_e ds$  of a material is of the order of 10-20 [32].

**Inverse Adding-Doubling method.** A numerical approach to the RTE is called *inverse adding-doubling* which was recently introduced by Prahl *et al.* [33]. The term *inverse* refer to the usual process of extracting the intrinsic optical properties of a sample from the measurements of observables like total transmission and reflection. The IAD program does this "by repeatedly guessing the optical properties and comparing the expected observable with the observable measurements". The term *adding-doubling* refers to the method introduced by van de Hulst (1962) [34] and Plass *et al.* (1973) [35].

The doubling method assumes that transmission and reflection of the incident light at a certain angle for a slab of turbid media of any thickness are known. Then, transmission and reflection for a slab of the same turbid media but twice as thick can be obtained by dividing the slab into two identical slabs and doubling the contribution of transmission and reflection. Thus, transmission and reflection for a thick slab of turbid media can be calculated by starting from a thin slab whose properties are known, as obtained by absorption and single scattering measurement, for example, and doubling them until the

total thickness is achieved. The term "adding" is used to generalize to the case where we divide the thick sample in an arbitrary number of dissimilar thin slabs and then transmission and reflection for the thick slab are obtained by adding the contribution from any of the thin slabs. This extension allows to use the same methods for multilayered turbid media characterized by layers with different optical properties as well. Then, the transmission from the thick turbid media is calculated by adding the contributions from any different slab [30].

**Monte Carlo Simulations.** Another numerical approach to the solution of the RTE is the Monte Carlo (MC) method.

According to the definition of any MC method given by Lux and Koblinger [36] any Monte Carlo method requires a stochastic model, where the value of the mathematical expectation of a certain random variable is the value of the physical property to be determined by means of the numerical calculation. This mathematical expectation is calculated as the average of the series of the independent values associated to the random variable. The series of independent values is given by the random numbers following the distribution law of the random variable to determine.

Monte Carlo simulation in turbid media is based on the numerical simulation of the random walk into the medium of any photon in a package constituting the incident light and the repetition of the simulations for all photons in the package.

**Monte Carlo versus deterministic methods.** We would like to emphasize the fact that deterministic and Monte Carlo methods solve the same problem, i.e. (V)RTE, or more in general the transport equation, whatever its expression is integral or integro-differential. Often there is some misunderstanding about the fact that deterministic methods solve the integro-differential expression of the transport equation, while Monte Carlo methods solve the integral expression of the problem. This comes mostly from the fact that deterministic methods are presented when dealing with the scalar differential formulation of the transport problem, while Monte Carlo methods when dealing with the integral formulation of the problem.

In fact, in the discrete ordinates method the space phase divided into many small boxes, then, as the particle travels in the space it moves from one box to another within a certain amount of time. This is an example of finite-difference and finite-elements method [37]. As the boxes become progressively smaller the same does the time to travel from one box to another, the particle traces a differential distance of space in a differential amount of time. Hence, in the limit, the integro-differential expression, which presents derivatives in space and time seems to better suit the description of the transport problem. On the other hand, Monte Carlo describes transport in terms of particles freely traveling in the medium between events of collisions well separated in time and space. As a consequence, the integral expression of the RTE, which does not present either time or space derivatives, better suits the integral formulation of the problem. However, when a sufficiently large number of trajectories is taken into account, Monte Carlo and deterministic methods eventually provide exactly the same answers for the quantities of interest.

## 2.5 Conclusion

This chapter was devoted to a reasonably self-contained overview of the essential features of the propagation of (unpolarized or polarized) light in scattering media. We restricted the scope of this review to the topics relevant to the experimental results as well as the numerical simulations presented in the following chapters. For example, we limited the presentation to the case of spherical scatterers, which will be the only ones considered in this work, even though further developments including anisotropic scatterers may eventually prove necessary to fully account for the experimental data taken on tissues. We first considered the single scattering regime, and evaluated the total scattering cross-section of a spherical particle. This part was presented in detail due to its fundamental interest and its relevance for all the following, in particular the independence of this cross-section with respect to polarization.

We then presented the theory of the single scattering of polarized waves, again by spherical particles, with particular emphasis on the corresponding angular distributions and Mueller matrices, as provided by the Mie theory, which is very shortly outlined.

Then we addressed the more complex topic of multiple scattering. After having formulated the essential assumptions of independent scattering and absence of interference effects, we defined the usual scattering parameters, namely the mean free path, the anisotropy and several other parameters deduced from these and/or including absorption effects, such as the albedo.

We then established the radiative transfer equation, both in scalar and vectorial forms. This derivation is based on local detail balance between the incident beam attenuation due to scattering and the reverse effect, which is the result of "reverse" scattering into the incident beam and the contribution of the sources. Even though this equation may also be established from first principles derivation based on Maxwell equations [38], this more rigorous approach was not presented due to its formal complexity.

The final part was devoted to a short review of various methods to solve the (V)RTE, among which the Monte Carlo method which has been used in the simulations realized in this work, and which will be described in detail in the next chapter.

# Chapter 3

## Monte Carlo solution of the VRTE

### 3.1 Introduction

The Monte Carlo method was first proposed by Metropolis and Ulam [39] (1949). It has meanwhile advanced to a powerful tool in many disciplines. Here, we will first discuss its specificities with respect to other methods, and then outline its application to the solution of radiative problems, with the essential steps of the algorithm described in more details in the following sections.

According to the general definition of the Monte Carlo method by Lux and Koblinger [40], whatever the application of the Monte Carlo method, a stochastic model is built, where the values of the physical quantity (in our case the Mueller matrix coefficients of the scattering medium) are nothing else but the mean values of certain random variables. These values are obtained by the averaging over multiple independent samples.

The principle of statistical sampling, behind Monte Carlo method, dates back to the eighteenth century, but because of the long time and the labor required by the calculations it was not applied before the advent of computer. Only in mid 1946, when computer had recently become a reality, the mathematician Stanislaw Ulam realized that it could turn the statistical sampling principle into a practical tool. Ulam discussed the idea with the mathematician John Von Neumann, who proceeded to outline a computerized statistical approach to the problem of diffusion and multiplication (by fission) in an assembly containing a fissile material. Among the researchers that developed the Monte Carlo method is Nicholas C. Metropolis who gave it his name. Metropolis technique uses the Monte Carlo method for finding the equilibrium energy, at a given temperature, of a system of many interacting particles. The Monte Carlo has also more strictly mathematical application, namely, estimating the value of complex, many-dimensional integrals [37].

The Monte Carlo takes advantage of the speed of electronics computer to make use of statistical sampling a practical technique for solving complicated problems. Monte Carlo methods are especially useful for those complicated problems that cannot be modeled by deterministic methods.

#### 3.1.1 Overview of the applications of Monte Carlo method

The contents of this subsection is taken from Ref. [37].

**Nuclear energy.** Monte Carlo simulations are of great importance in the context of criticality safety. In particular, when dealing with the prevention of inadvertent assembly

masses of fissile material, it is needed to assess whether a given amount of fissile material in a given geometry constitutes a critical mass or whether a chemical reaction involving fissile material can lead to the assembly of a critical mass. While answering such questions by physical experimentation would be far too dangerous, Monte Carlo simulation is a safe, reliable way to do it.

In the domain of nuclear energy Monte Carlo simulations serve a variety of purposes, such as the design of shielding and spent-fuel storage ponds and estimate the radiation dose received by the operators, or the design assemblies so that the fuel is "burned" more efficiently, which implies cheaper electricity and less nuclear waste.

Talking about nuclear safeguards, a cornerstone is the inspection of nuclear facilities to ensure that no "special" nuclear materials are stolen from the facilities. The non-destructive assay technique are based on detecting either the radiation emitted by certain isotopes in the course of decay or the radiation emitted by the products of nuclear reaction induced in the isotopes by irradiation with neutrons and or gamma rays. Monte Carlo has helped in designing many of the detector used in such inspections.

Research about controlled nuclear fusion to produce energy is continuing, motivated by the absence of hazardous fission product and consumption of naturally abundant fuel (deuterium). The Monte Carlo has long been the premier code used for studying the transport of neutrons and photons produced by fusion reaction. Another application of Monte Carlo in fusion research is studying ways to prevent damage to personnel and equipment by fusion-produced radiation.

**Geology.** Monte Carlo simulations play important roles also in the search for oil. The pattern of scattering of neutrons and gamma rays from rocks formation can indicate the presence of oil in the rock. Monte Carlo simulations can predict the pattern of an oil-bearing rock. Then by comparing the measured and simulated scattering pattern of oil-bearing rocks obtained respectively using Monte Carlo method and introducing a specific tool in a hole in the rock formation, it is possible to know about the oil content in the rock.

**Space exploration.** When dealing with the exploration of space, radiations are intense and could cause invasive bursts on the astronauts. Hence, simulating the effect of the radiation on the equipment and personnel is preliminary to the exploration of space. Monte Carlo and other method of calculation have helped design shielding to protect the astronauts and demonstrating that, in case of solar shares, they were safer outside the shelter than inside!

**Medical applications.** Medicine is the third largest domain of application of nuclear reactions, raking behind only energy and defense. Some examples of the nuclear medicine technologies are the boron neutron-capture therapy and the positron-emission tomography (PET). The boron capture therapy is a selective technique used to kill the tumors. This consists of injecting cancer patient with stable isotope boron-10 and irradiating the patient with neutron. Boron is chosen because of its preference in collecting in tumor cells and facility in capturing neutrons due to its large cross-section. Then, Monte Carlo is used to determine the neutron dose and energy spectrum that kill the tumor and not the patient. PET is a non destructive technique for observing metabolism in situ. It consists of detecting the gamma rays resulting from the reaction of positrons and electrons in cells, after the ingestion of the radiative active isotope oxygen-15 contained in

water rather than the usual, non-radiative isotope oxygen-16. For example, PET scan can reveal the part of heart that is dead and need to be replaced rather than repaired. Monte Carlo simulations can help interpreting properly the images, which are blurred by the effect of scattering by photons and electrons. Similarly Monte Carlo can help in many other medical technologies including computer-assisted tomography, radiation therapy for cancer, and protection of medical personnel from nuclear radiation and x-ray.

The studies more directly related to the biomedical optics are presented in the next subsection.

### 3.1.2 Application to the radiative transfer problem

**Motivation.** The Monte Carlo method is particularly well suited to the study of the radiative transport. In fact, this technique is so pre-eminently realistic for radiative transport so that the calculations are also called "numerical experiments" of radiative transport.

The greatest advantage of using Monte Carlo methods when dealing with numerically solving the radiative transport problem is that it is able to handle complex geometries. This comes from the fact that, when propagating a photon in a medium inside an object, using Monte Carlo methods, the choice of next segment along the random path is determined by identifying the surface closest to the traveling photon. Hence, only the geometry in the vicinity of that photon located at any point in the medium is of interest. By looking locally at the object, its geometry can be described by the combination of many simple objects, such as rectangular parallelepipeds, ellipsoids, cylinders, cones and so on. However, even if a "combinatorial" object is easier to handle, its description is not that general as the model given by means of its boundary-surfaces. In fact, a "surface-sense" object is characterized by the combination of bounding surfaces, each of which is assigned of two values (sometimes each surface is assigned of one single value while the sign (+ or -) establishes on which side of the bounding surface the object lies. [37]

On the other hand, the greatest drawback of using Monte Carlo methods to solve the radiative transport problem is its cost in terms of computation time. Usually, the algorithm is stopped when the variances of the quantities of interest become smaller than predefined target values. Of course, the smaller these target values, the more accurate is the final result. The standard variances decrease with  $\frac{1}{n}$  (standard deviations with  $\frac{1}{\sqrt{n}}$ , where  $n$  is the number of photons), and so the number of times that the calculation is repeated. This corresponds to repeating the simulation for a single photon many times, generating each time a different history for the single photon. Since a certain level of accuracy has to be ensured, we need to go round to the time consumption problem. Four types "variance-reduction" techniques are available: truncation, population control, modification and pseudodeterministic methods [37]. Truncation involves ignoring aspects of the problem that are irrelevant or inconsequential. Population control involves sampling more important portions of the sampled group of photons (the population) more often and less important group of photon less often. Modification methods, or probability modification, involve sampling from a fictitious but convenient distribution rather than the true distribution characterizing the population and weighting the results accordingly. Pseudodeterministic methods involve replacing a portion (or portions) of random walk by deterministic or expected-value results.



**Brief review of the topic.** Over the past fifty years, polarized light propagation through scattering media has been studied by many groups and in particular by the atmospheric optics and oceanography community. Chandrasekhar in 1950 obtained an exact solution of the radiative transfer equation (RTE) for the simplest geometry of plane-parallel atmosphere with Rayleigh scattering [41, 42]. On the other hand, for more complex geometries this equation becomes untractable analytically, making it necessary to revert to numerical solutions, using the methods outlined at the end of the previous chapter. The first numerical solution of the vector radiative transfer equation (VRTE) with multiple scattering by means of a Monte Carlo method was achieved by Kattawar and Plass [43].

In the field of biomedical optics, Monte Carlo programs have been used to model laser tissue interaction, fluorescence and many other phenomena. In optical imaging and diagnostics, the intensity of the input and output light (transmission, reflection, absorption, scattering and fluorescence) are the only measurable quantities; the optical properties of a biological sample are the unknowns. The objective is to retrieve the tissue optical properties, such as  $\mu_s$ ,  $\mu_a$  and  $g$  from measurable quantities, by solving an inverse scattering problem. As these quantities may be related to the nature of the tissue and may be different for healthy and pathological samples, this technique may provide new non-invasive diagnostic tools. The forward problem is solved first, by calculating the measurable output quantities by means of known values of the optical parameters that define a possible model of the biological sample. An efficient implementation of the forward problem solution is prerequisite for the typically variational numerical solution of the inverse problem [44].

Here we can cite only a few examples of such investigations. Ledanois and Virmont [45] evaluated theoretically the characterization of a spherical object embedded in a scattering and absorbing medium from CW (continuous-wave) and modulated illumination.

Wang *et al.* [46] developed a Monte Carlo code to solve the RTE in multilayered tissues. This code was subsequently generalized for polarized light and birefringent scattering samples [47] and used later for time-resolved experiments [48]. Bartel and Hielscher [49] developed a Monte Carlo model that uses a local coordinate system to keep track of the polarization reference frame.

Ramella-Roman *et al.* [50, 51] developed three Monte Carlo codes for the backscattered Mueller matrix, including the effect of skewed illumination. These codes are freely available for download. Another freely available Monte Carlo code has been proposed by D. Côté and A. Vitkin [52].

Jaillon and Saint-Jalmes [53] used backscattered patterns obtained with focussed polarized illumination to determine the medium anisotropy factor  $g$ . Falconet *et al.* [54] later showed that a Fourier analysis of the backscattered patterns observed with linear polarization could provide a simple way to accurately estimate  $g$ . Dillet *et al.* [55] also used Monte Carlo simulations to validate approximate analytical formulas describing the backscattered Mueller images of samples illuminated by a focussed source, from which the volume fraction of the particles could be retrieved.

Tinet *et al.* [56] developed a fast semianalytical Monte Carlo based algorithm to simulate time-resolved measurements of light propagation in turbid media. Later the same group used Monte Carlo simulations for real-time determination of absorption coefficients in multilayered tissues [57, 58].

For the interested reader, an extensive list of the programs using the Monte Carlo method to solve the radiative transport equation for polarized light in scattering media

(haze and clouds, inhomogeneous atmosphere-ocean system, dusty spiral galaxy, slab geometry, optically active media, birefringent media, monodisperse solutions of polystyrene spheres, layered media), to study the optical properties (polarization, optical activity birefringence, speckles) by measuring diverse physical quantities (electric field, Stokes vectors, degree of polarization, Mueller matrix) of light, in multiple configuration (angles of scattering), is available in [50]. The Monte Carlo programs are listed by quantity of polarimetric information calculated by the code, where the Mueller matrix constitutes the most complete information about the medium, which makes any program an improvement of another. The list includes Monte Carlo codes that use diverse methods to work around the problem of high time consumption when dealing with high accuracy of the result.

## 3.2 The algorithm

The algorithm described in this section is the one implemented in a code previously used at LPICM [59], where it was brought by Guy Ledanois. This code is written in Fortran 90 and was conceived to describe the propagation of a polarized light beam in a cuvette filled with a scattering medium. We adapted this code to the propagation of diffuse light in turbid media such as tissue. This included changing the description of the light source from focused to diffuse; modifying the geometry of the sample from single layer with a flat surface to multilayer with irregular interfaces and then handling the resolution of the Fresnel law; substituting monodisperse scatterers to bimodal population of scatterers and redefining the scattering parameter; introducing the absorption by the embedding medium and accounting for the scattering parameter in the Lambert-Beer law; performing multi-spectral calculation and using dispersion law for the optical refractive index as well as for the absorption coefficient. Simulations were run by 8 independent calculators set at specific value of the model parameters any time. The run-time for a simulation was from an hour to a week depending on the number of photons of same state of polarization per launch (1–200) as well as on the number of launch (10000–100000) and the characteristics of the medium (longer run-time for larger scatterers) in order to achieve desired accuracy.

Each photon, modeled as a particle, is emitted by a point source, with a given polarization and follows a trajectory within an object comprising scatterers immersed in homogeneous surrounding media and interfaces. The trajectory consists of a succession of straight-line paths between scattering, refraction or reflection events. The effects of these events are described statistically. We currently exclude the absorption by scattering particles while we may take into account possible absorption by the medium where the scatterers are immersed. While elastic scattering changes the direction of propagation but not the energy of the photons, the absorption by the medium gradually reduces the statistical weight of a photon.

This procedure is repeated with "packages" of photons whose initial parameters are defined statistically in order to reproduce the relevant features of the illumination beams (spatial intensity distribution, polarization and the like). The outgoing photons are collected into "boxes" defined from the characteristics of the detectors (geometry, sensitivity to the polarization...). Within each box, the photon intensities are averaged incoherently. No speckle effect is taken into account in this code, as our imaging polarimeter is illuminated with spatially incoherent light. These averages eventually provide the quantities of interest, such as the output spatial and/or angular distributions, as well as the Mueller

matrix of the sample. The procedure is described in detail in the following sections.

### 3.2.1 Generation of random numbers with given probability distributions

The statistical treatment of each step simply means that the quantity of interest, such as the free path length before the next event, or the direction taken by the photon due to its scattering, for example, are drawn according to known probability distributions, e.g. a decreasing exponential for the free path length, and an angular distribution derived from Mie theory for the scattering on spherical particles. We now describe in detail how to generate random numbers with given probability distributions.

**Single real variables.** Let us consider a random variable  $y$ , which is supposed to follow the probability distribution  $P(y)$  between the lower and upper boundaries  $y_0$  and  $y_1$ , meaning that the probability  $dP$  to find this variable in an interval  $dy$  around the value  $y$  ( $y_0 \leq y \leq y_1$ ) is given by

$$dP = P(y) dy, \quad (3.1)$$

then the cumulative probability  $f_P(y)$  is defined as

$$f_P(y) = \int_{y_0}^y P(u) du. \quad (3.2)$$

As a result, when  $y$  varies between  $y_0$  and  $y_1$ ,  $f_P(y)$  varies between 0 and 1, with the distribution probability  $Q(f_P)$ , which is related to  $P$  by the straightforward relation

$$Q(f_P) df_P = P(y) dy, \quad (3.3)$$

leading to

$$Q(f_P) = P(y) \frac{1}{\frac{df_P}{dy}} = 1. \quad (3.4)$$

In other words,  $f_P$  is uniformly distributed between 0 and 1, a very useful result for numerical simulations, as all numerical pseudorandom number generators provide series of "random" numbers uniformly distributed in the  $[0, 1]$  interval.

The generation of the random variable  $y$  with a prescribed distribution  $P$  is then based on the generation of a random variable  $f_P$  equidistributed between 0 and 1, followed by one of the two following procedures.

- *Analytical inversion of Eq.(3.2).* As an example of this procedure, we can consider the propagation of photons within a homogeneous absorbing and/or scattering medium. The probability that a photon propagates over a distance  $y$  without being absorbed nor scattered is a decaying exponential:

$$P(y) dy = \mu_e e^{-\mu_e y} dy, \quad (3.5)$$

where  $\mu_e$  is the extinction coefficient, the reciprocal of the photon mean free path ( $\ell_e$ ) in the considered medium. In this case, Eq.(3.2) becomes:

$$f_P = \int_0^y \mu_e e^{-\mu_e y} dy = (1 - e^{-\mu_e y}) \quad (3.6)$$

or

$$y = \frac{\ln(1 - f_P)}{\mu_e} = \frac{\ln(z)}{\mu_e} \quad (3.7)$$

where  $z$ , like  $f_P$ , is also equidistributed over the  $[0, 1]$  interval, and thus can be drawn by a standard numerical random number generator to provide the variable  $y$  following the distribution given by Eq.(3.5).

- *Acceptance-rejection method.* This method is based on simultaneous numerical equidistributed drawing of  $y$  in the prescribed interval  $[y_0, y_1]$  (if both boundaries are finite) and  $x$  between 0 and 1. Then  $f_P(y) = \int_{y_0}^y P(u) du$  is calculated and compared with  $x$ . If  $f_P(y) \leq x$  then the drawn value of  $y$  is retained, otherwise it is rejected. For a large number  $N$  of draws, the probability for  $f_P$  to be found in the  $[0, z]$  interval is given asymptotically by

$$P(0 \leq f \leq z) \approx \frac{N(x \geq z)}{N} \approx 1 - z. \quad (3.8)$$

As a result, this "rejection method" [50] ensures that the retained values of  $f_P(y)$  are equidistributed between 0 and 1, implying that  $y$  is distributed in the  $[y_0, y_1]$  interval according to  $P$ .

**Multiple variables.** The above idea can easily be generalized to the case of multiple variables. This generalization will be detailed for the case of two variables  $(\theta, \varphi)$ , which is particularly relevant for the multiple scattering problem. Generalization to more than two variables is straightforward.

The variables  $(\theta, \varphi)$  are to be distributed according to the joint probability distribution function  $P(\theta, \varphi)$  limited to the finite intervals  $[\theta_1, \theta_2]$  and  $[\varphi_1, \varphi_2]$ , respectively.

- *Acceptance-rejection method.* In a similar way as for a single variable, we define the two-dimensional cumulative probability function as

$$f_P(\theta, \varphi) = \int_{\theta_1}^{\theta} \int_{\varphi_1}^{\varphi} P(u, v) du dv \quad (3.9)$$

which is again uniformly distributed over the  $[0, 1]$  interval. The acceptance-rejection method is thus generalized as follows: three independent random numbers  $(\theta, \varphi, x)$  are drawn with uniform probabilities over the intervals  $[\theta_1, \theta_2]$ ,  $[\varphi_1, \varphi_2]$  and  $[0, 1]$ , respectively. Then, if  $f_P(\theta, \varphi) \leq x$  the pair of values  $(\theta, \varphi)$  is accepted, otherwise it is rejected.

- *Composition method.* Let's now consider a case for which the probability density function  $P(\theta, \varphi)$  can be decomposed into the sum of two positive and non-zero functions as

$$P(\theta, \varphi) = q_1(\theta, \varphi) + q_2(\theta, \varphi). \quad (3.10)$$

The functions  $q_1$  and  $q_2$  are not density probability functions since they are not normalized. Denoting by  $F_1$  and  $F_2$  their norms (i.e. their integrals over the full finite range of variations of  $(\theta, \varphi)$ ) the probability density function  $P(\theta, \varphi)$  can be written as a linear combination of two probability density functions  $P_1(\theta, \varphi)$  and  $P_2(\theta, \varphi)$  as:

$$P(\theta, \varphi) = F_1 \frac{q_1(\theta, \varphi)}{F_1} + F_2 \frac{q_2(\theta, \varphi)}{F_2} = F_1 P_1(\theta, \varphi) + F_2 P_2(\theta, \varphi). \quad (3.11)$$

This equation can be interpreted as a division of all possible events generating the  $(\theta, \varphi)$  variables into two mutually exclusive classes, with overall relative weights  $F_1$  and  $F_2$ . To numerically generate the  $(\theta, \varphi)$  pairs, one draws a number, here denoted as  $u$ , which is uniformly distributed in the interval  $[0, 1]$  and is used as a criterion to choose one of the two classes of events to be considered: if  $u$  is smaller than  $\frac{F_1}{F_1+F_2}$ , than the pair  $(\theta, \varphi)$  is drawn following the probability density function  $P_1$ , otherwise it is drawn following the probability density function  $P_2$ . Obviously, this method is of particular interest if the expressions of the two probability density functions  $P_1$  and  $P_2$  are simpler than the expression of the original probability density  $P$ .

### 3.2.2 Individual photon trajectories

All over its trajectory the current status of a photon is described by the group of coordinates  $\{\mathbf{r}, \mathbf{S}(\mathbf{e}_x, \mathbf{e}_y, \mathbf{e}_z)\}$ .  $\mathbf{r}$  is the initial position in a fixed laboratory reference frame.  $\mathbf{S} = [I, Q, U, V]^T$  is the four-dimensional Stokes vector describing the state of polarization of a photon.  $\mathbf{S}$  is defined in the orthonormal system of coordinates  $(\mathbf{e}_x, \mathbf{e}_y, \mathbf{e}_z)$ , where the unit vector  $\mathbf{e}_z$  indicates the current direction of propagation of the considered photon. The orientation of the couple of unit vectors  $(\mathbf{e}_x, \mathbf{e}_y)$  could, in principle be chosen arbitrarily. However, as shown below, each event (scattering, reflection, refraction...) naturally leads to well definite choices of the orientation of these vectors in the  $(x, y)$  plane.

In its *step one*, the algorithm defines the initial status of the injected photons. All over the trajectory, the decision on the nature of the next event and on the location of the photon at the next step constitutes the *step two* of the algorithm. If the photon next location is inside the medium (propagation, scattering, interface), then, according to the nature of the event, the actual direction of propagation and state of polarization associated to the photon change into new ones. The former transformation constitutes the *step three* of the algorithm. As the photon propagates, the new direction of propagation and state of polarization update the actual ones. The updating defines the *step four* in the algorithm and leads back to *step two*. On the other hand if the photon next location is outside the medium (boundary) then the photon is discarded and this is the *last step* of the algorithm.

The details of the process will be illustrated below by the construction of a single polarized photon history, as described in the next paragraphs.

**Definition of the incoming photon statistics.** A "package" of  $N$  photons are assumed to start from the  $N$  points of a grid that faces the surface of the medium up to cover it. The initial direction of propagation, as well as the polarization state, are assumed to be the same for all the photons of the package. These initial conditions correspond to a numerical experiment with a spatially diffuse but collimated illumination (of course, other illumination geometries could be simulated as well). The trajectories of all photons are followed until the photon is detected or lost, as explained in the following paragraphs.

Then, another package of photons is launched, with the same spatial parameters, but a different polarization. This initial polarization state has to be varied over the surface of the Poincaré sphere widely enough to allow an adequately accurate estimation of the sample Mueller matrix. As described in more detail in section 3.2.3, the initial polarization states can be defined in two ways:

- the sampling can be limited to a set of *four polarization states*, with four linearly independent Stokes vectors. In this case, the optimal choice corresponds to four polarization states whose Stokes vectors are located at the tips of a regular tetrahedron on the Poincaré sphere,
- alternatively, the input Stokes vectors can be *sampled statistically* over the whole surface of the Poincaré sphere. As discussed below, this last procedure has been found to be the most effective in terms of calculation time for multiple scattering media.

This overall procedure is repeated until a sufficiently low variance is achieved on the output Mueller matrix.

**Scattering by spheres embedded in an homogeneous medium.** In this part, we neglect events other than the interaction with the spherical scatterers, as if the medium with these scatterers were infinite. The interaction with various boundaries, such as the "lateral" walls of a container, or the boundaries between successive layers in a layered system, or the absorption, will be described in the following paragraph.

As it has been shown in the previous section (see Eq.(3.5)) the distance  $d$  over which a photon propagates in the scattering medium between two scattering events is a random variable defined as

$$d = \frac{\ln(z)}{\mu_e} \quad (3.12)$$

where  $z$  is a random number uniformly distributed between 0 and 1 and  $\mu_e$  [ $\text{cm}^{-1}$ ] is the inverse of the mean free path of monodisperse solution of scattering spheres that is denoted as  $\ell$  [cm]. This mean free path is defined by the expression  $\ell_e = N_s \sigma_e$ , where the  $N_s$  is the density of the scatterers and  $\sigma_e$  the extinction cross-section (extinction = absorption + scattering) of a single sphere. This cross-section has the dimensions of a surface.

Then, the probability that the photon is scattered through various angles is calculated as function of the relevant parameters (the photon energy, the scatterer radius, the index contrast between the scatterer and the surrounding medium...) by means of the Mie theory (see Appendix B). This probability or cross-section is a necessary input for solving the problem.

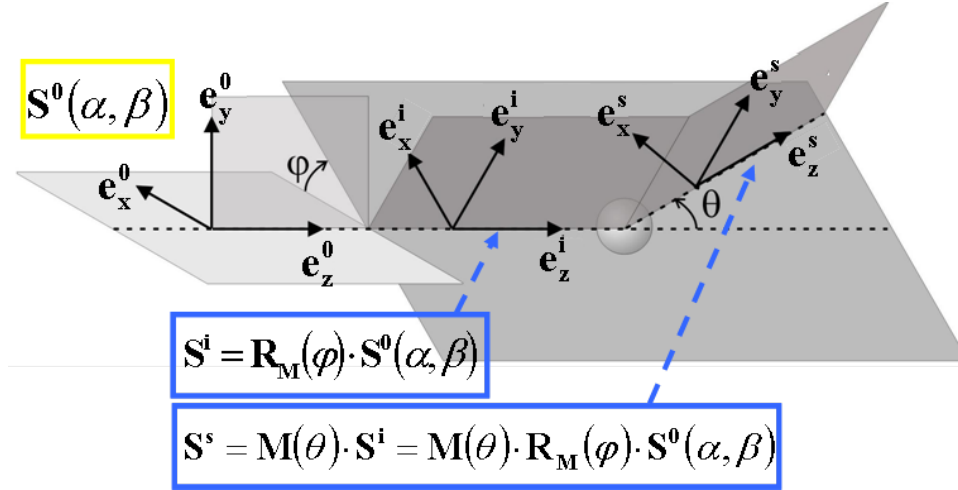


**Figure 3.1:** The angles  $(\theta, \varphi)$  are drawn according to a law depending on two non-independent parameters. The initial local reference frame  $(\mathbf{e}_x^0, \mathbf{e}_y^0, \mathbf{e}_z^0)$  is rotated by the angle  $\varphi$  in order to put the incident reference frame  $(\mathbf{e}_x^i, \mathbf{e}_y^i, \mathbf{e}_z^i)$  in the local reference frame. After the scattering by the sphere, the polarization is given by the Mie theory in the system of axes of the scattering  $(\mathbf{e}_x^s, \mathbf{e}_y^s, \mathbf{e}_z^s)$ , which becomes the new local system of reference [23].

The scattering event transforms the wave incident on the scatterer along the direction  $\Omega'$  into a scattered wave travelling along the direction  $\Omega$ . As the photon bounces on a scattering sphere the vector basis is rotated so that the unit vectors  $\mathbf{e}_x$  and  $\mathbf{e}_y$  match the unit vectors parallel and perpendicular to the scattering plane (usually indicated by the symbols  $\parallel$  and  $\perp$ , respectively). This allows to take advantage from the geometrical symmetries of the scattering matrix defined in the scattering plane.

The Mie theory is used to evaluate the angular distribution probability of the scattering direction  $\Omega$  as well as the corresponding Mueller matrix. As shown in Fig. 3.1, the direction of the vector  $\Omega$  is defined by its polar and azimuthal angles  $(\theta, \varphi)$ .

Let  $\mathbf{S}^0 = [I, Q, U, V]^T$  be the Stokes vector of the incident photon, defined in the local reference system  $(\mathbf{e}_x^0, \mathbf{e}_y^0, \mathbf{e}_z^0)$ . The Stokes vector associated with the scattered photon traveling along the direction of scattering  $\Omega = (\sin \theta \cos \varphi, \sin \theta \sin \varphi, \cos \theta)$  is obtained from the Stokes vector associated to the incident photon throughout the two following steps:

1.  $\mathbf{S}^0$  and  $(\mathbf{e}_x^0, \mathbf{e}_y^0, \mathbf{e}_z^0)$  are rotated around the direction of propagation  $\mathbf{e}_z^0$  by the angle  $+\varphi$ , which constitutes a rotation in the Stokes space and the real space respectively described by the matrix  $\mathbf{R}_M(\varphi)$  suitable for Stokes vectors (see Eq.1.51) as:

$$\mathbf{S}^i(\varphi) = \mathbf{R}_M(\varphi) \cdot \mathbf{S}^0, \quad \begin{cases} \mathbf{e}_x^i = \cos \varphi \mathbf{e}_x^0 + \sin \varphi \mathbf{e}_y^0 \\ \mathbf{e}_y^i = -\sin \varphi \mathbf{e}_x^0 + \cos \varphi \mathbf{e}_y^0 \\ \mathbf{e}_z^i = \mathbf{e}_z^0. \end{cases} \quad (3.13)$$

The rotation of the local reference plane by the angle  $\varphi$  places the initial local reference system  $(\mathbf{e}_x^0, \mathbf{e}_y^0, \mathbf{e}_z^0)$  into the scattering plane;

2.  $\mathbf{M}(\theta)$  is the Mueller matrix defined in Eq. 2.24, which describes the scattering by a single sphere along the angle  $\theta = \widehat{\mathbf{e}_z^i, \mathbf{e}_z^s}$  in the scattering plane. The Stokes vector

associated to the scattered photon denoted as  $\mathbf{S}^s$  is obtained from the Stokes vector  $\mathbf{S}^i$  by means of the transformation described by the matrix  $\mathbf{M}(\theta)$  in the scattering reference frame. The scattering reference frame is obtained rotating the incident reference frame by the direction  $\mathbf{e}_y^i$  perpendicular to the reference plane about the angle  $\theta$ :

$$\mathbf{S}^s(\theta, \varphi) = \mathbf{M}(\theta) \cdot \mathbf{R}_M(\varphi) \cdot \mathbf{S}^0, \quad \begin{cases} \mathbf{e}_x^s = \cos \theta \mathbf{e}_x^i + \sin \theta \mathbf{e}_z^i \\ \mathbf{e}_y^s = \mathbf{e}_y^i \\ \mathbf{e}_z^s = \sin \theta \mathbf{e}_x^i + \cos \theta \mathbf{e}_z^i. \end{cases} \quad (3.14)$$

The intensity  $dI_s$  of the light scattered in a small solid angle  $d\Omega$  around the direction  $\mathbf{u}$  is expressed by the first components of the Stokes vector associated to the scattered photons

$$dI_s = i_s(\theta, \varphi) d\Omega, \quad (3.15)$$

with

$$\begin{aligned} i_s(\theta, \varphi) &= m_{11}(\theta)I + m_{12}(\theta) \cos(2\varphi)Q - m_{12}(\theta) \sin(2\varphi)U = \\ &= \frac{1}{2} [ |S_1(\theta)|^2 (I - Q \cos(2\varphi) + U \sin(2\varphi)) + |S_2(\theta)|^2 (I + Q \cos(2\varphi) - U \sin(2\varphi)) ] \end{aligned} \quad (3.16)$$

where  $|S_1(\theta)|^2 = (m_{11} - m_{12})$  and  $|S_2(\theta)|^2 = (m_{11} + m_{12})$  are the absolute values squared of the complex amplitude functions. The total intensity of the scattered light in the space is obtained by integrating the intensity of the scattered light along the generic direction of propagation over all directions of propagation included in the sphere of unit volume as:

$$I_s = \int i_s d\Omega = 2\pi \int_{\theta=0}^{\theta=\pi} \int_{\varphi=0}^{\varphi=2\pi} i_s(\theta, \varphi) \sin \theta d\theta d\varphi. \quad (3.17)$$

Since we have supposed to have a single wavelength incident light on the scattering media, then the total intensity of the scattered light in any direction of propagation in the space, denoted by the angles  $(\theta, \varphi)$ , is proportional to the number of the photons that scatter along that direction. It comes that the total scattered intensity is proportional to the total number of photons that scatter in every direction in the space. This function is known as *angular probability density function* and is denoted as  $P(\theta, \varphi)$ .

The combined probability density function of the the pairs  $(\theta, \varphi)$  is expressed as:

$$P(\theta, \varphi) d\theta d\varphi = \frac{i_s(\theta, \varphi)}{I_s} \sin \theta d\theta d\varphi. \quad (3.18)$$

In order to describe a scattering event, one has to draw the direction of scattering  $(\theta, \varphi)$  following the angular probability density function  $P(\theta, \varphi)$  and then calculate the change in polarization along the new direction of propagation. Since the angular probability density function characterizing the scattering is a joint probability density function of the random variables  $\theta$  and  $\varphi$ , one applies the acceptance-rejection method outlined in



section 3.2.1 can be used to generate these angles: three independent random numbers denoted as  $\theta_0$ ,  $\varphi_0$  and  $\xi$  all are drawn as random variables uniformly distributed within the intervals of values  $[0, \pi]$ ,  $[0, 2\pi]$  and  $[0, \max_{(\theta, \varphi)} \{i_s(\theta, \varphi)\}]$ , respectively; if  $\xi \leq i_s(\theta_0, \varphi_0)$  then the pair  $\theta_0, \varphi_0$  is accepted as the next direction of scattering, otherwise it is refused and the drawing is repeated again.

This probability of acceptance is always smaller than 0.5 (limit case for very small scattering particles) since the scattering intensity is mostly forward and backward directed. The probability that the pair  $(\theta_0, \varphi_0)$  is accepted decreases with the increase of the radius of the scattering spheres, leading to a high percentage of rejections and thus a "waste" of calculation time.

The acceptance-rejection method can be improved by choosing for the  $\xi$  those expression that suit better the specificity of the differential scattering section. As a consequence, the method for generating random numbers become more complex and the computational time depends on the size of the spheres. In order to work around this problem, the density probability function  $P(\theta, \varphi)$  is written as the sum of positive terms and the joint probability method described in section 3.2.1 is applied.

Let's choose  $\varphi_0 \in [0, 2\pi]$  and  $W \in [0, 1]$  to be defined by the following expression:

$$Q = IW \cos(2\varphi_0) \quad U = IW \sin(2\varphi_0) \quad (3.19)$$

which is always possible since the degree of polarization is smaller than 1. By noticing that

$$Q \cos(2\varphi) + U \sin(2\varphi) = IW \cos(2(\varphi - \varphi_0)) \quad (3.20)$$

the expression of the two-dimensional probability density function  $P(\theta, \varphi)$  gets changed its expression in Eq.(3.18) into

$$P(\theta, \varphi) = \frac{I}{I_s} (t_1(\theta, \varphi) + t_2(\theta, \varphi)) \quad (3.21)$$

with

$$t_i(\theta, \varphi) = |S_i(\theta)|^2 \sin \theta \left[ 1 - W + 2W \sin^2(\varphi - \varphi_0 + (i-1)\frac{\pi}{2}) \right], \quad i = 1, 2. \quad (3.22)$$

The norms of  $t_1$  and  $t_2$  are the integrals over the unit sphere

$$T_{1,2} = \int_{\theta=0}^{\theta=\pi} \int_{\varphi=0}^{\varphi=2\pi} t_{1,2}(\theta, \varphi) d\theta d\varphi = 2\pi \int_{\theta=0}^{\theta=\pi} |S_{1,2}(\theta)|^2 \sin \theta d\theta. \quad (3.23)$$

From

$$t_1(\theta, \varphi) + t_2(\theta, \varphi) = \frac{i_s(\theta, \varphi)}{I} \sin \theta \quad (3.24)$$

we immediately get

$$\frac{I_s}{I} = T_1 + T_2 \quad (3.25)$$

which, in turn, implies that

$$P(\theta, \varphi) = \frac{T_1}{T_1 + T_2} \frac{t_1(\theta, \varphi)}{T_1} + \frac{T_2}{T_1 + T_2} \frac{t_2(\theta, \varphi)}{T_2}, \quad (3.26)$$

where

$$P_{1,2}(\theta, \varphi) = \frac{t_{1,2}(\theta, \varphi)}{T_{1,2}} \quad (3.27)$$

are the density probability functions related to the functions  $t_1$  and  $t_2$ . We may notice that the random variables  $\theta$  and  $\varphi$  are statistically independent, as each of the expressions of  $P_1$  and  $P_2$  is the product of a function  $P_{\theta,i}$  of  $\theta$  only and a function  $P_{\varphi,i}$  of  $\varphi$  only (with  $i = 1$  or  $2$ ).

To summarize, the angles  $(\theta, \varphi)$  are generated in four steps

1. The composition method outlined after Eq.(3.11) is used first, to decide which of the combined probabilities  $P_1(\theta, \varphi)$  or  $P_2(\theta, \varphi)$  will be followed;
2. Once the index 1 or 2 is chosen, the angle  $\theta$  is defined by applying the inversion method to the probability density

$$P_{\theta,i}(\theta) = \frac{|S_i(\theta)|^2 \sin \theta}{\int_0^\pi |S_i(\theta)|^2 \sin \theta d\theta} \quad (3.28)$$

via a numerical calculation of its cumulative probability density;

3. Then, the method of compositions is applied again to the probability density

$$P_{\varphi,i}(\varphi) = \frac{1}{2\pi}(1 - W) + W \frac{\sin^2(\varphi - \varphi_0 + (i - 1)\frac{\pi}{2})}{\pi} \quad (3.29)$$

as this probability density is the sum of the constant  $\frac{1}{2\pi}(1 - W)$  and the function

$$g_i(\varphi) = \frac{W}{\pi} \sin^2(\varphi - \varphi_0 + (i - 1)\frac{\pi}{2}); \quad (3.30)$$

4. Finally, if the previous step selects the constant,  $\varphi$  is drawn uniformly in the  $[0, 2\pi]$  interval; otherwise  $\varphi$  is determined by applying once more the inversion method to the probability density  $G_i(\varphi) = \frac{1}{W}g_i(\varphi)$  obtained by normalizing  $g_i$ .

**Interaction with interfaces and layered media.** Let's consider a photon whose current location is  $\mathbf{r}_n$  and which flies along the direction  $\mathbf{\Omega}_n$ . We call  $d_0$  the distance separating  $\mathbf{r}_n$  from the closest interface in the direction  $\mathbf{\Omega}_n$ . A distance  $d$  is drawn according to the probability function given in Eq.(3.5). If  $d > d_0$ , then the next location of the photon to be considered is at the interface in  $\mathbf{r}_{n+1} = \mathbf{r}_n + d_0\mathbf{\Omega}_n$ , where it undergoes a reflection or a transmission; conversely, if  $d < d_0$ , then the next photon location is at the scatterer's location  $\mathbf{r}_{n+1} = \mathbf{r}_n + d\mathbf{\Omega}_n$  and it undergoes an event of scattering as described in the previous paragraphs.

When dealing with the encounter of the photon with an interface between two semi-infinite media, we use the Fresnel's laws to describe the two possible events, namely the reflection and transmission at the interface. Actually, any time the photon encounters an interface, one has to choose between reflection and transmission. This choice is realized as follows:

- first, the frame of reference ( $\mathbf{e}_x$ ,  $\mathbf{e}_y$ ,  $\mathbf{e}_z$ ) is rotated so that ( $\mathbf{e}_x$ ,  $\mathbf{e}_y$ ) are respectively parallel and perpendicular to the incidence plane. In other words the  $x$  and  $y$  axes coincide with the usual  $\parallel, \perp$  axes in which the Fresnel laws are most conveniently expressed,
- then, calling  $R_{\parallel} = r_{\parallel}^2$  and  $R_{\perp} = r_{\perp}^2$  the intensity reflection coefficients for the  $\parallel$  and  $\perp$  polarizations ( $r_{\parallel}$  and  $r_{\perp}$  being the usual *field amplitude reflectivities* appearing in the reflection Jones matrix), the actual reflectivity for an incoming Stokes vector  $\mathbf{S} = [I, Q, U, V]^T$  is

$$R = \frac{1}{2} [(r_{\parallel}^2 + r_{\perp}^2) + Q(r_{\parallel}^2 - r_{\perp}^2)] . \quad (3.31)$$

A random number  $p_R$  is generated with uniform probability in the interval  $[0, 1]$  and compared with  $R$ .

If  $p_R \leq R$  then the photon is reflected at the interface, otherwise it is transmitted. In the new location at the interface, the new state of polarization of the photon is given by means of the Fresnel's law, while the new direction of flying is obtained by means of the Snell's law, so that the new status of the photon is completely described.

When dealing with a model involving several layers of scattering media, then the algorithm is applied to each layer identified by the index  $i$  with the proper mean free path  $\ell_i$ .

**Interaction with a lambertian.** A totally depolarizing, lambertian partially reflecting surface is a special case of an interface. A lambertian reflecting surface is often used in multilayer models as the "bottom" interface to "lump" the contributions of the deepest layers into a single response, provided that these layers are strongly depolarizing.

A lambertian is characterized by an angular distribution of the scattered light independent of the direction of the incoming light, and which follows the Lambert's law

$$I(\theta, \varphi) d\Omega = Z_i \frac{a}{\pi} \cos \theta d\Omega = Z_i \frac{a}{\pi} \cos \theta \sin \varphi d\theta d\varphi \quad (3.32)$$

where  $d\Omega$  is the collection solid angle,  $Z_i$  the illumination power, and  $a$  the lambertian albedo, which defines the fraction of the illumination power which is backscattered into the full  $\pi$  solid angle, or, in other words, the probability that an incoming photon has to be backscattered.

The Monte Carlo treatment of the backscattering on a lambertian is quite straightforward. From Eq.(3.32) above, we see that the azimuthal angle  $\varphi$  is uniformly distributed between 0 and  $2\pi$ , while the normalized distribution of the polar angle  $\theta$  is given by

$$P_{L,\theta}(\theta)d\theta = \sin(2\theta)d\theta \quad (3.33)$$

from which we get the cumulative probability

$$x(\theta) = \int_0^\theta \sin(2u) du = \frac{1}{2} (1 - \cos(2\theta)). \quad (3.34)$$

A number  $\zeta$  uniformly distributed in the interval  $[0, 1]$  is drawn and the polar and azimuthal angles are calculated as:

$$\theta = \frac{1}{2} \arccos(1 - 2\zeta), \quad \varphi = 2\pi\zeta. \quad (3.35)$$

For a partially reflecting lambertian  $a < 1$ , some of the photons impinging on the scattering medium get lost in the medium while the others are backscattered.

A random number  $\bar{a}$  uniformly distributed in the interval  $[0, 1]$  is generated and its value is compared with the albedo  $a$  of the lambertian. Then, if  $\bar{a} \leq a$  the photon is backscattered as described above, otherwise the photon is absorbed.

As the lambertian is assumed to be totally depolarizing, the backscattered photons emerge with a Stokes vector  $\mathbf{S} = [1, 0, 0, 0]^T$ .

**Photon collection.** Typically, scattering experiments are carried out with a CCD (Charge-Coupled Device) camera coupled with an imaging optical system. In most cases, the surface of the sample under study is directly imaged on the CCD. In this case, each pixel of the detector is conjugated with a well defined (small) surface element  $dS$  of the sample. As a result, the photons reaching this pixel are those leaving  $dS$  with a direction within the solid angle  $\Omega_d$  defined by the imaging system. Then one obtains a *space-resolved* polarimetric image of the sample surface. All the simulated and almost all the experimental data presented in this thesis are of this type.

Alternatively, it may be interesting to collect *angle-resolved* polarimetric data, typically with a sufficiently small illuminated area to make it sure that the photons collected in a given direction are coming from the entire illuminated area. Two experimental detection setups can be used for this purpose:

1. The most traditional is based on a *goniometric mount* supporting both the optics and the detector. A small pinhole is usually placed at the image focal point of the optics, to define a small acceptance solid angle for the light allowed to reach the (usually single) detector. This mount is then rotated, typically around one axis, but a two-axis rotation is also possible. An angular scan is then required, in most cases, to obtain the desired information;
2. An alternative solution consists in *imaging on a 2D camera the back focal plane of a lens* featuring a large numerical aperture (N.A.). Typically this lens is a microscope objective. When compared with the goniometric mount, the main advantage of this solution is the simultaneous acquisition of 2D angle resolved data over all the solid angle defined by the lens N.A. The corresponding drawbacks are:

- a limitation of the polar angle to about  $65^\circ$  for the usual high N.A. objectives,

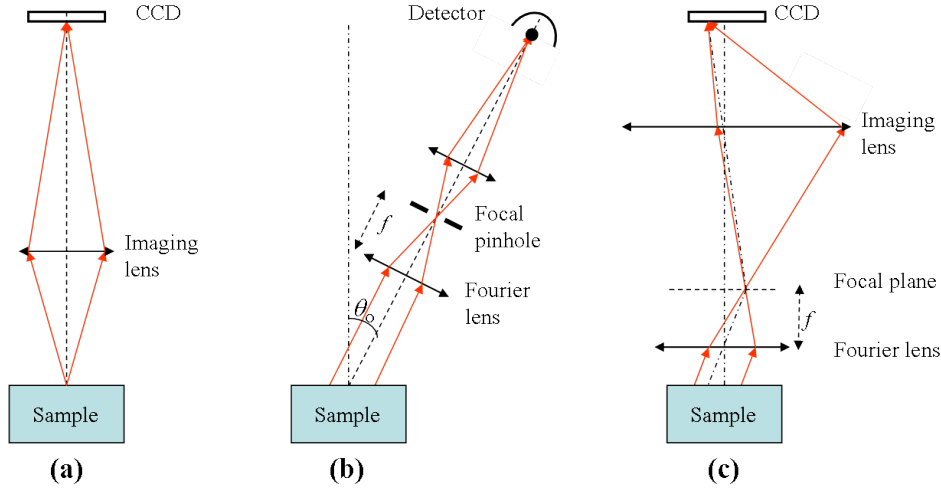


**Figure 3.2:** Schematic representation of typical photon collection systems. (a): real space imaging of the surface sample. (b): goniometric mount for angle resolved measurements. (c): angular resolved collection system imaging the back focal plane of a high N.A. Fourier lens.

- a possible decrease in angular resolution at the highest polar angles, as for quasi-stigmatic optics (which include microscope objectives), each exit direction defined by the polar and azimuthal  $(\theta, \varphi)$  is mapped in the final image as a point located at the azimuth  $\varphi$  and at radial distance from the center proportional to  $\sin \theta$ ,
- possible artefacts due to the objective Mueller matrix, which may become significantly different from unity at large polar angles.

However, these drawbacks can be properly handled. The potential of this technique has been demonstrated for grating metrology as well as the characterization of various natural or artificial photonic structures [60]. Moreover, as discussed in the last chapter, this technique may also prove useful to constrain the parameters of tissue optical models, by measuring the angular distribution of the light scattered in the forward direction from samples whose thickness can be selected in order to enhance (or decrease) the contribution of single scattering events.

Fig. 3.2 schematizes the three types of setup.

As already stated, the simulations presented in this work have been realized for a direct imaging configuration, with 0.025 cm sided detectors disposed over a squared grid covering the 1 cm radius surface of the camera objective. Then, we have simulated the polarized light scattering that is detected by the 1600 (40 x 40) detectors, with, however, a very small N.A.: as discussed in the following paragraph, we used a "non-analog" game where the photons were assumed to impinge the CCD pixels under quasi-normal incidence.

**The non-analog game.** So far, we implicitly assumed that the number of photons collected by any single detector –together with the resulting polarization– is evaluated by simply counting the number of photons actually impinging on the detector in the simulation, and summing up their Stokes vectors. However, this conceptually simple procedure leads in many cases to prohibitive calculation times.

To reduce the computational burden, we choose to evaluate the photons flux  $\Phi_{ij}$  eventually impinging on the detector  $(i, j)$  by the method known as the *non-analog game*.

Let's consider the photon  $k$  (belonging to a package of  $N$  photons) that propagates into the medium and reaches a scatterer or an interface with the energy  $E_k$ . By bouncing into a sphere or an interface, this photon gets scattered or refracted or reflected with an angular distribution probability given either by the Mie theory for the scattering by a sphere or by the Snell-Fresnel's equations for the interaction with a surface. Calling  $(\theta_{ij}^k, \varphi_{ij}^k)$  the polar and azimuthal angles (in the proper reference frame centered at the current position of the photon), defining the initial direction of the optical path joining the current photon position and the detector  $(i, j)$  and  $d\Omega_{i,j}^k$  the solid angle under which the photon "sees" the same detector, the probability that the photon is directly sent into this pixel after the current interaction event is given by

$$\Phi_{ij}^k = W_k P(\theta_{ij}^k, \varphi_{ij}^k) T_{ij}^k d\Omega_{i,j}^k \quad (3.36)$$

where

1.  $P$  is the angular distribution probability for the scattered photon ( $P$  is defined by Eq.(3.21) while it takes the form of a Dirac  $\delta_D$  function for the interaction with an interface);
2.  $T_{ij}^k$  is the probability that the photon reaches the detector from its current position. This quantity is evaluated as the product of the transmission coefficients through the scattering media and the interfaces present on the optical path to the detector. The contribution to each pixel is proportional to the probability of the photon to reach the detector without other scattering. In our case, for each event we consider only the pixel located at the orthogonal projection of the current photon position on the sample surface. This is equivalent to considering an imaging system in real space with a very small N.A.;
3.  $W_k$  is a "weight" attributed to the photon, whose initial value is equal to 1, and which decreases at each event described by Eq.(3.36) by the quantity  $\Phi_{ij}^k$ , to properly take into account, at each step, the probability that the photon has already been detected.

Finally the flux at point estimation at location of detector  $(i, j)$  for the whole photon package is simply the sum of contributions of all the  $N$  photons:

$$\Phi_{ij} = \sum_{k=1}^N \Phi_{ij}^k. \quad (3.37)$$

Moreover, each individual photon trajectory is ended when the photon gets lost in the geometrical sense, meaning that it has been scattered in the vacuum outside the sample in directions where it cannot reach the detector anymore.

### 3.2.3 Evaluation of the Mueller matrix

Let's first consider a package comprising  $N$  photons with the same Stokes vector  $\mathbf{S}^i$  for all of them. The output of the Monte Carlo simulation provides an estimation of the

emerging intensities and polarizations for all the detectors taken into account. Of course, this procedure needs to be repeated, with the same  $\mathbf{S}^i$ , until the predefined variance on the result is reached. As a result, we obtain, for each detector, the output Stokes vector

$$\mathbf{S}^o = \mathbf{M} \cdot \mathbf{S}^i. \quad (3.38)$$

Of course, in order to fully determine  $\mathbf{M}$ , this procedure must be repeated with several input Stokes vectors  $\mathbf{S}^i$ . This can be achieved in (at least) two different ways, as discussed hereafter.

**Minimal sampling.** To determine  $\mathbf{M}$  we need at least four input Stokes vectors  $\mathbf{S}_k^i$  (with the integer  $k$  varying between 1 and 4), these vectors being the columns of a "polarization modulation" matrix  $\mathbf{W}$ . The four output Stokes vectors  $\mathbf{S}_k^o$  can also be considered as the columns of an output matrix  $\mathbf{F} = \mathbf{M} \cdot \mathbf{W}$ . Provided the four Stokes vectors  $\mathbf{S}_k^i$  are linearly independent,  $\mathbf{W}$  can be inverted, and  $\mathbf{M}$  is obtained as

$$\mathbf{M} = \mathbf{F} \cdot \mathbf{W}^{-1}. \quad (3.39)$$

As it will be discussed later, in connection with the optimization of Mueller polarimeters, the noise propagation from  $\mathbf{F}$  to  $\mathbf{M}$  is optimized (i.e. the noise on the elements of  $\mathbf{M}$  is minimized for a given noise level in  $\mathbf{F}$ ) when  $\mathbf{W}$  is "as close as possible" to a unitary matrix, a condition equivalent to choosing the  $\mathbf{S}_k^i$  at the tip of a regular tetrahedron at the surface of the Poincaré sphere.

Of course, the matrix  $\mathbf{M}$  can be *overdetermined* by using more than four input Stokes vectors. If so,  $\mathbf{W}$  becomes a rectangular matrix, with more than four columns. As a result,  $\mathbf{M}$  can still be calculated according to Eq.(3.39), where the inverse of  $\mathbf{W}$  must be replaced by its pseudoinverse. It is not clear, however, whether for the same computation time this overdetermination provides better final results, in terms of variances of the elements of  $\mathbf{M}$ , than the minimal sampling with four input vectors.

**Statistical sampling.** This alternative approach is based on a statistical sampling of the input Stokes vectors at the surface of the Poincaré sphere. If we call  $\alpha$  and  $\beta$  the polar and azimuthal angles on this sphere ( $\alpha = \frac{\pi}{2} - 2\chi$ ,  $\beta = 2\psi$ , where the angles  $\psi$  and  $\chi$  have been defined in section 1.3.2), a generic Stokes vector  $\mathbf{S}^i$  at the surface of the sphere takes the form

$$\mathbf{S}^i(\alpha, \beta) = [1, \cos \alpha, \sin \alpha \cos \beta, \sin \alpha \sin \beta]^T. \quad (3.40)$$

The angles  $\alpha$  and  $\beta$  are distributed over the intervals  $[0, \pi]$  and  $[0, 2\pi]$  respectively according to a joint probability density  $P(\alpha, \beta)$ .

We now define the 4 x 4 correlation matrix  $\mathbf{D}$  of the input Stokes vector components as

$$\int_{\alpha=0}^{\alpha=\pi} \int_{\beta=0}^{\beta=2\pi} \mathbf{S}^i(\alpha, \beta) \cdot [\mathbf{S}^i(\alpha, \beta)]^T P(\alpha, \beta) d\alpha d\beta = \mathbf{D}. \quad (3.41)$$

Similarly, the correlation matrix  $\mathbf{G}$  of the components of the output and input Stokes

vectors is given by

$$\begin{aligned}\mathbf{G} &= \iint \mathbf{S}^o(\alpha, \beta) \cdot [\mathbf{S}^i(\alpha, \beta)]^T P(\alpha, \beta) d\alpha d\beta \\ &= \mathbf{M} \iint \mathbf{S}^i(\alpha, \beta) \cdot [\mathbf{S}^i(\alpha, \beta)]^T P(\alpha, \beta) d\alpha d\beta = \mathbf{M} \cdot \mathbf{D}.\end{aligned}\tag{3.42}$$

As for the minimal sampling described in the previous paragraph,  $\mathbf{M}$  is obtained by inverting  $\mathbf{D}$ :

$$\mathbf{M} = \mathbf{G} \cdot \mathbf{D}^{-1}\tag{3.43}$$

provided  $\mathbf{D}$  is non-singular, a condition which depends on the definition of  $P(\alpha, \beta)$ . In this respect, we made the simplest possible choice, namely a uniform distribution of  $(\alpha, \beta)$  over the intervals  $[0, \pi]$  and  $[0, 2\pi]$ . Then  $\mathbf{D}$  takes the diagonal form

$$\mathbf{D} = \pi^2 \begin{bmatrix} 2 & 0 & 0 & 0 \\ 0 & 1 & 0 & 0 \\ 0 & 0 & \frac{1}{2} & 0 \\ 0 & 0 & 0 & \frac{1}{2} \end{bmatrix}.\tag{3.44}$$

**Stop criterion.** As a reasonable compromise between computation time and accuracy, the simulations are considered as converged when the standard deviation of any coefficient of the Mueller matrix  $M_{ij}$  normalized by the first one  $M_{11}$  ( $M_{ij}/M_{11}$ ,  $i, j = 1, 2, 3, 4$ ,  $i \cdot j \neq 1$ ) denoted as  $M_{ij}^*$ , is smaller than 1.5%. This choice is justified by the fact that the experimental Mueller matrices are provided in normalized form, without quantitative values for the  $M_{11}$  element.

By applying the Central Limit Theorem for any coefficient we obtain the values belonging to the interval  $\pm 3\%$  around its mean values at a 95% level of confidence.

It turns out that in our conditions, with the statistical sampling of the input Stokes vectors the procedure converges faster than with the minimum sampling. The former has thus been used throughout this work.

### 3.3 Conclusion

In this chapter we outlined the Monte Carlo algorithm we have modified and used for the investigations reported in the following chapters. All the essential steps have been described, including the definition of individual photon trajectories, statistical samplings and evaluation of the sample Mueller matrix measured with various instrumental geometries.

Perhaps the greatest advantage of using the Monte Carlo method to simulate physical experiments, is its liability to handle complex sample geometries and particular illumination and detection setups. This method is thus the most suitable to realistic modelling of tissue polarimetric response aimed at defining new diagnostic tools. Accurate modelling is indeed necessary to optimize the experimental parameters to enhance the useful contrasts between healthy and pathological zones: purely empirical optimization would require a



clinical trial for each envisioned configuration! As discussed in the following chapters, such models may involve many experimental parameters, especially if these models are supposed to reach the accuracy needed for a realistic diagnostic tool. These parameters should be constrained, if possible by different experiments, to reduce the ambiguities arising when too many parameters are involved in the fit. There again the capability of the Monte Carlo technique to handle various geometries is decisive to run such simulations.

# Chapter 4

## Experimental activity

### 4.1 Introduction

Polarimetric imaging is based on the analysis of the modification of the incident light *polarization* due to interaction with the sample. As such, it may provide different and complementary information with respect to the usual imaging based on *intensity* measurements. Polarimetric imaging may be implemented in several ways, based on various ways to generate the incident polarization and to analyze its counterpart of the emerging light.

For example, only two images are required for orthogonal state contrast (OSC). These two images are typically taken with parallel and perpendicular linear polarizations, and then combined to display the OSC image, which is has also been called improperly degree Of linear polarization, or DOLP. The same approach may be applied to orthogonal states of circular polarization, to display the degree of circular polarization, or DOCP. These techniques provide contrasts which may be useful in various fields, i.e. in dermatology [61]. However, OSC techniques can completely characterize only special samples, with simple polarimetric responses, such as pure depolarizers.

Conversely, in the most general case, a complete characterization of the sample requires Mueller polarimetry, which is based on the acquisition of 16 images (with four input and four output polarization states). These images can subsequently be treated by various algorithms to "extract" the essential polarimetric effects, namely the diattenuation, the retardation and the depolarization, by using one (or several) decomposition techniques outlined in section 1.4.3.

In this chapter, we will present the experimental part of this work, which includes data taken with three different setups, namely:

- a full Mueller imaging system, designed to make real-space images of the surface of a scattering medium under focussed illumination, developed at Laboratoire de Physique des Interfaces et des Couches Minces (LPICM) of Palaiseau, France, at the very beginning of this work,
- a Fourier space polarimetric imaging system, developed during a three months stay at the Oregon Health and Science University (OHSU) of Portland, Oregon, in Pr. Steven Jacques' team,
- a full Mueller real space imaging system, located in the Pathology Department of Institut Mutualiste Montsouris (IMM), an hospital in Paris, where various tissues (uterine cervix cone biopsies, colon samples...) have been imaged *ex vivo*.

	Mueller polarimeter with focused illumination	Goniometric polarimeter	Fourier space imaging polarimeter	Real-space Mueller imaging polarimeter
<b>Application</b>	Spatially homogenous medium $\mu'_s$	Determination of the scatterer size	2D image	2D imaging of any kind of sample
<b>Advantage</b>	Accurate information due to the spatial pattern of the backscattered light	Full angular range of investigation	Fast	Full field, integration to <i>in vivo</i> colposcopy
<b>Disadvantages</b>	Does not work for spatially inhomogeneous sample	Slow (point measurement)	Limited to 60° with microscope objective	Difficult to reduce the time of measurement

**Table 4.1:** Comparison between the three different setups developed in this work.

In Table 4.1 we compare the three experimental approaches pointing out applications, advantages and disadvantages of each method.

## 4.2 Mueller imaging with focussed illumination

This part of the work was aimed at reproducing the results published by Hielscher *et al.* [62], to get a first set of reliable experimental data to compare with Monte Carlo simulations of Mueller images of scattering samples taken in the backscattering geometry.

### 4.2.1 The instrument

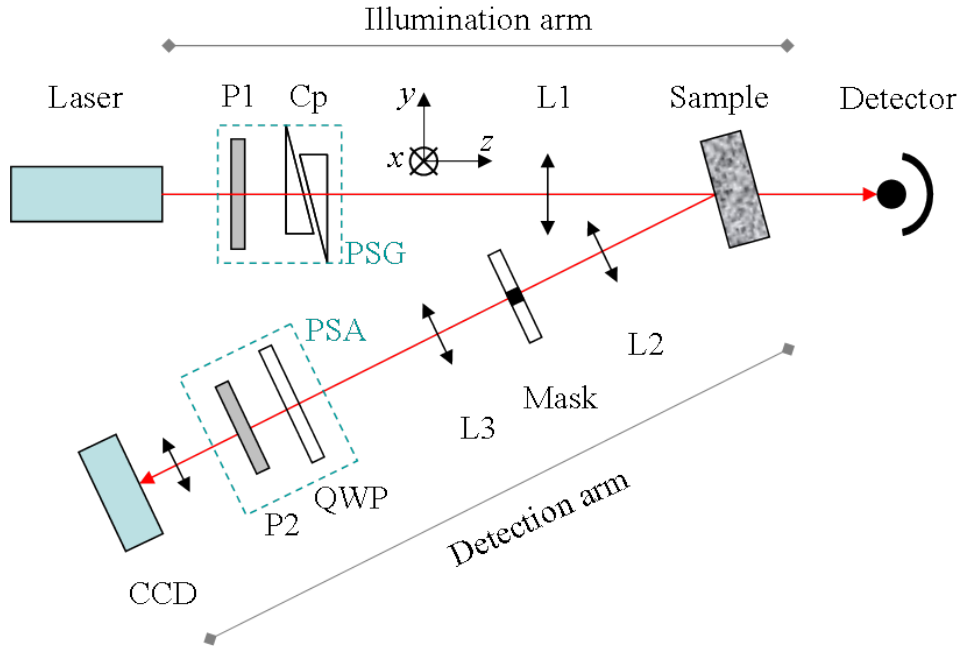


**Figure 4.1:** Scheme of the Mueller polarimeter for real space imaging of a scattering sample in backscattering geometry and focussed illumination.

**The experimental setup.** This polarimeter is schematized in Fig. 4.1. The source, a Helium Neon (HeNe) laser, is well suited for an operation with tightly focussed beam on the surface of the sample. The polarization of the beam incident on the sample is defined by a Polarization State Generator (PSG), composed of a dichroic plastic polarizer and a Babinet-Soleil-Bravais compensator (Cp) consisting of two wedged quartz plates with parallel fast axes and a translation plate allowing to vary the effective quartz thickness seen by the light beam. In addition of being adjustable in retardation, this compensator may also be oriented at will in the  $xy$  plane. A photo of this device with its mount is shown in Fig. 4.2.

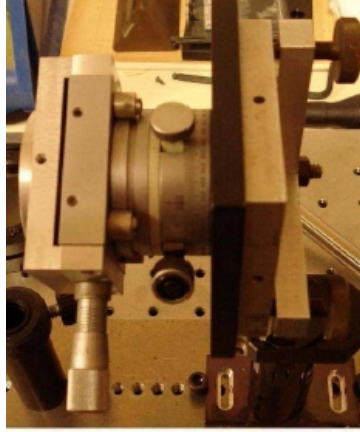


**Figure 4.2:** The Babinet-Soleil-Bravais compensator with its mechanical mount.

In contrast, the polarizer is kept oriented horizontally (in the  $x$  direction) and the laser can be rotated to accurately adjust the overall illumination intensity to match the dynamical range of the CCD. The compensator retardation is adjusted either to  $180^\circ$  ( $\lambda/2$ ), to generate linearly polarized states with various azimuths, or to  $90^\circ$  ( $\lambda/4$ ), to generate right and left circular polarizations. The polarizations actually used in the measurements were linear, at  $0^\circ$ ,  $90^\circ$ ,  $+45^\circ$  and  $-45^\circ$ , respectively labelled H, V, P, M. The right and left circular polarizations are labelled R and L, respectively.

The lens L1 focusses the beam onto the sample surface. The fraction of the beam transmitted through the sample is measured by a single detector, to evaluate the photon mean free path  $\ell_s$  in the scattering sample as described below.

The sample surface is imaged on a CCD by the lenses L2 and L3 and the CCD objective. A tiny mask is inserted in the focal plane of L2 to reject the specular reflection of the laser beam on the front surface of the sample, which would otherwise strongly saturate the CCD.

The polarization of the backscattered light is analyzed by a Polarization State Analyzer (PSA) consisting of a true zero order quarter wave plate (QWP) made of quartz and a second plastic dichroic polarizer P2. Both elements can be rotated at will in the transverse plane of the emerging beam. The incoming polarization is then projected onto linear states by setting the fast axis of the QWP parallel to the transmission axis of P2, both at the chosen azimuth. The projection on circular states is achieved by setting the axes of QWP and P2  $45^\circ$  apart from each other. The basis polarization states of the PSA actually used are the same as those of the PSG, and they also labelled H, V, P, M, R, L. Actually, PSAs comprising a linear polarizer and a QWP are very widespread, but they are usually operated by rotating only the QWP and letting the polarizer fixed. However, by doing so the incoming state of polarization is projected onto elliptical states,

which would need an extra calibration procedure that we avoided with the polarizer and QWP settings described above.

The camera used for the image acquisition was a CCD from Princeton Instruments Inc., with 575 x 384 pixels and a A/D conversion dynamics of 14 bits. This camera was operated at room temperature, with a significant temperature dependent offset due to the dark current. Consequently, periodic measurements of this dark current had to be performed by taking an image with the CCD whip "in the dark", to be subtracted from the subsequently measured images.

**The measurement procedure.** The PSG and the PSA were manually adjusted to sequentially generate the six input and six output polarization basis states. The Mueller image of the sample was then calculated from the 36 raw images corresponding to the whole set of possible combinations of these states after subtraction of the dark current which was done before each run. The overall acquisition time for a complete Mueller measurement was typically 1 hour.

The combinations of the raw images providing the Mueller matrices are the same as those used by Hielscher *et al.* [62] and are reported in Fig. 4.3.

$M_{11}:$ (OO)	$M_{12}:$ (HO-VO)/2	$M_{13}:$ (PO-MO)/2	$M_{14}:$ (LO-RO)/2
$M_{21}:$ (OH-OV)/2	$M_{22}:$ (HH+VV)/4 - (HV+VH)/4	$M_{23}:$ (PH+MV)/4 - (PV+MH)/4	$M_{24}:$ (LH+RV)/4 - (LV+RH)/4
$M_{31}:$ (OP-OM)/2	$M_{32}:$ (HP+VM)/4 - (HM+VP)/4	$M_{33}:$ (PP+MM)/4 - (PM+MP)/4	$M_{34}:$ (LP+RM)/4 - (LM+RP)/4
$M_{41}:$ (OL-OR)/2	$M_{42}:$ (HL+VR)/4 - (HR+VL)/4	$M_{43}:$ (PL+MR)/4 - (PR+ML)/4	$M_{44}:$ (LL+RR)/4 - (RL+LR)/4

$O = \star$    
  $H = \longleftrightarrow$    
 $P = \nearrow$    
 $L = \curvearrowleft$   
 $V = \updownarrow$    
 $M = \searrow$    
 $R = \curvearrowright$

**Figure 4.3:** Table of combinations of the raw images used to retrieve the Mueller images [62].

In the table shown in Fig. 4.3, the meaning of the labels H, V, P, M, R and L is the same as in the previous paragraph. The first label identifies the incident polarization and the second the detected one: for example HP means that the sample is illuminated with H polarization while the PSA is adjusted for projection on P polarization. The label "O" identifies unpolarized states. As such states could not be generated directly by the PSG and the PSA, they were "synthesized" from polarized measurements by taking the average of the images corresponding to two orthogonal states (H and V, or P and M, or L and R).

**Evaluation of the accuracy.** The accuracy of the polarimeter was evaluated by comparing the measured Mueller matrices with their expected counterparts for well characterized optical elements, namely a dichroic polarizer and a retardation plate. This procedure was implemented in two steps:

1. The scattering sample was replaced by a ground metal plate, whose Mueller matrix  $\mathbf{M}_0$  is close to that of a mirror, i.e.  $\text{diag}(1, 1, -1, -1)$ .  $\mathbf{M}_0$  was then measured.
2. The test sample was inserted, either in the illumination or in the detection arm, without removing the metallic plate. The composite matrix  $\mathbf{M}$  was then measured, and then the sample matrix  $\mathbf{M}_s$  was extracted as  $\mathbf{M}_s = \mathbf{M}_0^{-1} \cdot \mathbf{M}$  if the sample was inserted in the illumination arm while  $\mathbf{M}_s = \mathbf{M} \cdot \mathbf{M}_0^{-1}$  if this sample was set in the detection arm.

As test samples, we used a dichroic polarizer and a mica retardation plate specified to be quarter wave at  $\lambda = 532$  nm. For both samples, the experimental matrix to be compared with the theory was  $\mathbf{M}_s^*$ , i.e. the matrix  $\mathbf{M}_s$  normalized by its  $M_{s11}$  element, to eliminate the overall transmission factor for unpolarized light, for which the instrument was not calibrated. Moreover, both components were measured at different azimuths, to explore the accuracy of the instrument on a "diversified" set of data. The theoretical formulas are provided in Appendix A.

The results obtained with the polarizer inserted in the illumination arm and measured at various azimuths between  $90^\circ$  and  $180^\circ$  are summarized in Fig. 4.4.

While the polarizer could be considered as perfect, the retardation of the mica plate at  $\lambda = 633$  nm had to be measured. This was done in a standard way, by placing both the mica plate and the compensator with their axes aligned with respect to each other at  $45^\circ$  of the axes of crossed linear polarizers. The retardation  $\delta_R$  of the mica plate was then determined from the setting of the compensator for which a good extinction was observed between the crossed polarizers, implying that the retardation  $\delta_R$  had been compensated by that of the Babinet-Soleil-Bravis. Of course, the compensator had been previously calibrated, by pointing the settings for which the phase retardation was a multiple of  $180^\circ$ . This procedure eventually provided  $\delta_R = 74.2^\circ \pm 1^\circ$ . The results obtained with the mica retarder also inserted in the illumination arm are shown in Fig. 4.5.

From the above data and the theoretical formulas in Appendix A we can define for each measured matrix two quantifiers of the accuracy, namely the overall root mean square deviation ( $rms$ ) and the largest error ( $e_{max}$ ) among the 15 normalized elements  $M_{ij}^*$ . The 15 elements of each Mueller matrix were normalized by  $M_{11}$ . The values of these quantifiers obtained from the data shown above are summarized in Table 4.2.

Azimuth	$0^\circ$	$30^\circ$	$45^\circ$	$60^\circ$	$90^\circ$	$135^\circ$
<b>rms <math>\mathbf{M}_P</math></b>	0.023	0.022	0.024	0.022	0.025	
<b><math>e_{max}</math> <math>\mathbf{M}_P</math></b>	0.061	0.039	0.053	0.046	0.058	
<b>rms <math>\mathbf{M}_R</math></b>	0.040	0.043	0.039	0.037	0.038	0.032
<b><math>e_{max}</math> <math>\mathbf{M}_R</math></b>	0.092	0.094	0.093	0.073	0.097	0.084

**Table 4.2:** Overall root means square ( $rms$ ) and largest error ( $e_{max}$ ) for the Mueller matrix of the dichroic polarizer ( $\mathbf{M}_P$ ) and mica retarder ( $\mathbf{M}_R$ ) measured at different azimuth angles. Each Mueller matrix was normalized by its  $M_{S11}$  ( $\mathbf{S} = \mathbf{P}$  and  $\mathbf{R}$ , respectively).

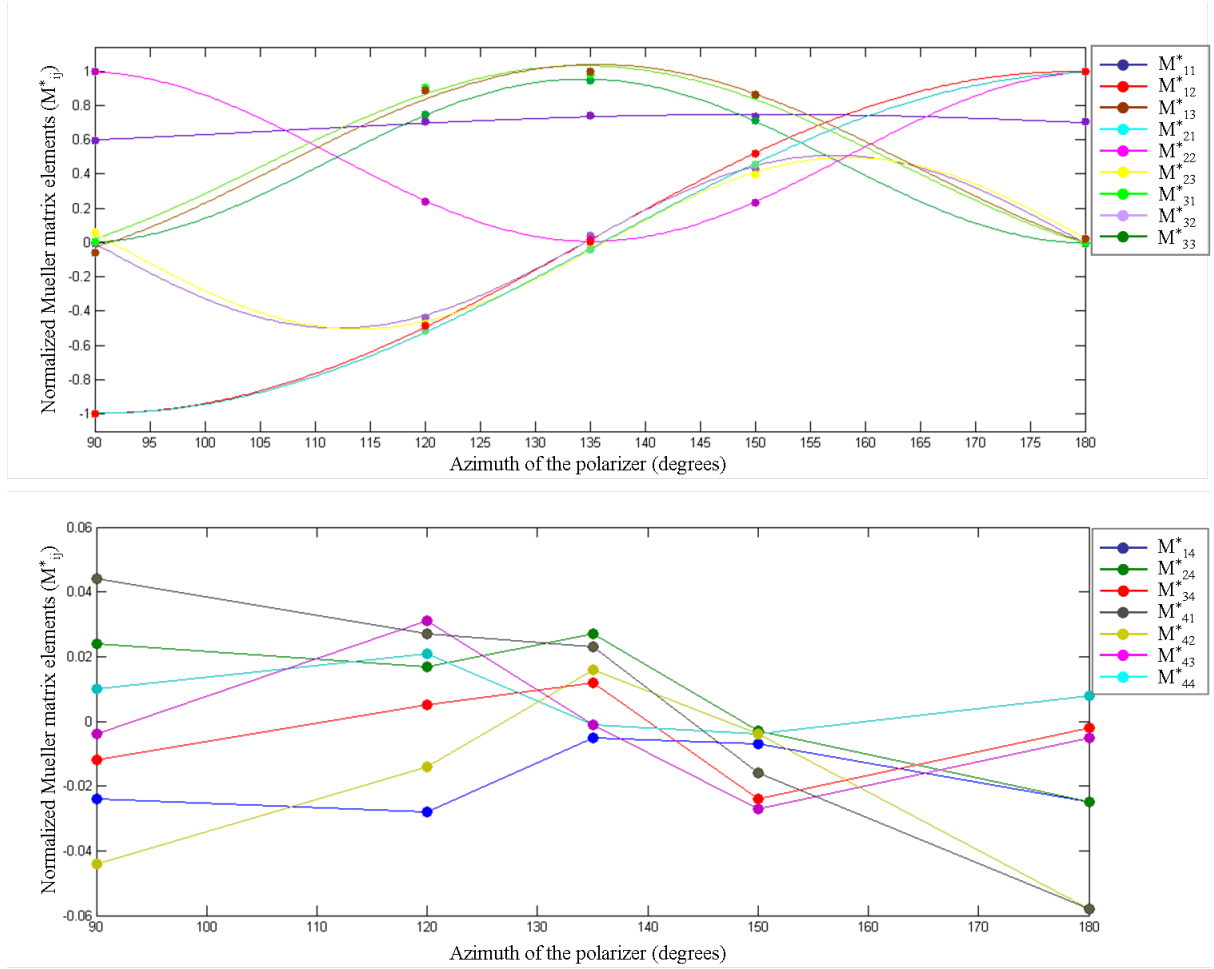


**Figure 4.4:** Mueller matrices of the polarizer set a various azimuths. All elements but  $M_{11}$  are normalized by  $M_{11}$  ( $M_{ij}^*$ ,  $i, j = 1, 2, 3, 4$ ). *Top*: elements expected to be nonzero. The solid lines are fits by sine functions. *Bottom*: theoretically vanishing elements.

The polarizer and the retarder were also measured in the detection arm, with very similar results. Overall, the accuracy achieved without any specific calibration procedure was considered as quite satisfactory, and was indeed sufficient for the studies on the sphere suspensions described in the next subsection.

#### 4.2.2 Results on suspensions of polystyrene spheres in water

We performed the measurements and simulations of polarimetric images of two different suspensions of polystyrene spheres in water (radii  $r_1 = 50$  nm and  $r_2 = 1500$  nm, optical index contrast  $m = 1.59/1.33$  for both samples). For these studies we used the three cells shown in Fig. 4.6. The cylindrical cell, with metallic sidewalls and glass front and rear faces, was used for Mueller imaging of suspensions of polystyrene spheres in water.

The 1 mm thick cell was used to determine the mean free path  $\ell_s$  of the suspensions by measuring the intensity of the transmitted beam, which was not detectable after the thick cell. This mean free path had to be determined experimentally with a good accuracy to be used as an input parameter for the simulations. The anisotropy parameter  $g$  and the directional mean free path  $\ell'_s$  were determined theoretically, from the sphere radii and the index contrast  $m$ . The result of this characterization of the two studied suspensions

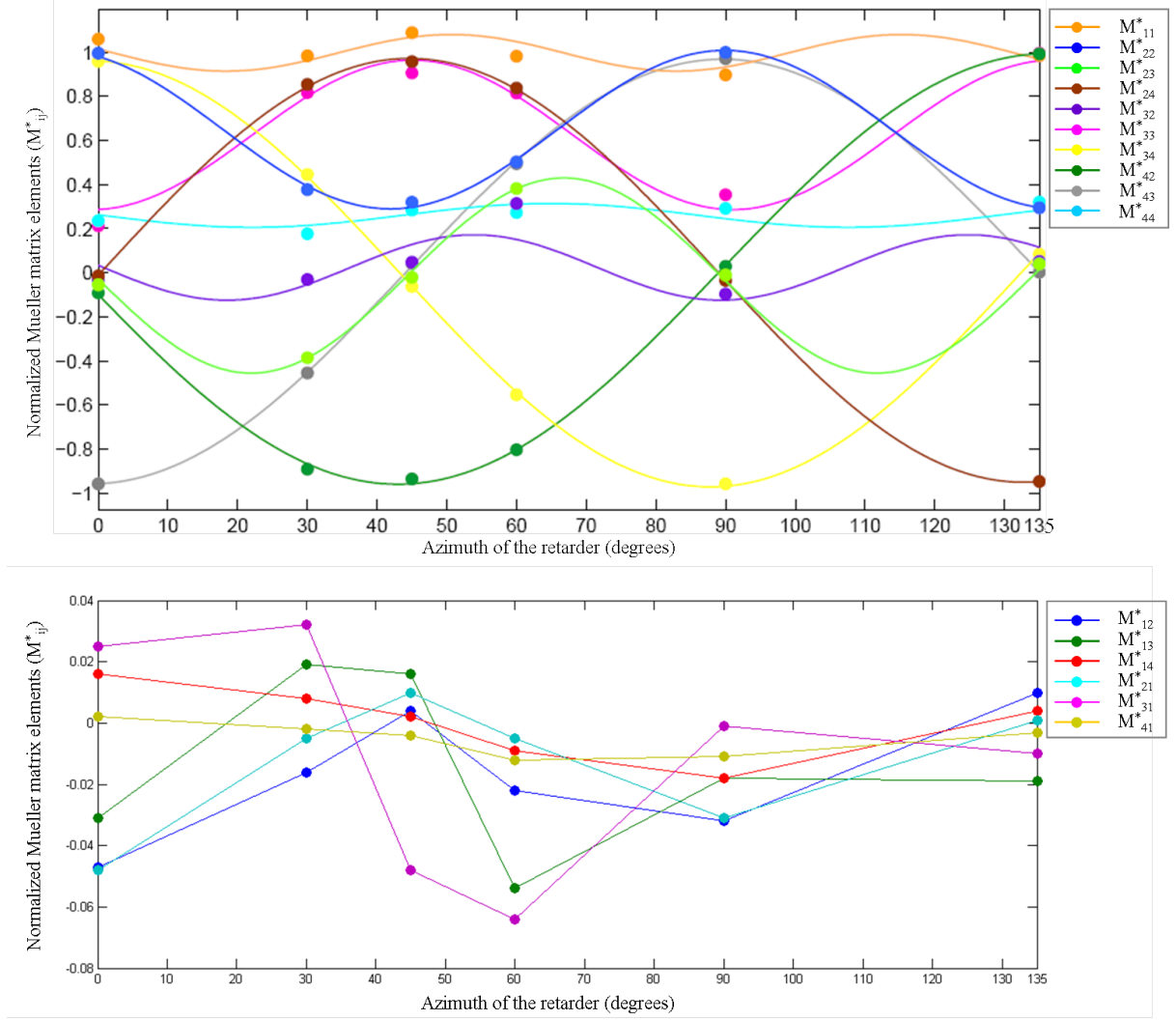


**Figure 4.5:** Analogous to Fig. 4.4 for the mica retarder.

are summarized in Table 4.3

The Mueller images of the two sphere suspensions characterized as explained above are shown in Fig. 4.7, together with Monte Carlo simulations realized with the relevant values of the radii  $r_i$ , the index contrast  $m$  and the mean free path  $\ell_s$ . These matrices are given in normalized form: every element  $M_{ij}$  is divided by  $M_{11}$ , except, of course,  $M_{11}$  itself, which is displayed in arbitrary units. The same scales have been used for the experimental data and the simulations, both for transversal dimensions (2 cm width) as well as color scales (between -0.2 to 0.2) for the normalized elements  $M_{ij}^*$ .

Two main conclusions can be drawn from these results:

- The essential features observed by Hielscher *et al.* [62] are reproduced: "small" sphere suspensions ( $r_1 = 50$  nm, Rayleigh scattering regime) exhibit essentially radially oriented diattenuation and zero retardation, while the opposite (radial retardation without diattenuation) is seen for "large" particles ( $r_2 = 1500$  nm, Mie scattering regime).
- The agreement between experiment and simulations is quite good: the current version of the code is validated.



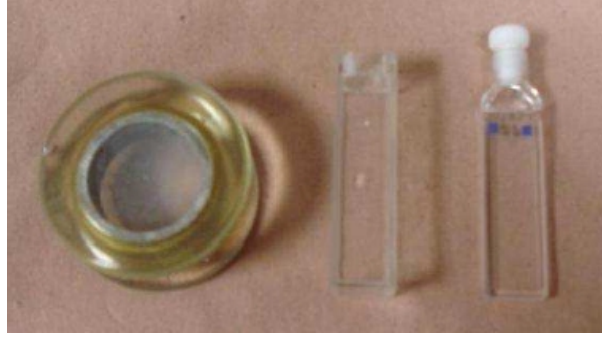


**Figure 4.6:** Photo of the cuvettes used for the measurements on suspensions of polystyrene spheres in water. From *left to right*: the 1 cm thick and 2 cm diameter cylindrical cell used for Mueller imaging, a square based 1 cm thick cell, and the 1 mm thick rectangular cell.

Sample	Cell + water	$r_1 = 50 \text{ nm}$	$r_2 = 1500 \text{ nm}$
<b>Signals [mV]</b>	3580	1370	537
<b>Transmission</b>	1	0.383	0.15
$\ell_s \text{ [mm]}$		1.04	0.53
$g$		0	0.5
$\ell'_s \text{ [mm]}$		0.383	0.15

**Table 4.3:** Raw data and deduced scattering parameters for the two sphere suspensions.

In the following, we will consider real space polarimetric imaging with uniform illumination. As the setup used for the measurements described above did not allow full field illumination, here we present only space averages of the images shown in Fig. 4.7. These averaged images are spatially uniform. as the butterfly patterns with azimuthal dependence proportional to the sine or the cosine of the aimuthal angle  $\varphi$  or its double  $2\varphi$  average to zero only the diagonal terms remain, with the following values (values for the off-diagonal terms are given to show the signal to noise ratio)

$$\begin{bmatrix} \mathbf{1} & 2.5 \cdot 10^{-5} & 2.7 \cdot 10^{-5} & 1.1 \cdot 10^{-5} \\ 3 \cdot 10^{-5} & \mathbf{0.174} & 1.6 \cdot 10^{-5} & 1.4 \cdot 10^{-5} \\ 0.9 \cdot 10^{-5} & 2.9 \cdot 10^{-6} & -\mathbf{0.174} & 8.3 \cdot 10^{-5} \\ -5.1 \cdot 10^{-5} & -2.7 \cdot 10^{-5} & 2.1 \cdot 10^{-5} & -\mathbf{0.066} \end{bmatrix} \quad (4.1)$$

for the small spheres, and

$$\begin{bmatrix} \mathbf{1} & 1.3 \cdot 10^{-5} & 4.6 \cdot 10^{-5} & 1.8 \cdot 10^{-5} \\ -1.8 \cdot 10^{-5} & \mathbf{0.083} & 6.3 \cdot 10^{-5} & 2.5 \cdot 10^{-5} \\ 5.8 \cdot 10^{-6} & 4.3 \cdot 10^{-6} & -\mathbf{0.083} & 6.2 \cdot 10^{-5} \\ -7.6 \cdot 10^{-5} & -1.9 \cdot 10^{-5} & 5.4 \cdot 10^{-5} & -\mathbf{0.328} \end{bmatrix} \quad (4.2)$$

for the large ones. These matrices are written *in extenso* to show the "signal to noise" ratio, given by the off-diagonal terms, which should be zero, and are of the order of  $10^{-5}$ . These simulations thus confirm the general trends already reported [63] for the diagonal terms of the Mueller matrix of isotropic scattering media:

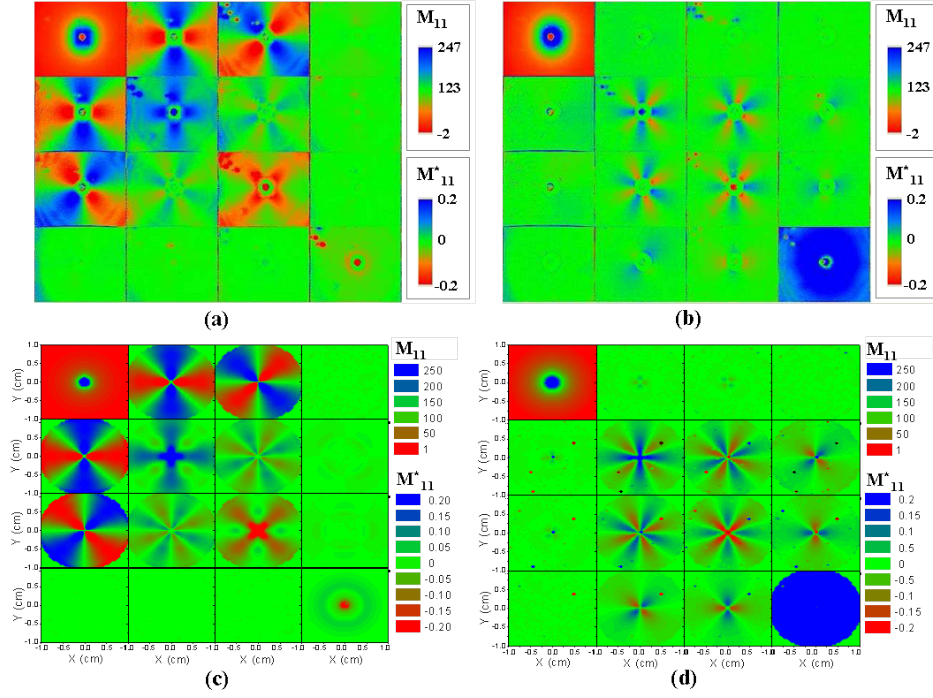


**Figure 4.7:** Backscattering Mueller matrix images of suspensions of polystyrene spheres in water, taken at  $\lambda = 633$  nm. (a, b): measured; (c, d): simulated. Sphere radii:  $r_1 = 50$  nm for (a) and (c),  $r_2 = 1500$  nm for (b) and (d). The central spot on the experimental images (a) and (b) is the shadow of the mask which eliminates the specular reflection on the front surface of the cell containing the suspensions.

$$|M_{22}^*| = |M_{33}^*| > |M_{44}^*| \quad (4.3)$$

for the Rayleigh scattering regime, while the opposite,

$$|M_{22}^*| = |M_{33}^*| < |M_{44}^*| \quad (4.4)$$

holds for the Mie scattering regime. As we will see later, the vast majority of the tissue samples that we studied in backscattering behave as depolarizers with diagonal Mueller matrices. Moreover, these matrices always obey Eq.(4.3). At first sight, this behaviour seems to indicate that the contribution of the nuclei in the backscattered light is negligible, as this contribution is expected to obey Eq.(4.4), due to the radius of nuclei, which is typically  $2 \mu\text{m}$  or more.

However, we should keep in mind that the index contrast  $m$  between the nuclei and the cytoplasm is much lower than for polystyrene spheres and water. It is well known [64] that for  $m \approx 1$  even particles much larger than the wavelength behave as small scatterers, which corresponds to the *Rayleigh-Gans* scattering regime (described in subsection 2.2.3). If this regime has been well characterized for the usual single scattering parameters (such as the cross-section or the angular distribution), to our knowledge the Mueller matrix in the backscattering geometry has not been studied. We thus carried out various simulations in this regime. A typical result is shown in Fig. 4.8, which is similar to that seen in Fig. 4.7 for "true" Rayleigh regime. The larger noise is due to a very large scattering anisotropy ( $g \approx 1$ ), which drastically decreases the number of detected

photons in the backward direction with respect to the previous simulation.

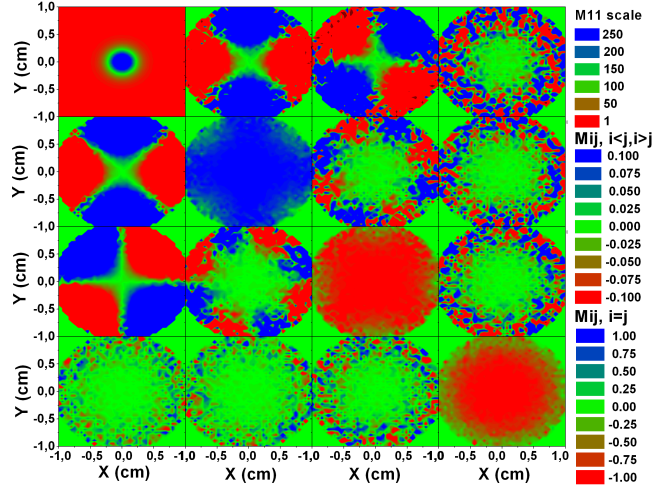


**Figure 4.8:** Simulated backscattering Mueller matrix image of a scattering medium under focussed illumination, with  $m = 1.03$  and  $r = 3 \mu m$ .

At this point, we may conclude that the contribution of the nuclei in the backscattered light may be quite small due to the strong anisotropy of the scattering, but this contribution is likely to be of Rayleigh type, in agreement with the observations on real tissues. However we will see later that the situation is more complex, with Mueller matrices of Mie type appearing for realistic conditions if only the nuclei are taken into account in the model.

### 4.3 Angle resolved Mueller imaging of thin tissues

As discussed in more detail in the next subsection, Fourier space imaging (FSI) provides the angular distribution of the light emerging from the sample in a "snapshot", by imaging the back focal plane of a lens set in front of the sample to collect this emerging light. FSI provides full 2D angular distributions very quickly, with simple setups, while standard 2D goniometry typically requires a sophisticated mechanical mount to allow the two dimensional angular scan of the detector, in a highly time consuming procedure. However, the price to pay for this advantage of FSI is a limitation of the angular field to the Numerical Aperture (N.A.) of the collecting lens, while classical goniometry may scan the full range of polar angles, from  $0^\circ$  to  $90^\circ$ . Of course both techniques have been used to measure the angular distributions of *intensities*. However, by adding a PSG in the illumination arm and a PSA in the detection arm, it is conceptually straightforward to make these techniques polarization sensitive. The measured quantities are then *angle-resolved Mueller matrices*.

Many applications can be envisioned for polarization sensitive FSI, including the characterization of scattering or diffracting systems. In our case, the main interest of this technique is the study of optically thin tissue samples, where single scattering is dominant. This kind of measurements may prove very helpful to *constrain the values of the parameters* involved in the models aimed at reproducing the measured polarimetric responses of tissues. As shown in the next chapter, even quite "simple" models may involve many

parameters, and the constraints coming from single scattering data may be essential to avoid ambiguities in the interpretation of the experimental data.

In this section, we will describe the sample preparation, the angular resolved polarimeters, and more particularly the FSI setup developed during my two months stay at Oregon Health and Science University, Portland, in Pr. Steven Jacques' team, in collaboration with Amy Winkler, another PhD candidate. We will also show the first results obtained with these setups on the thin samples prepared as shown below.

### 4.3.1 The sample preparation

Ideally, the following measurements should have been performed in pure single scattering regime. To this end, the sample thickness  $h$  must be much smaller than the scattering mean free path  $\ell_s$ . In other words, the optical depth  $d_o = h/\ell_s$  must be much smaller than 1. For an order of magnitude estimation of the contributions of multiple scattering we can assume that the probability  $P_k$  for a photon to experience exactly  $k$  scatterings is reasonably well described by a Poissonian distribution:

$$P_k = \frac{d_o^k}{k!} e^{-d_o} \quad (4.5)$$

where  $d_o$  is the sample optical depth. Actually this law would be rigorously valid for scatterings at small angles, but for a rough estimation it may be used anyway. As a result we get

$$\frac{P_2}{P_1} \approx \frac{d_o}{2} \quad (4.6)$$

which confirms the intuitive criterion  $d_o \ll 1$  for single scattering operation. However, the smaller  $d_o$ , the smaller the scattered intensity. Thus we had to find a good compromise between the limitation of the multiple scattering contribution and the need to achieve a reasonable signal to noise ratio. This compromise was found for  $d_o \approx 1$ , meaning that one third of the photons suffer two scatterings.

For all the measurements described in the following (excepted those on honey) we used 150  $\mu\text{m}$  thick cells composed of two microscope plates separated by coverslips, as shown in Fig. 4.9.

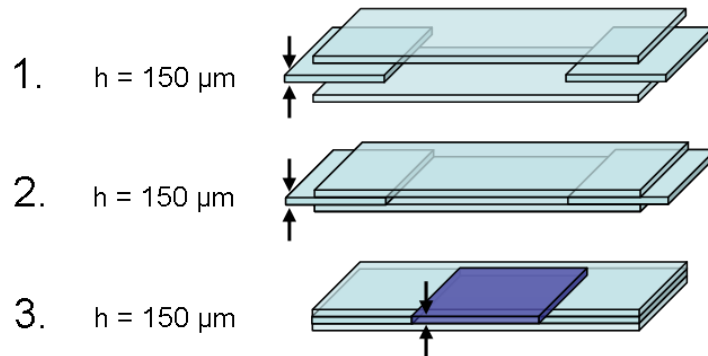


**Figure 4.9:** Mounting of the 150  $\mu\text{m}$  thick cell used for phantom or tissue measurements.

**Tissue phantom.** This phantom consisted of suspensions of polystyrene spheres in distilled water (sphere diameter  $d_s = 2\ \mu\text{m}$ , refractive indexes of the medium and sphere  $n_m = 1.33$ ,  $n_s = 1.59$ , respectively, density of spheres per  $\mu\text{m}^3$   $N_s = 1\%$ ). The scattering mean free path of these suspensions was evaluated by Mie theory as  $\ell_s \approx 166\ \mu\text{m}$ , leading to  $d_o \approx 0.9$ , a slightly more favorable value for single scattering than the "target"  $d_o = 1$ .

**Biological tissues.** We cut very thin slices (approximately  $150\ \mu\text{m}$  thick) of fresh vegetables and frozen tendon to provide biological thin samples. We placed the sample in the  $150\ \mu\text{m}$  thick cell as described above. In order to create a humid chamber such to prevent the sample to dry we placed a small piece of humid paper together with the sample.

We also measured honey at room temperature to provide another biological sample with optical activity. In this case we used a 3 cm thick quartz cuvette to get measurable polarization rotations.

### 4.3.2 The polarimetric components and measurement procedure

**The polarization state generator and analyzer.** The two setups described in this section are all based on the polarimetric design schematized in Fig. 4.10. The horizontally (H) polarized output of a HeNe laser is sent into a PSG comprising a half wave plate (HWP), a linear polarizer (P) and a quarter wave plate (QWP). The half wave and the polarizer can be rotated in the HV plane. The quarter wave plate can be removed, or oriented so that its optical axes coincide with the transmission axis of the polarizer P to generate linearly polarized states. This plate was then set with its optical axis at  $+45^\circ$  from the incident linear polarization to produce circularly polarized states. In principle, the HWP could be sufficient to generate any linear polarization by rotating the input H polarization of the HeNe. However, this input polarization is not perfectly linear at the laser output, and is further degraded if additional optics are inserted between the laser and the PSG. The polarizer P is thus necessary to recover well defined linear polarizations, to be used directly or to be converted to left and right circular states by the quarter wave plate. The PSA is composed of the same elements placed in reverse order, excepted the HWP, which is no longer necessary.

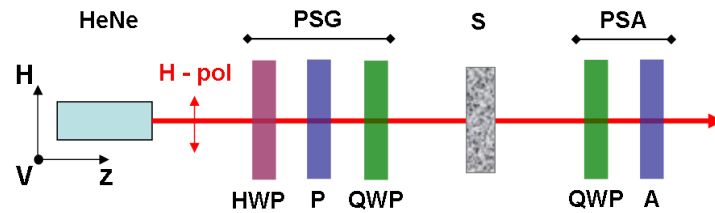


**Figure 4.10:** General scheme of the polarimetric components of the angularly resolved polarimeters described in this section. HWP: half wave plate, P: polarizer, QWP: quarter wave plate, S: sample, A: analyzer.

The polarization states generated by the PSG and analyzed by the PSA are the same as in the polarimeter described in the previous section, namely H (linear horizontal), V (linear vertical), P and M (linear,  $+45^\circ$  and  $-45^\circ$ ), R and L (right and left circular). The settings of the PSG and PSA elements used to generate these states are summarized in Tables 4.4 and 4.5.

Polarization state	HWP [°]	P [°]	QWP [°]
<b>H</b>	0	0	removed
<b>V</b>	45	90	removed
<b>P</b>	45	45	removed
<b>M</b>	45	315	removed
<b>R</b>	45	90	+45
<b>L</b>	45	90	-45

**Table 4.4:** Settings of the PSG for the generation of the six input polarization states.

Polarization state	QWP [°]	P [°]
<b>H</b>	removed	0
<b>V</b>	removed	90
<b>P</b>	removed	45
<b>M</b>	removed	315
<b>R</b>	45	0
<b>L</b>	-45	90

**Table 4.5:** Settings of the PSA for the analysis of the six output polarization states.

**The measurement procedure.** In total 36 raw data are taken to determine the polarimetric response of the system. These measurements involve 6 input states of polarization and 6 analyzed states of polarization, H, V, P, M, R, L. As already mentioned, the shorthand for the intensity measured here is  $I$  with two subscripted letters indicating the generated and analyzed state of polarization, respectively. For example, if H is the state of polarization of the incident light, then the light traveling is denoted as  $I_H$  and if P is the state of polarization analyzed, then the measurement is denoted as  $I_{HP}$ . Given any state of polarization of the incident light, the Stokes vector of the scattered light  $\mathbf{S} = [I, Q, U, V]^T$  is obtained by calculating its components as

$$Q = I_{.H} - I_{.V}; \quad U = I_{.P} - I_{.M}; \quad V = I_{.R} - I_{.L} \quad (4.7)$$

where the dot replacing the shorthand of the state of polarization of the incident light stays for "any" state of polarization.

For comparison between theory and measurements we found more convenient to cast the results as a 6 x 4 matrix, that we call "Polarimetric Matrix", rather than the usual Mueller matrix (4 x 4). While the columns of the polarimetric matrix are the components of the normalized output Stokes vectors, as for the Mueller matrix, the lines are the input polarization states H, V, P, M, L and R. In some cases, the input states are reduced to four. The details of the plotted quantities are shown in Fig. 4.11. Another reason to use this matrix instead of the usual Mueller matrix is the normalization of each component of the output Stokes vector by the relevant combination of orthogonal states, a procedure which is probably more robust against the above mentioned errors in the evaluation of the intensity than that used previously for the usual Mueller matrix.

The overall intensity is evaluated in multiple ways:





the directly transmitted beam, to allow an easier detection of the scattered component close to the incident direction. The PSA and the detector (a photodiode) are placed on a rotating mount to take angle-resolved data by changing the detection angle in the  $xz$  plane.

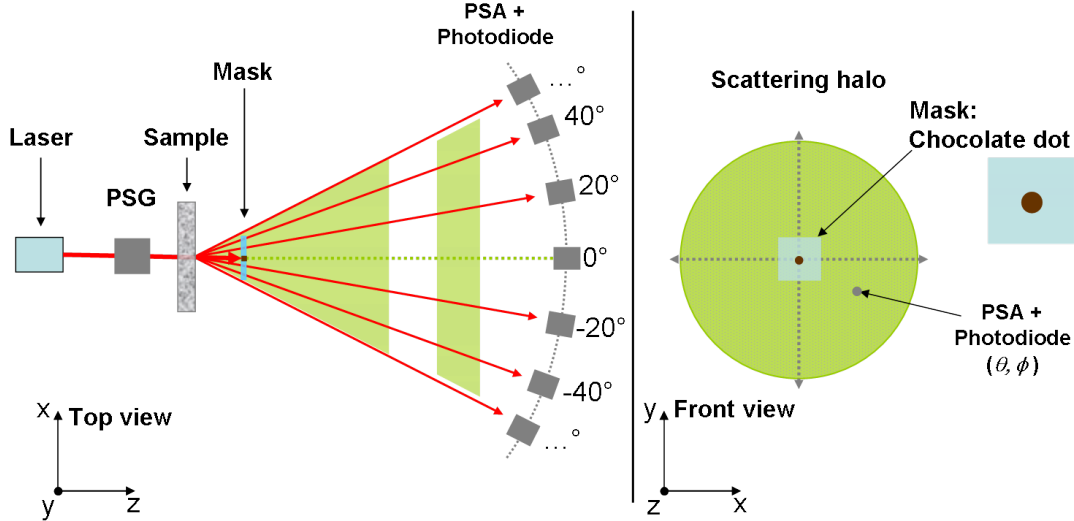


**Figure 4.12:** Scheme of a goniometric polarimeter. *Left:* top view, showing the angular scan of the detection arm around the  $y$  axis. *Right :* front view, showing the 2D scattering "halo" as seen by an observer looking into the  $-z$  direction.

**Results.** We used the tissue phantom described above (aqueous suspension of polystyrene spheres in the  $150\ \mu\text{m}$  cell). With the goniometric system one of the main issues was to separate the scattering signal from the noise. To this purpose we implemented a lock-in detection of the signal modulated by a mechanical chopper. Nevertheless, the signal to noise ratio remained too low to make measurements for all polarimetric configurations. Hence we decided to perform angular measurements only in the HH configuration, which provided the largest signal. The result is shown in Fig. 4.13. We obtained a reasonable agreement with the predictions based on Mie theory, with, however, some "blurring" of the curve, making the dip expected at  $20^\circ$  hardly visible. This blurring might be due to the contribution of multiple scattering.

#### 4.3.4 The Fourier space imaging polarimeter

**Operating principle.** The basics of this instrument is illustrated in Fig. 4.14. As described in any optics textbook, a lens focuses an incident parallel beam in its forward focal plane into a point at the intersection of the focal plane and a line parallel to the beam and crossing the lens in its center. The same happens for a parallel beam propagating in the reverse direction, and which is focussed in the back focal plane.

This well known description of the focussing lens properties makes use of geometrical optics. In the wave description of light, these properties can be recast as follows: in the paraxial approximation, for any beam travelling in the "forward" direction the field in the forward focal plane is the Fourier transform of the field in the back focal plane, and vice versa, of course, for any beam propagating in the opposite direction. This is why the focal planes are also called FT (for Fourier transform) planes.



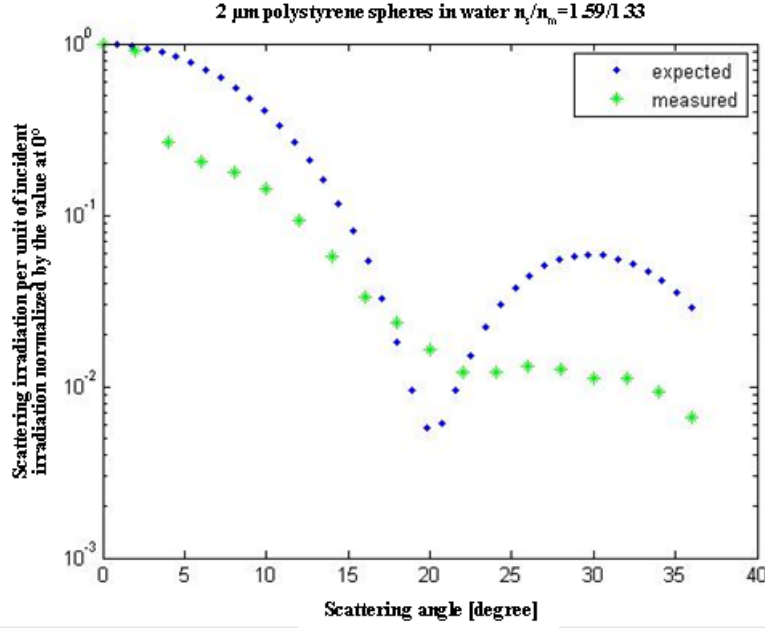


**Figure 4.13:** Goniometric polarimeter measured (green crosses) and expected (blue dots) angular distributions from the tissue phantom in the HH polarization states.

As a result, the lens maps the incident light angular distribution into its back focal plane, where it can be conveniently visualized by a 2D detector such as a CCD camera. Depending on the respective sizes of the image in the forward FT plane and of the 2D sensor of the camera, an imaging system with the appropriate magnification may be inserted between the FT plane and the CCD sensor. Moreover, for polarimetric measurements a PSG and a PSA may be inserted in the illumination and detection arms respectively.

In the paraxial approximation, assuming the emitting part of the sample is small with respect to the lens diameter, the angular range  $[-\alpha_m, \alpha_m]$  which can be mapped by a lens with focal length  $f$  and diameter  $D$  is defined by

$$\alpha_m = \arctan\left(\frac{D}{2f}\right) \quad (4.10)$$

which yields  $\alpha_m = 26.6^\circ$  for the lens used in the following, with  $D = f = 25.4$  mm.

**The setup.** The complete Fourier space imaging polarimeter is schematized in Fig. 4.15. Fig. 4.16 shows a photo of the setup.

This setup comprises all the elements cited above, namely a HeNe laser, a PSG, a PSA, a FT lens, an imaging lens LI and a CCD. Due to space limitations on the breadboard, the setup has been folded with two mirrors (M1 and M2). The lens LI was chosen and positioned in order to demagnify the FT image by a factor of 8.8, to match the 2.9 mm height of the CCD sensor. Moreover, a beam de-expander has been added before the mirrors, to reduce the size of the illuminated zone. This beam de-expander is a telescopic setup, comprising a 500 mm focal length plano-convex lens and a 10X microscope objective, whose focal length is 18 mm. As it is well known, such a system decreases the beam size, but increases the beam divergence by the same factor, so that

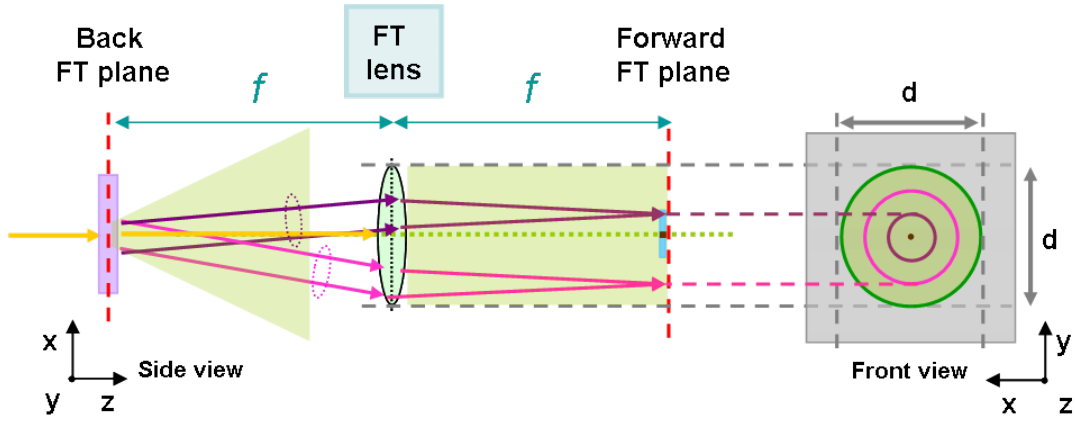


**Figure 4.14:** Principle of Fourier Imaging. *Left:* side view, showing the paths of incident parallel beams getting focussed in the forward Fourier plane. *Right:* front view of the image in the Fourier plane, showing the 2D angular intensity distribution seen by an observer looking into the  $-z$  direction.

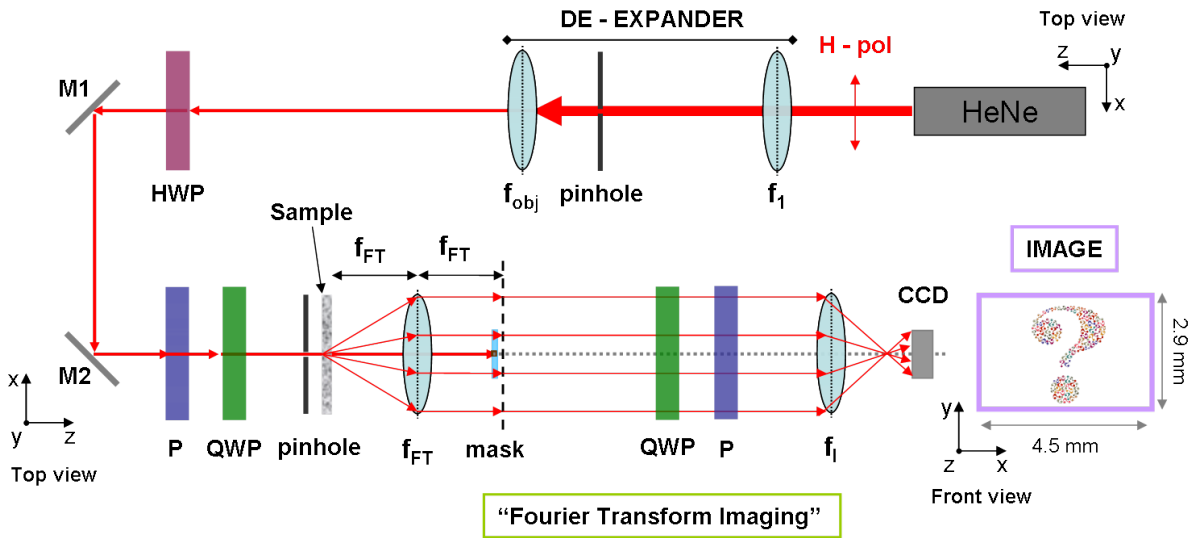


**Figure 4.15:** Scheme of the complete Fourier imaging polarimeter. This figure is a top view of the setup, excepted the image at the bottom right, which is shown in front view.

in the far field the beam size may actually *increase*. To reduce this divergence, a  $35\ \mu\text{m}$  diameter pinhole was added at the common focal point of the 500 mm front lens and the microscope objective. Another pinhole was added just before the sample, to reduce the beam size to about 1 mm on the sample.

**Angular calibration.** In order to obtain accurate calibration of the position of the CCD sensor as a function of the angle of the incoming beam we used a glass wedge set at the sample position to deviate the beam by a known angle, in this case  $10^\circ$ . The wedge was mounted on a rotation stage, thus allowing to vary the azimuthal angle at constant polar angle.

Fig. 4.17 shows a composite image obtained by superimposing eight images taken with the wedge rotated by  $45^\circ$  between two successive acquisitions, and a scattering sample providing an angular distribution which can be considered as uniform over the relevant angular range. This image shows a halo whose radius is 1.6 times that of the

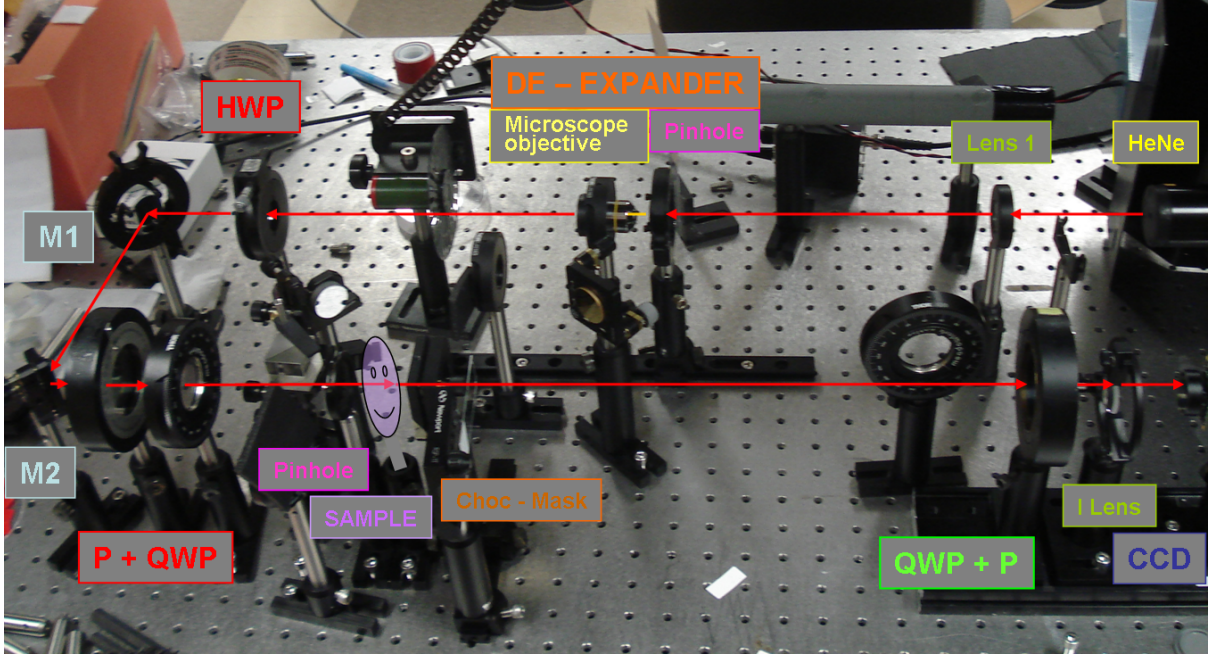


**Figure 4.16:** Photo of the complete Fourier imaging polarimeter.

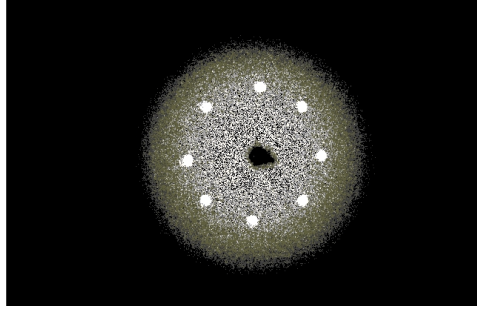


**Figure 4.17:** Superposition of the CCD images taken with a uniform scatterer or with a wedge deviating the beam by  $10^\circ$  set at eight equally spaced azimuths.

circle defined by the eight bright spots, corresponding to a polar angle equal to  $10^\circ$ . The accessible angular range is thus limited to  $16^\circ$  and not  $26.6^\circ$  as expected. This limitation is certainly due to a vignetting effect related to the diameter of LI lens, which was the largest available for the relevant focal length. We thus decided to proceed with this limitation.

**Polarimetric calibration.** The Fourier imaging system was characterized polarimetrically, by measuring the polarimetric matrix of air, without and then with the FT lens. These matrices are shown in Figs. 4.18 and 4.19.

In both cases, we expected  $HQ = PU = RV = 1$  and  $VQ = MU = LV = -1$  as the only non-vanishing elements. Without the FT lens, the maximum error, close to 5 % occurs in the MQ element. With the lens inserted the maximum error, of the order of 8 % affects LQ and LU. As for the overall intensities, the values measured for P and M incident states are one-third to one-half of the other values: this is due to the setting of the HWP, which leaves the light incident on the PSG in the H polarization, while the first polarizer is rotated to  $45^\circ$ .

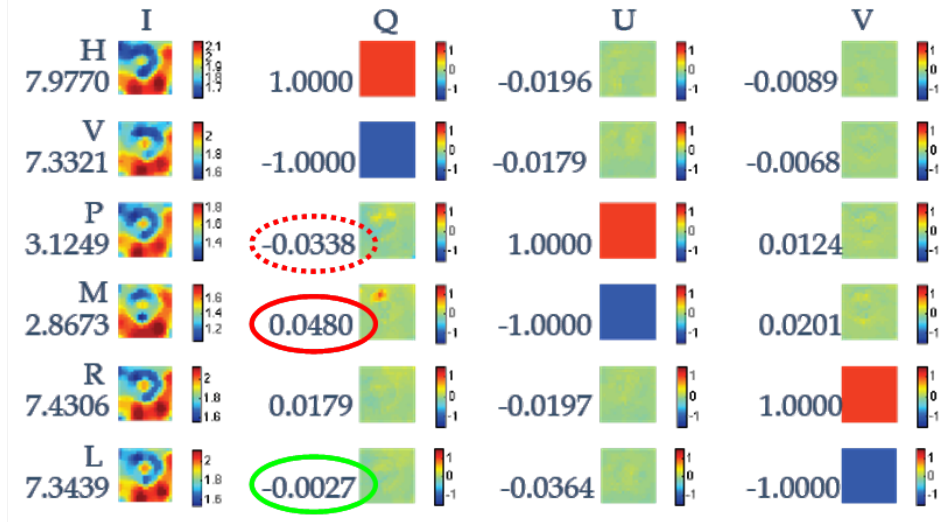


Figure 4.18: Polarimetric matrix of air measured with the FT lens removed.

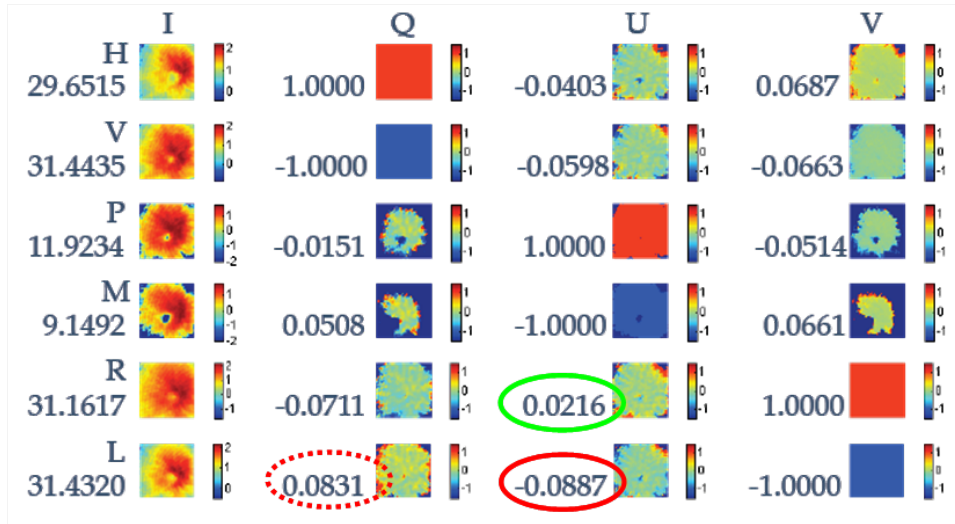


Figure 4.19: Polarimetric matrix of air measured with the FT lens inserted.

### 4.3.5 Results

**Microspheres.** We first measured the polarimetric matrix of the aqueous suspension of polystyrene spheres described above (subsection 4.3.1). The matrix is not complete, as the input M and L states have not been included. These data have also been simulated by Pr. Steven Jacques' Monte Carlo code. Measured and simulated data are shown in bottom and top panels of Fig. 4.20, respectively.

The ring structure visible in these simulations is not found in the experiments. However, the simulations were actually carried out for a total angular range equal to  $45^\circ$ , corresponding to a maximum polar angle of  $22.5^\circ$  from the sample normal. We already saw that the experimentally accessible total angular range is  $16^\circ$ , due to a vignetting effect at the imaging lens. Moreover, in the simulations the considered polar angle is defined *within the sample*, while in the experiments the polar angle is measured *outside the sample*. As a result, the refraction from water to air has to be taken into account (the effect of the parallel glasses is negligible at the considered angles), resulting in an angular magnification of 1.33. Thus the accessible angular range within the sample is reduced by



the same factor, and is then equal to  $16^\circ/1.33 \approx 12^\circ$ . This range is materialized in the top left panel of Fig. 4.20 as white squares. Even though the experimental data are noisy and show some centering defaults and possibly other systematic errors the main patterns are visible (with, however, opposite signs in all elements but HQ, VQ, PU and RV, certainly due to different conventions in the measurements and the simulations). The scales for these four elements are explicated by green or yellow arrows and by corresponding square frames around the images.

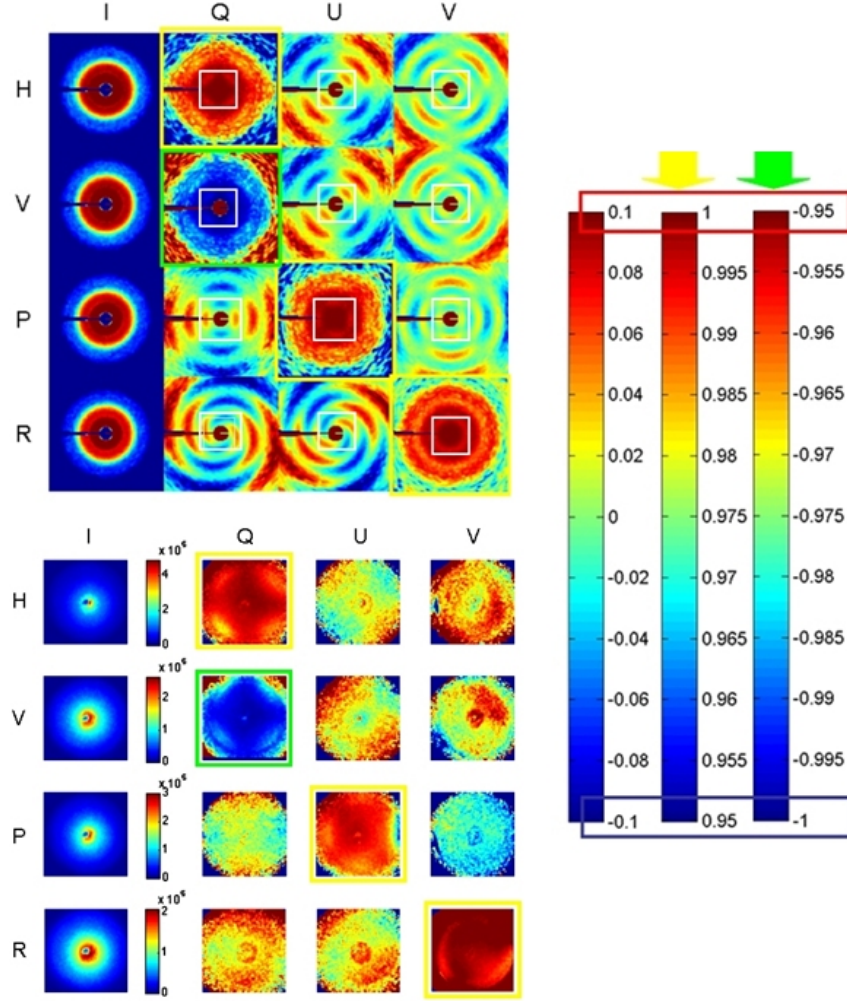


**Figure 4.20:** Partial polarimetric matrix of the sphere polystyrene suspension. *Top left panel:* simulations for an internal  $45^\circ$  angular range. *Bottom left panel:* measurements on an external  $16^\circ$  angular range. The colorbars on the right define the scales of the HQ, VQ, PU and RV elements for both images. The white squares in the simulations indicate the experimentally accessible ranges.

**Honey.** Honey is measured in the polarimeter to see the effect of optical activity (circular birefringence) on scattering. The honey is poured into a 3 cm fused quartz cuvette. Optical activity causes linearly polarized light to rotate and the amount of rotation is referred to as "optical rotation". The optical rotation due to the honey sample was measured by sending in linearly polarized light and rotating the analyzer to minimize the signal (which is easier than rotating to maximize the signal). The optical rotation is consistently  $7^\circ$  for multiple linear polarization states, meaning H is attenuated with the

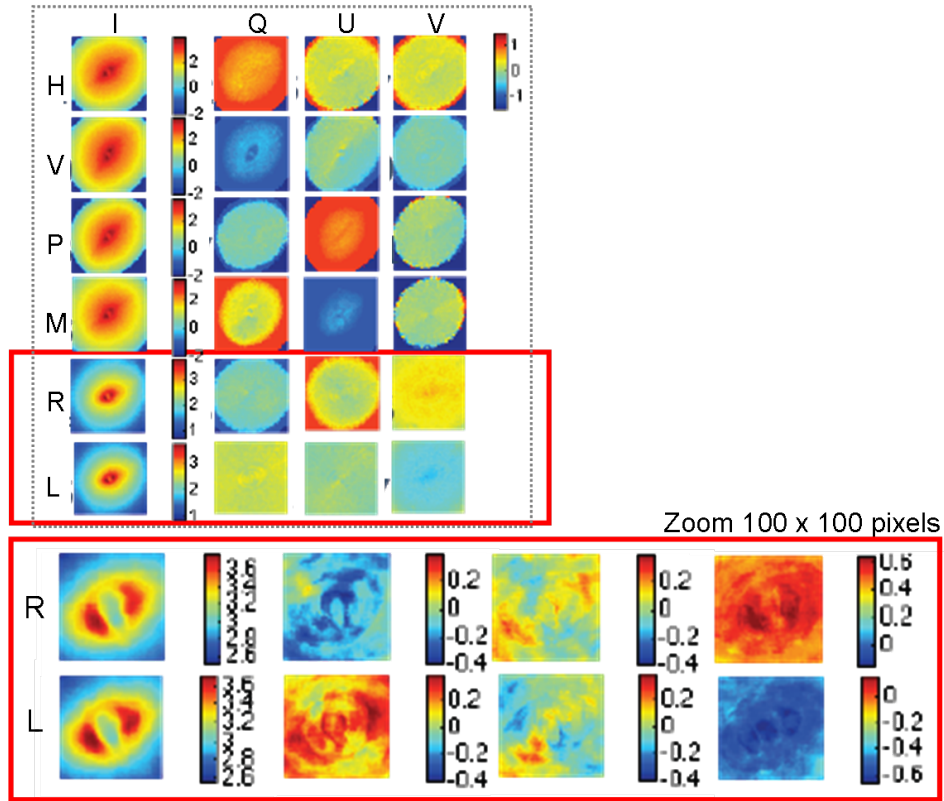


**Figure 4.21:** Measured complete polarimetric matrix of honey.

polarizer at  $97^\circ$  instead of  $90^\circ$ ; V is attenuated at  $7^\circ$  instead of  $0^\circ$ , and so. Fig. 4.21 shows the measured I, Q, U, V, where Q, U, V are normalized, for six input polarization states. Scattering occurs within the honey sample itself, perhaps from small air bubbles or honey crystals. The measurements with R and L incident show a particularly interesting pattern, suggestive of a rotated version of the simulated pattern shown in the previous section. The figure below zooms in the center  $100 \times 100$  pixels for the R and L rows, scaled for enhanced contrast.

From the first figure, note the significant depolarization when R and L are incident. For comparison, Fig. 4.22 shows the same data, but with Q, U, V vector normalized by the degree of polarization.

Further analysis of the data suggested the presence of linear birefringence in addition to optical activity (circular birefringence). Linear birefringence changes R and L circular polarization states, while optical activity does not. Therefore, by analyzing the I, Q, U, V vectors with R and L incident, the effect of linear birefringence can be isolated. One method of quantifying the change in polarization state is to compute the "Stokes rotation". The Stokes rotation is the angular distance between the input and the exiting Stokes vectors on the Poincaré sphere (see subsection 1.4.2).

Let us recall that the axes Q and U, representing H and V, and P and M respectively, form the equatorial plane of the sphere, while V, representing R and L, is its polar axis. The Stokes rotation in the equatorial plane is equal to twice the optical rotation. For example, the optical rotation from H to P is  $45^\circ$ , while the Stokes rotation between H to P is  $90^\circ$ . To measure the Stokes rotation, the dot product is computed between the input and the output polarization states. The dot product is proportional to the cosine of the angular distance, or Stokes rotation, between two vectors. To compare the input

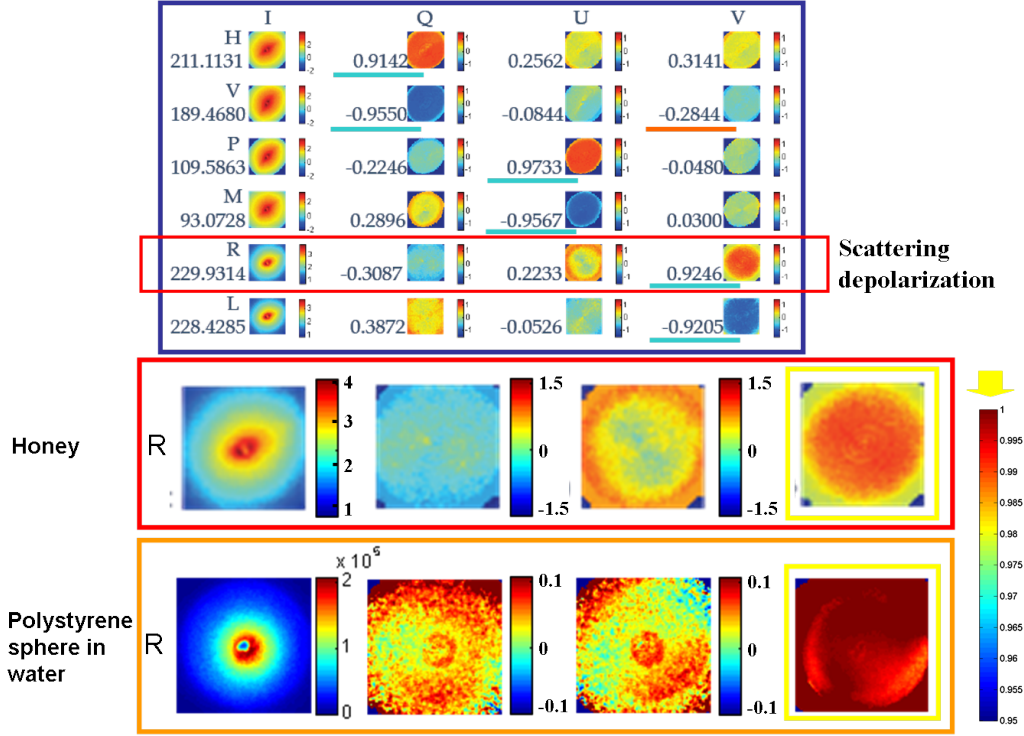


**Figure 4.22:** Measured polarimetric matrix of honey normalized by the degree of polarization. Comparison with the R row of the measured polarimetric matrix for the polystyrene sphere suspension described above.

and the output Q, U, V, the elements Q, U, V are normalized by the vector amplitude, such that  $\sqrt{Q^2 + U^2 + V^2} = 1$ . Then the inverse cosine of the dot product is computed to solve for the angular distance. Fig. 4.23 shows the results as a function of scattering angle for R (on the left) and L (on the right) incident polarization states.

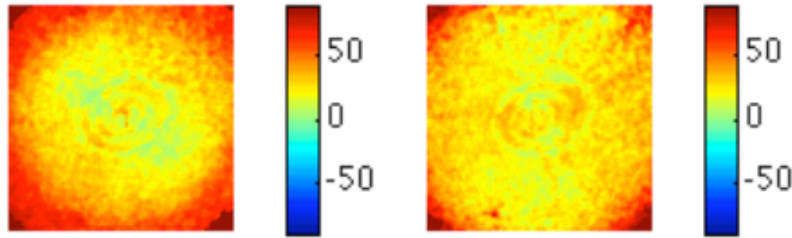


**Figure 4.23:** Rotation of the Stokes vectors on the Poincaré sphere for R (left panel) and L (right panel) input polarization states.

Note the rings as well as a rotating Maltese cross pattern. The mean rotation, considering only the center 100 x 100 pixels, for R and L is 18.9° and 22.5°, respectively.

While the optical rotation (circular birefringence) of 7° should influence all linear polarization states (H, V, P, M) equally (in fact we measure optical rotation for H and V incident as equal and we suppose to be the same for P and M incident –optical rotation does not affect R and L) the influence of linear birefringence depends on the axis of rotation. We thus have to measure the Stokes rotation for all incident polarization states (H, V, P, M, R, L). Both linear and circular birefringence show up simultaneously for each linear polarization state while measuring the Stokes rotation for circular polarization

states provides linear birefringence only, because optical rotation does not affect R and L.

As outlined in subsection 1.4.2, the action of a homogeneous retarder on the Poincaré sphere is a rotation by an angle  $\delta$  around an axis passing by the points on the sphere surface corresponding to the two orthogonal polarization eigenstates. The angle  $\delta$  is nothing else but the retardation between the two eigenstates.

Calling  $\mathbf{R}$  the unit vector defining one of the two eigenstates on the surface of the Poincaré sphere, for small enough values of  $\delta$  an incident Stokes vector  $\mathbf{S}^i$  is transformed into:

$$\mathbf{S}^o = \mathbf{S}^i + \delta \mathbf{R} \times \mathbf{S}^i \quad (4.11)$$

where " $\times$ " stands for the cross product of the two vectors. Actually, for all cases relevant to this study the retardations to be considered are small enough for the Eq. (4.11) to be valid.

The unit vector  $\mathbf{R}$  can be decomposed into

$$\mathbf{R} = \cos \chi \mathbf{R}_L + \sin \chi \mathbf{R}_C \quad (4.12)$$

where  $\chi$  is the ellipticity of the retarder eigenstates, while  $\mathbf{R}_C$  and  $\mathbf{R}_L$  are respectively the projections of  $\mathbf{R}$  on the polar axis and the equatorial plane of the Poincaré sphere. Thus these unit vectors represent the circular and linear retarders "embedded" in  $\mathbf{R}$ .

For circular input polarizations (R or L) the Stokes vector  $\mathbf{S}^i$  is parallel to  $\mathbf{R}_C$ . In this case the cross product of the input and output Stokes vectors is:

$$\mathbf{S}^i \times \mathbf{S}^o = \delta \cos \chi \mathbf{S}^i \times (\mathbf{R}_L \times \mathbf{S}^i) \quad (4.13a)$$

$$= \delta \cos \chi [(\mathbf{S}^i \cdot \mathbf{S}^i) \mathbf{R}_L - (\mathbf{S}^i \cdot \mathbf{R}_L) \mathbf{S}^i] \quad (4.13b)$$

$$= \delta \cos \chi \mathbf{R}_L \quad (4.13c)$$

and thus the azimuth of  $\mathbf{R}_L$  in the equatorial plane of the Poincaré sphere is given by that of  $\mathbf{S}^i \times \mathbf{S}^o$ . Fig. 4.24 shows the direction of  $\mathbf{R}_L$  as a function of the scattering angle, in the central region (100 x 100 pixels) of the FT image, for R (on the left) and L (on the right) input polarizations. This azimuth varies between  $-180^\circ$  and  $-90^\circ$ , corresponding respectively to the V and M states (or yL and ML in Fig. 1.4). Moreover, the dependence of the  $\mathbf{R}_L$  azimuth is reversed when the input polarization is switched from R to L.

The symmetric scattering dependence of the rotation axis for R and L suggests that linear birefringence may not effect the average optical rotation over scattering angle (averaging the Stokes rotation for R and L we obtain 0, approximately, which makes sense as it is the measure for the linear birefringence, but not for optical rotation. Thus averaging Stokes rotation measurements we eliminate the effect of linear birefringence and get the exact Stokes rotation as twice the optical rotation). The mean Stokes rotation considering the center 100 x 100 pixels is  $22.4^\circ$  and  $21^\circ$  for H and V and  $14.7^\circ$  and  $14.6^\circ$  for P and M. Assuming the effect of linear birefringence is negligible when averaging over scattering angle, the Stokes rotation should be twice the optical rotation. Half the average Stokes rotation for P and M is equal to the measured optical rotation  $7^\circ$  within



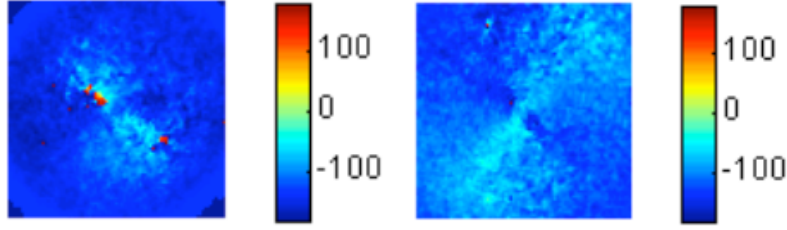


**Figure 4.24:** Azimuth of the linear birefringence vector  $\mathbf{R}_L$  on the equator of the Poincaré sphere as a function of the scattering angle, for R (*left panel*) and L (*right panel*) input circular polarizations.

experimental error, while half the average Stokes rotation for H and V is between  $10^\circ$  and  $11^\circ$ ,  $3^\circ$  to  $4^\circ$  different from the measured optical rotation.

The error in the measurement for H and V may be due to an error in shifting the raw images. To calculate I, Q, U and V the raw images are subtracted from one another. Unfortunately, due to the system tilt that changes with orientation of polarizers and wave plates, the images need to be shifted in software in order to be properly aligned.

**Tendon.** A central goal of our project was to measure the polarization scattering properties of tissue. To this end, we collected data from a thin piece of leg of tendon from mice.

As a test of the system, data were collected from the tendon in three different orientations  $0^\circ$ ,  $22.5^\circ$  and  $45^\circ$  (the sample is mounted on a rotation gear). Fig. 4.25 are the measured I, Q, U, and V for six input polarization states as the tendon is rotated from  $0^\circ$  to  $45^\circ$ .

As before with honey, the Stokes rotation between the incident and the exiting Stokes vector can be computed. Fig. 4.26 show the Stokes rotation for H, V, P, M, R and L as the tendon rotate from  $0^\circ$  to  $45^\circ$ . Note that when the tendon is oriented vertically, the H and V states do not change, but P, M, R and L rotate on the Poincaré sphere by approximately  $180^\circ$ . Similarly, when the tendon is oriented at  $45^\circ$ , P and M do not change, but H, V, R and L rotate of  $180^\circ$ . When the tendon is rotate at  $22.5^\circ$ , H, V, P and M rotate approximately  $90^\circ$  and R and L rotate  $180^\circ$ . These measurements are consistent and suggest that the tendon behaves like a half wave linear retarder.

## 4.4 Real space Mueller imaging of thick tissues

### 4.4.1 Overview of this activity

These images have been taken within a collaboration aimed at using polarimetric imaging to enhance the visualization of cancerous or precancerous (dysplastic) regions of the uterine cervix. This examination, also called *colposcopy*, is notoriously difficult and requires a great experience to localize the dysplastic lesions, the best locations for biopsies and the boundary of surgical removal of the pathological tissue. More details are given in the following.

This collaboration, funded by ANR (the French National Agency for Research) involved the following partners:

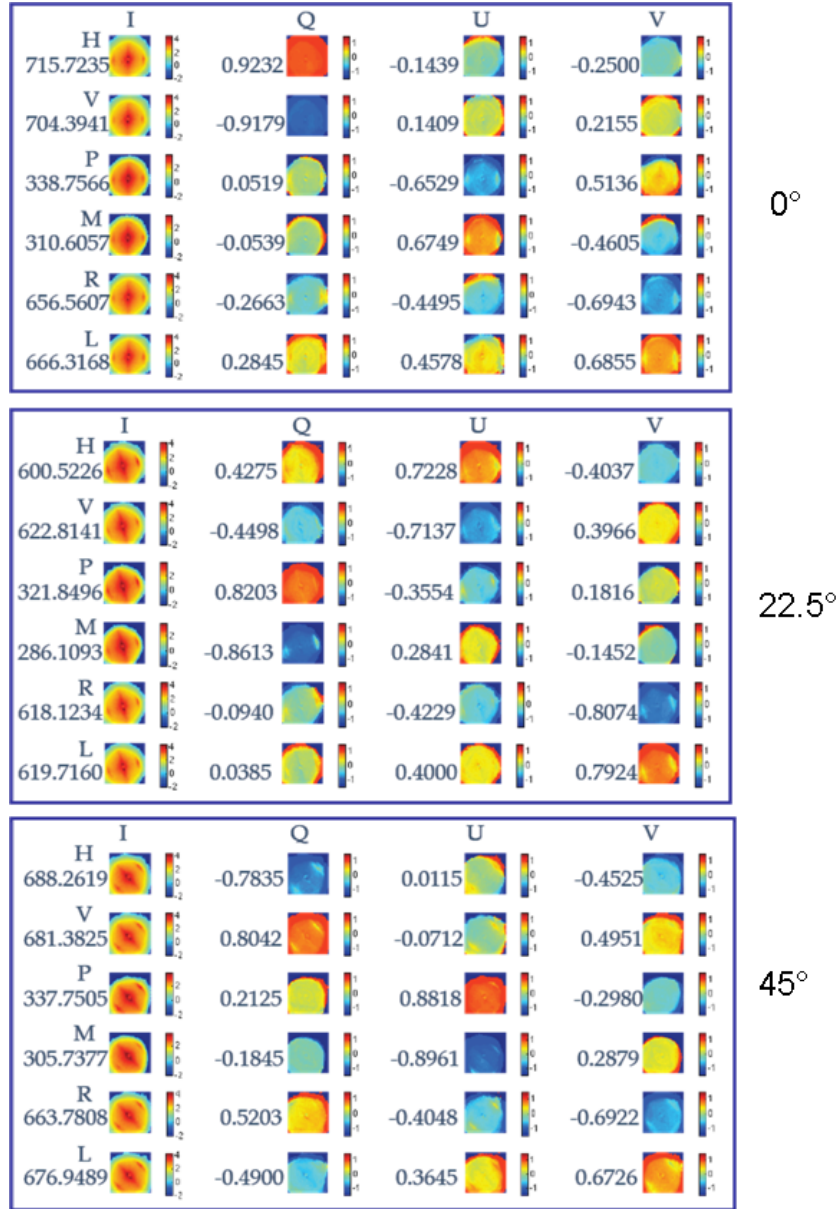


**Figure 4.25:** Polarimetric images of tendon oriented at  $0^\circ$ ,  $22.5^\circ$ ,  $45^\circ$

- the Laboratoire de Physique des Interfaces et des Couches Minces (LPICM), for the developments of a first polarimetric colposcope, based on OSC imaging,
- the Institut Mutualiste Montsouris (IMM), an hospital located at the south of Paris, and which has been involved in two ways: the *in vivo* examination of 145 patients in a clinical trial of the OSC colposcope carried out at the Gynaecology Department and the examination of *ex vivo* tissues (conizations and colon samples) at the Pathology Department,
- the Laboratoire des Sciences de l'Image, de l'Informatique et de la Télédétection - Télédétection, Radiométrie et Imagerie Optique (LSIIT - TRIO), at Louis Pasteur University of Strasbourg, to develop new techniques, based on Bayesian approach, for the treatment of polarimetric images,
- the Biomedical Statistics Department at la Pitié-Salpêtrière, another hospital in

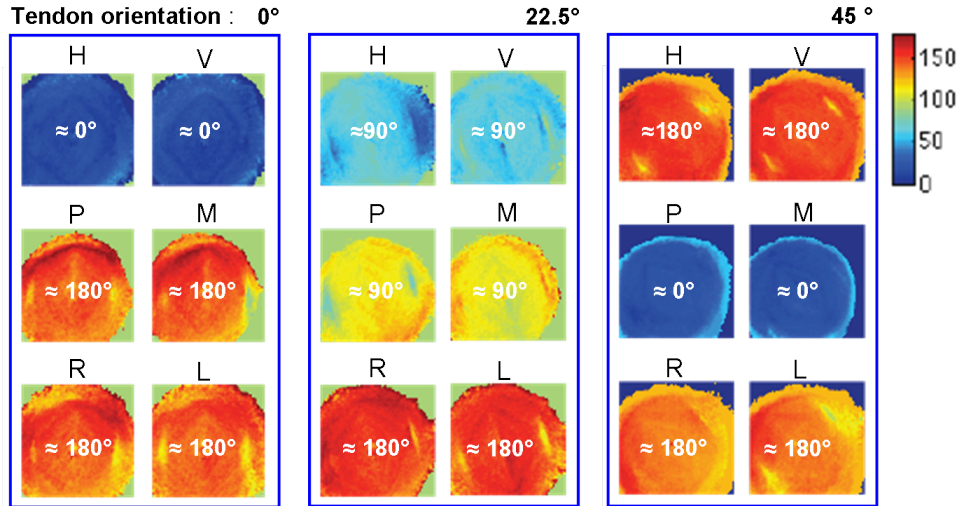


**Figure 4.26:** Stokes rotation for H/V, P/M, R/L

Paris, for the monitoring of the clinical trial and the statistical treatment of the acquired data on biopsies and conizations.

- the company Horiba Jobin Yvon, which has been running a long term collaboration with LPICM for the development of ellipsometric and polarimetric instrumentation, for a possible industrialization of the instruments developed during this project.

Here we will briefly describe the imaging polarimeter used at the IMM Pathology Department to examine the *ex vivo* samples, and typical results obtained on these samples, essentially by Dr. Angelo Pierangelo.

#### 4.4.2 The Mueller imaging polarimeter

This instrument is schematized in Fig. 4.27. The sample is illuminated by a halogen source, via a bunch of optical fibers, a diffuser and a condenser. The image is acquired by a CCD with 256 x 256 pixels, equipped with a zoom lens which allows to vary the field of view from 2 x 2 to 6 x 6 cm<sup>2</sup> approximately. Before the zoom, a close-up lens is used to form a virtual image at a large enough distance from the lens to allow easy focussing. Interference filters are used to acquire quasi-monochromatic images, at wavelengths varying between 500 and 700 nm in steps of 50 nm, with a bandwidth equal to 20 nm full width half maximum.

The polarization modulation and analysis are performed by a PSG and a PSA which both comprise a linear polarizer and two nematic liquid crystal (NLC) cells, which act as variable retarders. Each NLC cell features an electrically controlled linear retardation between slow and fast axes whose orientation is constant. The PSA is the mirror image of the PSG, with the linear analyser placed after the NLCs. The angles  $\theta_1$  and  $\theta_2$  defining the orientations of the NLCs fast axes with respect to the polarizer transmission axis in the PSG have been chosen so that with a suitable choice of the NLC retardations the PSG can sequentially generate four polarization states whose Stokes vectors are at the tips of a regular tetrahedron on the Poincaré sphere. The same applies to the PSA, which projects the Stokes vector to be analyzed onto another set of four states with their Stokes vectors at the tips of a regular tetrahedron. This choice has been shown [65, 66, 67] to optimize the noise propagation from raw data to the corresponding Mueller matrix: for a

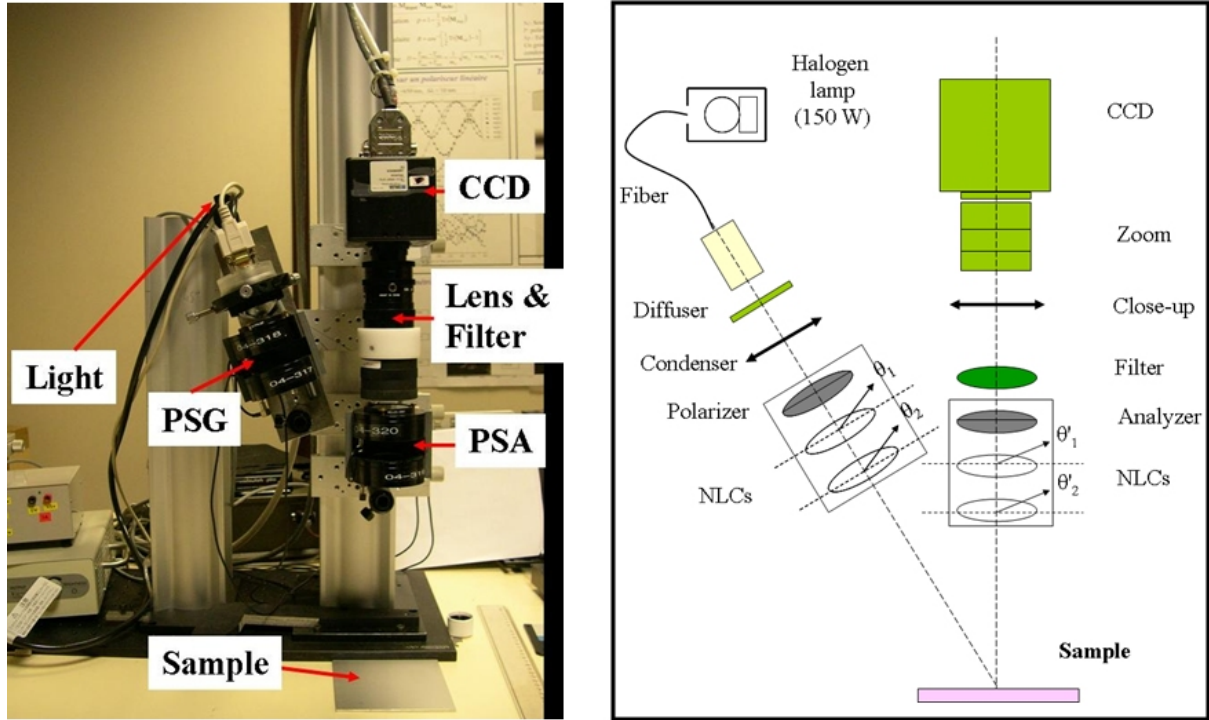


**Figure 4.27:** Photo (*left*) and scheme (*right*) of the full Mueller imaging system installed at the IMM Pathology Department.

given noise level on the raw images, the noise on the Mueller images is minimized. More information on similar NLC based polarimeters is reported in [68, 69].

However, with this choice all the polarization basis states of the PSG and PSA are elliptical, so that the Mueller matrix cannot be extracted from the raw data by simple relationships as it was the case for the two polarimeters described so far. Actually, if we consider the four basis states of the PSG as the column vectors of a matrix  $\mathbf{W}$  (usually called the modulation matrix of the PSG), and the basis states of the PSA as the line vectors of the analysis matrix  $\mathbf{A}$ , then the 16 raw data are the elements of a  $4 \times 4$  real matrix  $\mathbf{B}$  given by

$$\mathbf{B} = \mathbf{A}\mathbf{M}\mathbf{W} \quad (4.14)$$

where the  $\mathbf{M}$  is the Mueller matrix of the sample. This matrix can thus be calculated from the raw data by inverting  $\mathbf{A}$  and  $\mathbf{W}$  provided these matrices are known, i.e. the system is *calibrated*.

The calibration of a system like the imaging polarimeter we are describing is a very difficult task by the usual approach involving a detailed model of the instrument, as this system is a "stack" of many elements, each of which may introduce serious artefacts which may be difficult to understand and model properly.

A very different approach has been followed at LPICM [70] to develop the eigenvalue calibration method (ECM), which has been successfully used on many different Mueller polarimeters. Without getting into details, which would be outside the scope of this manuscript, this method can accurately retrieve the matrices  $\mathbf{W}$  and  $\mathbf{A}$  from four measurements on calibration samples by linear algebra techniques, without any modelling of the instruments. Moreover, the calibration samples are not very specific (typically one



can use linear polarizers, retardation plates other than half wave) and do not need to be accurately known, as they are characterized during the calibration procedure itself. Of course, our imaging polarimeter was calibrated at each wavelength by using ECM, and provided polarimetric images with a typical maximum error of the order of 0.02 to 0.03 on the normalized elements  $M_{ij}^* = M_{ij}/M_{11}$ ,  $i, j = 1..4$   $i \cdot j \neq 1$ .

If the calibration process is somewhat time-consuming (about 2 hours for the seven wavelengths, to be repeated typically every two days) the measurement of a full Mueller image takes about 10 seconds.

### 4.4.3 Typical results on cone biopsies

**Overview of the anatomy and pathology of the uterine cervix.** The innermost part of the cervix (the *endocervix*) is covered by a *columnar epithelium*, which exudes the cervical mucus, while the outer part (the *exocervix*) is coated by *malpighian epithelium*, typically 300  $\mu\text{m}$  thick. These epithelia are separated from the underlying connective tissue by the *basal membrane*, covered by a layer of cells which normally proliferate slowly to provide young cells which get differentiated while migrating towards the surface and regenerating the tissue.

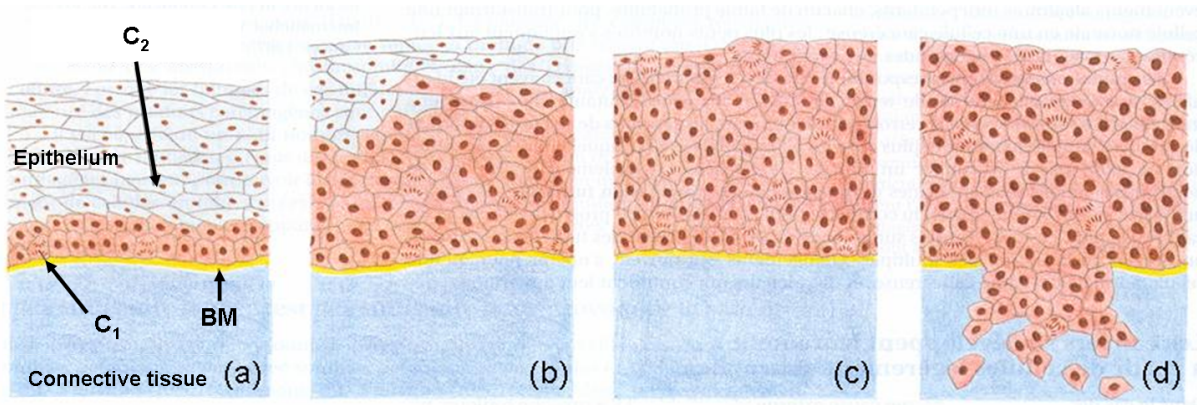


**Figure 4.28:** Outline of the evolution of cervical cancer. (a): CIN I. BM: basal membrane,  $C_1$ : proliferating cells at the basal membrane,  $C_2$ : differentiated cells, with condensed nuclei; (b): CIN II; (c): CIN III; (d): Invasive cancer.

The evolution of a cervical cancer is schematized in Fig. 4.28. The cell proliferation at the basal membrane increases, and the young cells migrate towards the surface without undergoing the normal differentiation process: in particular, their nuclei remain larger than those of normal epithelial cells, a feature which is used by pathologists to identify the anomalous cells and to determine the thickness of the invaded epithelium.

The disease is staged as follows: when the invaded thickness  $h_i$  is less than one quarter of the total epithelium thickness  $h_e$ , the disease is called CIN I, which means "*Cervical Intraepithelial Neoplasia*", at its first stage. When  $h_e/3 \leq h_i \leq 2h_e/3$ , the disease is at stage CIN II. When epithelium is totally invaded but the basal membrane is still intact, the stage is CIN III. Subsequently, the malignant cells perforate at the basal membrane and invade the underlying connective tissue. The disease then becomes an *invasive cervical cancer*, which can metastasize and may be lethal.

Fortunately, this evolution is very slow: it typically takes 10 years for untreated patients to evolve from CIN I to invasive cancer. As a result, the detection of anomalous cells by the Pap smear (or Papanicolaou test) procedure can be very efficient. In case of

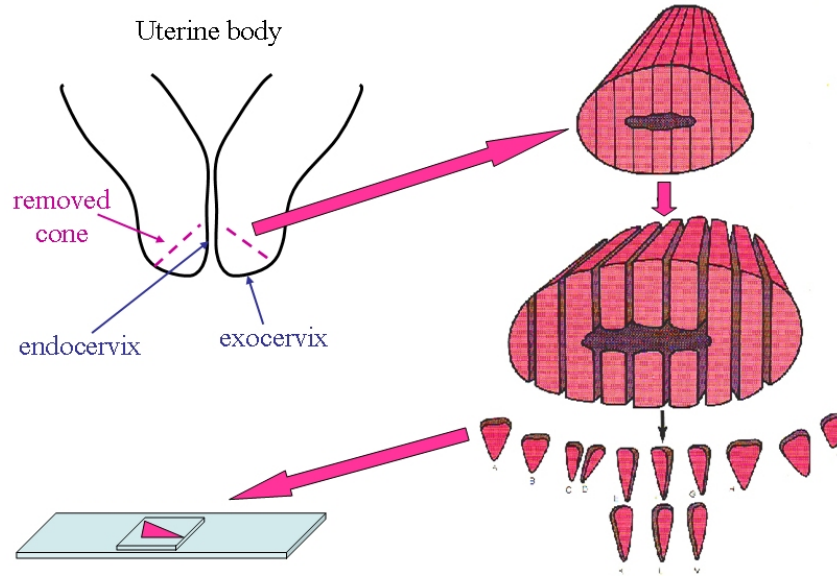


**Figure 4.29:** Surgical removal of a cone at the front end of uterine body (*top left*) and subsequent processing (*right and bottom left*).

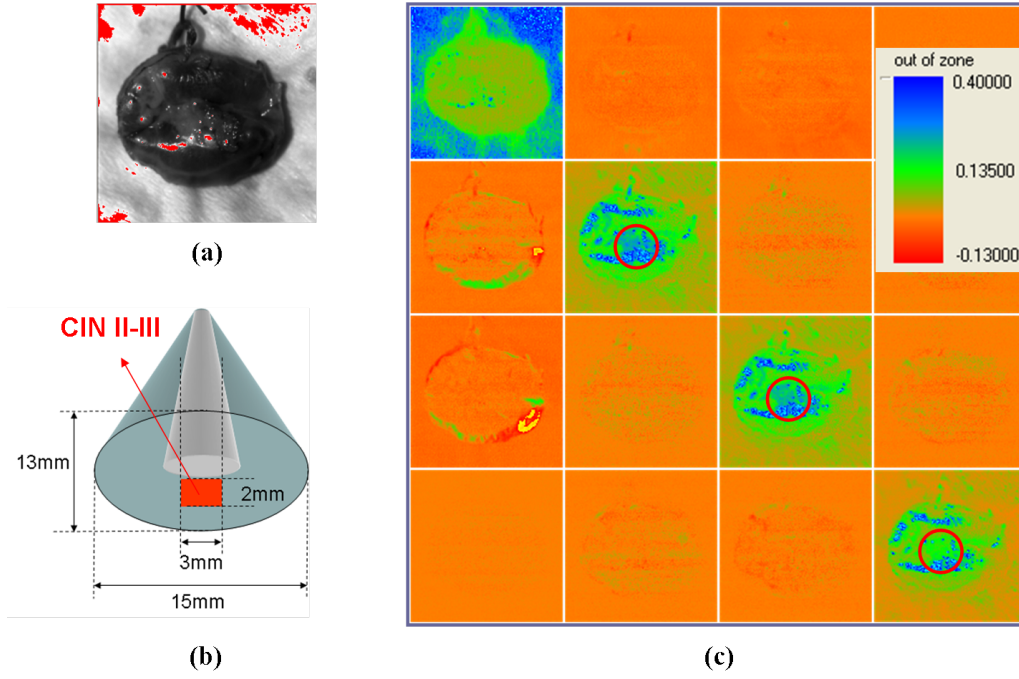
positive result, the cervix is examined with a binocular magnifying system (*colposcope*) to localize the anomalous zones, if any, and take small biopsies for further confirmation by a pathologist. Again, if the result is positive (or if the Pap alone suggests that there may be an anomalous zone in the endocervix, which cannot be visualized by colposcopy) a *cone biopsy* is taken from the front part of the cervix, to remove the anomalous zones and thus cure the disease. Overall, the mortality of women which comply with this procedure is about 70% lower than that of women who don't. This technique is by far the most efficient cancer prevention based on systematic screening.

The cone biopsies are typically 2 cm in diameter, while their height varies from less than 1 cm to 2 cm. After removal, they are fixed in formalin and cut into a few millimeter thick slices. Then their water content is substituted by paraffin and very thin (about 5  $\mu\text{m}$  thick) cuts are taken from each slice, stained and examined by standard optical microscopes. This procedure is summarized in Fig. 4.29.

During the colposcopic examination the cervix is stained by diluted acetic acid first and then by iodine. Anomalous regions get whiter with acetic acid, and are not stained by iodine. However, besides CIN, many different benign lesions may occur, such as hyperkeratosis, metaplasia or ectropion. As a result, the diagnosis of CIN is based on visual appreciation of subtle changes in shades, and is very operator dependent. Even experienced colposcopists may fail to detect dysplastic zones, or, conversely, may overestimate their sizes, which may lead to cone biopsies much larger than necessary, which, in turn, may decrease the mechanical strength of the cervix and endanger future pregnancies. It is therefore of high interest to develop new techniques, such as polarimetric imaging, to improve the colposcopy performance.

**Polarimetric images of *ex vivo* cone biopsies.** As a first example, we show in Fig. 4.30 a sample featuring only one anomalous zone, with a CIN II-III dysplasia.

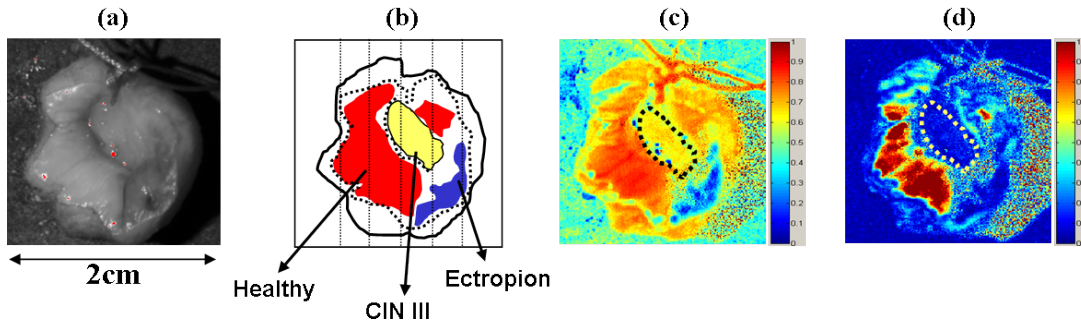
This image is essentially *diagonal*, which means that the sample behaves as a *pure depolarizer*, without any significant diattenuation or retardation. Moreover, the normalized diagonal Mueller elements  $M_{ii}^*$  ( $i = 1..4$ ) are larger in the anomalous zone than in the



**Figure 4.30:** (a): White light photo of the cone biopsy; (b): Localization of a CIN II - III lesion from pathology; (c): Mueller image of the biopsy at 550 nm, with all elements normalized by  $M_{11}$ . The scale of these  $M_{ij}^*$ ,  $i, j = 1..4$ ,  $i \cdot j \neq 1$  elements is shown by the colorbar at the upper right corner of the figure.

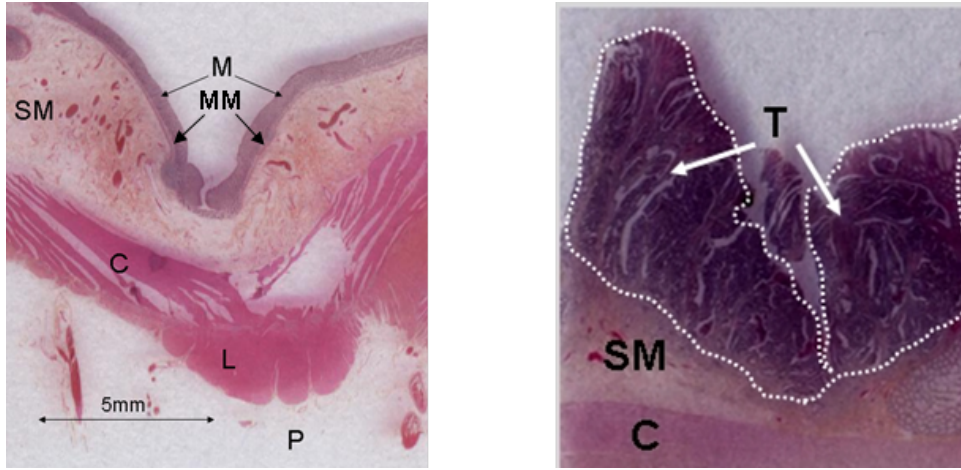
healthy regions, indicating that the CIN lesion appears *less depolarizing* than the surrounding tissue. (The other apparently less depolarizing features which look like "lines" at the top, the left part and the bottom of the sample are artefacts due to localized quasi-specular reflections which saturate the CCD). Furthermore, over the entire image we observe that  $M_{22}^* = M_{33}^* > M_{44}^*$ , indicating that the tissue behaves like an isotropic depolarizer for linearly polarized light, with a Rayleigh type response (the depolarization is stronger for circular incident polarization), suggesting that "small" scatterers or "large soft" scatterers may be dominant and may account for this Rayleigh or Rayleigh-Gans behaviour.

Fig. 4.31 shows another example of cone biopsy, with healthy tissue, a CIN III dysplasia and an ectropion. The healthy and anomalous regions have been mapped by detailed pathology examination, as shown in panel (b) of the figure. In the raw Mueller



**Figure 4.31:** (a): White light photo of the sample; (b): Mapping of the lesions, reconstructed from histological examination of slides taken along the thin vertical lines; (c): Depolarization image at 500 nm; (d): Retardation image at 500 nm.





**Figure 4.32:** *Left:* Microscopic structure of a healthy colon sample, with its different layers: the mucosa (M), the submucosa (SM), the circular muscular tissue (C), the longitudinal muscular tissue (L) and the pericolic tissue (P). The very thin muscularis mucosa (MM) separates M from SM. *Right:* microscopic structure of a pathological sample, with a budding tumor (T) invading the mucosa and submucosa, with the underlying tissues still intact. Taken from [72].

image taken at 500 nm (not shown here) the diagonal elements are still the largest, but we also observe significant non-diagonal terms, which justify a Lu Chipman decomposition. The result of this decomposition is summarized in the other panels ((c) and (d)) of the figure.

Now the healthy region still displays strong depolarization, but also clearly measurable birefringence, which was not seen in the previous example. Moreover, the presence of retardation (or possibly diattenuation) was also observed *in vivo*, with an OSC colposcope [71]. Actually, the second cone was definitely thicker than the first one, and thus, *a priori* more representative of the very thick tissue observed *in vivo*. This issue is not yet really understood and clearly requires further work.

The depolarization image could easily be segmented into three regions, with decreasing depolarization powers, corresponding respectively to healthy tissues, CIN III and ectropion. However, the retardation image proves also very useful to help distinguishing healthy from anomalous regions.

#### 4.4.4 Typical results on colon samples

**Overview of the anatomy and pathology of colon.** Normal colon tissue is organized in three layers (see Fig. 4.32). From the internal cavity, or lumen, outwards these layers are: the internal coating or mucosa, the middle coat or muscularis externa propria and the external coat or pericolic tissue (serosa). The mucosa includes a superficial thin layer of epithelium on loose connective tissue. The epithelium is a one-cylindrical-cell layer without capillaries. It receives oxygen and nutriment from the underlying connective tissue by means of exchanges through the basal membrane (BM) which separates the epithelium from the underlying connective tissue which includes capillaries [73]. The BM is a thin layer of specialized extracellular matrix (ECM) that holds the epithelium and where the healthy epithelial cells regenerate and malignant cells, if present, start proliferating. The ECM is a complex mixture of proteins and carbohydrates which aggregate to form protein molecules with short residual or without carbohydrate chains (such as



collagens and elastin) and protein-polysaccharide molecules such as proteoglycan, with much larger amounts of carbohydrates than proteins. The ECM is the main component of the loose connective tissue whose cells are embedded in an amorphous mixture of proteoglycan molecules. In particular, the loose connective tissue of the colon mucosa and submucosa layers is a mesh-like tissue with fluid matrix, whose principal constitutive protein is collagen. The mucosa is composed of a network of densely arranged very fine collagen fibrils; in contrast the submucosa is almost entirely composed of a dense network of larger collagen fibers. In healthy mucosa the average collagen fibril size is similar to that of the organelles and is of the order of a fraction of a micron. The average size of collagen fibers of submucosa is typically about few microns [74]. The inner part of this connective tissue constitutes the submucosa. The colon mucosa and submucosa layers fold themselves into finger-like shapes for the colon inner part, while for other organs (e.g. uterus) these layers remain flat. As a consequence, when the colon inner surface is observed at a certain distance, the sample may appear as "mixture" of epithelial and connective tissues with the BM close to the surface.

The muscularis mucosa (MM) is a very thin layer separating the mucosa from the submucosa and similarly to the submucosa it is composed of a network of densely packed large collagen fibers which scatter light predominantly in the forward direction [74]. Most of the light propagating into the mucosa penetrates into the submucosa. The submucosa comprises larger blood vessels compared to mucosa. As a result, the light incident on the mucosa is more heavily absorbed in the submucosa, especially in the green part of the spectrum, where the haemoglobin features the highest absorption. Hence, only a small fraction of the incident light can penetrate into the deeper layers [74, 75, 76]. Typically the thicknesses of the mucosa and submucosa are comparable. Moreover, as the muscularis mucosa is very thin and probably features a scattering behavior quite similar to that of the submucosa, in the model it will be lumped together with the submucosa into a single layer, referred to as the submucosa throughout the rest of this paper.

**Polarimetric images of *ex vivo* colon sample.** We show a typical example of Mueller image of a colon sample (see Fig. 4.33), taken from [77].

Again, this image is essentially *diagonal*. This sample comprises both healthy (bottom left) and tumoral (top right) regions (see Fig. 4.33a). At this stage of the disease (exophytic growth in the mucosa, with the underlying tissues still untouched) the tumor is less depolarizing than the healthy part, as seen previously with cone biopsies. The contrast between the two regions is clearly enhanced in the polarimetric images  $M_{22}^*$  and  $M_{33}^*$  with respect to the intensity image  $M_{11}$  (at the top left corner), showing the potential of the technique for early tumor detection (see Fig. 4.33b).

At subsequent stages, the tumor gets *ulcerated*, corresponding to a decrease of the upper tumoral layer, while the underlying tissues are progressively invaded and destroyed. Due to its dependence on the thickness of the tumoral layer as well as the nature of the tissue left intact beneath the tumor, the polarimetric response varies in a non-monotonic fashion with the advancement of the disease.

Quite generally, with increasing wavelength in the visible range the overall depolarization of thick tissues increases, due to a decrease of light absorption by hemoglobin, which in turn allows more scattering events to occur. However, multispectral Mueller imaging has shown to be very helpful for the optical staging of the tumor. As these issues are outside the scope of this manuscript, the interested reader is referred to [72, 78].

In this manuscript we present the current state of advancement of our work aimed

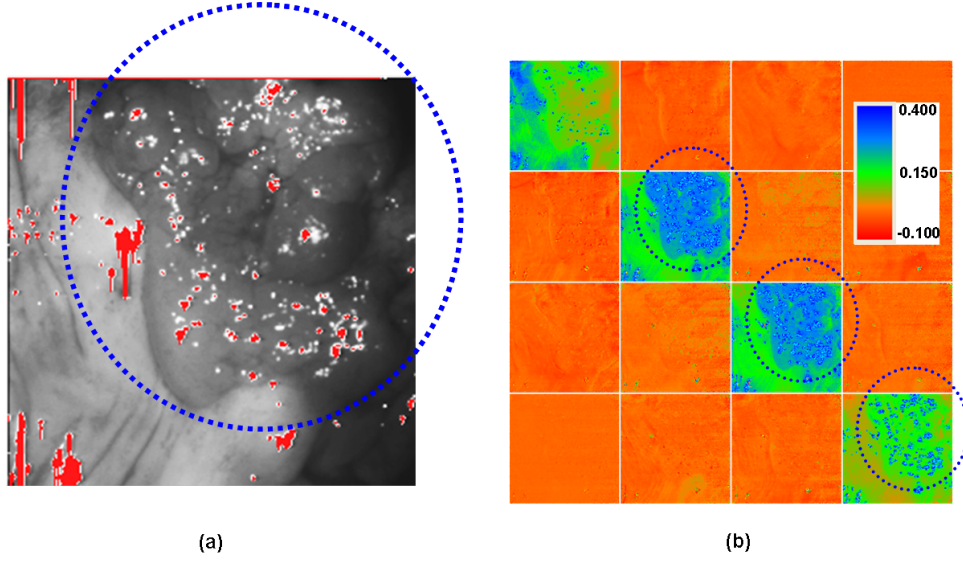


**Figure 4.33:** (a): Ordinary photo of a colon sample, showing a tumor in the area inside the circle in the upper right part of the image; (b): Normalized Mueller matrix image of the same sample. The scale of the normalized elements is given by the colorbar. The image was taken at 550 nm [72, 77].

at defining a realistic, yet tractable model of the polarimetric response of healthy and pathological colon samples.

## 4.5 Conclusion

In this chapter, divided in three main parts, we reviewed the experimental activity which have been undertaken in the course of this work.

The first part was devoted to the realization and use of an imaging polarimeter for the study of scattering samples in background scattering geometry with focussed illumination. This study was carried out at LPICM. The polarization was modulated and analysed by manually adjusting various optical components. The instrument accuracy was carefully evaluated and found to be of the order of 0.04 on the average, a quite acceptable value for the envisioned studies. This instrument was then used to characterize two suspensions of polystyrene spheres in water, with 50 nm and 1500 nm sphere radii. The expected patterns typical for Rayleigh and Mie scattering were observed and reproduced by the Monte Carlo code described in the previous chapter, a result which definitely validated this code. Moreover, simulations for large and "soft" scatterers (i.e. with a refractive index close to that of water), clearly demonstrated that in this case, which may be relevant for the light scattering by cell nuclei, the response is Rayleigh-like.

The second part was devoted to the realization and use of two angle resolved polarimeters for the study of optically thin samples where single scattering was expected to dominate. These studies were carried out during a three month stay at Oregon Healthy and Science University, in Pr. Steven Jacques' team. Both polarimeters used the same PSG and PSA, comprising linear polarizer and a quarter-wave plate, with an additional half wave plate in the PSG. Again, all these elements had to be rotated manually to sequentially generate the required polarization states. The samples were included in thin

cells to make sure that single scattering contributions were dominant.

The first polarimeter, based on a single detector on a goniometric mount, provided data over a broad angular range, but with too small signal to noise ratio for the full polarimetric measurements. However, the results obtained on aqueous suspensions of polystyrene spheres were quite close to the expectations.

The second instrument was based on the Fourier optical imaging technique: the sample is placed on the object plane of a (ideally large N.A.) lens, which maps the angular distribution of light emerging from the sample in its image focal plane. The actually implemented system provided a total angular range of  $16^\circ$ . The polarimetric accuracy was comparable to that of the first instrument, with average errors of the order of 0.05.

The polarimetric angular spectra obtained with the suspension of polystyrene spheres were again in good agreement with expectations. On a (much thicker) honey sample the optical activity was well measured, in spite of strong depolarization. Moreover, this sample exhibited linear birefringence, with an interesting (and not yet fully understood) dependence of the azimuth of the axes with the scattering angle. These measurements would have been extremely time consuming and difficult to carry out with standard goniometric systems. Finally, a sample of mice tendon was characterized, and found to behave as a half wave plate.

The third part describes selected results obtained with a full Mueller imaging system on *ex vivo* samples of human tissues. This polarimeter, which used nematic liquid crystals in its PSG and PSA, performed the acquisition of a full Mueller image in less than 10 seconds. This instrument was installed at the Pathology Department of Institut Mutualiste Montsouris and was routinely used to image various *ex vivo* samples, and more precisely uterine cervix cone biopsies and colon samples. This activity was part of a broader project aimed at developing a tool based on polarimetric imaging for enhanced visualization of cervix precancerous zones, a notoriously difficult task with current standard imaging techniques. Mueller images of cone biopsies prior to fixation in formalin showed that the healthy regions exhibit birefringence, in agreement with previous observations *in vivo* with a OSC imaging system. This birefringence disappears in anomalous zones, which behave as pure depolarizers. In these zones the amount of depolarization seems also to be a good diagnostic tool to distinguish precancerous and benign lesions.

These still preliminary results, if confirmed by further studies on a sufficient number of samples, suggest that full Mueller polarimetry (possibly with a color CCD, to get superimposable images at three wavelengths) may be a very powerful technique to identify and characterize anomalous cervix regions *in vivo*, by providing separate depolarization, retardation (and possibly diattenuation) images, while with less complete techniques, such as OSC, the corresponding information remain "entangled" in images which are then difficult to interpret.

Finally, the motivation to study colon samples is twofold. First, on such samples the cancerous lesions are much easier to localize than on cone biopsies, as they are larger and thicker, and thus provide easier to use test samples to develop theoretical models of tissue polarimetric response. Second, if polarimetric imaging proves able to provide accurate enough "optical staging" of the tumor, it could be used to make the whole pathology characterization faster and cheaper.

In this manuscript, we considered only tumors at their initial stage, with a cancerous layer "budding" over underlying intact tissue layers. The essential result is that all investigated tissues, healthy or cancerous, had a Rayleigh-like response, with a larger de-

polarization for circular rather than linear polarization. Moreover, cancerous "budding" regions exhibited a lower depolarization power than healthy regions.

These results provide the criteria used to develop a realistic modelling of colon tissue, along the lines presented in the next chapter.



# Chapter 5

## Towards a realistic model of colon tissue

### 5.1 The proposed model of *ex vivo* colon optical response

To model the propagation of polarized light in *ex vivo* colon samples we have represented such samples as multilayered scattering structures. In a first step we assumed that the mucosa and the submucosa layers consist of a surrounding medium with monodisperse scattering spheres. Due to very small thickness of the muscularis mucosa and the similarity between the muscularis mucosa and submucosa optical properties, the muscularis mucosa will be included in the submucosa layer in our model. All underlying layers were lumped into a totally depolarizing lambertian substrate. In a second step, we considered the layers with bimodal populations representing both the collagen spheres and the subcellular organelles – the most important scatterers – within each layer.

We used the description of normal colon tissue proposed in [74] to specify the characteristics of each scattering layer. The scattering spheres with radius  $r$ , and optical index  $n_s$  were embedded in an extra cellular matrix with optical index  $n_m$ . The photon mean free path  $\ell_s$  was defined as  $\frac{1}{N_s\sigma_s}$ , where  $N_s$  is the number density of scatterers and  $\sigma$  is their scattering cross-section [64]. The number density  $N_s$  was calculated from the volume fraction  $F_s$  of the scatterers (i.e. the volume occupied by scatterers per cubic centimeter of sample) as  $V_r = \frac{4}{3}\pi r^3$  is the volume of a single spherical scatterer of radius  $r$ .

All layers of the virtual sample were placed within a cylinder (diameter 1 cm, variable depth  $h$ , see Fig. 5.1a ). The lateral walls of cylinder were assumed to be totally absorbing. The bottom of cylinder was either absorbing or lambertian substrate. The diffuse illumination ( $\lambda = 633$  nm) was propagated along the axis of the cylinder.

Each single layer is thus characterized by the radius  $r$  of the scattering spheres, their number density  $N_s$ , which determines the photon mean free path  $\ell_s$ , the optical index contrast,  $m = \frac{n_s}{n_m}$ ; and the layer thickness  $h_i$ . For the layer with bimodal population, the radii, number density and optical index contrast of the two types of scatterers are different:  $r_1, r_2, \ell_{s1}, \ell_{s2}, m_1$  and  $m_2$ .

The semi-infinite lambertian substrate is a totally depolarizing, partially reflecting medium, such that the intensity of the backscattered light follows the cosine law of the polar angle  $\theta$  of the scattered light, while being uniformly distributed over the azimuthal

angle  $\phi$ . More precisely the intensity  $I(\theta, \phi)$  [ $\text{W sr}^{-1}$ ] backscattered into a solid angle  $d\Omega$  around the angles  $(\theta, \phi)$  is given by:

$$I(\theta, \phi) d\Omega = \frac{aZ_0}{\pi} \cos \theta d\Omega \quad (5.1)$$

where  $Z_0$  is the illumination power [ $\text{W}$ ] incident on the lambertian and  $a$  its albedo. This is a first approximation of the response of the underlying layers, based on the assumption of a complete randomization of the polarization and emerging direction of the backscattered photons due to a large number of scattering events.

Finally, as shown in Fig. 4.32, in dysplastic or cancerous colon tissue this structure gets disorganized and its morphology may change with respect to that of healthy tissue. In particular, in cancerous regions the surface may remain flat or may develop an exophytic growth (adenomatous polyps). The possible changes in sample morphology have also been considered in our model by deforming the multilayered structure in two different ways, as shown below.

The stochastic paths of the incident photons were simulated numerically by means of Monte Carlo algorithm. The diffuse light illumination of the sample was modelled with the photons impinging the sample surface at a random location. At each scattering event the changes of photon polarization and direction of propagation were calculated making use of the exact Mie solution for the scattering of plane wave on spherical particle. The implementation of the rejection method and flux-at-point estimation technique allowed us to accelerate the convergence of the statistical algorithm [59]. Moreover, all the Mueller matrices given in the following were obtained by integrating the photon flux over the entire sample surface.

We first performed the simulation with the single layer model varying the values of model parameters in order to identify the impact of each individual parameter on the ratio of linear to circular polarization of the backscattering light. Then we performed the simulation with the double layer model to find out if the single layer model can be considered as an approximation of the complex multilayered structure of the colon tissue.

## 5.2 Results and discussion

### 5.2.1 Multilayered structures with monodisperse scatterers within each layer

**Single layer (mucosa) on top of a lambertian.** For the principal model parameters we retained the average values given in [74]. The mucosa tissue was described as a suspension of medium collagen spheres ( $r = 200 \text{ nm}$ ) at at 12% volume fraction in physiological liquid ( $\ell_s = 53.7 \text{ }\mu\text{m}$ ,  $m = \frac{1.46}{1.38}$ ,  $h_1 = 0.5 \text{ mm}$ ). The submucosa tissue was modelled as a suspension of large collagen spheres ( $r = 1.75 \text{ }\mu\text{m}$ ), at 50% volume fraction in physiological liquid ( $\ell_s = 19.69 \text{ }\mu\text{m}$ ,  $m = \frac{1.38}{1.36}$ ,  $h_2 = 0.7 \text{ mm}$ ). No absorption (either from the medium or from the spheres) was taken into account at this point.

The value of the lambertian albedo  $a$  was chosen in order to account for the absorption by the mucosa and submucosa layers and the global contribution from the deeper layers. We considered reasonable to vary albedo  $a$  values between 0 and 0.3.

In a first instance, we considered the mucosa alone, on top of a lambertian representing the submucosa and all underlying layers (see Fig. 5.1a). With nominal values

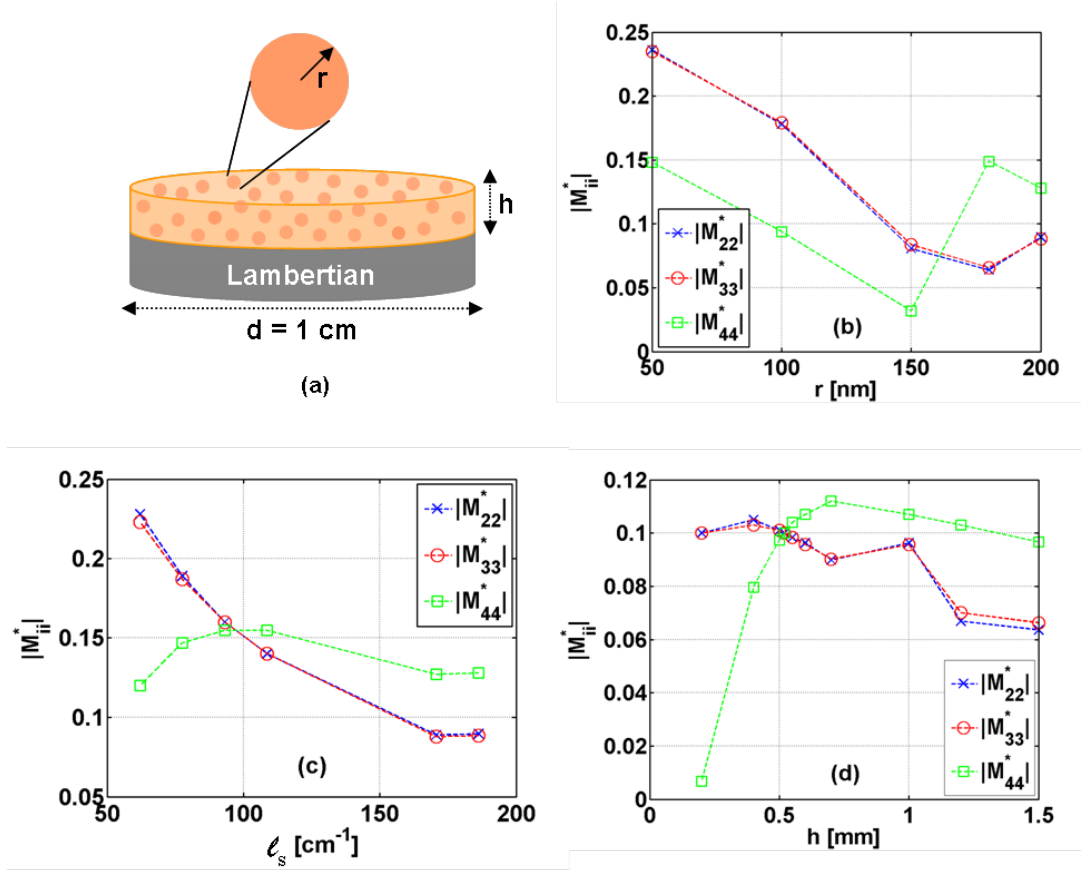


**Figure 5.1:** Absolute values of the diagonal elements  $|M_{ii}^*|$  of the backscattering Mueller matrix normalized to  $|M_{11}|$ , simulated at  $\lambda = 633 \text{ nm}$  (a): for mono-dispersed scattering medium on a lambertian substrate, modelling the mucosa on underlying layers. Each parameter was varied while keeping the others constant at the nominal values for the mucosa ( $r = 200 \text{ nm}$ ,  $\ell_s = 53.7 \mu\text{m}$ ;  $m = \frac{1.46}{1.38}$ ,  $h = 0.5 \text{ mm}$ ). (b): variation of the sphere radius  $r$  with lambertian albedo  $a = 0$ ; (c): variation of the  $\ell_s$  with  $a = 0$ , (d): variation of the scattering layer thickness with  $a = 0.3$ .

of parameters for mucosa given above and a totally absorbing lambertian ( $a = 0$ ) the simulated Mueller matrix of the sample obeys the relation:

$$|M_{22}^*| = |M_{33}^*| < |M_{44}^*|. \quad (5.2)$$

This is typical for Mie scattering regime [77]. The albedo  $a$  had to be increased to 0.3 to make all the diagonal matrix elements equal, which is not yet what is observed in experiments, namely a  $M_{44}^*$  element being significantly smaller than both  $M_{22}^*$  and  $M_{33}^*$ . As a result, the single layer model with the nominal values of the parameters for the mucosa is certainly not adequate.

Seeking for the characteristics of the phantom tissue that could reverse the regime of scattering from Mie to Rayleigh-like we tuned the model parameters one by one while keeping others constant. The results are summarized in Fig. 5.1.

We first decreased the radius of the scattering spheres from 200 nm to 50 nm to determine the typical size of organelles which may reverse the scattering regime from Mie to Rayleigh. It turned out that this regime reversal occurred already at 150 nm radius (Fig. 5.1b).



Alternatively, we reduced the volume fraction of the 200 nm radius scattering spheres from 12% to 4%, leading to an increase of the light mean free path  $\ell_s$  from 53.7  $\mu\text{m}$  to 161.11  $\mu\text{m}$  (or a reduction of  $\mu_s = \frac{1}{\ell_s}$  from 186.20 to 62.07  $\text{cm}^{-1}$ ). Increasing  $\ell_s$  is equivalent to shortening the thickness of the scattering medium, thus reducing the number of scattering events. A transition from Mie to Rayleigh scattering regimes is observed when  $\mu_s$  decreases, with a threshold at  $\mu_s = 95 \text{ cm}^{-1}$  (see Fig. 5.1c). This result suggests that multiple scattering may induce a Mie regime when the number of scattering events is large enough, even for "small" scatterers, for which a Rayleigh regime would be expected and is indeed observed at lower concentrations.

We also explored the influence of the sample thickness  $h$ , between 0.2 and 1.5 mm (Fig. 5.1d). For this study, the volume fraction of the collagen spheres (with radius 200 nm), was fixed at 6% corresponding to a  $\ell_s$  equal to 107.4  $\mu\text{m}$ , so that the experimental criterion was held among the diagonal elements of the Mueller matrix. Moreover, the lambertian albedo  $a$  was set equal to 0.3 to account for the absorption by the medium of the mucosa tissue phantom and the global contribution (absorption and scattering) to the reflected intensity from the layers beneath the mucosa. Fig. 5.1d shows a transition from Rayleigh to Mie regimes when  $h$  increases, a result consistent with the previously discussed evolution of the scattering regime with  $\mu_s$ . When layer thickness  $h$  increases, the average number of scattering events increases too, leading to the same trend as that observed when scattering coefficient  $\mu_s$  increases.

The fact that the simulated Mueller matrices of the sample, described as a suspension of collagen spheres ( $r = 200 \text{ nm}$ ) at 12% volume fraction in physiological liquid ( $\ell_s = 53.7 \mu\text{m}$ ,  $m = \frac{1.46}{1.38}$ ,  $h = 0.5 \text{ mm}$ ) obtained by varying one model parameter ( $r$ ,  $\ell_s$ ,  $h$ ) at time, for reasonable values of the parameters obey to the relation in Eq.(5.2) typical of Mie scattering, while the occurrence of Mie scattering is never seen experimentally, lead the conclusion that the proposed model of colon tissue is not realistic. It is therefore natural to explore the polarimetric response of more complex structures, which might provide better models of the complex colon tissue structure.

### **Double layer structure (submucosa and mucosa) on top of the lambertian.**

We performed simulations with two superimposed layers, representing the mucosa and submucosa, instead of a single one, on top of the lambertian substrate. We set the parameters of the mucosa and submucosa layers at the nominal values defined at the beginning of this section. The results of these simulations are shown in Fig. 5.2.

Histogram (1) represents the diagonal matrix elements of a single layer system representing the submucosa alone, which behaves as a Rayleigh scatterer, but with unrealistically low values of the  $M_{ii}^*$ . In contrast, the histograms (2) and (3) of the diagonal Mueller matrix elements, calculated with lambertian albedos equal to 0.1 and 0.3 respectively, are typical of the Mie scattering regime. Moreover, the absolute values of the  $|M_{ii}^*|$  are practically identical to those shown on Fig. 5.1 for the same parameters of the mucosa scatterers.

The fact that the relation between the diagonal elements of the simulated backscattering Mueller matrix image of the multilayered model remains unchanged compared to that of the single-mucosa-layered model confirms that the single-layered model is a quite good approximation of colon tissue. This observation supports the idea that only a small fraction of the incident light reaches the submucosa layer and an even smaller fraction is backscattered from the submucosa, without any major effect on the total polarimetric response. As a result, in the following we will consider only models with a single layer

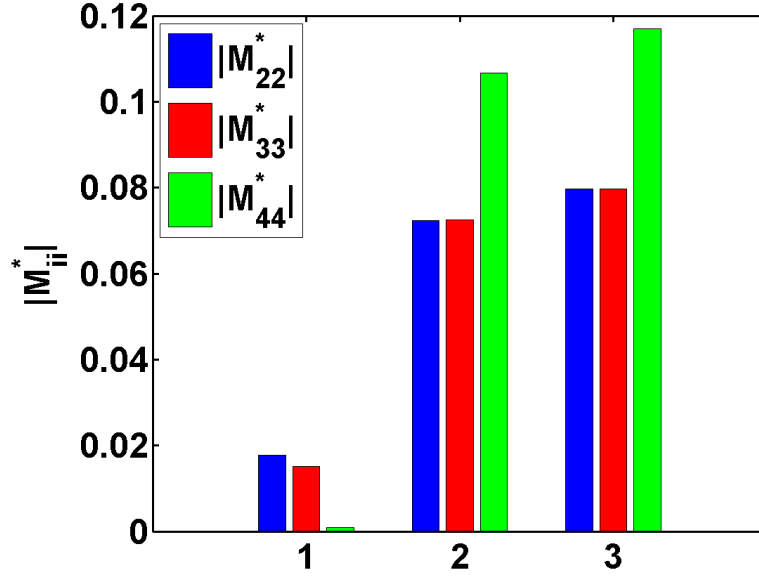


**Figure 5.2:** Absolute values of the diagonal elements of the backscattering Mueller matrix normalized by  $|M_{11}|$  simulated at  $\lambda = 633$  nm. (1): single layer representing the submucosa ( $r = 1.75$   $\mu\text{m}$ ,  $\ell_s = 19.69$   $\mu\text{m}$ ,  $m = \frac{1.38}{1.36}$ ,  $h = 0.7$  mm) on absorbing substrate (albedo  $a = 0$ ). (2): two layers representing the submucosa (same parameters as above) and mucosa ( $r_1 = 200$  nm,  $\ell_s = 53.7$   $\mu\text{m}$ ,  $m = \frac{1.46}{1.38}$ ,  $h = 0.5$  mm) on lambertian substrate of albedo  $a = 0.1$ . (3): same as (2), with  $a = 0.3$ .

above the lambertian.

**Influence of the layer shapes: simulations of budding tumors.** Normally the initial stage of colon cancer development is linked to the growth of a polyp (exophytic growth). So the question arises: can the polarimetric signature of the cancerous part be affected by not only the changes on microscopic level (uncontrolled cell growth, increase in cellular density) but on macroscopic level (morphological transformation of the sample surface) as well? To answer this question we modified the model geometry (see Fig. 5.3).

We assumed that the colon tissue undergoes a uniform deformation originating from the deep layers and pushing upwards the flat Rayleigh-like mucosa ( $r = 200$  nm,  $m = \frac{1.46}{1.38}$ ,  $\ell_s = 107.41$   $\mu\text{m}$ ,  $h = 0.5$  mm;  $a = 0$ ) while preserving its thickness and optical properties, as in [79]. We also assumed that the exophytic growth covers a surface of a circle with diameter  $d_s = 0.5$  cm (which is one half of the diameter  $d$  of the whole sample). We performed the simulations for different heights  $h_s$  of the bump (0.5 mm, 1 mm, 2 mm) to mimic the incremental growth of the colon tissue deformation. As shown on the right panel of Fig. 5.3, these morphological changes do not reverse the scattering regime, they only modify the absolute values of the diagonal elements of the Mueller matrix.

However the Rayleigh-like relation between the diagonal elements of the Mueller matrix does not hold anymore when the morphological changes are combined with an increase of the mucosa layer thickness. Fig. 5.4(a, c) represents two different modelled non-uniform deformations of colon tissue originating in the mucosa layer.

In Fig. 5.4a the exophytic growth is described as an expansion of the mucosa tissue covering a surface of radius equal to one half of the radius of the initial sample while developing upwards ( $R_s = 0.25$  cm;  $h_s = 0.5$  mm, 1 mm, 2 mm). In Fig. 5.4c the

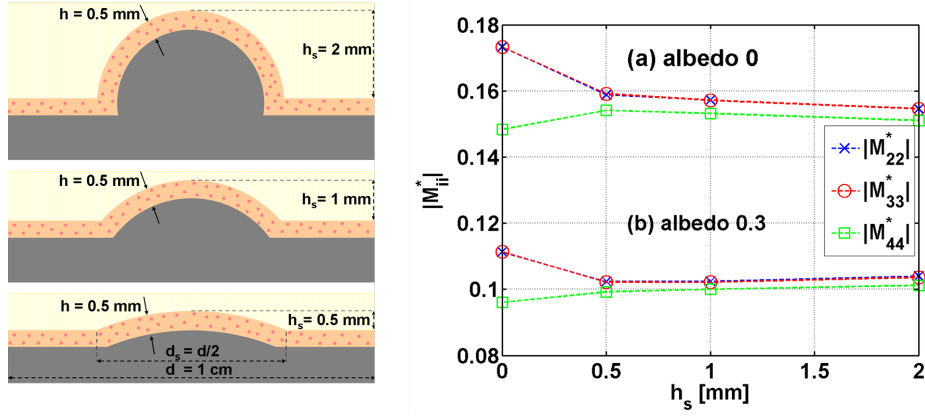


**Figure 5.3:** *Left:* sequence illustrating evolving exophytic growth in colon tissue as uniform (constant thickness) morphological deformation of the superficial layer (mucosa). *Right:* absolute values of the normalized diagonal elements  $|M_{ii}^*|$  calculated at  $\lambda = 633$  nm for the following scatterer parameters  $r = 200$  nm,  $\mu_s = 93.101$  cm $^{-1}$ ;  $m = \frac{1.46}{1.38}$ ,  $h = 0.5$  mm, albedo  $a = 0$  (a) or  $a = 0.3$  (b).

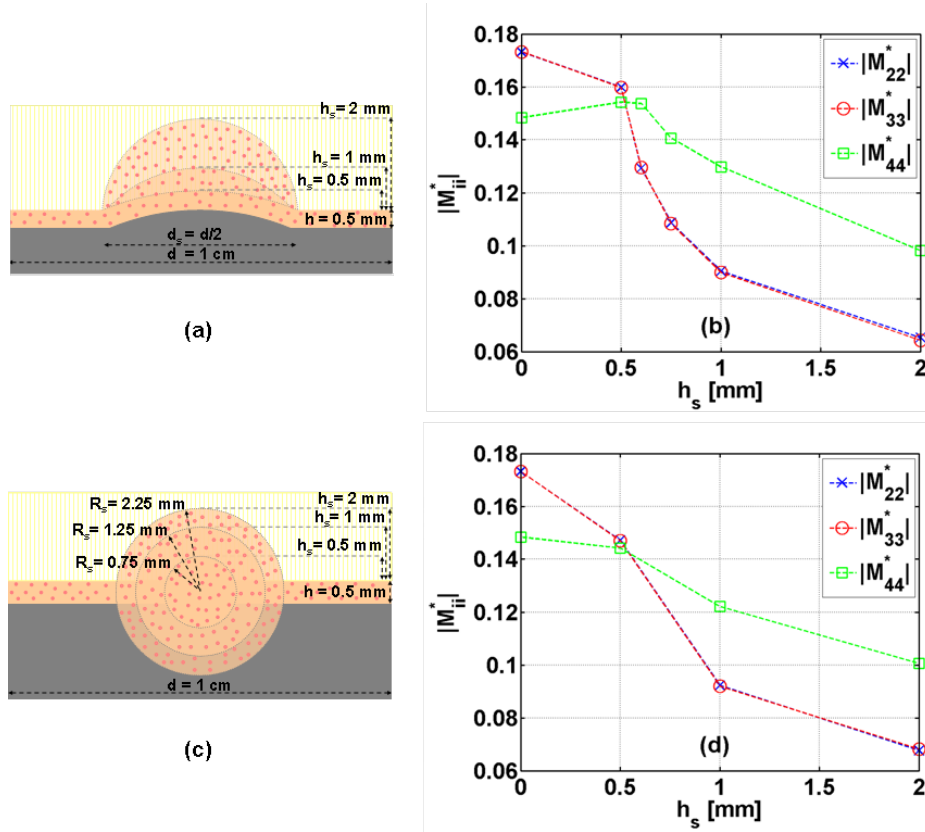


**Figure 5.4:** *Left:* two illustrations of exophytic growth originating in the mucosa, whose thickness increases in a non-uniform fashion (a, c). *Right:* absolute values of the normalized diagonal elements  $|M_{ii}^*|$  of the backscattering Mueller matrix calculated at  $\lambda = 633$  nm for a single mucosa layer ( $r = 200$  nm,  $\mu_s = 93.1$  cm $^{-1}$ ;  $m = \frac{1.46}{1.38}$ ,  $h = 0.5$  mm) on absorbing substrate (albedo  $a = 0$ ), with  $h_s$  varying from 0 (flat surface) to 2 mm (b); or  $R_s$  from 0 to 2.25 mm (d).

exophytic growth is described as radially symmetric expansion of the mucosa tissue that invades the deeper layer while also developing in height ( $R_s = 0.75$  mm,  $h_s = 0.5$  mm;  $R_s = 1.25$  mm,  $h_s = 1$  mm,  $R_s = 2.25$  mm,  $h_s = 2$  mm).

The results shown in Fig. 5.4(b, d) clearly indicate that the scattering regime for the deformed sample changes from Rayleigh-like to Mie when the height/radius of the budding area increases. This trend is consistent with that seen on flat surfaces and shown in Fig. 5.4d. However we never experimentally observed any inversion for the diagonal coefficients of the measured Mueller matrix images of the light backscattered from healthy or cancerous colon tissue.

The essential conclusion that can be drawn from the results presented in this subsection is thus that the models involving only monodisperse populations of scatterers are prone to switches between the two scattering regimes, for reasonable values of the various parameters, in contradiction with the experimental data. It is therefore mandatory to "stabilize" the model so that in all "realistic" cases the outcome is a Rayleigh scattering regime.

### 5.2.2 Multilayered structures with bimodal populations of scatterers

We now consider bimodal populations in each layer, an approach which seems reasonable to better reproduce the variety of scatterers actually found in real tissues. Moreover, due to their isotropic scattering, small scatterers may significantly impact the polarimetric response in the backscattering geometry, even at relatively low concentrations, with a strong Rayleigh type contribution, thus improving the qualitative agreement with experimental data.

In our refined model we represented the scatterers in epithelial cells in the mucosa layer – by their nuclei, the scatterers in connective tissue – by collagen in the extracellular matrix, the scatterers in cytoplasm and the extracellular matrix – by suborganelles in physiological liquid. In particular we have described the mucosa layer as collagen-like spheres ( $r_1 = 200$  nm,  $n_2 = 1.46$ ) and nuclei-like spheres ( $R_2 = 3\mu\text{m}$ ,  $n_2 = 1.4$ ) or sub-organelles/protein ( $r_2 = 50$  nm) in physiological liquid (optical index contrast  $m(\lambda) = \frac{n_s(\lambda)}{n_m}$ ,  $n_m = 1.38$ ; absorption coefficient  $\mu_a(\lambda)$ ) filling the cylinder described above (diameter 1 cm; depth,  $h$ ), with diffuse illumination at different wavelengths  $\lambda = 500, 550, 600, 633, 650, 700$  nm propagating along the axis of the cylinder. We kept the totally depolarizing lambertian substrate with typical albedo value of 0.3 to model the contribution of the layers beneath the mucosa layer. The Monte Carlo algorithm was modified in order to take into account the bimodal population of scatterers and a possible absorption by the surrounding medium. The scatterers themselves were still considered as non-absorbing (this limitation will be removed in future work). The overall scattering parameter  $\mu_s$  of the scattering medium was calculated as the sum of the scattering parameters  $\mu_{s_i} = N_i \sigma_i$  of the embedded monodisperse media. The overall mean free path of the medium is thus

$$\ell_s = \frac{1}{\sum_i N_{s_i} \sigma_{s_i}}. \quad (5.3)$$

The average Mueller matrix of the sample was defined as weighted average of Mueller matrices of the monodisperse media [59].

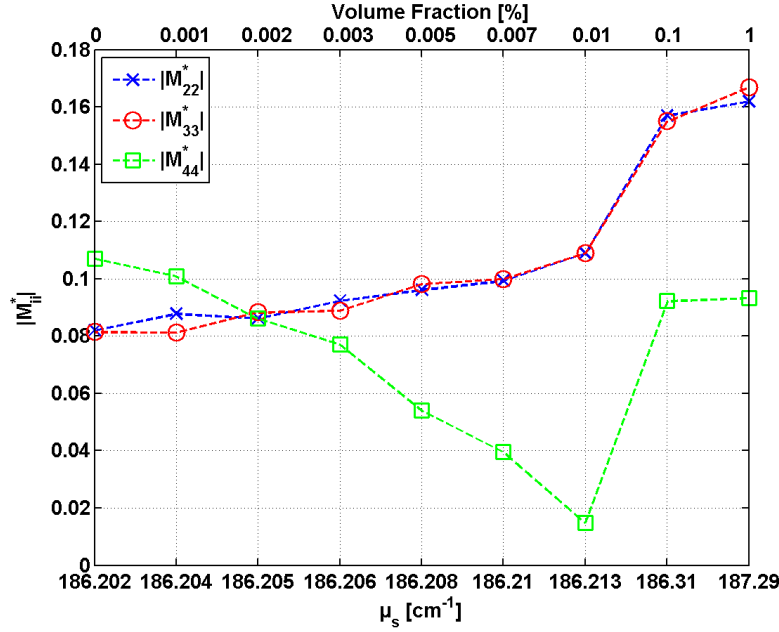


**Figure 5.5:** Normalized diagonal elements of the simulated backscattering Mueller matrices at  $\lambda = 633$  nm for a single-layer with a bimodal population of scatterers ( $r_1 = 200$  nm;  $r_2 = 50$  nm;  $m = \frac{1.46}{1.38}$ ), lambertian albedo  $a = 0.3$ . The images were calculated with  $r_1$ -sphere at 12% volume fraction varying the concentration of  $r_2$ -sphere from 0% (monodisperse population  $\mu_s = 186.202$  cm $^{-1}$ ) till 1%.

**Preliminary studies with bimodal populations for  $\lambda = 633$  nm.** To investigate the effect of the suborganelles we excluded the nuclei from the phantom tissue. The simulations were performed for collagen spheres at 12% volume fraction and varying the volume fraction of the suborganelles in the phantom tissue from 0.001% to 1% [80], which make the  $\ell_s$  decrease from 55.49 to 53.39  $\mu\text{m}$  ( $r_1 = 200$  nm,  $r_2 = 50$  nm,  $m = 1.058$ ,  $\lambda = 633$  nm) and compared to the simulation without the suborganelles (monodisperse phantom tissue,  $\ell_s = 53.7$   $\mu\text{m}$ ). The insertion of the suborganelles modified the scattering regime of the phantom tissue already at 0.003% of volume fraction ( $\ell_s = 53.7$   $\mu\text{m}$ ,  $\mu_s = 186.206$  cm $^{-1}$ ) as it is shown in Fig. 5.5. This trend is certainly due to a rapid increase of the Rayleigh type contribution due to the small spheres to the backscattered light. Increasing the concentration of the small spheres enhances the Rayleigh type contribution over the Mie type contribution due to the large spheres and strengthens the Rayleigh-like nature of the backscattering from the phantom tissue with bimodal population. It manifests itself as growing divergence between the  $|M_{22}^*|$ ,  $|M_{33}^*|$  and  $|M_{44}^*|$  values in Fig. 5.5.

We point out that  $M_{44}$  coefficient takes negative values as the concentration of the small spheres overpass 0.01% volume fraction, which explains the kink in the curve of  $|M_{44}^*|$  in Fig. 5.5.

However, to better assess the influence of organelles on the respective magnitudes of  $|M_{22}^*|$ ,  $|M_{33}^*|$  and  $|M_{44}^*|$  elements, we performed the series of simulations for different layer thicknesses with volume fractions kept constant at 12% for the medium (radius 200 nm) scatterers while the volume fraction for the small (radius 50 nm) scatterers was varied from 0% to 1%. Fig. 5.6 shows the diagonal element values versus layer thickness ranging from 0.5 to 10 mm.

In contrast with the monodisperse models investigated in the previous section, the bimodal population model does not change its scattering regime with the layer thickness

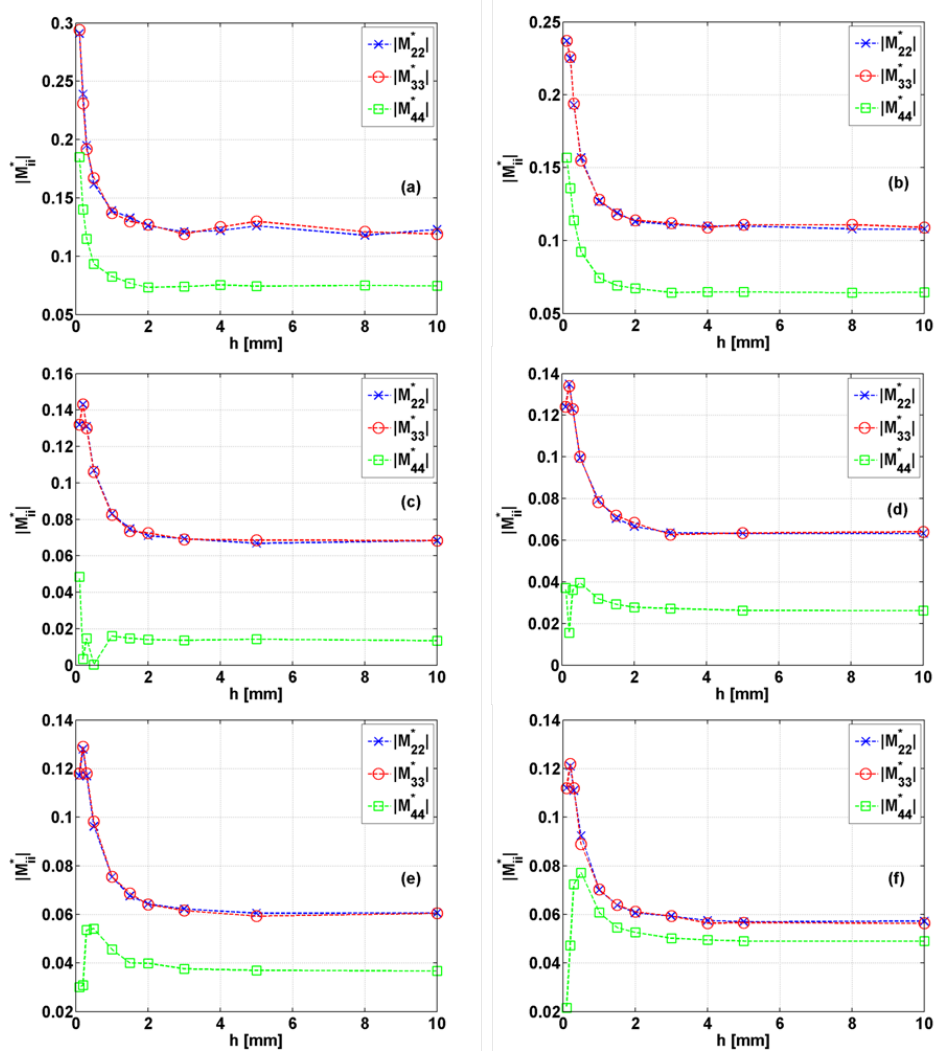


**Figure 5.6:** Normalized diagonal coefficients of the simulated backscattering Muller matrices at  $\lambda = 633$  nm for a single-layer with bimodal population of scatterers ( $r_1 = 200$  nm;  $r_2 = 50$  nm;  $m = \frac{1.46}{1.38}$ , lambertian albedo  $a = 0.3$ ). The images were calculated at different volume fraction of the  $r_2$ -sphere (a): 1%; (b): 0.1%; (c): 0.01%; (d): 0.007%; (e): 0.005%; (f): 0.003%.

$\lambda$ [nm]	500	550	600	633	650	700
$\mathbf{m}(\lambda) = \mathbf{n}_s(\lambda)/\mathbf{n}_m$	1.076	1.071	1.066	1.064	1.062	1.059
$\mu_s(\lambda)$ [ $\text{cm}^{-1}$ ]	570.72	394.86	279.29	224.43	201.25	148.27
$\mu_a(\lambda)$ [ $\text{cm}^{-1}$ ]	2.22	4.56	0.70	0.20	0.15	0.09

**Table 5.1:** Spectrally resolved optical index contrast  $\mathbf{m}$ , scattering parameter  $\mu_s$  and absorption coefficient  $\mu_a$  of the bimodal population tissue phantom.

increase. Moreover, at all concentration of the small scatterers, the diagonal coefficients of the Mueller matrix obey the experimental criterion (Eq.(5.2)) (Rayleigh scattering regime).

**Preliminary studies with bimodal populations for  $\lambda = 633$  nm.** To take into account the wavelength dependence of the simulated results the values of optical index contrast, scattering and absorption coefficients have been calculated as a function of the wavelength from the optical dispersion laws defined in Appendix C (Eqs.(C.1)-(C.6)). The results are reported in Table 5.1. The absorption from the medium was included in the model by modifying the extinction coefficient:

$$\mu_e = \mu_s + \mu_a \quad (5.4)$$

where  $\mu_s$  is the scattering coefficient,  $\mu_a$  is the absorption coefficient. The value of scattering albedo  $\beta$  used in Lambert-Beer law [50, 51], [81]-[83] was defined as:

$$\beta = \frac{\mu_s}{\mu_s + \mu_a} \quad (5.5)$$

The data shown in Table 5.1 suggest that introducing the absorption should hardly change the polarimetric response. The results presented in Fig. 5.7 clearly confirm this point.

### 5.3 Conclusion

Wavelength dependent *ex vivo* measurements of colon tissue show that this tissue behaves as a pure depolarizer throughout the visible spectrum. The relation between the diagonal elements of the experimental backscattering Mueller matrices provides the criterion to discard wrong models of colon tissue. Colon tissue was described using multilayered model with monodisperse or bimodal populations of scatterers. Monte Carlo simulations of the light backscattered from monodisperse single mucosa layer with 200 nm scatterers showed that the scattering regime switches between Mie and Rayleigh-like regimes according to the value of model parameters (scatterer radius  $r$ , scattering coefficient  $\mu_s$ , layer thickness  $h$ ), implying that the monodisperse single layer (mucosa) model is not adequate for complex colon tissue. Simulated backscattering Mueller matrix images of the double layer (mucosa and submucosa) model with monodisperse (radius 200 nm) mucosa and monodisperse (radius 1.75  $\mu\text{m}$ ) submucosa layers illustrated that adding to the model the monodisperse single submucosa layer does not impact the regime of scattering of the monodisperse single mucosa layer. As a result, the single layer (mucosa) model constitutes a valid simplification of colon tissue.

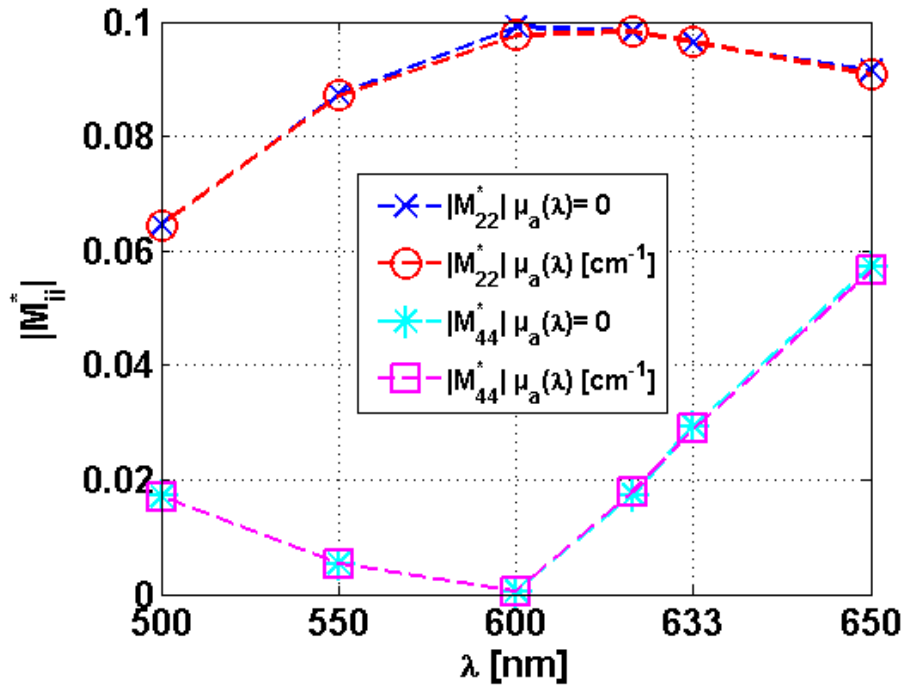


**Figure 5.7:** Spectral dependence of normalized diagonal coefficients of the simulated backscattering Mueller matrices images with diffuse light illumination for single layer bimodal population model of colon tissue ( $r_1 = 200$  nm at 12% volume fraction value;  $r_2 = 50$  nm at 0.01% volume fraction value,  $h = 0.5$  mm, lambertian albedo  $a = 0.3$ ). The images were calculated using the values of optical index contrast,  $\ell_s$  and absorption coefficient reported in Table 1 in non absorbing  $\mu_a(\lambda) = 0$ , and absorbing  $\mu_a(\lambda)$  medium.



The possible effects of the budding shape of tumors at early stages were also investigated by describing the tumor as a monodisperse scattering layer over a lambertian, assuming that the budding was due to either the mucosa or the lambertian. In both cases unrealistic Mie scattering regimes were observed for reasonable parameter values. We therefore concluded that the monodisperse model of the mucosa had to be rejected.

Conversely, the simulations of the backscattering Mueller matrix images of the bimodal population model showed that the mixture comprising small and medium (compared to wavelength) scatterers was in the Rayleigh regime of scattering already at small volume concentration of the small scatterers. Moreover the ratio of linear to circular polarization of the backscattering Mueller matrix of the phantom tissue always obeyed the experimental criterion (see Eq.(5.2)) while varying the thickness of the layer, a result which was not obtained by simulations involving only monodisperse scatterers with radius 200 nm representing the collagen. This means that the presence of the small scatterers stabilizes the optical response of the phantom tissue in the Rayleigh regime of scattering, ensuring for qualitative agreement between experimental and simulations. The simulations of the backscattering Mueller matrix images of the phantom tissue mixing large (representing the nuclei), medium and small (representing the cell organelles and suborganelles respectively) scatterers need to be performed to attain quantitative agreement between experiment and modelling. Including the absorption by the medium in our model did not modify the relation between the diagonal elements of the Mueller matrix and their absolute values at all studied wavelengths. However, the absorption can not be neglected in the realistic model of colon tissue. The next step will be to introduce the absorbing scatterers to the model in order to reproduce the experimentally observed spectral dependence of diagonal elements of the Mueller matrix. The identification of the key model parameters providing quantitative agreement between experimental and modelling at various stages of cancer evolution can help in the interpretation of the experimental data and consequently, in proper cancer staging and early cancer detection.

# Conclusion and perspectives

This manuscript reports the first attempt performed at LPICM to develop realistic, yet tractable models of the polarimetric response of tissues, the ultimate goal being a thorough understanding of the experimentally observed contrasts between healthy and pathological samples, both *in vivo* and *ex vivo*. Ideally, polarimetric imaging may emerge as an efficient technique for optical biopsy, with high sensitivities and specificities for well identified diseases, as uterine cervix CIN. Tissue models typically include multilayer structures with spherical scatterers in each layer, and totally depolarizing lambertian at the bottom, to account for the strongly depolarized light backscattered from the deep tissue layers.

This work included an experimental part, with polarimetric measurements carried out in various optical configurations.

Full Mueller matrix imaging with focussed illumination was performed on suspensions of polystyrene spheres in water, and was used to validate the Monte Carlo simulation code used throughout this study to solve the radiative transfer equation describing the propagation of polarized light in scattering media. Very good quantitative agreement was found between experimental and simulated Mueller images, which were quite different for the Rayleigh and Mie regimes, occurring respectively when the scatterer radius was smaller or larger than the optical wavelength. Moreover, simulations carried out for a low refractive index contrast between the scatterers and the surrounding medium provided images of the Rayleigh type, corresponding to the Rayleigh-Gans regime. This latter result may be relevant to the scattering by cell nuclei, whose refractive index is very close to that of cytoplasm. On the whole, Mueller imaging in backscattering configuration with focussed illumination might be useful to characterize biological samples, provided they are sufficiently uniform over sizes of the order of the "directional mean free path"  $\ell'_s$ .

Another set of experiments were carried out on an angle-resolved polarimeter mounted during a three-month stay at Oregon Healthy and Science University of Portland. This instrument included a Fourier optics imaging system, which allowed a snapshot acquisition of angle resolved Mueller matrix over  $360^\circ$  azimuthal angle and  $0^\circ$ - $16^\circ$  polar angle. Within this relatively small aperture we observed a clear dependence of the linear birefringence of a honey sample on the scattering angle, in addition to the expected optical activity. This effect is not yet fully understood. Other samples, namely suspensions of polystyrene spheres in water and mice tendon, were also studied. These samples were thin enough to ensure a dominant contribution of single scattering in the observed patterns.

This technique is a very promising one, provided it is implemented with very large numerical aperture optics, such as microscope objectives. For our purpose, such studies in single scattering regime may be very helpful to constrain some parameters relevant to the tissue model, such as the size of the scatterers embedded in the tissue. Exfoliation techniques may also be used to carry out such studies on well identified tissue layers,

such as the mucosa, the submucosa or even the pericolic tissue in the case of colon. Such "guidelines" may be essential for the correct interpretation of real space polarimetric images of *ex vivo* or *in vivo* tissues.

The third instrument used in this experimental part was a liquid crystal based real space imaging polarimeter, operated at the Pathology Department of Institut Mutualiste Montsouris. Many uterine cone biopsies and colon samples were imaged at various wavelengths between 500 and 700 nm. Most of these samples were found to be almost pure depolarizers, with a depolarizing power increasing with increasing wavelength. This trend is certainly related to the decrease of absorption by hemoglobin from the green to the red part of the spectrum, leading to an increase of the average number of scattering events that photons suffer before leaving the sample backwards. Another very general observation was that all tissues were found to scatter light in the Rayleigh or Rayleigh-Gans regimes, with larger depolarization for circular rather than linear incident polarization. Moreover, at initial stages of tumor evolution, tumoral regions appeared to be less depolarizing than healthy tissue. Finally, we observed on thick cone biopsies a complex polarimetric response, with a good correlation between detailed polarimetric characteristics (birefringence and depolarization) and the nature of the tissue (healthy, CIN III, ectropion). These results are very encouraging for the use of multispectral full Mueller polarimetry in colposcopy.

In the simulation part, which was the core of this work, we investigated various models for the tissue polarimetric response. Our priority was to reproduce the most generally observed characteristics, and primarily the systematically observed Rayleigh type responses. For colon tissue, we considered that the most efficient scatterers were collagen structures, with refractive index 1.46, and radii of the order of 200 nm in the mucosa (the most superficial layer) and 1.75  $\mu\text{m}$  in the submucosa (the underlying layer). The simplest model, comprising a single layer (the mucosa) over a lambertian representing all the underlying layers, was found to be very unstable, with transitions from Rayleigh to Mie regimes when the parameters (scatterer radius, mean free path and mucosa thickness) were varied within reasonable limits for real tissues. Inclusion of a second layer, representing the submucosa, brought only very minor changes, probably due to the strong anisotropy of the scattering to large collagen structures, leading to a very small contribution of the "large" scatterers in the backward direction. Coming back to a single layer on top of a lambertian, we found the same kind of "instabilities" when geometrical changes were introduced to mimic a budding tumor.

In contrast, the introduction of small scatterers, even at tiny concentrations, were found to "stabilize" the response to a Rayleigh type. These small scatterers may represent intracellular organelles, which may even not be visible with optical microscopes.

We believe that these results are likely to be the starting point of new developments which may lead to the elaboration of realistic models which could be used as "guidelines" for the interpretation of observed polarimetric responses. Given the number of parameters involved even in "simple" models, a first independent evaluation of some of them by angle resolved polarimetry in single scattering regime would be very helpful. The implementation of a polarimeter devoted to these studies is underway at LPICM.

Finally, we would like to stress that this work was a contribution to the now well established collaboration of the LPICM optical team with medical doctors, aimed at developing new instruments to be actually used in clinical practice.

# Appendix A

## Jones and Mueller matrices

Given the Jones matrix

$$\mathbf{J} = \begin{bmatrix} T_{11} & T_{12} \\ T_{21} & T_{22} \end{bmatrix} \equiv \begin{bmatrix} T_2 & T_3 \\ T_4 & T_1 \end{bmatrix} \quad (\text{A.1})$$

The associated Mueller matrix is obtained as

$$\mathbf{M} = \begin{bmatrix} \frac{1}{2}(M_2 + M_3 + M_4 + M_1) & \frac{1}{2}(M_2 - M_3 + M_4 - M_1) & S_{23} + S_{41} & -D_{23} - D_{41} \\ \frac{1}{2}(M_2 + M_3 - M_4 - M_1) & \frac{1}{2}(M_2 + M_3 - M_4 + M_1) & S_{23} - S_{41} & -D_{23} + D_{34} \\ S_{24} + S_{31} & S_{24} - S_{31} & S_{21} - S_{34} & -D_{21} + D_{34} \\ D_{24} + D_{31} & D_{24} - D_{31} & D_{21} + D_{34} & S_{21} - S_{34} \end{bmatrix} \quad (\text{A.2})$$

where

$$\begin{cases} M_k = T_k \overline{T_k} \\ S_{ki} = S_{ik} = \frac{1}{2}(T_i \overline{T_k} + T_k \overline{T_i}) \\ -D_{ki} = D_{ik} = \frac{j}{2}(T_i \overline{T_k} - T_k \overline{T_i}) \end{cases} \quad (\text{A.3})$$

Optical device	Eigenvalues	Eigenvectors	Jones matrix
Free space			$\begin{bmatrix} 1 & 0 \\ 0 & 1 \end{bmatrix}$
Isotropic absorbing material $\mathbf{p}^2 = \mathbf{k}$			$\begin{bmatrix} p & 0 \\ 0 & p \end{bmatrix}$
Linear polarizer in its axes at $\psi = 0$	$P_1$	$\begin{bmatrix} 1 \\ 0 \end{bmatrix}$	$\begin{bmatrix} P_1 & 0 \\ 0 & 0 \end{bmatrix}$
	0	$\begin{bmatrix} 0 \\ 1 \end{bmatrix}$	
Linear polarizer at $\psi = \frac{\pi}{2}$	0	$\begin{bmatrix} 1 \\ 0 \end{bmatrix}$	$\begin{bmatrix} 0 & 0 \\ 0 & P_2 \end{bmatrix}$
	$P_2$	$\begin{bmatrix} 0 \\ 1 \end{bmatrix}$	
Linear polarizer at $\psi = \frac{\pi}{4}$	$P_1$	$\frac{1}{\sqrt{2}} \begin{bmatrix} 1 \\ 1 \end{bmatrix}$	$\frac{P_1}{2} \begin{bmatrix} 1 & 1 \\ 1 & 1 \end{bmatrix}$
	0	$\frac{1}{\sqrt{2}} \begin{bmatrix} -1 \\ 1 \end{bmatrix}$	
Linear polarizer at $\psi$	$P_1$	$\begin{bmatrix} C_\psi \\ S_\psi \end{bmatrix}$	$P_1 \begin{bmatrix} C_\psi^2 & C_\psi S_\psi \\ C_\psi S_\psi & S_\psi^2 \end{bmatrix}$
	0	$\begin{bmatrix} -S_\psi \\ C_\psi \end{bmatrix}$	
Right circular polarizer	$P_1$	$\frac{1}{\sqrt{2}} \begin{bmatrix} 1 \\ j \end{bmatrix}$	$\frac{P_1}{2} \begin{bmatrix} 1 & -j \\ j & 1 \end{bmatrix}$
	0	$\frac{1}{\sqrt{2}} \begin{bmatrix} j \\ 1 \end{bmatrix}$	
Left circular polarizer	0	$\frac{1}{\sqrt{2}} \begin{bmatrix} 1 \\ j \end{bmatrix}$	$\frac{P_2}{2} \begin{bmatrix} 1 & j \\ -j & 1 \end{bmatrix}$
	$P_2$	$\frac{1}{\sqrt{2}} \begin{bmatrix} j \\ 1 \end{bmatrix}$	
Elliptical polarizer	$P_1$	$\begin{bmatrix} C_\alpha \\ S_\alpha e^{j\delta} \end{bmatrix}$	$\begin{bmatrix} P_1 C_\alpha^2 & P_1 e^{-j\delta} C_\alpha S_\alpha \\ P_1 e^{j\delta} C_\alpha S_\alpha & P_1 S_\alpha^2 \end{bmatrix}$
	0	$\begin{bmatrix} -S_\alpha e^{j\delta} \\ C_\alpha \end{bmatrix}$	

$$C_\alpha = \cos(\alpha); \quad S_\alpha = \sin(\alpha)$$

$$C_{2\alpha} = C_{2\chi} C_{2\psi}; \quad S_{2\alpha} C_\delta = C_{2\chi} S_{2\psi}; \quad S_{2\alpha} S_\delta = S_{2\chi}$$

$$q_1 = \frac{1}{2}(P_1^2 + P_2^2); \quad q_2 = \frac{1}{2}(P_1^2 - P_2^2); \quad q_3 = P_1 P_2$$

**Table A.1:** Jones matrices of diattenuators [2, 84].

Optical device	Eigenvalues	Eigenvectors	Jones matrix
<b>Linear dichroic polarizer in its axes</b> at $\psi = 0$	$P_1$	$\begin{bmatrix} 1 \\ 0 \end{bmatrix}$	$\begin{bmatrix} P_1 & 0 \\ 0 & P_2 \end{bmatrix}$
	$P_2$	$\begin{bmatrix} 0 \\ 1 \end{bmatrix}$	
<b>Linear dichroic polarizer</b> at $\psi = \frac{\pi}{4}$	$P_1$	$\frac{1}{\sqrt{2}} \begin{bmatrix} 1 \\ 1 \end{bmatrix}$	$\frac{1}{2} \begin{bmatrix} P_1 + P_2 & P_1 - P_2 \\ P_1 - P_2 & P_1 + P_2 \end{bmatrix}$
	$P_2$	$\frac{1}{\sqrt{2}} \begin{bmatrix} -1 \\ 1 \end{bmatrix}$	
<b>Linear dichroic polarizer</b> at $\psi$	$P_1$	$\begin{bmatrix} C_\psi \\ S_\psi \end{bmatrix}$	$\begin{bmatrix} P_1 C_\psi^2 + P_2 S_\psi^2 & (P_1 - P_2) C_\psi S_\psi \\ (P_1 - P_2) C_\psi S_\psi & P_1 S_\psi^2 + P_2 C_\psi^2 \end{bmatrix}$
	$P_2$	$\begin{bmatrix} -S_\psi \\ C_\psi \end{bmatrix}$	
<b>Circular dichroic polarizer</b>	$P_1$	$\frac{1}{\sqrt{2}} \begin{bmatrix} 1 \\ j \end{bmatrix}$	$\frac{1}{2} \begin{bmatrix} P_1 + P_2 & -j(P_1 - P_2) \\ j(P_1 - P_2) & P_1 + P_2 \end{bmatrix}$
	$P_2$	$\frac{1}{\sqrt{2}} \begin{bmatrix} j \\ 1 \end{bmatrix}$	
<b>Elliptical dichroic diattenuator</b>	$P_1$	$\begin{bmatrix} C_\alpha \\ S_\alpha e^{j\delta} \end{bmatrix}$	$\begin{bmatrix} P_1 C_\alpha^2 + P_2 S_\alpha^2 & (P_1 - P_2) e^{-j\delta} C_\alpha S_\alpha \\ (P_1 - P_2) e^{j\delta} C_\alpha S_\alpha & P_1 S_\alpha^2 + P_2 C_\alpha^2 \end{bmatrix}$
	$P_2$	$\begin{bmatrix} -S_\alpha e^{j\delta} \\ C_\alpha \end{bmatrix}$	

$$C_\alpha = \cos(\alpha); \quad S_\alpha = \sin(\alpha)$$

$$C_{2\alpha} = C_{2\chi} C_{2\psi}; \quad S_{2\alpha} C_\delta = C_{2\chi} S_{2\psi}; \quad S_{2\alpha} S_\delta = S_{2\chi}$$

$$q_1 = \frac{1}{2}(P_1^2 + P_2^2); \quad q_2 = \frac{1}{2}(P_1^2 - P_2^2); \quad q_3 = P_1 P_2$$

**Table A.2:** Jones matrices of diattenuators [2, 84].

Optical device	Mueller matrix	Diattenuation vector
Free space	$\begin{bmatrix} 1 & 0 & 0 & 0 \\ 0 & 1 & 0 & 0 \\ 0 & 0 & 1 & 0 \\ 0 & 0 & 0 & 1 \end{bmatrix}$	
Isotropic absorbing material $p^2 = k$	$\begin{bmatrix} k & 0 & 0 & 0 \\ 0 & k & 0 & 0 \\ 0 & 0 & k & 0 \\ 0 & 0 & 0 & k \end{bmatrix}$	
Linear polarizer in its axes at $\psi = 0$	$\frac{P_1^2}{2} \begin{bmatrix} 1 & 1 & 0 & 0 \\ 1 & 1 & 0 & 0 \\ 0 & 0 & 0 & 0 \\ 0 & 0 & 0 & 0 \end{bmatrix}$	$\begin{bmatrix} 1 \\ 0 \\ 0 \end{bmatrix}$
Linear polarizer at $\psi = \frac{\pi}{2}$	$\frac{P_2^2}{2} \begin{bmatrix} 1 & -1 & 0 & 0 \\ -1 & 1 & 0 & 0 \\ 0 & 0 & 0 & 0 \\ 0 & 0 & 0 & 0 \end{bmatrix}$	$\begin{bmatrix} -1 \\ 0 \\ 0 \end{bmatrix}$
Linear polarizer at $\psi = \frac{\pi}{4}$	$\frac{P_1^2}{2} \begin{bmatrix} 1 & 0 & 1 & 0 \\ 0 & 0 & 0 & 0 \\ 1 & 0 & 1 & 0 \\ 0 & 0 & 0 & 0 \end{bmatrix}$	$\begin{bmatrix} 0 \\ 1 \\ 0 \end{bmatrix}$
Linear polarizer at $\psi$	$\frac{P_1^2}{2} \begin{bmatrix} 1 & C_{2\psi} & S_{2\psi} & 0 \\ C_{2\psi} & C_{2\psi}^2 & C_{2\psi}S_{2\psi} & 0 \\ S_{2\psi} & C_{2\psi}S_{2\psi} & S_{2\psi}^2 & 0 \\ 0 & 0 & 0 & 0 \end{bmatrix}$	$\begin{bmatrix} C_{2\psi} \\ S_{2\psi} \\ 0 \end{bmatrix}$
Right circular polarizer	$\frac{P_1^2}{2} \begin{bmatrix} 1 & 0 & 0 & 1 \\ 0 & 0 & 0 & 0 \\ 0 & 0 & 0 & 0 \\ 1 & 0 & 0 & 1 \end{bmatrix}$	$\begin{bmatrix} 0 \\ 0 \\ 1 \end{bmatrix}$
Left circular polarizer	$\frac{P_2^2}{2} \begin{bmatrix} 1 & 0 & 0 & -1 \\ 0 & 0 & 0 & 0 \\ 0 & 0 & 0 & 0 \\ -1 & 0 & 0 & 1 \end{bmatrix}$	$\begin{bmatrix} 0 \\ 0 \\ -1 \end{bmatrix}$
Elliptical polarizer	$\frac{P_1^2}{2} \begin{bmatrix} 1 & C_{2\alpha} & S_{2\alpha}C_\delta & S_{2\alpha}S_\delta \\ C_{2\alpha} & C_{2\alpha}^2 & C_{2\alpha}S_{2\alpha}C_\delta & C_{2\alpha}S_{2\alpha}S_\delta \\ S_{2\alpha}C_\delta & C_{2\alpha}S_{2\alpha}C_\delta & C_\delta^2 S_{2\alpha}^2 & C_\delta S_\delta S_{2\alpha}^2 \\ S_{2\alpha}S_\delta & C_{2\alpha}S_{2\alpha}S_\delta & C_\delta S_\delta S_{2\alpha}^2 & S_\delta^2 S_{2\alpha}^2 \end{bmatrix}$	$\begin{bmatrix} C_{2\alpha} \\ S_{2\alpha}C_\delta \\ S_{2\alpha}S_\delta \end{bmatrix}$

$$C_\alpha = \cos(\alpha); \quad S_\alpha = \sin(\alpha)$$

$$C_{2\alpha} = C_{2\chi}C_{2\psi}; \quad S_{2\alpha}C_\delta = C_{2\chi}S_{2\psi}; \quad S_{2\alpha}S_\delta = S_{2\chi}$$

$$q_1 = \frac{1}{2}(P_1^2 + P_2^2); \quad q_2 = \frac{1}{2}(P_1^2 - P_2^2); \quad q_3 = P_1P_2$$

**Table A.3:** Mueller matrices of diattenuators [2, 84].

Optical device	Mueller matrix	Diattenuation vector
Linear dichroic polarizer in its axes (at $\psi = 0$ )	$\frac{1}{2} \begin{bmatrix} q_1 & q_2 & 0 & 0 \\ q_2 & q_1 & 0 & 0 \\ 0 & 0 & q_3 & 0 \\ 0 & 0 & 0 & q_3 \end{bmatrix}$	$\frac{q_2}{q_1} \begin{bmatrix} 1 \\ 0 \\ 0 \end{bmatrix}$
Linear dichroic polarizer at $\psi = \frac{\pi}{4}$	$\begin{bmatrix} q_1 & 0 & q_2 & 0 \\ 0 & q_3 & 0 & 0 \\ q_2 & 0 & q_1 & 0 \\ 0 & 0 & 0 & q_3 \end{bmatrix}$	$\frac{q_2}{q_1} \begin{bmatrix} 0 \\ 1 \\ 0 \end{bmatrix}$
Linear dichroic polarizer at $\psi$	$\begin{bmatrix} q_1 & q_2 C_{2\psi} & q_2 S_{2\psi} & 0 \\ q_2 C_{2\psi} & q_1 C_{2\psi}^2 + q_3 S_{2\psi}^2 & C_{2\psi} S_{2\psi} (q_1 - q_3) & 0 \\ q_2 S_{2\psi} & C_{2\psi} S_{2\psi} (q_1 - q_3) & q_1 S_{2\psi}^2 + q_3 C_{2\psi}^2 & 0 \\ 0 & 0 & 0 & q_3 \end{bmatrix}$	$\frac{q_2}{q_1} \begin{bmatrix} C_{2\psi} \\ S_{2\psi} \\ 0 \end{bmatrix}$
Circular dichroic polarizer	$\begin{bmatrix} q_1 & 0 & 0 & q_2 \\ 0 & q_3 & 0 & 0 \\ 0 & 0 & q_3 & 0 \\ q_2 & 0 & 0 & q_1 \end{bmatrix}$	$\frac{q_2}{q_1} \begin{bmatrix} 0 \\ 0 \\ 1 \end{bmatrix}$
Elliptical dichroic diattenuator	$\begin{bmatrix} q_1 & q_2 C_{2\alpha} & q_2 S_{2\alpha} C_\delta & q_2 S_{2\alpha} S_\delta \\ q_2 C_{2\alpha} & q_1 C_{2\alpha}^2 + q_3 S_{2\alpha}^2 & C_{2\alpha} S_{2\alpha} C_\delta (q_1 - q_3) & C_{2\alpha} S_{2\alpha} S_\delta (q_1 - q_3) \\ q_2 S_{2\alpha} C_\delta & C_{2\alpha} S_{2\alpha} C_\delta (q_1 - q_3) & C_\delta^2 (q_1 S_{2\alpha}^2 + q_3 C_{2\alpha}^2) + q_3 S_\delta^2 & C_\delta S_\delta S_{2\alpha}^2 (q_1 - q_3) \\ q_2 S_{2\alpha} S_\delta & C_{2\alpha} S_{2\alpha} S_\delta (q_1 - q_3) & C_\delta S_\delta S_{2\alpha}^2 (q_1 - q_3) & S_\delta^2 (q_1 S_{2\alpha}^2 + q_3 C_{2\alpha}^2) + q_3 C_\delta^2 \end{bmatrix}$	$\frac{q_2}{q_1} \begin{bmatrix} C_{2\alpha} \\ S_{2\alpha} C_\delta \\ S_{2\alpha} S_\delta \end{bmatrix}$

$$C_\alpha = \cos(\alpha); \quad S_\alpha = \sin(\alpha)$$

$$C_{2\alpha} = C_{2\chi} C_{2\psi}; \quad S_{2\alpha} C_\delta = C_{2\chi} S_{2\psi}; \quad S_{2\alpha} S_\delta = S_{2\chi}$$

$$q_1 = \frac{1}{2}(P_1^2 + P_2^2); \quad q_2 = \frac{1}{2}(P_1^2 - P_2^2); \quad q_3 = P_1 P_2$$

**Table A.4:** Mueller matrices of diattenuators [2, 84].



Optical device	Eigenvalues	Eigenvectors	Jones matrix
<b>Linear retarder</b> (phase shift $\delta_R$ ) in its axes ( $\psi = 0$ )	$e^{j\frac{\delta_R}{2}}$ $e^{-j\frac{\delta_R}{2}}$	$\begin{bmatrix} 1 \\ 0 \end{bmatrix}$ $\begin{bmatrix} 0 \\ 1 \end{bmatrix}$	$\begin{bmatrix} e^{j\frac{\delta_R}{2}} & 0 \\ 0 & e^{-j\frac{\delta_R}{2}} \end{bmatrix}$
<b>Linear retarder</b> (phase shift $\delta_R$ ) at $\psi = \frac{\pi}{4}$	$e^{j\frac{\delta_R}{2}}$ $e^{-j\frac{\delta_R}{2}}$	$\begin{bmatrix} 0 \\ 1 \end{bmatrix}$ $\frac{1}{\sqrt{2}} \begin{bmatrix} -1 \\ 1 \end{bmatrix}$	$\begin{bmatrix} C_{\frac{\delta_R}{2}} & jS_{\frac{\delta_R}{2}} \\ jS_{\frac{\delta_R}{2}} & C_{\frac{\delta_R}{2}} \end{bmatrix}$
<b>Linear retarder</b> (phase shift $\delta_R$ ) at $\psi$	$e^{j\frac{\delta_R}{2}}$ $e^{-j\frac{\delta_R}{2}}$	$\begin{bmatrix} C_\psi \\ S_\psi \end{bmatrix}$ $\begin{bmatrix} -S_\psi \\ C_\psi \end{bmatrix}$	$\begin{bmatrix} C_\psi^2 e^{j\frac{\delta_R}{2}} + S_\psi^2 e^{-j\frac{\delta_R}{2}} & jS_{\frac{\delta_R}{2}} S_{2\psi} \\ jS_{\frac{\delta_R}{2}} S_{2\psi} & S_\psi^2 e^{j\frac{\delta_R}{2}} + C_\psi^2 e^{-j\frac{\delta_R}{2}} \end{bmatrix}$
<b>Linear quarterwave retarder</b> (phase shift $\delta_R = \frac{\pi}{2}$ ) in its axes ( $\psi = 0$ )	$e^{j\frac{\pi}{4}}$ $e^{-j\frac{\pi}{4}}$	$\begin{bmatrix} 1 \\ 0 \end{bmatrix}$ $\begin{bmatrix} 0 \\ 1 \end{bmatrix}$	$\begin{bmatrix} e^{j\frac{\pi}{4}} & 0 \\ 0 & e^{-j\frac{\pi}{4}} \end{bmatrix}$
<b>Linear quarterwave retarder</b> (phase shift $\delta_R = \frac{\pi}{2}$ ) in its axes ( $\psi = \frac{\pi}{4}$ )	$e^{j\frac{\pi}{4}}$ $e^{-j\frac{\pi}{4}}$	$\begin{bmatrix} 0 \\ 1 \end{bmatrix}$ $\frac{1}{\sqrt{2}} \begin{bmatrix} -1 \\ 1 \end{bmatrix}$	$\begin{bmatrix} \frac{1}{2}e^{j\frac{\pi}{4}} + \frac{1}{2}e^{-j\frac{\pi}{4}} & j\frac{\sqrt{2}}{2} \\ j\frac{\sqrt{2}}{2} & \frac{1}{2}e^{j\frac{\pi}{4}} + \frac{1}{2}e^{-j\frac{\pi}{4}} \end{bmatrix}$
<b>Halfwave linear retarder</b> (phase shift $\delta_R = \pi$ ) in its axes ( $\psi = \frac{\pi}{4}$ )	$e^{j\frac{\pi}{2}}$ $e^{-j\frac{\pi}{2}}$	$\begin{bmatrix} 0 \\ 1 \end{bmatrix}$ $\frac{1}{\sqrt{2}} \begin{bmatrix} -1 \\ 1 \end{bmatrix}$	$\begin{bmatrix} \frac{1}{2}e^{j\frac{\pi}{2}} + \frac{1}{2}e^{-j\frac{\pi}{2}} & j \\ j & \frac{1}{2}e^{j\frac{\pi}{2}} + \frac{1}{2}e^{-j\frac{\pi}{2}} \end{bmatrix}$
<b>Right circular retarder</b>	$e^{j\frac{\delta_R}{2}}$ $e^{-j\frac{\delta_R}{2}}$	$\frac{1}{\sqrt{2}} \begin{bmatrix} 1 \\ j \end{bmatrix}$ $\frac{1}{\sqrt{2}} \begin{bmatrix} j \\ 1 \end{bmatrix}$	$\begin{bmatrix} C_{\frac{\delta_R}{2}} & S_{\frac{\delta_R}{2}} \\ -S_{\frac{\delta_R}{2}} & C_{\frac{\delta_R}{2}} \end{bmatrix}$
<b>Left circular retarder</b>	$e^{j\frac{\delta_R}{2}}$ $e^{-j\frac{\delta_R}{2}}$	$\frac{1}{\sqrt{2}} \begin{bmatrix} j \\ 1 \end{bmatrix}$ $\begin{bmatrix} 1 \\ j \end{bmatrix}$	$\frac{1}{2} \begin{bmatrix} C_{\frac{\delta_R}{2}} & -S_{\frac{\delta_R}{2}} \\ S_{\frac{\delta_R}{2}} & C_{\frac{\delta_R}{2}} \end{bmatrix}$
<b>Elliptical retarder</b>	$e^{j\frac{\delta_R}{2}}$ $e^{-j\frac{\delta_R}{2}}$	$\begin{bmatrix} C_\alpha \\ S_\alpha e^{j\delta} \end{bmatrix}$ $\begin{bmatrix} -S_\alpha e^{j\delta} \\ C_\alpha \end{bmatrix}$	$\begin{bmatrix} C_\alpha^2 e^{j\frac{\delta_R}{2}} + S_\alpha^2 e^{-j\frac{\delta_R}{2}} & jS_{\frac{\delta_R}{2}} S_{2\alpha} e^{-j\delta} \\ jS_{\frac{\delta_R}{2}} S_{2\alpha} e^{j\delta} & S_\alpha^2 e^{j\frac{\delta_R}{2}} + C_\alpha^2 e^{-j\frac{\delta_R}{2}} \end{bmatrix}$

$$C_\alpha = \cos(\alpha); \quad S_\alpha = \sin(\alpha);$$

$$d = C_{2\alpha} S_{\frac{\delta_R}{2}} = C_{2\chi} C_{2\psi} S_{\frac{\delta_R}{2}}; \quad e = S_{2\alpha} C_\delta S_{\frac{\delta_R}{2}} = C_{2\chi} S_{2\psi} S_{\frac{\delta_R}{2}};$$

$$f = S_{2\alpha} S_\delta S_{\frac{\delta_R}{2}} = C_{2\chi} S_{\frac{\delta_R}{2}}; \quad g = C_{\frac{\delta_R}{2}}.$$

**Table A.5:** Jones matrices of retarders [2, 84].

Optical device	Mueller matrix	Retardance vector
Linear retarder (phase shift $\delta_R$ ) in its axes ( $\psi = 0$ )	$\begin{bmatrix} 1 & 0 & 0 & 0 \\ 0 & 1 & 0 & 0 \\ 0 & 0 & C_{\delta_R} & S_{\delta_R} \\ 0 & 0 & -S_{\delta_R} & C_{\delta_R} \end{bmatrix}$	$\delta_R \begin{bmatrix} 1 \\ 0 \\ 0 \\ 0 \end{bmatrix}$
Linear retarder (phase shift $\delta_R$ ) at $\psi = \frac{\pi}{4}$	$\begin{bmatrix} 1 & 0 & 0 & 0 \\ 0 & C_{\delta_R} & 0 & -S_{\delta_R} \\ 0 & 0 & 1 & 0 \\ 0 & S_{\delta_R} & 0 & C_{\delta_R} \end{bmatrix}$	$\delta_R \begin{bmatrix} 0 \\ 1 \\ 0 \\ 0 \end{bmatrix}$
Linear retarder (phase shift $\delta_R$ ) at $\psi$	$\begin{bmatrix} 1 & 0 & 0 & 0 \\ 0 & C_{2\psi}^2 + S_{2\psi}^2 C_{\delta_R} & C_{2\psi} S_{2\psi} (1 - C_{\delta_R}) & -S_{2\psi} S_{\delta_R} \\ 0 & C_{2\psi} S_{2\psi} (1 - C_{\delta_R}) & S_{2\psi}^2 + C_{2\psi}^2 C_{\delta_R} & C_{2\psi} S_{\delta_R} \\ 0 & S_{2\psi} S_{\delta_R} & -C_{2\psi} S_{\delta_R} & C_{\delta_R} \end{bmatrix}$	$\delta_R \begin{bmatrix} C_{2\psi} \\ S_{2\psi} \\ 0 \\ 0 \end{bmatrix}$
Linear quarterwave retarder (phase shift $\delta_R = \frac{\pi}{2}$ ) in its axes ( $\psi = 0$ )	$\begin{bmatrix} 1 & 0 & 0 & 0 \\ 0 & 1 & 0 & 0 \\ 0 & 0 & 0 & 1 \\ 0 & 0 & -1 & 0 \end{bmatrix}$	$\delta_R \begin{bmatrix} 1 \\ 0 \\ 0 \\ 0 \end{bmatrix}$
Linear quarterwave retarder (phase shift $\delta_R = \frac{\pi}{2}$ ) in its axes ( $\psi = \frac{\pi}{4}$ )	$\begin{bmatrix} 1 & 0 & 0 & 0 \\ 0 & 1 & 0 & -1 \\ 0 & 0 & 1 & 0 \\ 0 & 1 & 0 & 0 \end{bmatrix}$	$\delta_R \begin{bmatrix} 0 \\ 1 \\ 0 \\ 0 \end{bmatrix}$
Halfwave linear retarder (phase shift $\delta_R = \pi$ ) in its axes ( $\psi = \frac{\pi}{4}$ )	$\begin{bmatrix} 1 & 0 & 0 & 0 \\ 0 & -1 & 0 & 0 \\ 0 & 0 & 1 & 0 \\ 0 & 0 & 0 & -1 \end{bmatrix}$	$\delta_R \begin{bmatrix} 0 \\ 1 \\ 0 \\ 0 \end{bmatrix}$
Right circular retarder	$\begin{bmatrix} 1 & 0 & 0 & 0 \\ 0 & C_{\delta_R} & S_{\delta_R} & 0 \\ 0 & -S_{\delta_R} & C_{\delta_R} & 0 \\ 0 & 0 & 0 & 1 \end{bmatrix}$	$\delta_R \begin{bmatrix} 0 \\ 0 \\ 0 \\ 1 \end{bmatrix}$
Left circular retarder	$\begin{bmatrix} 1 & 0 & 0 & 0 \\ 0 & C_{\delta_R} & -S_{\delta_R} & 0 \\ 0 & S_{\delta_R} & C_{\delta_R} & 0 \\ 0 & 0 & 0 & 1 \end{bmatrix}$	$\delta_R \begin{bmatrix} 0 \\ 0 \\ -1 \\ 0 \end{bmatrix}$
Elliptical retarder	$\begin{bmatrix} 1 & 0 & 0 & 0 \\ 0 & d^2 - e^2 - f^2 + g^2 & 2(de + fg) & 2(df - eg) \\ 0 & 2(de - fg) & -d^2 + e^2 - f^2 + g^2 & 2(e f - dg) \\ 0 & 2(df + eg) & 2(e f + dg) & -d^2 - e^2 + f^2 + g^2 \end{bmatrix}$	$\delta_R \begin{bmatrix} C_{2\alpha} \\ S_{2\alpha} C_{\delta} \\ S_{2\alpha} S_{\delta} \end{bmatrix}$

$$\begin{aligned}
C_{\alpha} &= \cos(\alpha); & S_{\alpha} &= \sin(\alpha); \\
d &= C_{2\alpha} S_{\frac{\delta_R}{2}} = C_{2\chi} C_{2\psi} S_{\frac{\delta_R}{2}}; & e &= S_{2\alpha} C_{\delta} S_{\frac{\delta_R}{2}} = C_{2\chi} S_{2\psi} S_{\frac{\delta_R}{2}}; \\
f &= S_{2\alpha} S_{\delta} S_{\frac{\delta_R}{2}} = C_{2\chi} S_{\frac{\delta_R}{2}}; & g &= C_{\frac{\delta_R}{2}}.
\end{aligned}$$

Table A.6: Mueller matrices of retarders [2, 84].



# Appendix B

## Outline of Mie theory

The contents of this subsection is taken from H. C. van de Hulst, Ref. [64].

The Maxwell's equations describe the propagation of an electromagnetic wave in a medium. The solution of the Maxwell's equation for a scattering sphere in a host medium constitutes the complete solution of the Mie problem, which includes the wave propagating inside (incident) and outside (scattered) the sphere. This formal solution in spherical coordinates constitutes the Mie theory. In order to retrieve the essential features of Mie theory we need to solve the Maxwell's equations for the scattering by an homogenous sphere of arbitrary size  $r_s$  and refractive index  $n_s$  of a plane wave propagating in an homogenous, linear optical medium of refractive index  $n_m$  (refractive index contrast of the scattering medium  $m = n_s/n_m$ ).

Let's consider the Maxwell's equations

$$\nabla \cdot \mathbf{D}(\mathbf{r}, t) = \rho \qquad \nabla \times \mathbf{E}(\mathbf{r}, t) = -\frac{\partial \mathbf{B}(\mathbf{r}, t)}{\partial t} \qquad (\text{B.1a})$$

$$\nabla \cdot \mathbf{B}(\mathbf{r}, t) = 0 \qquad \nabla \times \mathbf{H}(\mathbf{r}, t) = \mathbf{J} + \frac{\partial \mathbf{D}(\mathbf{r}, t)}{\partial t} \qquad (\text{B.1b})$$

where

$$\mathbf{D} = \varepsilon \mathbf{E} \qquad \mathbf{B} = \mu \mathbf{H} \qquad \mathbf{J} = \sigma \mathbf{E}. \qquad (\text{B.2})$$

The meaning of the symbols is:  $t$  = time,  $\mathbf{D}$  = dielectric displacement,  $\rho$  = charge densities,  $\mathbf{E}$  = electric field strength,  $\mathbf{B}$  = magnetic induction or magnetic flux density,  $\mathbf{H}$  = magnetic field strength,  $\mathbf{J}$  = current density,  $\varepsilon$  dielectric constant (or permittivity) of the medium,  $\mu$  = permeability of the medium,  $\sigma$  = electrical conductivity of the medium. An homogenous medium is characterized by constant values of  $\varepsilon$  and  $\mu$ . In particular, for linear optical materials  $\rho = 0$ ,  $\mathbf{J} = 0$ ,  $\sigma = 0$  and Eq.(B.1) can be reformulated as

$$\nabla \cdot \mathbf{D}(\mathbf{r}, t) = 0 \qquad \nabla \times \mathbf{E}(\mathbf{r}, t) = -\frac{\partial \mathbf{B}(\mathbf{r}, t)}{\partial t} \qquad (\text{B.3a})$$

$$\nabla \cdot \mathbf{B}(\mathbf{r}, t) = 0 \qquad \nabla \times \mathbf{B}(\mathbf{r}, t) = \mu \varepsilon \frac{\partial \mathbf{D}(\mathbf{r}, t)}{\partial t}. \qquad (\text{B.3b})$$

Taking curl ( $\nabla \times$ ) of Eqs.(B.3) and operating simple substitutions lead to formal decoupling the electro-magnetic ( $\mathbf{E}$ ,  $\mathbf{B}$ ) problem and expressing the electric and magnetic problems by the well-known vector wave equations

$$\nabla^2 \mathbf{E}(\mathbf{r}, t) - \mu\varepsilon \frac{\partial^2 \mathbf{E}(\mathbf{r}, t)}{\partial t^2} = 0 \quad (\text{B.4a})$$

$$\nabla^2 \mathbf{B}(\mathbf{r}, t) - \mu\varepsilon \frac{\partial^2 \mathbf{B}(\mathbf{r}, t)}{\partial t^2} = 0. \quad (\text{B.4b})$$

Due to the dual nature of the electromagnetic wave all considerations and results concerning the electrical problem are applicable to the magnetic problem. Hence, we can solve the problem of an electric wave  $\mathbf{E}$  propagating in a scattering medium and adapt the results to the magnetic wave  $\mathbf{B}$  to get the complete solution of the Maxwell's equation.

A monochromatic wave propagating in a scattering medium has the form

$$\mathbf{E}(\mathbf{r}, t) = \Re\{\mathbf{E}_0 e^{j(\mathbf{k} \cdot \mathbf{r} - \omega t)}\}. \quad (\text{B.5})$$

The hypothesis of a monochromatic wave simplifies Eq.(B.4a) into

$$\frac{\partial^2 \mathbf{E}(\mathbf{r}, t)}{\partial t^2} = -\omega^2 \mathbf{E}(\mathbf{r}, t) \quad (\text{B.6})$$

and leads the following expression of the vector wave equation

$$\nabla^2 \mathbf{E}(\mathbf{r}, t) + k^2 n_m^2 \mathbf{E}(\mathbf{r}, t) = 0 \quad (\text{B.7})$$

where  $k = \omega \sqrt{\mu_0 \varepsilon_0} = \omega/c = 2\pi/\lambda$  is the propagation constant (or wave number) in vacuum, with  $\mu_0$  and  $\varepsilon_0$  stand for vacuum permeability and permittivity. The wavelength in vacuum follows from it by  $\lambda = 2\pi/k$ . The parameter  $n_m$  is the *real refractive index* at the frequency  $\omega$  (complex refractive index  $n_m^c = \sqrt{\varepsilon - \frac{4\pi j\sigma}{\omega}}$ ). An additional result found from Eqs.(B.3) for an homogenous medium is that any rectangular components ( $x, y, z$ ) of  $\mathbf{E}$  ( $E_x, E_y, E_z$ ) verify the scalar wave equation

$$\nabla^2 f(r, t) + k^2 n_m^2 f(r, t) = 0 \quad (\text{B.8})$$

whose simplest type of solution is a plane wave. In particular a plane wave travelling in the positive  $z$  direction at any point of the space P of rectangular components ( $x, y, z$ ) has the expression

$$f = e^{-jkn_m z + j\omega t}. \quad (\text{B.9})$$

The scalar wave equation can be separated in spherical components and at any point of the space P of spherical components ( $r \cos \varphi \sin \theta, r \sin \varphi \sin \theta, r \cos \theta$ ) has elementary

solutions of the following type:

$$f_{ln} = \left. \begin{matrix} \cos l\varphi \\ \sin l\varphi \end{matrix} \right\} P_n^l(\cos \theta z_n(kn_m r)). \quad (\text{B.10})$$

Here  $n$  and  $l$  are integer:

$$n \geq l \geq 0; \quad (\text{B.11})$$

the first factor can be either a cosine or a sine; the second factor is an associated Legendre polynomial; the third factor may be any spherical Bessel function, defined by

$$z_n(\alpha) = \sqrt{\frac{\pi}{2\alpha}} Z_{n+1/2}(\alpha) \quad (\text{B.12})$$

in terms of Bessel functions. The general solution of the scalar wave equation (B.10) is a linear combination of such elementary solutions. Within all possible solutions of the scalar wave equation those which verify the vector wave equation can be found from the following theorem, which is stated without proof [85]. If  $f$  satisfies the scalar wave equation, the vectors  $\mathbf{M}_f$  and  $\mathbf{N}_f$  defined by

$$\mathbf{M}_f = \nabla \times (rf) \quad (\text{B.13a})$$

$$kn_m \mathbf{N}_f = \nabla \times \mathbf{M}_f \quad (\text{B.13b})$$

satisfy the vector wave equation and are, moreover, related by

$$kn_m \mathbf{M}_f = \nabla \times \mathbf{N}_f. \quad (\text{B.14})$$

A simple substitution shows that, if  $u$  and  $v$  are two solutions of the scalar wave equation and  $\mathbf{M}_u$ ,  $\mathbf{N}_u$ ,  $\mathbf{M}_v$ ,  $\mathbf{N}_v$  are the derived vector fields, the Maxwell equations B.3 are satisfied by

$$\left. \begin{matrix} \mathbf{E} = \mathbf{M}_v + j\mathbf{N}_u \\ \mathbf{H} = n_m(-\mathbf{M}_u + j\mathbf{N}_v) \end{matrix} \right\}. \quad (\text{B.15})$$

The full components of  $\mathbf{M}_f$  and  $\mathbf{N}_f$  are

$$M_r = 0, \quad kn_m N_r = \frac{\partial^2(rf)}{\partial r^2} + k^2 n_m^2 r f, \quad (\text{B.16a})$$

$$M_\theta = \frac{1}{r \sin \theta} \frac{\partial(rf)}{\partial \varphi}, \quad kn_m N_\theta = \frac{1}{r} \frac{\partial^2(rf)}{\partial r \partial \theta}, \quad (\text{B.16b})$$

$$M_\varphi = -\frac{1}{r} \frac{\partial(rf)}{\partial \theta}, \quad kn_m N_\varphi = \frac{1}{r \sin \theta} \frac{\partial^2(rf)}{\partial r \partial \varphi} \quad (\text{B.16c})$$

where the spherical components of the solution of the vector wave equation are written

in terms of the scalar solution and its first and second derivatives.

We now come to the Mie problem, that is the scattering of a plane wave by an homogeneous sphere. We assume that the embedding medium and the material of the scattering sphere have arbitrary refractive indexes  $n_m$  and  $n_s$ , respectively. We assume that the incident wave is linearly polarized. The origin is taken at the center of the sphere, the  $z$  axis is taken as the direction of propagation of the wave and  $x$  axis in the plane of the electrical vibration. Then the incident electromagnetic wave (propagating in the outside medium,  $n_m$ ) of amplitude 1 has the expression:

$$\mathbf{E} = \mathbf{a}_x e^{-jkn_m z + j\omega t} \quad (\text{B.17a})$$

$$\mathbf{H} = \mathbf{a}_y e^{-jkn_m z + j\omega t} \quad (\text{B.17b})$$

where  $\mathbf{a}_x$  and  $\mathbf{a}_y$  are the unit vector along the  $x$  and  $y$  axes.

It can be proved (but we omit the derivation) that the same fields propagating in the embedding medium towards the scattering sphere, and constituting the *outside, incident wave*, are written in the form given in Eq.(B.15) by choosing  $u$  and  $v$  as

$$u = e^{j\omega t} \cos \varphi \sum_{n=1}^{\infty} (-j)^n \frac{2n+1}{n(n+1)} P_n^1(\cos \theta) j_n(kn_m r) \quad (\text{B.18a})$$

$$v = e^{j\omega t} \sin \varphi \sum_{n=1}^{\infty} (-j)^n \frac{2n+1}{n(n+1)} P_n^1(\cos \theta) j_n(kn_m r) \quad (\text{B.18b})$$

which contains the elementary solutions  $P_n^l$  with  $l = 1$  only and where  $j_n(kn_m r)$  is the spherical Bessel function derived from the Bessel function of the first kind,  $J_{n+\frac{1}{2}}$ .

The form of the incident wave (outside the sphere) sets the expression of the complete solution, which consists of the incident and scattered waves. By taking into account the boundary conditions and the conditions to be verified at infinity, the *outside, scattered wave* is found to have the expression:

$$u = e^{j\omega t} \cos \varphi \sum_{n=1}^{\infty} -a_n (-j)^n \frac{2n+1}{n(n+1)} P_n^1(\cos \theta) h_n^{(2)}(kn_m r) \quad (\text{B.19a})$$

$$v = e^{j\omega t} \sin \varphi \sum_{n=1}^{\infty} -b_n (-j)^n \frac{2n+1}{n(n+1)} P_n^1(\cos \theta) h_n^{(2)}(kn_m r). \quad (\text{B.19b})$$

where we find the same elementary solution  $P_n^1$  only, as in the expression of the incident wave (Eq.(B.18));  $h_n^{(2)}(kn_m r)$  is the spherical Bessel function derived from the Bessel function of the second kind  $H_{n+\frac{1}{2}}^{(2)}$  and has been chose for its asymptotic behavior,

$$h_n^2(kn_m r) \sim \frac{j^{n+1}}{kn_m r} e^{-jkn_m r}, \quad (\text{B.20})$$

when combined with the factor  $e^{j\omega t}$ , represents an outgoing spherical wave, as is required for the scattered wave;  $a_n$  and  $b_n$  are the coefficient to be determined [85].

Similarly, the *inside wave* has the expression:

$$u = e^{j\omega t} \cos \varphi \sum_{n=1}^{\infty} n_s c_n (-j)^n \frac{2n+1}{n(n+1)} P_n^1(\cos \theta) j_n(kn_s r) \quad (\text{B.21a})$$

$$v = e^{j\omega t} \sin \varphi \sum_{n=1}^{\infty} n_s d_n (-j)^n \frac{2n+1}{n(n+1)} P_n^1(\cos \theta) j_n(kn_s r). \quad (\text{B.21b})$$

Here  $c_n$  and  $d_n$  are another pair of undetermined coefficients, and the choice of  $j_n(kn_s r)$  comes along with the refractive indexes of the media inside and outside the sphere are respectively  $n_s$  and  $n_m$ .

In order to find the undetermined coefficient ( $a_n, b_n, c_n, d_n$ ) we need to look at the condition at the boundary between the medium inside and outside the sphere which. So far we have considered a sharp boundary between the two media characterized by finite refractive indexes  $n_s$  and  $n_m$ , respectively. Let denote as  $\mathbf{n}$  the unit vector normal to the boundary surface, directed from medium  $n_s$  to medium  $n_m$  and  $(\mathbf{E}/\mathbf{H})^m$  and  $(\mathbf{E}/\mathbf{H})^s$  the fields outside and inside the sphere, respectively. Then from Maxwell's equations (B.3) we derive the boundary conditions for the *tangential components*:

$$\mathbf{n} \times (\mathbf{H}^m - \mathbf{H}^s) = 0 \quad (\text{B.22a})$$

$$\mathbf{n} \times (\mathbf{E}^m - \mathbf{E}^s) = 0 \quad (\text{B.22b})$$

for the *normal components*:

$$\mathbf{n} \cdot (n_m^2 \mathbf{E}^m - n_s^2 \mathbf{E}^s) = 0 \quad (\text{B.23a})$$

$$\mathbf{n} \cdot (\mathbf{H}^m - \mathbf{H}^s) = 0. \quad (\text{B.23b})$$

The set of boundary conditions ensure the continuity of the wave propagation at the boundary between the medium inside and outside the sphere. They may be made complete by introducing the surface charge density  $\delta$  and ensuring the conservation of the charge at the boundary:

$$\mathbf{n} \cdot (\mathbf{I}^m - \mathbf{I}^s) + \frac{d\delta}{dt} = 0 \quad (\text{B.24a})$$

$$\mathbf{n} \cdot (\varepsilon_m \mathbf{E}^m - \varepsilon_s \mathbf{H}^s) = 4\pi\delta. \quad (\text{B.24b})$$

There are no surface density here since  $n_s$  and  $n_m$  are supposed finite and surface density exist only if  $n_s$  and  $n_m$  infinite. Moreover, in the hypothesis of homogenous linear optical material ( $n_s, n_m$  real), i.e. the boundary between two dielectrics charge surface density does not exists either and Eqs. B.24 simplify as

$$\mathbf{n} \cdot (\mathbf{I}^m - \mathbf{I}^s) = 0 \quad (\text{B.25a})$$

$$\mathbf{n} \cdot (\varepsilon_m \mathbf{E}^m - \varepsilon_s \mathbf{H}^s) = 0. \quad (\text{B.25b})$$



We need to introduce the Riccati-Bessel functions which differ from the spherical Bessel function by adding an additional factor  $z$ :

$$\psi_n(z) = zj_n(z) = (\pi z/2)^{1/2} \mathbf{J}_{\mathbf{n}+1/2}(z) = S_n(z) \quad (\text{B.26a})$$

$$\chi_n(z) = -zn_n(z) = -(\pi z/2)^{1/2} \mathbf{N}_{\mathbf{n}+1/2}(z) = C_n(z) \quad (\text{B.26b})$$

$$\zeta_n(z) = zh_n^{(2)}(z) = (\pi z/2)^{1/2} \mathbf{H}_{\mathbf{n}+1/2}^{(2)}(z) = C_n(z). \quad (\text{B.26c})$$

$\psi_n(z)$ ,  $\chi_n(z)$  and  $\zeta_n(z)$  are the notations introduced in 1909 by Debye; the notations  $S_n$  and  $C_n$  are most common at present. By virtue of

$$\mathbf{H}_{\mathbf{n}}^{(2)}(z) = J_n(z) - jN_n(z) \quad (\text{B.27})$$

we get

$$\zeta_n(z) = \psi_n(z) + j\chi_n(z). \quad (\text{B.28})$$

The derivatives of these functions will be denoted by primes. The arguments are:

$$x = kn_m r_s, \quad y = kn_s r_s. \quad (\text{B.29})$$

With this notations the boundary conditions, expressed by the continuity of the four functions placed in brackets, assume the forms:

$$\left[ \frac{1}{n_s} u \right] : \quad \psi_n(x) - a_n \zeta_n(x) = n_s c_n \psi_n(y) \quad (\text{B.30a})$$

$$\left[ n_s \frac{\partial(ru)}{\partial r} \right] : \quad \psi'_n(x) - a_n \zeta'_n(x) = c_n \psi'_n(y) \quad (\text{B.30b})$$

$$[v] : \quad \psi_n(x) - b_n \zeta_n(x) = d_n \psi_n(y) \quad (\text{B.30c})$$

$$\left[ \frac{\partial(rv)}{\partial r} \right] : \quad \psi'_n(x) - b_n \zeta'_n(x) = n_s d_n \psi'_n(y). \quad (\text{B.30d})$$

On eliminating  $c_n$  from the first pair and  $d_n$  from the second pair of equations we obtain the solutions:

$$a_n = \frac{\psi'_n(y)\psi_n(x) - n_s \psi_n(y)\psi'_n(x)}{\psi'_n(y)\chi_n(x) - n_s \psi_n(y)\chi'_n(x)} \quad (\text{B.31a})$$

$$b_n = \frac{n_s \psi'_n(y)\psi_n(x) - \psi_n(y)\psi'_n(x)}{n_s \psi'_n(y)\chi_n(x) - \psi_n(y)\chi'_n(x)}. \quad (\text{B.31b})$$

For  $c_n$  and  $d_n$  we find fractions with the same respective denominators and as common numerator:

$$\psi'_n(x)\zeta_n(x) - \psi_n(x)\zeta'_n(x) = j. \quad (\text{B.32})$$

This complete the solution of the problem at any point inside and outside the sphere.

Let's consider the scattered wave. In particular we want to take a point P at a very large distance from the scattering sphere. Then, we can substitute to  $h_n^{(2)}(kn_m r_s)$  its asymptotic expression given in Eq.(B.20) and we obtain the scattered wave in the form:

$$u = -\frac{j}{kn_m r} e^{-jkn_m r + j\omega t} \cos \varphi \sum_{n=1}^{\infty} a_n \frac{2n+1}{n(n+1)} P_n^1(\cos \theta) \quad (\text{B.33a})$$

$$v = -\frac{j}{kn_m r} e^{-jkn_m r + j\omega t} \sin \varphi \sum_{n=1}^{\infty} b_n \frac{2n+1}{n(n+1)} P_n^1(\cos \theta). \quad (\text{B.33b})$$

The spherical components of the scattered wave can be written as [85]

$$E_r = H_r \longrightarrow 0 \quad (\text{B.34a})$$

$$E_\theta = H_\varphi = -\frac{j}{kn_m r} e^{-jkn_m r + j\omega t} \cos \varphi S_2(\theta) \quad (\text{B.34b})$$

$$-E_\varphi = H_\theta = -\frac{j}{kn_m r} e^{-jkn_m r + j\omega t} \sin \varphi S_1(\theta) \quad (\text{B.34c})$$

where

$$S_1(\theta) = \sum_{n=1}^{\infty} \frac{2n+1}{n(n+1)} \{a_n \pi_n(\cos \theta) + b_n \tau_n(\cos \theta)\}, \quad (\text{B.35a})$$

$$S_2(\theta) = \sum_{n=1}^{\infty} \frac{2n+1}{n(n+1)} \{b_n \pi_n(\cos \theta) + a_n \tau_n(\cos \theta)\} \quad (\text{B.35b})$$

and

$$\pi_n(\cos \theta) = \frac{1}{\sin \theta} P_n^1(\cos \theta) \quad (\text{B.36a})$$

$$\tau_n(\cos \theta) = \frac{d}{d\theta} P_n^1(\cos \theta). \quad (\text{B.36b})$$

The perpendicular and parallel components of the scattered wave are

$$\begin{cases} E_{s\perp} = -E_\varphi \\ E_{s\parallel} = E_\theta \end{cases} \quad (\text{B.37})$$

The situation is illustrated in Fig. B.1. The plane of reference is defined by the specific directions of propagation of the incident  $\mathbf{E}_0$  and scattered wave  $\mathbf{E}_s$  and  $(\mathbf{e}_{0\parallel}, \mathbf{e}_{0\perp})$  and  $(\mathbf{e}_{s\parallel}, \mathbf{e}_{s\perp})$  are the basis that decompose the amplitude vector of the incident and scattered

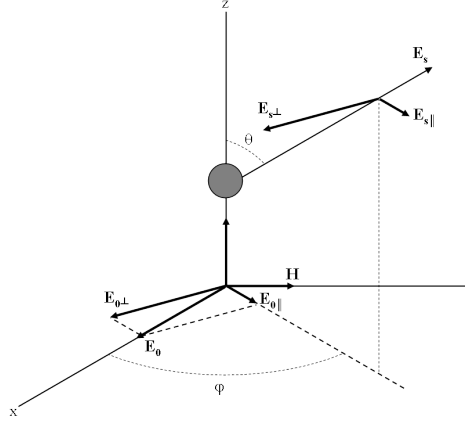


**Figure B.1:** Decomposition of electric vectors of incident and scattered waves.

wave respectively, such that

$$\mathbf{E}_0 = E_{0||}\mathbf{e}_{0||} + E_{0\perp}\mathbf{e}_{0\perp} \quad (\text{B.38a})$$

$$\mathbf{E}_s = E_{s||}\mathbf{e}_{s||} + E_{s\perp}\mathbf{e}_{s\perp}. \quad (\text{B.38b})$$

In particular, when the basis of the incident wave is

$$\begin{cases} e_{0||} = \sin \varphi \\ e_{0\perp} = \cos \varphi \end{cases} \quad (\text{B.39})$$

where  $\varphi$  is the rotation of the basis of the incident wave around the  $z$  axis, then the basis of the scattered wave is

$$\begin{cases} e_{s||} = \cos \varphi \\ e_{s\perp} = -\sin \varphi. \end{cases} \quad (\text{B.40})$$

Then Eq.(B.34) can be reformulated as

$$\mathbf{E}_s = S_2(\theta)E_{0||}\mathbf{e}_{s||} + S_1(\theta)E_{0\perp}\mathbf{e}_{s\perp} \quad (\text{B.41})$$

and  $S_1(\theta)$  and  $S_2(\theta)$  are the amplitude functions of the spherical components of the scattered wave, respectively. The same equation can be written as

$$\begin{bmatrix} E_{s||} \\ E_{s\perp} \end{bmatrix} = \begin{bmatrix} S_2(\theta) & 0 \\ 0 & S_1(\theta) \end{bmatrix} \cdot \begin{bmatrix} E_{0||} \\ E_{0\perp} \end{bmatrix} \quad (\text{B.42})$$

where the diagonal matrix is the Jones matrix of a single scattering sphere in the reference frames defined by  $(\mathbf{e}_{0||}, \mathbf{e}_{0\perp})$  and  $(\mathbf{e}_{s||}, \mathbf{e}_{s\perp})$ .

In the expression of the spherical components of the wave scattered by an homogenous sphere in any point in the far-field zone (Eqs.(B.34)) we may recognize the expression of an outgoing spherical wave, in which the energy flows outward from the particle. In fact the

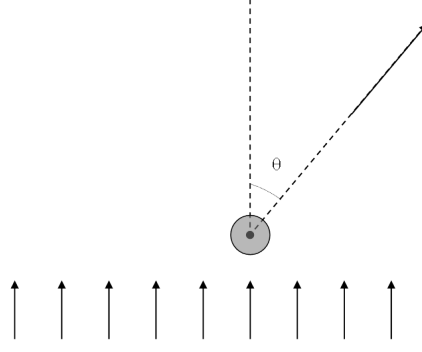


**Figure B.2:** Definition of the scattering angle. Incident light is from below [86].

general expression of a spherical wave in a point P at a large distance  $r$  from the particle is

$$s = S(\theta, \varphi) \frac{e^{-jkn_m r + j\omega t}}{jkn_m r} = S_0 e^{-jkn_m r} \quad (\text{B.43})$$

where  $S_0 = S(\theta, \varphi) \frac{e^{j\omega t}}{jkn_m r}$  and  $S(\theta, \varphi)$  is the amplitude function of the scattering particle ( $S(\theta, \varphi)/k^2$  is an area).  $S(\theta, \varphi)$  is dimensionless and is a function of the direction of P given by the polar and azimuthal angles  $(\theta, \varphi)$  that it forms with the direction of propagation of the incident light and the azimuth angle but not of its position ( $r$ ), it depends on the form, size and orientation with respect to the incident wave of the scattering particle and on the state of polarization of the incident wave. In particular, any amplitude function  $S_i(\theta)$  ( $i = 1, 2$ ) depends on the distance ( $r^{-1}$ ), the direction of scattering given by the polar angle of P ( $\theta$ ) (see Fig. B.2).

Let  $I_0$  be the intensity of the incident light,  $I_s(\theta, \varphi)$  the intensity of the scattered light in P. Since  $I_s(\theta, \varphi)$  must be proportional to  $I_0$  and  $r^{-2}$  we may write [86]

$$I_s = \frac{I_0 S(\theta, \varphi)}{k^2 n_m^2 r^2}. \quad (\text{B.44})$$

The relative values of  $I_s(\theta, \varphi)$ , or of  $S(\theta, \varphi)$  may be plotted in a polar diagram, as a function of  $\theta$  in a fixed plane through the direction of propagation. This diagram is called *scattering diagram* of the particle (Figs. 2.2, 2.4). Dividing  $S(\theta, \varphi)$  by  $k^2 n_m^2 \sigma_s$ , where  $\sigma_s$  is the scattering cross-section defined in section 2.15 we obtain the *phase function* which is dimensionless and its integral over all directions is 1.

The full relation indicating how the intensity and state of polarization of the scattered light depend on the intensity and state of polarization of the incident light are contained in the matrix equation

$$\begin{bmatrix} I \\ Q \\ U \\ V \end{bmatrix} = \frac{1}{k^2 n_m^2 r^2} \mathbf{S} \begin{bmatrix} I_0 \\ Q_0 \\ U_0 \\ V_0 \end{bmatrix} \quad (\text{B.45})$$

where  $[I, Q, U, V]^T$  and  $[I_0, Q_0, U_0, V_0]^T$  are the Stokes vectors associated to the scattered and incident light respectively. The matrix  $\mathbf{S}$  consists of 16 components  $S_{ij}$  ( $i, j = 1..4$ ) function of the incidence and scattering directions. The first of the four equations contained in this matrix equation is

$$I_s = \frac{1}{k^2 n_m^2 r^2} \{S_{11}I_0 + S_{12}Q_0 + S_{13}U_0 + S_{14}V_0\}. \quad (\text{B.46})$$

Then by comparing this equation to Eq.(B.44) we observe that

$$S = S_{11} + S_{12} \frac{Q_i}{I_i} + S_{13} \frac{U_i}{I_i} + S_{14} \frac{V_i}{I_i} \quad (\text{B.47})$$

which specifies the manner in which  $S$  depends on the state of polarization of the incident light, defined by the quantities  $Q_0/I_0$ ,  $U_0/I_0$ ,  $V_0/I_0$ . For incident natural light

$$S = S_{11}. \quad (\text{B.48})$$

In the most general case  $S$  is asymmetric. For a single scattering particle the number of independent constants reduces to 7 because 9 relations exist between the 16 elements [87]. For an homogenous spherical particle it is characterized by 3 independent constants  $i_1$ ,  $i_2$  and  $\delta$  defined above and which are function of the angle  $\theta$ . In this case 10 of the 16 components are zero, and other 6 are quadratic functions of the complex amplitude functions  $S_1(\theta)$  and  $S_2(\theta)$ .

In conclusion the whole computational problem behind the Mie theory resolves in the computation of the numbers  $S_1(\theta, \varphi)$ ,  $S_2(\theta, \varphi)$ . Generally, the scattered light is elliptically polarized even if the incident light has linear polarization, and  $S_1(\theta, \varphi)$ ,  $S_2(\theta, \varphi)$  are complex number with different phase which justify the computation of their complex conjugate  $\overline{S}_1(\theta, \varphi)$ ,  $\overline{S}_2(\theta, \varphi)$  and their intensity as  $|S_1(\theta, \varphi)|^2$ ,  $|S_2(\theta, \varphi)|^2$ .

# Appendix C

## Wavelength dependence of model parameters

The dispersion law for collagen was defined as [88, 89]:

$$n_{collagen}(\lambda) = 1.426 + \frac{19476}{\lambda^2} - \frac{1131066900}{\lambda^4}. \quad (C.1)$$

where  $\lambda$  is expressed in nm. The medium refractive index was kept constant ( $n_m = 1.38$ ).

The absorption coefficient of the medium was modelled as the sum of the absorption coefficients of haemoglobin,  $\beta$ -carotene [90] and water [91]:

$$\mu_a(\lambda) = \mu_a^{Hb}(\lambda) + \mu_a^{\beta-car}(\lambda) + \mu_a^{water}(\lambda). \quad (C.2)$$

The absorption coefficient of haemoglobin was corrected by the factor  $C_{diff}(\lambda, bvr)(<1)$  suggested by Veen [92] and Svaasand [93] to account for the effects of vessel packing:

$$C_{diff}(\lambda, bvr) = \frac{1 - \exp[-2\mu_a^{blood}(\lambda)]bvr}{2\mu_a^{blood}(\lambda)bvr} \quad (C.3)$$

where  $bvr$  is the effective blood vessel radius in mm and  $\mu_a^{blood}(\lambda)$  is the absorption coefficient of whole blood:

$$\mu_a^{blood}(\lambda) = \ln(10)C_{Hb}(\alpha\varepsilon_{HbO_2}(\lambda) + (1 - \alpha)\varepsilon_{Hb}(\lambda))/64500 \quad (C.4)$$

where  $C_{Hb}$  is the concentration of haemoglobin expressed in mg/mL,  $\alpha$  is the degree of oxygen saturation of haemoglobin,  $\varepsilon_{HbO_2}(\lambda)$  and  $\varepsilon_{Hb}(\lambda)$  are the extinction coefficients of oxygenated and deoxygenated haemoglobin, expressed in  $\text{cm}^{-1} \text{mole}^{-1}L$  [94, 95].  $C_{Hb}$  is normally equal to 150 mg/ml. We set the value of 70% for  $\alpha$  [74] and the value of 3  $\mu\text{m}$  for  $bvr$ , since the diameter of capillary is varied between 5 and 7  $\mu\text{m}$  [76] and its lower limit was estimated as 2.5  $\mu\text{m}$  [89]. The absorption coefficient of the whole blood was

multiplied by the volume fraction of blood in tissue  $V_{Hb}$  which approximated 2% [74]. The absorption coefficient of haemoglobin is given by the expression:

$$\mu_a^{Hb}(\lambda) = C_{diff}(\alpha, bvr)V_{Hb}\mu_a^{blood}(\lambda). \quad (C.5)$$

The absorption coefficient of  $\beta$ -carotene (in  $\text{cm}^{-1}$ ) is given by:

$$\mu_a^{\beta\text{-carotene}}(\lambda) = C_{\beta\text{-car}} \log(10) \varepsilon_{\beta\text{-car}}(\lambda) \quad (C.6)$$

where the  $C_{\beta\text{-car}}$  is the concentration of  $\beta$ -carotene( $\lambda$ ) [mg/ml] and  $\varepsilon_{\beta\text{-car}}(\lambda)$  is its extinction coefficient [95].

# Bibliography

- [1] K. K. Sharma, "Chapter 1. Light waves" in *Optics. Principles and applications*, (Elsevier, London, 2006).
- [2] F. Boulvert, "Analyse de milieux fortement diffusants par polarimétrie de Mueller et méthodes optiques cohérentes. Application à l'étude du syndrome cutané d'irradiation aigüe ," *Thèse de doctorat, Université de Bretagne Occidentale* (in French), 2006.
- [3] D. Goldstein, "Chapter 4. The Stokes polarization parameters" in *Polarized Light*, Second Edition, Revised and Expanded, (Marcel Dekker, New York, 2003).
- [4] V. V. Tuchin, L. V. Wang, and D.A. Zinnyakov, "Introduction" in *Optical Polarization in Biomedical Application* BIOMEDICAL AND MEDICAL PHYSICS, BIOMEDICAL ENGINEERING, (Springer-Verlag, Berlin Heidelberg, 2006).
- [5] D. Goldstein, "Chapter 3. The polarization ellipse" in *Polarized Light*, Second Edition, Revised and Expanded, (Marcel Dekker, New York, 2003).
- [6] K. K. Sharma, "Chapter 3. Polarization of light waves" in *Optics. Principles and applications*, (Elsevier, London, 2006).
- [7] J. J. Gil, "Characteristic properties of Mueller matrices," *J. Opt. Soc. Am. A* **17**(2), 328-334 (2000).
- [8] R. Barakat, "Conditions for the physical realizability of polarization matrices characterizing passive systems," *J. Mod. Optics* **34**(12), 1535-1544 (1987).
- [9] A. B. Kostinski, C. R. Givens, and J. Kwiatkowski, "Constraints on Mueller matrices of polarization optics," *Appl. Opt.* **32**(9), 1646-1651 (1993).
- [10] K. Kim, L. Mandel, and E. Wolf, "Relationship between Jones and Mueller matrices for random media," *J. Opt. Soc. Am. A* **4**(3), 433-437 (1987).
- [11] J. J. Gil, "A depolarization criterion in Mueller matrices," *Opt. Acta* **32**(3), 259-261 (1985).
- [12] D. G. M. Anderson and R. Barakat, "Necessary and sufficient conditions for a Mueller matrix to be derivable from a Jones matrix," *J. Opt. Soc. A*, **11**(8), 2305-2319 (1994).
- [13] S.-Y. Lu and R. A. Chipman, "Interpretation of Mueller matrices based on polar decomposition," *J. Opt. Soc. Am. A* **13**(5), 1106-1113 (1996).
- [14] J. Morio and F. Goudail, "Influence of the order of diattenuator, retarder and polarizer in polar decomposition of Mueller matrix," *Opt. Lett.* **29**(19), 2234-2236 (2004).



- [15] R. Ossikovski, A. De Martino, and S. Guyot, "Forward and reverse product decompositions of depolarizing Mueller matrices," *Opt. Lett.* **32**(6), 689-691 (2007).
- [16] M. Anastasiadou, S. Ben Hatit, R. Ossikovski, S. Guyot, and A. De Martino, "Experimental validation of the reverse polar decomposition of depolarizing Mueller matrices," *J. European Opt. Soc. - Rapid Publications* 2, 07018, 1-6 (2007).
- [17] R. Ossikovski, "Analysis of depolarizing Mueller matrices through a symmetric decomposition," *J. Opt. Soc. Am. A* **26**(5), 1109-1118 (2009).
- [18] H. C. van de Hulst, "Chapter 4. Wave propagation in a medium containing scatterers," in *Light scattering by small particles* (Dover, New York 1981).
- [19] [http://fr.wikipedia.org/wiki/Fichier:Mie\\_scattering.svg](http://fr.wikipedia.org/wiki/Fichier:Mie_scattering.svg) .
- [20] H. C. van de Hulst, "Chapter 6. Particles small compared to the wavelength)," in *Light scattering by small particles* (Dover, New York 1981).
- [21] V. V. Tuchin, L. V. Wang, and D.A. Zinnyakov, "Chapter 4. Polarized light interaction with strongly scattering media" in *Optical Polarization in Biomedical Application* BIOMEDICAL AND MEDICAL PHYSICS, BIOMEDICAL ENGINEERING, (Springer-Verlag, Berlin Heidelberg, 2006).
- [22] D. A. Meneley, "Week 3-Neutron transport equation," 1-9, 16 February 2001, [http://www.nuceng.ca/ep712/Neutron\\_Transport\\_Equation.pdf](http://www.nuceng.ca/ep712/Neutron_Transport_Equation.pdf).
- [23] B. Kaplan, *Applications métrologiques de l'ellipsométrie de Mueller*, Thèse de doctorat, Ecole polytechnique, Paris, France, 23 April 2002.
- [24] G. I. Bell and S. Glasstone, *Nuclear reactor theory*, Van Nostrand Reinhold, New York, 1970.
- [25] J. Lenoble, *Radiative Transfer in Scattering and Absorbing Atmospheres : Standard Computational Procedures* BIOMEDICAL AND MEDICAL PHYSICS, BIOMEDICAL ENGINEERING, (Deepak, Hampton, VA, 1985).
- [26] M. H. Niemz, *Laser-Tissue Interactions: Fundamentals and Applications*, Third, Revised Edition, (Springer, New Jersey, 2004).
- [27] A. J. Welch, G. Yoon and M. J. C. Van Gemert, "Practical models for light distribution in laser-irradiated tissue," *Lasers in Surgery and Medicine* **6**(6), 488-493 (1987).
- [28] P. S. Mudgett and L. W. Richards, "Multiple Scattering Calculations for Technology," *Appl. Opt.* **10**(7), 1485-1502 (1971).
- [29] A. Ishimaru, *Wave Propagation and Scattering in Random Media*, (Academic, New York, 1978).
- [30] S. Jacques, "Chapter 2. Light-matter" in *Inedit Book* Portland, OR 97225, 2009.
- [31] A. Ishimaru, "Diffusion of Light in turbid material," *Appl. Opt.* **28**(12), 2210-2215 (1989).

- [32] V. V. Tuchin, "Chapter 1, "Chapter 1. Optical properties of Tissues with Strong (Multiple) Scattering," in *Tissue Optics*, SPIE, Bellingham, Washington (2000).
- [33] S. Prahl, *Optical property measurements using the inverse adding-doubling program*, Oregon Medical Laser Center, Portland OR 97225, March 1995.
- [34] H. C. van de Hulst, *A new look at multiple scattering*, tech. rep., NASA Institute for Space Studies, (New York, 1962).
- [35] G. N. Plass, G. W. Kattawar, and F. E. Catchings, *Matrix operator theory of radiative transfer. 1: Rayleighscattering*, Appl. Opt. **12**(2) , 314–329 (1973).
- [36] I. Lux and L. Koblinger, *Monte-Carlo particle transport methods : neutron and photon calculations*, CRC Press, Boca Raton, 1991.
- [37] J. S. Hendricks, "A Monte Carlo Code for particle transport-an algorithm for all seasons," *Los Alamos Science*. **22**, 31-43 (1994),
- [38] P.-W. Zhai, Y. Hu, C. R. Trepte, and P. L. Lucker, "A vector radiative transfer model for coupled atmosphere and ocean systems based on successive order of scattering method," Opt. Express **17**(4), 2057-2079 (2009).
- [39] N. Metropolis and S. Ulam, "The Monte Carlo method," J. Am. Stat. Soc. **44**(247), 335-341, (1949).
- [40] Ivan Lux and Laszlo Koblinger, *Monte Carlo Transport Methods: Neutron and Photon Calculations*, (CRC Press 1991).
- [41] S. Chandrasekhar, *Radiative Transfer* (Oxford Clarendon Press, 1950).
- [42] S. Chandrasekhar and D. Elbert, "The Illumination and polarization of the sunlight sky on Rayleigh scattering," Trans. Am. Phil. Soc. **44**(6) (1954).
- [43] G. W. Kattawar and G. N. Plass "Radiance and polarization of multiple scattered light from haze and clouds," Appl. Opt. **7**(8), 1519-1527, (1968).
- [44] V. V. Tuchin, L. V. Wang, and D. A. Zinnyakov, "Chapter 9. Monte Carlo Modeling of Polarization Propagation" in *Optical Polarization in Biomedical Application* BIOMEDICAL AND MEDICAL PHYSICS, BIOMEDICAL ENGINEERING (Springer-Verlag, Berlin Heidelberg, 2006).
- [45] G. Ledanois and J.A. Virmont, "Optical medical diagnostic and imaging," Proc SPIE **3194**, 405-408 (1998).
- [46] L. Wang, S. L. Jacques, and L. Zheng, "Monte-Carlo modeling of light transport in multi-layered tissues," Comput. Methods Programs Biomed **47**(2), 131-146 (1995).
- [47] X. Wang and L. V. Wang, "Propagation of light in birefringent media: a Monte Carlo study," J. Biomed. Opt. **7**(3), 279-290 (2002).
- [48] X. Wang, L. V. Wang, C. W. Sun, and C. C. Yang, "Polarized light propagation through scattering media: time-resolved Monte Carlo simulations and experiments," J. Biomed. Opt. **8**(4), 608–617 (2003).

- [49] S. Bartel and A. Hielsher, "Monte Carlo simulations of the diffuse backscattering Mueller matrix for highly scattering media," *Appl. Opt.* **39**(10), 1580-1588 (2000).
- [50] J. C. Ramella-Roman, S. A. Prahl, and S. L. Jacques, "Three Monte Carlo programs of polarized light transport into scattering media: part I," *Opt. Express* **13**(12), 4420-4438 (2005), available for download at <http://omlc.orgi.edu/software/polarization/>
- [51] J. C. Ramella-Roman, S. A. Prahl, and S. L. Jacques, "Three Monte Carlo programs of polarized light transport into scattering media: part II," *Opt. Express* **13**(12), 10392-10405 (2005).
- [52] D. Coté, I. A. Vitkin, "Robust concentration determination of optically active molecules in turbid media with validated three-dimensional polarization sensitive Monte Carlo calculations," *Opt. Express* **13**(1), 148-163 (2005) Available at <http://www.novajo.ca/ont-canc-inst-biophotonics/>
- [53] F. Jaillon and H. Saint-Jalmes, "Description and time reduction of a Monte Carlo code to simulate propagation of polarized light through scattering media," *Appl. Opt.* **42**(16), 3290-3296 (2003).
- [54] J. Falconet, R. Sablong, E. Perrin, F. Jaillon, and H. Saint-Jalmes, "Analysis of simulated and experimental backscattered images in turbid media in linearly polarized light: estimation of the anisotropy factor," *Appl. Opt.* **47**(31), 5811-5820 (2008).
- [55] J. Dillet, C. Baravian, F. Caton, and A. Parker, "Size determination by use of two-dimensional Mueller matrices backscattered by optically thick random media," *Appl. Opt.* **45**(19), 4669-4678 (2006).
- [56] E. Tinetti, S. Avrillier, and J. M. Tualle, "Fast semianalytical Monte Carlo simulation for time-resolved light propagation in turbid media," *J. Opt. Soc. Am. A* **13**(9), 1903-1915 (1996).
- [57] S. Avrillier, E. Tinetti, J.-M. Tualle, F. Costes, F. Revel, and J.-P. Ollivier, "Real-time inversion using Monte Carlo results for the determination of absorption coefficients in multilayered tissues: application to noninvasive muscle oximetry (Part 2)," in *Diagnostic Optical Spectroscopy in Biomedicine*, T. G. Papazoglou and G. A. Wagnieres, eds., *Proc. SPIE* **4432**, 75-84 (2001).
- [58] J.-M. Tualle, H. L. Nghiem, D. Etti, R. Sablong, E. Tinetti, and S. Avrillier, "Asymptotic behavior and inverse problem in layered scattering media," *J. Opt. Soc. Am. A* **21**, 24-34, (2004).
- [59] B. Kaplan, G. Ledanois, and B. Drévilon. "Mueller matrix of dense polystyrene latex sphere suspensions: measurements and Monte Carlo simulation," *Appl. Opt.* **40**(16), 2769-2777 (2001).
- [60] S. Ben Hatit, *Polarimétrie de Mueller résolue en angle*, Thèse de l'Ecole polytechnique, Paris, France, 21 January 2009.
- [61] S. L. Jacques, R. Samatham, S. Isenath, and K. Lee, "Polarized light camera to guide surgical excision of skin cancers," *Proc. SPIE* **6842**, 68420I 1-7 (2008).

- [62] A. H. Hielscher, A. A. Eick, J. R. Mourant, D. Shen, J. P. Freyer, and I. J. Biagio, "Diffuse backscattering Mueller matrices of highly scattering media," *Opt. Exp.* **1**(13), 441-453 (1997).
- [63] V. Sankaran, J. T. Walsh, Jr., and D. J. Maitland, "Comparative study of polarized light propagation in biologic tissues," *J. Biomed. Opt.* **7**(3), 300-306 (2002).
- [64] H. C. van de Hulst, *Light scattering by small particles*, (Dover, New York, 1981).
- [65] D. S. Sabatke, M. R. Descour, E. L. Dereniak, W. C. Sweatt, S. A. Kemme, and G. S. Phipps, "Optimization of retardance for a complete Stokes polarimeter", *Opt. Lett.* **25**(11), 802-804 (2000).
- [66] J. S. Tyo, "Noise equalization in Stokes parameter images obtained by use of variable-retardance polarimeters," *Opt. Lett.* **25**(16), 1198-1200 (2000).
- [67] M. S. Smith, "Optimization of a dual-rotating retarder Mueller matrix polarimeter," *Appl. Opt.* **41**(13), 2488-2493 (2002).
- [68] A. De Martino, Y. K. Kim, E. Garcia-Caurel, B. Laude, and B. Dré villon, "Optimized Mueller polarimeter with liquid crystals," *Opt. Lett.* **28**(8), 616-618, (2003).
- [69] B. Laude-Boulesteix, A. De Martino, B. Dré villon, and L. Schwartz, "Mueller polarimetric imaging system with liquid crystals," *Appl. Opt.* **43**(14), 2824-2832 (2004).
- [70] E. Compain, S. Poirier, and B. Dré villon, "General and self-consistent method for the calibration of polarization modulators, polarimeters and Mueller matrix ellipsometers," *Appl. Opt.* **38**(16), 3490-3502 (1999).
- [71] A. Pierangelo, private communication.
- [72] A. Pierangelo, A. Benali, M. R. Antonelli, T. Novikova, P. Validire, B. Gayet, and A. De Martino, "Ex-vivo characterization of human colon cancer by Mueller polarimetric imaging," *Opt. Express* **19**(2), 1582-1593 (2011).
- [73] J.-M. André, M. Catala, J.-J. Morère, E. Escudier, G. Katsanis, and J. Poirier, "Histologie: les tissus," (Faculté de Médecine, Université Pierre et Marie Curie, PAES) (2007-8),  
<http://www.chups.jussieu.fr/polys/histo/histoP1/histoP1.pdf/>.
- [74] D. Hidović-Rowe and E. Claridge, "Modelling and validation of spectral reflectance for the colon," *Phys. Med. Biol.* **50**(6), 1071-1093 (2005).
- [75] G. Zonios, L. T. Perelman, V. Backman, R. Manoharan, M. Fitzmaurice, J. Van Dam, and M. S. Feld, "Diffuse reflectance spectroscopy of human adenomatous colon polyps in vivo," *Appl. Opt.* **38**(31), 6628-6637 (1999).
- [76] S. A. Skinner and P. E. O'Brien, "The microvascular structure of the normal colon in rats and humans," *J. Surg. Res.* **61**(2), 482-490 (1996).
- [77] M. R. Antonelli, A. Pierangelo, T. Novikova, P. Validire, A. Benali, B. Gayet, and A. De Martino, "Mueller matrix imaging of human colon tissue for cancer diagnostics: how Monte Carlo modeling can help in the interpretation of experimental data," *Opt. Express* **18**(10), 10200-10208 (2010).

- [78] A. Pierangelo, S. Manhas, A. Benali, M. R. Antonelli, T. Novikova, P. Validire, B. Gayet, and A. De Martino, "Use of Mueller imaging for the staging of human colon cancer," *Proc. SPIE* **7895**, 78950E (2011) DOI: 10.1117/12.878248.
- [79] G. I. Zonios, R. M. Cothren, J. T. Arendt, J. Wu, J. Van Dam, J. M. Crawford, R. Manoharan, and M. S. Feld. "Morphological model of human colon tissue fluorescence," *IEEE Trans. Biomed. Eng.* **43**(2), 113-122 (1996).
- [80] M. Lualdi, A. Colombo, B. Farina, S. Tomatis, and R. Marchesini, "A phantom with tissue-like optical properties in the visible and near infrared for use in photomedicine," *Lasers Surg. Med.* **28**, 237-243 (2001).
- [81] R. Graaff, M. H. Koelink, F. F. M. de Mul, W. G. Zijlstra, A. C. M. Dassel, and J. G. Aarnoudse, "Condensed Monte Carlo simulations for the description of light transport," *Appl. Opt.* **32**(4), 426-434 (1993).
- [82] A. Kienle and M. S. Patterson, "Determination of the optical properties of turbid media from a single Monte Carlo simulation," *Phys. Med. Biol.* **41**, 2221-2227 (1996).
- [83] A. Sassaroli, C. Blumetti, F. Martelli, L. Alianelli, D. Contini, A. Ismaelli, and G. Zaccanti, "Monte Carlo procedure for investigating light propagation and imaging of highly scattering media," *Appl. Opt.* **37**(31), 7392-7400 (1998).
- [84] D. Goldstein, "Appendix B. Jones and Mueller Matrices" in *Polarized Light, Second Edition, Revised and Expanded*, (Marcel Dekker, New York, 2003).
- [85] H. C. van de Hulst, "Chapter 9. Rigorous scattering theory for spheres of arbitrary size (Mie Theory)," in *Light scattering by small particles* (Dover, New York 1981).
- [86] H. C. van de Hulst, "Chapter 1. Introduction)," in *Light scattering by small particles* (Dover, New York 1981).
- [87] H. C. van de Hulst, "Chapter 5. Polarized light and symmetry relations)," in *Light scattering by small particles* (Dover, New York 1981).
- [88] A. N. Bashkatov, E. A. Genina, V. I. Kochubey, and V. V. Tuchin, "Estimation of wavelength dependence of refractive index of collagen fibers of scleral tissue," *Proc. SPIE* **4162**, 265-268 (2000).
- [89] A. N. Bashkatov and E. A. Genina, "Water refractive index in dependence on temperature and wavelength: a simple approximation," *Proc. SPIE* **5068**, 393-395 (2003).
- [90] "Research in Biomedical Optics," MIT spectroscopy,  
<http://web.mit.edu/spectroscopy/research/biomedicaloptics.html>.
- [91] H. J. van Staveren, C. J. M. Moes, J. van Marle, S. A. Prahl, and M. J. C. van Gemert, "Light scattering in intralipid-10% in the wavelength range of 400-1100 nm," *Appl. Opt.* **30**(31), 4507-4514 (1991).
- [92] R. L. P. van Veen, W. Verkruijsse, and H. J. C. M. Sterenborg, "Diffuse-reflectance spectroscopy from 500 to 1060 nm by correction for inhomogeneously distributed absorbers," *Opt. Lett.* **27**(4), 246-248 (2002).

- [93] L. O. Svaasand, E. J. Fiskerstrand, G. Kopstad, L. T. Norvang, E. K. Svaasand, J. S. Nelson, and M. W. Berns, "Therapeutic response during pulsed laser treatment of port-wine stains: dependence on vessel diameter and depth in dermis," *Lasers Med. Sci.* **10**(4), 235-243 (1995).
- [94] S. Prahl "Optical Absorption of Hemoglobin," (Portland, OR: Oregon Medical Laser Center) (1999),  
<http://omlc.ogi.edu/spectra/hemoglobin/>.
- [95] H. Du, R.-C. A. Fuh, J. Li, L. A. Corkan, and J. S. Lindsey, "PhotochemCAD: a computer-aided design and research tool in photochemistry," *Photochem. and Photobiol.* **68**(2), 141-142 (1998).

**Abstract.** Improving the visualization of dysplastic regions of uterine cervix in vivo is essential for a better identification of the locations to biopsy and a better definition of the boundaries of the anomalous regions to be surgically removed. For this purpose we propose an innovative optical technique based on multispectral full Mueller polarimetric imaging in backscattering configuration. Measurements on ex vivo samples were performed to define the best acquisition procedures and data treatments for in vivo diagnosis. As this optimization requires thorough understanding of polarimetric contrasts between healthy and anomalous tissues, we simulated the propagation of polarized light in multilayer structures representative of real tissues. These structures typically involve an uppermost layer describing the epithelium and/or superficial connective tissue, on top of a totally depolarizing lambertian surface lumping the contribution of deeper layers. The simulations were performed by using a Monte Carlo code which has been modified and adapted to our topic. We thus showed that the contribution of the cell nuclei is in fact quite small in the backscattering geometry. For connective tissue, collagen fibers were modelled as 200 nm radius scatterers. Once more this contribution alone could not reproduce the main experimental features. Very small scatterers (50 nm typical radius) have to be included to account for the Rayleigh-like polarimetric response observed in all tissues, both healthy and diseased. These scatterers may be representative of proteins, whose concentration seems to be a crucial parameter to account for the observed contrasts. In this sense, polarimetric imaging may reflect not only the tissue morphology as seen by optical microscopy, but also its physiological state, which may be a very important point for cancer detection and staging.

**Resumé.** L'amélioration de la visualisation in vivo des lésions précancéreuse (dysplasies) du col utérin est essentielle pour mieux identifier les zones à biopsier et pour optimiser la définition des limites d'exérèse chirurgicale. Dans ce but nous étudions une nouvelle technique d'imagerie polarimétrique en rétrodiffusion, que nous avons mise en œuvre sur des échantillons ex vivo dans des configurations expérimentales variées afin d'optimiser le diagnostic in vivo. Comme cette optimisation passe par la compréhension des contrastes polarimétriques observés, nous avons réalisé de nombreuses simulations de la propagation de lumière polarisée dans des structures multicouche représentatives des tissus. Ces structures comprennent typiquement une couche comportant des diffuseurs dans une matrice homogène et représentant l'épithélium ou le tissu conjonctif superficiel, et un substrat lambertien totalement dépolarisant pour les couches plus profondes. Ces simulations ont été effectuées au moyen d'un code Monte Carlo que nous avons adapté à notre problématique. Nous avons ainsi montré que la contribution des noyaux cellulaires est très faible en rétrodiffusion. Pour le tissu conjonctif, les fibres de collagène, modélisées par des diffuseurs sphériques de 200 nm de rayon, donnent une contribution plus importante que les noyaux, mais ne reproduisent pas la réponse polarimétrique de type Rayleigh observée dans tous les tissus étudiés, qu'ils soient sains ou pathologiques. En revanche, l'inclusion de diffuseurs de taille nettement inférieure à la longueur d'onde, modélisés par des sphères de 50 nm, permet de reproduire cette réponse de manière très stable. Ces diffuseurs correspondent a priori aux protéines intracellulaires. Dans le cadre de ce modèle, les contrastes observés entre tissus sains et cancéreux s'expliquent essentiellement par une variation de la concentration de ces petits diffuseurs. Ce résultat, encore préliminaire, suggère que l'imagerie polarimétrique en rétrodiffusion peut être sensible non seulement à la morphologie, mais également à l'état physiologique du tissu, ce qui peut s'avérer important pour la détection sélective des dysplasies.